A THEORETICAL AND EXPERIMENTAL INVESTIGATION OF SURFACE STRUCTURES AND GAS-SURFACE INTERACTIONS

Thesis by

Chi-Ming Chan

In Partial Fulfillment of the Requirements

for the Degree of

Doctor of Philosophy

California Institute of Technology

Pasadena, California

1979

(submitted May 16, 1979)

博學而篤志
切問而近思

論語

This thesis is dedicated
to the study of
the Laws of Nature.

Acknowledgment

I would like to thank my research advisor, Professor W. Henry Weinberg for his assistance and inspiring guidance thoughtout this work. I also thank him for spending a great deal of his time and a lot of patience(Amen! - W.H.W.) in teaching me how to write technical papers(in return, W.H.W. is learning Chinese, too!). I owe very much to Dr. Steve Cunningham for teaching me how to handle scientific problems in efficient ways. I am grateful to Dr. M. A. Van Hove who taught me to do dynamical LEED calculations and gave me continuous assistance. To Professor K. L. Luke, I extend many thanks for teaching me experimental techniques in the course of his eight months at Caltech during his sabbatical leave from the California State University, Long Beach. I am also indebted to Dr. R. Aris, Hon Chung Lau, P. A. Thiel, E. D. Williams, Dr. S. P. Withrow, Dr. J. T. Yates and Jenna J. Zinck during the course of my work.

I am greatly indebted to my parents and members of my family for their support during my study in the United States. I enjoyed very much the tennis partnership with Arthur R. Brown, Vivek M. Joshi, Windsor Sung, Sai Wai Fu and Lucy Chen, as well as my friendship with Lincoln Yang, John Lun, Kenneth Wong, Paul Chan, Richard Chen and members of his family, Marilyn Sung, Mark Siddoway and Charunya Phichitkul.

The award of the Earle C. Anthony Fellowship from the California Institute of Technology and the award of American Vacuum Society Scholarships from the American Vacuum Society is gratefully acknowledged, as well as research support from the National Science Foundation (Grant No. DMR77-14976) and the Army Research Office (Grant No. DAHC04-75-0170).

Finally, this thesis could not have appeared in its final form without the able typing of Kathy Lewis

Abstract

The object of this thesis is to study gas-surface interactions in general, and the geometrical structures of surface and overlayers in particular. Low-energy electron diffraction is employed to determine the structure of both clean metal surfaces and overlayers. In addition, an analysis of thermal desorption mass spectrometry is presented.

In part II, a convolution-transform method of LEED analyses is described which has proved to be able to determine either contraction or expansion of the crystal surface. The results of analyses of clean Al(110), Ag(110), Ni(110), Rh(111) and Pt(111) surfaces obtained by this method are comparable with those obtained by more complicated dynamical calculations. Our results indicate that both (111) surfaces have the same structure as the bulk with a slight expansion or contraction of the topmost layer of atoms by less than 5% of the bulk interlayer spacing. The analyses of the fcc(110) surfaces reveal that a contraction of 4%, 5% and 7% of the bulk interlayer spacing occurs on the Al(110), Ni(110) and Ag(110) surfaces.

In part III, the atomic arrangement of general surfaces of Ir is discussed, namely, the (111), the reconstructed (110)-(1x2), and the unreconstructed (110) surfaces. Also, the surface structure of atomic overlayers of both oxygen and sulfur on these surfaces have been analyzed. Finally, the Debye temperature characteristics of both these surfaces of clean iridium are presented and compared.

In part IV, theoretical analyses of thermal desorption mass spectra are presented. The combined effect of heating rate and pumping speed on the thermal desorption spectra was considered. It is shown that considerable error in the determination of the activation energy and the pre-exponential factor of the desorption rate coefficient can be introduced by the combined effect of high heating rate and low pumping speed. It is found that for an accurate determination of the activation energy of desorption and the pre-exponential factor of first-order desorption, the reciprocal of the product of heating rate and pumping time constant should be large, i.e., greater than approximately 0.5.

Analytic expressions were derived which allow a determination of the activation energy of desorption and the pre-exponential factor of the desorption rate coefficient using parameters obtained easily from thermal desorption mass spectra. In particular, the spectral peak widths and the temperature at which the maximum rate of desorption occurs may be used to describe both first- and second-order desorption kinetics. Explicit applications of this method in the analysis of several important classes of desorption reactions are presented.

Table of Contents

Part I

Introduction

Low-energy electron diffraction has developed quite rapidly recently due to a better understanding of the electron-solid force laws governing the diffraction scattering. With this technique, we are able to determine the atomic arrangement at the surface of a solid, chemisorption bond lengths and binding locations of adsorbed atoms and molecules. This information is invaluable in understanding various surface phenomena including chemical reactions on surfaces.

The development of LEED began with a discovery at Bell Telephone Laboratories in 1925, where Clinton Davison and Lester Germer did the first diffraction experiment on a recrystallized nickel (111) surface. However, the theory of LEED did not become sufficiently sophisticated to determine surface structures definitely until the past ten years. Kyo Kambe, Eion McRae and John Beeby were the earlier workers who laid the foundation of the theoretical methods. Then came the work of Charles Duke and Charles Tucker as well as Robert Jones which modified LEED theory with the inclusion of inelastic damping in electron propagation in the solid. Later, agreement between experiment and theory was improved by John Pendry, David Tong, Donald Jepsen, Paul Marcus and Franco Jona, with the inclusion of more phase shifts into the calculations. Precise dynamical calculations are rather costly and require huge core storage. Perturbation schemes proposed by John Pendry have been able to cut down the cost substantially. Michel Van Hove and David Tong have successfully applied the perturbation schemes on various types of surfaces.

But even with the development of the perturbation schemes, the cost

for computation is often still very high, and the computer programming is not very easy to handle. Consequently, workers in this field tried to develop a simplified method to analyze LEED data. Barney Webb and Max Lagally proposed the constant momentum transfer averaging method in which they tried to select the kinematic features from the dynamical LEED data. Kinematic means single scattering, while dynamical means multiple scattering. After the kinematic features are extracted, surface structures can be determined directly using a method similar to X-ray crystallography. Uzi Landman and David Adams also proposed an analytical method originating from X-ray crystallography which they called the Fourier transform-deconvolution method to determine surface structures of clean metal crystals. Our work on the convolution-transform method was suggested by the method of Landman and Adams. The deconvolution method proposed by Landman and Adams is not stable when the data contain multiple scattering structure. The convolution-transform method which we developed does not have this defect and has proved to be able to determine contraction or expansion of the crystal surfaces. The results obtained by our method are also comparable with those obtained by dynamical calculations. The detailed formulation of the theory and the results of our analysis by the convolution-transform method are presented in Part II.

Iridium is used extensively in industrial heterogeneous catalysis. Some examples of its use are the following: isomerization, reforming and dehydrogenation of hydrocarbons. It is also commonly used in exhaust gas treatment and desulfurization of gas oil. Before we can understand how these catalysts function, we have to know some fundamental aspects concerning these catalytic systems. But to study catalytic reaction

mechanisms at a microscopic level is very difficult, so we must adopt a model based on ideal situations and compare the behavior of a real system with the ideal system. Fortunately, we have discovered that results of many reaction kinetic studies performed on the surface of a single crystal are very similar to the results of reaction kinetic studies performed on supported catalysts. This is a strong indication that we are adopting a reasonable point of view.

This atomic arrangement of metal surfaces and overlayer structures, chemisorptive bond lengths and binding locations of adsorbed atoms are vital ingredients in a full understanding of chemical reactions on surfaces. The clean Ir(110) and (111) surfaces and overlayer structures on these surfaces were studied by low-energy electron diffraction. Clean (110) and (111) surfaces of Ir were adopted as model catalysts. Oxygen, which is an important reactant (e.g., in partial and total oxidation reactions) and sulfur, which is a common poison in many catalytic systems, were chosen as overlayers on these surfaces for structural analyses. The results of these analyses provide vital information in the study of catalytic reactions and catalyst poisoning. The detailed results of these analyses are presented in Part III.

In order to understand heterogeneously catalyzed surface reactions, another ingredient which is of prime importance is the reaction rate parameters. During a heterogeneously catalyzed reaction (ignoring mass transfer), reactants first are adsorbed on a surface. In a bimolecular process the reaction takes place with one (Eley-Rideal) or both (Langmuir-Hinselwood) of the reactants chemisorbed on the surface, and finally the products of the reaction desorb from the surface. Desorption is the final

step in any catalytic reaction, so it is necessary to be able to calculate desorption rate parameters for different operating conditions. Thermal desorption mass spectrometry has been used extensively to determine these kinetic parameters. In this technique, the temperature of the substrate is increased, and the change in the partial pressure in the reactor is detected mass spectrometrically.

There are four important kinetic parameters which may be determined by a thermal desorption experiment: (1) the kinetic order of the desorption reaction, (2) the activation energy of desorption, (3) the pre-exponential factor of the desorption rate coefficient, and (4) the number of binding states of the admolecule. Redhead has shown that,

$$\frac{E_d}{kT_M^2} = \frac{\nu_o^{(1)}}{\beta} \exp\left(-\frac{E_d}{kT_M}\right) \text{ , for m=1} \qquad (1)$$

and

$$\frac{E_d}{kT_M^2} = \frac{\nu_o^{(2)}\sigma_o}{\beta} \exp\left(-\frac{E_d}{kT_M}\right) \text{ , for m=2} \qquad (2)$$

where E_d is the activation energy of desorption, k is the Boltzmann constant, T_M is the temperature at which the maximum desorption rate occurs, σ_o is the initial surface coverage, m is the order of the desorption reaction, β is the heating rate, and $\nu_o^{(m)}$ is the pre-exponential factor of the desorption rate coefficient for order m. The assumptions in the analysis of Redhead are the following: (1) The pumping speed is rapid compared to the rate of thermal desorption; (2) The substrate temperature is uniform; and (3) E_d is constant with respect to time and temperature. Eqs. (1) and (2) may be used to calculate E_d for an assumed pre-exponential factor. However, using an assumed value for the pre-exponential factor may result in a

considerable error in the determination of E_d. An alternate way to determine the value of E_d without having to assume a value for the pre-exponential factor à priori has also been suggested by Redhead. Using this method, one has to obtain first the value of $d(\ell n\beta)/d(\ell nT_M)$, and then calculate the value of E_d for first-order desorption kinetics from the expression

$$2 + \frac{E_d}{kT_M} = d(\ell n\beta)/d(\ell nT_M) \ . \qquad (3)$$

For second-order desorption kinetics, a plot of $\ell n(\sigma_o T_M^2)$ as a function of $1/T_M$ must be constructed, and the value of E_d/k is determined from the slope of the curve. To obtain an accurate determination of E_d, β has to be varied by several orders of magnitude. This is not always possible for the interesting case of desorption from the surfaces of bulk single crystals. If β is very small, wall or re-adsorption effects may be important; alternately β may not be too large due to limitations in heating massive single crystals. Even if β could be made very large, then multiple peaks might not be resolved. Furthermore, a plot of $\ell n\beta$ versus ℓnT_M is not linear. Hence, the application of Eq. (3) to determine an accurate value of E_d is difficult. These two methods of analyzing thermal desorption mass spectra have been used extensively by workers in this field, but they both have their own drawbacks, as mentioned above.

In Part IV, we describe a simple and rapid method to determine both the pre-exponential factor and the activation energy of the desorption rate coefficient. In principle, if the kinetic order of the desorption reaction is known, our method may be used to determine the activation energy as

well as the pre-exponential factor easily with one thermal desorption spectrum, i.e., only one value of β is needed. In our method of analysis, the following information has to be extracted from a thermal desorption spectrum. Consequently, the method is quite easy to apply in practice.

Redhead and Ehrlich have shown qualitatively the individual effect of pumping speed and heating rate on the shape and the peak position of a thermal desorption spectrum. However, no quantitative error analysis of the combined effects of heating rate and pumping speed has been made to date. In part IV, we demonstrate the importance of the combined effect of heating rate and pumping speed. It is shown that the "goodness" of a thermal desorption spectrum can be judged by the product of heating rate and pumping speed and not by the magnitude of each one individually. Furthermore, it is shown that in order to obtain a pressure profile during a thermal desorption measurement which is proportional to the desorption rate, the reciprocal of the product of heating rate and pumping time constant must be large, i.e., greater than approximately 0.5.

Studies concerning the adsorption of sulfur on the reconstructed Ir(110)-(1x2) surface are presented in Appendix I. The application of a nonlinear analysis using a multi-timing perturbative scheme on a isothermal, irreversible reaction occurring on a catalytic surface, where the activation energy of the rate limiting step is allowed to depend on the surface coverage of an intermediate species, is presented in Appendix II.

Part II

Surface Relaxation From Low-Energy Electron Diffraction Via a Transform Method

Chapter 1

DETERMINING SURFACE RELAXATION FROM LEED VIA A TRANSFORM METHOD

S. L. Cunningham, C. M. Chan and W. H. Weinberg

Journal of Vacuum Science and Technology, 14, 312 (1977)

A method for determining the degree of relaxation of a clean metal surface from realistic LEED data is presented using the complex Fourier transform of the beam intensity as a function of electron momentum (the Patterson function). As shown by Landman and Adams (*1*), the calculated Patterson function $P_c(z)$ corresponding to an analysis of kinematic (not dynamic) LEED data is given by the convolution integral

$$P_c(z) = \int_{-\infty}^{\infty} W(z')P_d(z - z')dz' \tag{1}$$

where $W(z)$ is the complex Fourier transform of the envelope of the LEED data in momentum space (specifically including the cut-off at finite momentum) and $P_d(z)$ is given by

$$P_d(z) = \sum_i g_i[\delta(z-z_i) + \delta(z+z_i)] \tag{2}$$

where the set $\{z_i\}$ is a map of all the distances between layers in the crystal surface region and the coefficients $\{g_i\}$ decrease in amplitude for increasing z_i. Combining Eqs. (1) and (2) gives

$$P_c(z) = \sum_i g_i[W(z-z_i) + W(z+z_i)] \tag{3}$$

In our method a quantity called the residual R is determined by

$$R^2 = \int_o^{\infty} [P_c(z) - P_o(z)]^2 dz \tag{4}$$

where $P_o(z)$ is the Patterson function of the actual LEED data. For an assumed set of positions $\{z_i\}$, the coefficients $\{g_i\}$ are determined in the least-square-sense to minimize the residual. By varying the positions of the delta functions as well as the value of the inner potential, and by looking for smallest residual as well as the most physical set of coefficients $\{g_i\}$, the structure can be determined.

To illustrate the method, we show in Fig. 1a the kinematic I-V curve for the (11) beam of a material with a bulk spacing of d = 2.23 Å, a surface layer relaxed outward by t = 9%, and an inner potential V_o = 16 eV. The constant line is the window function. For the case of a single layer relaxing, the set of positions $\{z_i\}$ can be completely determined by one parameter t to be

$$\{z_i\} = 0, nd, (n + t)d, n = 1,2,3 \ldots \quad (5)$$

By varying the choices of V_o and t, the residual can be calculated to give the surface shown in Fig. 1b. In Fig. 1c we show the topographic plot of this surface. The residual values have been normalized by dividing each value by

$$R_o = \int_o^\infty P_o^2(z)dz \ . \quad (6)$$

The minimum at V_o = 17 eV and t = 8% is very pronounced. The reasons why this minimum does not occur at exactly the correct solution for this kinematic data are fully discussed.

Using this method, the bulk of the work presented is the analysis of fully dynamic data (calculated) for four beams from the W(110) surface for assumed relaxation of t = 9%, -9%, and 0% as calculated by van Hove and Tong (*2*). We present analysis of data with different energy ranges as well as with different choices for the window function. We conclude that at its best the method can completely determine the surface relaxation and at its worst it can narrow down considerably the choices of structure which may have to be analyzed with multiple scattering programs. This is the first evidence that a transform method can determine the degree of relaxation of a highly dynamic scattering material.

References

1. U. Landman and D. L. Adams, J. Vac. Sci. Technol. 11, 195 (1974), 12, 260 (1975), 13, 363 (1975); Phys. Rev. Letters 33, 585 (1974); U. Landman, Faraday Disc. of Chem. Soc. 60, 230 (1975).

2. M. A. Van Hove and S. Y. Tong, Surface Sci. 54, 91 (1976).

Figure Caption

Figure 1: (a) Kinematic interference function and constant window function appropriate for W(110) using parameters in Ref. 2 and assuming V_o = 16 eV and a surface relaxation outward of t = 9%. (b) Plot of the residual R as a function of choice of inner potential V_o and % relaxation t. (c) Topographic contour plot of the surface in (b). All contours are separated by $\Delta R = 0.05$.

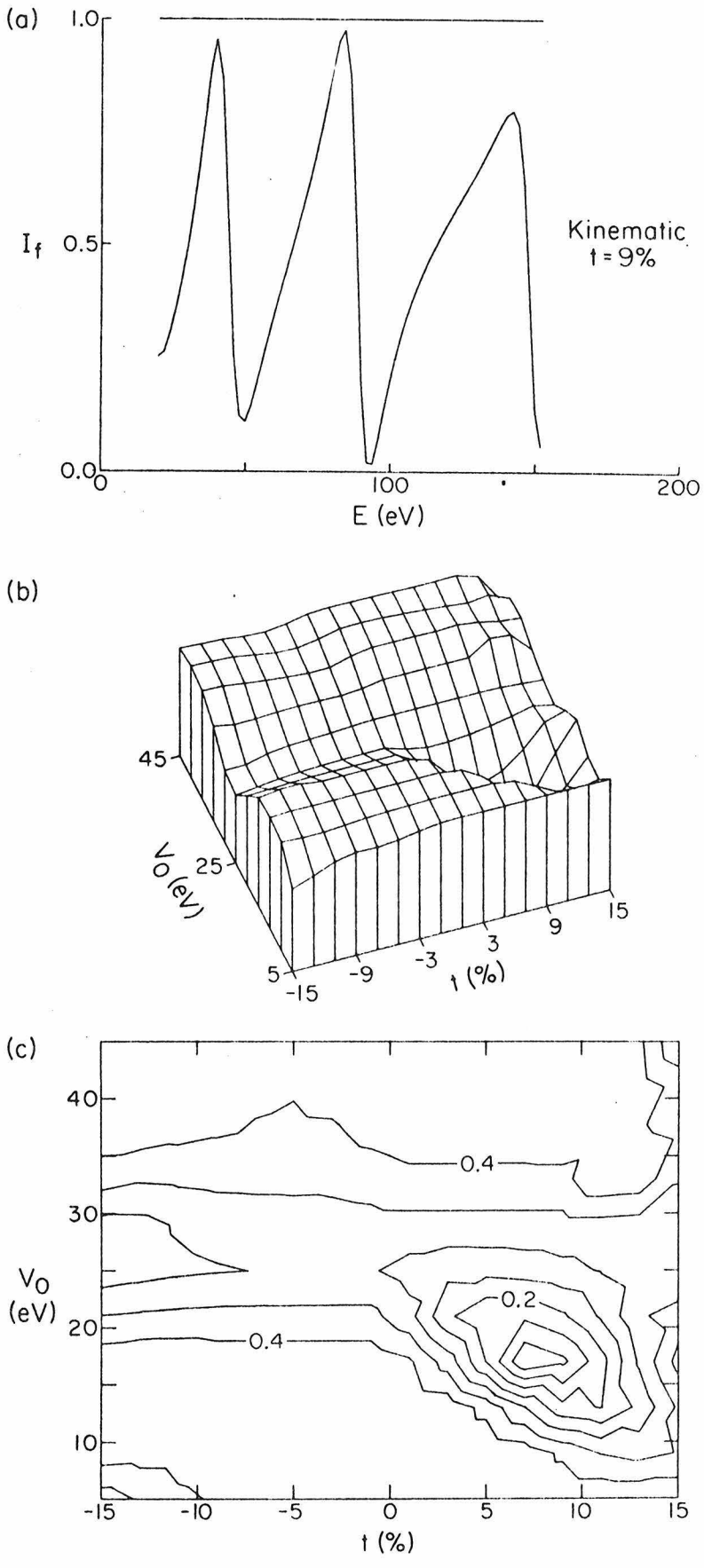
(a)
1.0
0.5
0.0
I_f
0
100
200
E (eV)
Kinematic
t = 9%
(b)
45
25
5
V_0 (eV)
-15
-9
-3
3
9
15
t (%)
(c)
40
30
20
10
V_0
(eV)
0.4
0.2
0.4
-15
-10
-5
0
5
10
15
t (%)

Figure 1

Chapter 2

DETERMINING SURFACE RELAXATION FROM LEED VIA A TRANSFORM METHOD

S. L. Cunningham, C.-M. Chan and W. H. Weinberg

Division of Chemistry and Chemical Engineering
California Institute of Technology
Pasadena, California 91125

Physical Review B 18, 1537-49 (1978)

ABSTRACT

A method for determining the atomic structure of a clean metal surface from LEED data is presented using the Fourier transform of the beam intensity as a function of electron momentum (the Patterson function). A model Patterson function which is made up of the convolution product of a window transform function and a series of delta functions representing the crystal layer spacing is fitted in a least-squares-sense to the Patterson function of the data. By varying the positions of the delta functions and examining the quality of the fit, the structure can be determined. The method is fully illustrated using model kinematic data from a surface which is both relaxed and unrelaxed. The approximations necessary to obtain a perfect fit between the Patterson function of the kinematic data and the convolution product are discussed showing that even ideal data cannot be analyzed to give an "exact" solution. Nevertheless, it is shown that the method is capable of determining structure even from data that are highly dynamic. This is illustrated by analyzing multiple scattering data for W(110) which have been calculated by Van Hove and Tong. Four non-equivalent beams are analyzed for inward relaxation, outward relaxation and no relaxation. The effect of using data with different energy ranges is discussed as well as different prescriptions for choosing the window transform function.

I. Introduction

The first data from Low-Energy Electron Diffraction (LEED) experiments were analyzed using a kinematic (single scattering) theory (*1*). For an assumed surface geometry, the intensity of diffracted electrons as a function of the electron energy was calculated using an old theory suitable for attenuated X-radiation (*2*). Although some intuitive structures were determined (*3*), it was generally concluded that theoretical calculations needed to include multiple scattering events (*4*). A large number of articles have been directed toward this problem (*5*). In general, multiple scattering calculations used for determining structures today are computationally expensive and time consuming although some workers have been developing methods which considerably reduce these drawbacks (*6*).

Recently, renewed interest has been directed toward using the kinematic scattering theory to understand surface structure. One thrust is to manipulate the data so as to enhance the single scattering structure and diminish the multiple scattering structure. This is the purpose of the data averaging scheme used by Lagally and co-workers (*7*) and more recently by Burkstrand et al. (*8*).

A second thrust is to use the technique familiar in X-ray structure analysis (*9*) of generating a Patterson map of the scattering centers. The Patterson function is the complex Fourier transform of the scattered intensity as a function of the change in the wave vector during the scattering. It is the auto-correlation function of the scattering centers which for X-rays is the charge density and for electrons is the atomic nucleii. This method immediately encounters a difficulty when applied to LEED data since the range of wave vector space available in the experiment is very small. Consequently, the Fourier transform contains many spurious features (*10*) which are difficult

to separate from real features due to crystal structure. Efforts to reduce the spurious structure by apodizing the data give such broad features in the Patterson function that the results are of very limited value (*11*). Nevertheless, some structures have been suggested (*12*) based on the analysis of the Patterson function.

Very recently, Landman and Adams have suggested a scheme to separate the spurious features from the structural information in the Patterson function (*13*). By recognizing that these extra features are Gibbs oscillations introduced by the finite range of the data, they were led to the conclusion that the observed Patterson function is the convolution product of a desired structure term and a "window" term that is the Fourier transform of a function in wave vector space which terminates the data. By performing a deconvolution of the observed Patterson function and the window function, they obtain the structure of the surface region. Landman and Adams (*14*) have applied this scheme to several experimental situations involving data which is highly kinematic and have found in each case that the surface is not relaxed.

This raises the following important questions which form the basis of this paper. First, can the deconvolution ideas be applied to realistic data that contain multiple scattering features? Second, is the method capable of determining surface relaxation, or does it always result in the bulk structure? We show in this paper that the deconvolution method of Landman and Adams (*13*,*14*) is not stable when the data contain multiple scattering structure, and, as a consequence, we have developed a new method (based on the same philosophy as the Landman-Adams approach) which does not have this defect. In addition, we demonstrate using realistic multiple scattering data for W(110) that our method can determine surface relaxation.

In the next section, we derive the full kinematic expression for the intensity of an arbitrary diffraction beam from the surface of an ABAB.... registry material where the surface layer has relaxed by an arbitrary amount. This expression is used to obtain an analytic expression for the Patterson function in order to understand the general form of the desired result. In Sec. III, we present the details of the convolution-transform method which we have developed to handle dynamic LEED data. In Sec. IV, we illustrate the method fully using ideal kinematic data for a surface relaxed inward by 9%, outward by 9%, and one that is not relaxed. This section is included to demonstrate ideal results for ideal data and to serve as a basis of comparison when dynamic data are analyzed. In Sec. V, we analyze realistic data for W(110) that have been calculated by a full multiple scattering program by Van Hove and Tong (*15*). We show the effects of considering different energy ranges of the data and present results for different choices of the window function. Results are shown for four different diffraction beams (00), (11), (20), and (02) as well as for surfaces relaxed by +9%, -9% and 0%. In Sec. VI, we summarize our conclusions.

II. Kinematic Theory

In order to understand the convolution-transform method of analyzing LEED data, we first present a general derivation of the kinematic scattering intensity for an arbitrary beam diffracted from the surface of a crystal with AB registry where the surface layer has undergone an arbitrary relaxation perpendicular to the surface. We will then transform this analytic expression to show the expected Patterson function for this ideal case.

The scattering amplitude, A, can be written in general as (*1,6a,16*)

$$A(E) = f(E) \sum_{\kappa} e^{-W(\kappa)} \alpha(\kappa,E) \sum_{j} e^{i\vec{S}\cdot\vec{r}_j(\kappa)} \sum_{\ell_1\ell_2} e^{i\vec{S}\cdot\vec{r}(\ell_1\ell_2)} \qquad (1)$$

where E is the energy of the incident electron, $e^{-W(\kappa)}$ is the square root of the Debye-Waller factor for the κ^{th} layer, $\alpha(\kappa,E)$ is the attenuation coefficient which is the amplitude at energy E that makes the round trip from the surface to the κ^{th} layer and back to the surface, $\vec{r}_j(\kappa)$ is the vector distance of the j^{th} basis atom in the κ^{th} layer, and $\vec{r}(\ell_1\ell_2)$ is the vector distance of the two-dimensional surface unit cell labelled by integers ℓ_1 and ℓ_2. The quantity $\vec{S}$ is the momentum transfer to the surface and is given by

$$\vec{S} = \vec{k}_f - \vec{k}_i \qquad (2)$$

where $\vec{k}_f$ ($\vec{k}_i$) is the wave vector of the electron after (before) the scattering event. The prefactor f(E) contains all contributions other than those explicitly included in the sums such as (i) the atomic scattering amplitude which is assumed to be identical for all scatterers, (ii) the Lorentz factor (*1,7a*), and (iii) the surface barrier reflectivity. These three contributions do not affect the analysis and can be absorbed into an energy dependent prefactor.

We specialize the derivation to apply to the structure of the (110)

surface of a body-centered-cubic material, with unit cell vectors given by

$$\begin{aligned} \vec{a}_1 &= a_o(\sqrt{2},0,0) \\ \vec{a}_2 &= a_o(0,1,0) \end{aligned} \tag{3}$$

where a_o is the nearest-neighbor separation distance. There are two atoms in the unit cell for each layer with coordinates given by

$$\vec{r}_j(\kappa) = \vec{\rho}_j(\kappa) + z(\kappa)\hat{z} \tag{4}$$

where the component parallel to the surface is

$$\begin{aligned} &\vec{\rho}_1(\kappa) = 0, \ \vec{\rho}_2(\kappa) = \tfrac{1}{2}(\vec{a}_1 + \vec{a}_2), && \kappa \text{ odd} \\ &\vec{\rho}_1(\kappa) = \tfrac{1}{2}\vec{a}_1, \ \vec{\rho}_2(\kappa) = \tfrac{1}{2}\vec{a}_2, && \kappa \text{ even} \end{aligned} \tag{5}$$

and where the layer coordinates are

$$\begin{aligned} z(1) &= 0 \\ z(\kappa) &= (\kappa - 1 + t)d \qquad \kappa \geq 2 \end{aligned} \tag{6}$$

The spacing between the layers in the bulk is given by d, and the fractional expansion of the distance between the first and second layers is given by t. This structure is shown in Fig. 1.

The last sum in Eq. (1) can be carried out to give

$$\sum_{\ell_1 \ell_2} e^{i\vec{S}\cdot\vec{r}(\ell_1\ell_2)} = \delta(\vec{S}_{||} - \vec{G}_{hk}) \tag{7}$$

where $\vec{S}_{||}$ is the component of $\vec{S}$ parallel to the surface, and the reciprocal lattice vector is

$$\vec{G}_{hk} = h\vec{b}_1 + k\vec{b}_2 \tag{8}$$

where

$$\vec{b}_1 = \frac{2\pi}{a_o}\left(\frac{1}{\sqrt{2}}, 0, 0\right)$$

$$\vec{b}_2 = \frac{2\pi}{a_o}(0, 1, 0) \tag{9}$$

and where the integers (h,k) identify the diffracted beam. Because there are two identical atoms in the unit cell defined in Fig. 1, not all of the beams given by Eq. (8) appear in the diffraction pattern. Instead, only those beams which have the sum (h + k) = even appear as is shown in the reciprocal lattice diagram in Fig. 1. Using Eq. (5), the sum over j in Eq. (1) yields

$$\sum_j e^{i\vec{G}_{hk}\cdot\vec{\rho}_j(\kappa)} = \begin{cases} 2 & , \kappa \text{ odd} \\ 2(-1)^h & , \kappa \text{ even} \end{cases} \tag{10}$$

For the Debye-Waller factor, we assume that $W(\kappa) = W$ for all values of $\kappa \geq 2$. This corresponds to the assumption that only the surface layer has a mean square amplitude different from the bulk value. For the following expressions, it will be convenient to define

$$D_s = e^{W-W(1)} \tag{11}$$

which is the square root of the ratio of the bulk and surface Debye terms. This term is a function of energy. In addition, we assume that the attenuation coefficient is written as

$$\alpha(\kappa,E) = \exp\left[-\frac{z(\kappa)}{2\lambda(E)}\left(\frac{1}{\cos\theta} + \frac{1}{\cos\theta'}\right)\right] \tag{12}$$

where $\lambda(E)$ is the inelastic mean free path of the electron and $\theta(\theta')$ is the angle relative to the surface normal of the incident (scattered) beam

inside the crystal. Using Eq. (6), Eq. (12) becomes

$$\alpha(\kappa,E) = \alpha^{\kappa-1+t} \qquad \kappa \geq 2 \tag{13}$$

where

$$\alpha = \exp\left[-\frac{d}{2\lambda(E)}\left(\frac{1}{\cos\theta} + \frac{1}{\cos\theta'}\right)\right] \tag{14}$$

Now the sum over κ in Eq. (1) can be carried out to give, after some manipulation,

$$A(E) = f(E)e^{-W}\left\{\alpha^{-t}D_s e^{-iStd} - 1 + [1 + (-1)^h \alpha e^{iSd}] \sum_{n=o}^{\infty} (\alpha^2 e^{i2Sd})^n\right\} \tag{15}$$

Here, S (with no subscript) is the momentum transfer perpendicular to the surface and for the (00) beam is given in terms of the energy and inner potential V_o as

$$S = 2\left(\frac{2m}{\hbar^2}\right)^{1/2}(V_o + E\cos^2\theta)^{1/2} \tag{16}$$

For an arbitrary (hk) beam, S must be calculated from the conservation of energy and parallel momentum conditions.

From Eq. (15) we obtain the scattered intensity for the (hk) beam for an arbitrary relaxation of the (110) surface of a bcc material as

$$\begin{aligned} I(S) = |f(E)|^2 e^{-2W}\Bigg\{ & 1 + \alpha^{-2t}D_s + \\ & \frac{1+\alpha^2+2(-1)^h\alpha\cos(Sd)}{1-\alpha^4}\left[-1 + 2\sum_{n=o}^{\infty}\alpha^{2n}\cos(2nSd)\right] \\ & + 2D_s\alpha^{1-t}\sum_{n=o}^{\infty}\alpha^{2n}\left[\alpha\cos\left((2n+2+t)Sd\right) + (-1)^h\cos\left((2n+1+t)Sd\right)\right] \\ & -2\sum_{n=o}^{\infty}\alpha^{2n}\left[(-1)^h\alpha\cos\left((2n+1)Sd\right) + \cos(2nSd)\right]\Bigg\} \end{aligned} \tag{17}$$

If we make three assumptions, this expression for the intensity can be Fourier transformed analytically to give the Patterson function

$$P(z) = \int_0^{\infty} I(S)e^{iSz}dS \quad . \tag{18}$$

First we assume that the range of the intensity as a function of momentum extends from $0 < S < +\infty$. Second, contrary to experimental evidence, we assume that the attenuation coefficient, α, is a constant not depending on energy (in reality it depends on energy both due to the energy dependence of the mean free path and the energy dependence of the angles θ and θ')[4]. Third, we assume that the Debye-Waller factor for the surface layer is the same as the bulk so that $D_s = 1$ and is independent of energy. With these last two assumptions, it is possible to separate Eq. (17) into two factors, the first being a function of energy which forms a smooth envelope to the second factor in braces which is the interference function. The interference function depends only on S through the cosine terms, and this fact is the result of the last two assumptions.

If we consider only the interference term in braces in Eq. (17), then the Patterson function in Eq. (18) becomes

$$\begin{aligned} P_d(z) = {} & 2\pi\left(\frac{\alpha^2}{1-\alpha^2} + D_s\alpha^{-2t}\right)\delta(z) + \frac{2\pi\alpha^3(-1)^h}{1-\alpha^2}\sum_{n=0}^{\infty}\alpha^{2n}\Big[\delta(z - d(2n+1)) \\ & + \delta(z + d(2n+1))\Big] + \frac{2\pi\alpha^4}{1-\alpha^2}\sum_{n=0}^{\infty}\alpha^{2n}\Big[\delta(z - d(2n+2)) + \delta(z + d(2n+2))\Big] \\ & + 2\pi D_s\alpha^{1-t}(-1)^h\sum_{n=0}^{\infty}\alpha^{2n}\Big[\delta(z - d(2n+1+t)) + \delta(z + d(2n+1+t))\Big] \\ & + 2\pi D_s\alpha^{2-t}\sum_{n=0}^{\infty}\alpha^{2n}\Big[\delta(z - d(2n+2+t)) + \delta(z + d(2n+2+t))\Big] \end{aligned} \tag{19}$$

This function has a fairly simple form. It is a series of delta functions symmetrically placed about $z = 0$. The first term, which is largest, represents the coefficient of the delta function at the origin. The second and third terms represent a series of delta functions placed at multiples of the bulk spacing with the odd numbered positions having a negative amplitude if h is odd. The last two terms are similar to the second and third, but now the delta functions are at multiples of the bulk spacing plus the surface layer spacing. As z becomes larger, the coefficients of all the delta functions become smaller in an exponential decay.

To illustrate this behavior, we show in panels (a) and (b) of Fig. 2 the interference function from Eq. (17) and the Patterson function from Eq. (19), respectively, for the case (hk) = (0,0), $\theta = \theta' = 0^{o}$, t = 15% and $\lambda = 1.12d$ (corresponding to a constant $\alpha = 0.41$). We present only a part of the interference function which is assumed to extend to $+\infty$, and we show only the coefficients of the delta functions for positive z. It is important to remember that this result can only be obtained with the assumptions of constant attenuation coefficient α and constant surface to bulk Debye-Waller ratio D_s. The Patterson function shows a doublet structure near every multiple of the bulk spacing even though only the surface layer is assumed to relax.

III. Convolution-Transform Method

There are five important differences between the interference function shown in Fig. 2a and experimental LEED data. Specifically, the calculated function (i) assumes a constant mean free path, (ii) sets the surface layer Debye temperature equal to the bulk, (iii) omits all multiple scattering structure, (iv) ignores the energy dependent envelope from the prefactor in Eq. (17), and (v) extends in momentum space to infinity.

In the convolution-transform method of analysis, the last two differences are dealt with exactly. This is demonstrated by multiplying the infinite interference function, $I_i(S)$, by a window function, $w(S)$, as shown in Fig. 2c to give data, $I_f(S)$, of a finite range as shown in Fig. 2e. The window function does not need to be a constant as shown but can be any function of S over the range where it is non-zero. In particular, the window function, $w(S)$, can include all of the energy dependent effects in the first factor of Eq. (17). This term cannot, however, account for the energy dependence of α and D_s since the energy dependence of these two quantities cannot be factored. In fact, in the convolution-transform method of analysis, there is no way to account for the first two differences mentioned above between the calculated and observed LEED intensities. That the method works nonetheless is due to the fact that for a small energy range, it is reasonable to assume that α and D_s are constant. The effect of multiple scattering on the analysis will be discussed in Sec. V.

If we use the finite range of the interference function as shown in Fig. 2e and calculate the Patterson function, Eq. (18), we obtain a complex quantity, the real part of which is shown in Fig. 2f and is labelled $P_o(z)$. This quantity is symmetric in z. In Fig. 2d, we show the Fourier transform, labelled $W(z)$, of the window function $w(S)$ in Fig. 2c. The structure (called

Gibbs oscillations) is due entirely to the finite nature of the window function. The convolution theorem states that since Fig. 2e is the product of Figs. 2a and 2c, then Fig. 2f is the convolution product of Figs. 2b and 2d. The problem of determining the structure of a relaxed surface can now be succinctly stated as: Given the Fourier transform of the data, $P_o(z)$, and of a chosen window, $W(z)$, what is the series of delta functions, $P_d(z)$, which gives the structure? This is a problem of deconvoluting two known functions to get a third which is unknown.

Landman and Adams (*13*) have presented a method for performing this deconvolution. We have found that their method is operational only when the deconvolution is exact or very nearly exact. In other words, their deconvolution procedure works only if $P_o(z)$ is very nearly the exact convolution product of $W(z)$ and $P_d(z)$. If there are some uncertainties introduced, however, their procedure does not work. Instead, spurious delta functions of large amplitude appear in the deconvolution result. As we have already shown, there are three sources of uncertainty which cause the convolution product to be only approximate: energy dependent α, energy dependent D_s, and multiple scattering. The fact that Landman and Adams (*14*) have obtained structures from real data is due, we believe, to the strongly kinematic nature of the data (this is more apparent when the data are plotted on a linear scale) and to the fact that the surfaces they analyzed do not relax.

As a consequence, we have developed a new method for determining the set of delta functions $P_d(z)$ which give the structure. The method is as follows: We assume that $P_o(z)$ and $W(z)$ are known. We assume that $P_d(z)$ has the form

$$P_d(z) = \sum_i g_i[\delta(z + z_i) + \delta(z - z_i)] \qquad (20)$$

where the set of numbers $\{z_i\}$ and $\{g_i\}$ are at present unknown. Due to this simple but general form, the convolution product of $W(z)$ and $P_d(z)$ can be performed to give a calculated Patterson function $P_c(z)$. We have

$$P_c(z) = \int_{-\infty}^{\infty} W(z')P_d(z - z')dz' \tag{21}$$

$$= \sum_i g_i[W(z + z_i) + W(z - z_i)] \tag{22}$$

In our method, we want to find the sets $\{z_i\}$ and $\{g_i\}$ which result in $P_c(z)$ being the same as $P_o(z)$.

We define a residual R given by

$$R^2 = \int_o^{\infty} [P_c(z) - P_o(z)]^2 \, dz \tag{23}$$

If the set $\{z_i\}$ is known, then the set of coefficients $\{g_i\}$ which minimizes the residual can be found by solving the set of linear equations determined by

$$\frac{\partial R^2}{\partial g_j} = 0 \tag{24}$$

This set of equations can be written in matrix form as

$$\sum_j A_{ij} g_j = B_i \tag{25}$$

where

$$A_{ij} = \int_o^{\infty} [W(z + z_i) + W(z - z_i)][W(z + z_j) + W(z - z_j)]dz \tag{26}$$

and

$$B_i = \int_o^{\infty} P_o(z)[W(z + z_i) + W(z - z_i)]dz \tag{27}$$

The set $\{g_i\}$ which is found from Eq. (25) is the best set possible for making the function $P_c(z)$ fit $P_o(z)$ in the least-squares-sense. However, it is possible that for some set of $\{z_i\}$, some of the coefficients $\{g_i\}$ will

be non-physical in that they will have the wrong sign. The correct sign can be determined from Eq. (19). There we see that if the integer h is even, all delta functions have a positive amplitude. If, on the other hand, h is odd, then the amplitude of the delta functions which are located at positions given by $z_n = (2n + 1)d$ and $z_n = (2n + 1 + t)d$ (for integral n) are negative, and all others are positive. Once the set $\{g_i\}$ subject to the physical constraint of having the proper sign is found, then the residual R can be calculated. The aim is to find the set of positions $\{z_i\}$ which minimize this residual.

We summarize the procedure to determine the structure as follows. First, a value of the inner potential V_o is chosen. This allows for the conversion of the energy axis to momentum so that the observed Patterson function $P_o(z)$ can be determined. Second, we choose a window function which terminates at the same energies as the data, and it is Fourier transformed to obtain W(z). The exact procedure for choosing this window is discussed later. Third, a set of positions $\{z_i\}$ is chosen for the delta functions. Since we are looking for relaxation of the surface layer, this set is given by

$$z_i = nd,\ (n + 1 + t)d,\ n = 0,1,2... \tag{28}$$

Here, d is the known layer spacing of the bulk material. Consequently, this complete set is characterized by one parameter t, the percentage relaxation of the surface layer. Fourth, the matrices $\underset{\approx}{A}$ and $\underset{\approx}{B}$ given in Eqs. (26) and (27) are generated. In practice, the integrals are truncated at $z = 10\text{Å}$ where the functions W(z) and $P_o(z)$ are both small. Fifth, Eq. (25) is solved numerically to determine the set $\{g_i\}$. Sixth, the set $\{g_i\}$ is examined to determine if all the terms have the physically correct sign. If not, then the value of z_i corresponding to the improper g_i is discarded from the set

$\{z_i\}$. This reduces the size of the matrices $\underset{\approx}{A}$ and $\underset{\approx}{B}$. Then the fifth step is repeated until all terms in the set $\{g_i\}$ have the correct sign. Seventh, we evaluate R from the square root of Eq. (23). Eighth, the previous steps are repeated with a change in the choice of the parameter t and later the parameter V_o. What we seek is a minimum in the value of R as a function of both t and V_o.

In the next section, we demonstrate this procedure for ideal kinematic data. Then, in Sec. V, we analyze dynamic data appropriate for the W(110) surface.

IV. Results - Kinematic Data

In Fig. 3a, we show the interference function for the (11) beam for the case of the surface layer relaxed outward by 9%. The curve was calculated for the case V_o = 16eV, D_s = 1, $\theta = 0^o$, d = 2.23 Å (appropriate for tungsten), and an energy dependent mean free path given by

$$\lambda(E) = \begin{cases} 2.5\text{Å}, & E < 25 \text{ eV} \\ 0.39(E + V_o)^{1/2} \text{ Å}, & E > 25 \text{ eV} \end{cases} \tag{29}$$

This choice corresponds to an imaginary inner potential of V_i = 5 eV and agrees well with experimental results for tungsten (*15*).

In Fig. 3b, we show the results of proceeding through the steps in the previous section using this interference function. Here the residual R is plotted against the variables V_o and t. The values have been normalized by dividing R by the quantity

$$R_o^2 = \int_o^\infty dz\ P_o^2(z) \tag{30}$$

This means that if the convoluted Patterson function, $P_c(z)$, were zero everywhere, then the plotted residual would have the value of unity. In Fig. 3c, we show the topographic plot of the surface in Fig. 3b. In Fig. 3c, as in all topographic plots in this paper, the difference in value between contours is $\Delta R = 0.05$. From this figure, it is evident that the minimum in the residual occurs at V_o = 17 eV and t = 8%.

This minimum in the residual surface will be characterized by its depth. We define a parameter Δ to be

$$\Delta = \frac{R_{ave} - R_{min}}{R_{ave}} \tag{31}$$

where R_{ave} is the average value of the residual over the region shown, and R_{min} is the value of the minimum residual. Even though these data are perfectly

kinematic and the correct window function was used (a constant in this case as shown in Fig. 3a), since α now is a function of energy, we do not obtain perfect agreement between $P_o(z)$ and $P_c(z)$. For this case $R_{min} = 0.055$, $R_{ave} = .376$, which gives $\Delta = 85\%$ — an 85% minimum.

In Figs. 4a and 4b, we show a similar situation where now the surface is assumed to relax inward by 9%. In this case, however, the residual surface has two minima, one near the correct position at $V_o = 15$ eV, $t = -8\%$ and a second spurious minimum at $V_o = 37$ eV, $t = +11\%$. Notice in Fig. 3c and 4b that even the "correct" minima in the residual surface do not occur exactly at the correct inner potential. This difference is due to the energy dependent mean free path. When α is taken to be constant, then in both cases we obtain perfect fits of 100% minima at the correct inner potential and relaxation values.

There are two criteria used to distinguish between multiple results. First is the depth of the minimum. When multiple minima occur in the residual surface, the one with greater depth is favored. In this example, the minimum at $V_o = 15$ eV, $t = -8\%$ has a depth of $\Delta = 72\%$, whereas the spurious minimum at $V_o = 37$ eV, $t = +11\%$ has a depth of $\Delta = 46\%$.

The second criterion is the "quality" of the set of coefficients $\{g_i\}$. In Figs. 5a and 5b, we show the sets of coefficients corresponding to the residuals found at the two minima in Fig. 4b. In Fig. 5a, we see that the correct solution has the expected doublet structure at each multiple of the bulk spacing. [Note that in all figures of this type in this paper we plot the magnitude of the coefficients for convenience. The actual coefficients near $z = d$ and $z = 3d$ are negative since this is the (11) beam.] In Fig. 5b, however, the spurious solution results in unusual relative weights given to the coefficients in the doublet at $z = d$, and some of the coefficients for

larger z are missing (indicated by the carets under the axis in Fig. 5b).

Why is it that for a perfectly kinematic spectrum we obtain multiple solutions in the residual? The reason is that for the short range of data used, there is a strong similarity between the spectrum for V_o = 17 eV and t = -9%, and the spectrum for V_o = 37 eV and t = +11%. Both of these spectra have structures at nearly the same position. We have found that when the data range is increased, then the minimum for the spurious solution gets considerably smaller, whereas the correct minimum remains. Since in real data we are limited to a short energy range due to surface sensitivity considerations, we must anticipate that we shall get multiple minima in our solutions. Unfortunately, the two criteria for distinguishing correct minima from spurious ones are not so unambiguous for real data as for this ideal case.

In Fig. 4a, we also show the interference function for an unrelaxed surface using the same parameters as in Fig. 3a. The energy dependent mean free path causes the peaks at higher energy to be larger. For this case, we obtain the residual surface shown in Fig. 4c. Here, the surface is characterized by a valley or trough extending across the figure for all values of t. There is no minimum at t = 0%.

This result can be understood when we examine the set of coefficients corresponding to the solutions at the bottom of the trough. In Fig. 5c, we show these coefficients for V_o = 17 eV as the parameter t is varied. All of the sets of coefficients appear the same. They have a finite value at multiples of the bulk spacing, but vanish at the relaxed spacing (indicated by the carots in the figure). What is happening is the following: Even though the set of positions $\{z_i\}$ contains a series of terms corresponding to a relaxation position, the best fit with the data occurs when these extra terms in $\{z_i\}$ have zero amplitude. Consequently, the fit is not affected by the choice of these extra positions. This manifests itself as

a residual value which is independent of t – hence the trough in Fig. 4c.

In summary, the plot of residual versus V_o and t gives a minimum at the relaxed position. If there are multiple minima, the depth and the set of $\{g_i\}$ can eliminate the spurious minima. If the crystal surface is unrelaxed, the residual surface is characterized by a trough. If it should happen that for real data, the residual surface seems ambiguous, then there is the additional test that all I-V curves at various angles of incidence and all (hk) beams from the same surface must indicate the same solution.

V. Results - W(110) Data

In this section, we demonstrate that our transform-convolution method is a viable method for determining relaxation on metal surfaces where the LEED data is highly dynamic. We choose to analyze calculated multiple scattering data rather than experimental data since it is possible with the calculated data to obtain curves for various degrees of relaxation. We choose the W(110) surface because tungsten is recognized to be a highly dynamic scatterer and because a complete set of I-V curves for four different beams, 17 different surface relaxation distances, and an energy range from 20 - 400 eV is available from work of Van Hove and Tong (*15*,*17*). From this large set of data, we arbitrarily pick the spectra for surfaces that are 9%, -9%, and 0% relaxed.

First, we analyze the effect of the data range on the results. For illustration, we examine the (11) beam for the case of t = 9%. In Fig. 6, at the top we show the I-V curve from 24 to 400 eV for this beam along with the window function used to analyze this curve. The topographic plots show the residual surfaces obtained as the energy range of the data is increased where the lower limit is 24 eV in each case, but the upper limit is 74 eV, 144 eV, 214 eV, and 296 eV for the surfaces (a), (b), (c), and (d), respectively. The topographic surface when the data range is 24 - 400 eV is virtually indistinguishable from (d). This sequence of data ranges, shown by the dashed lines on the I-V curve in Fig. 6, were chosen because each curve in the sequence includes one additional Bragg peak.

All four topographic plots show two minima, one near t = 8% and V_o = 40 eV and the other near t = -10% and V_o = 15 eV. The deeper minimum is for the positive relaxation in each case, and also the set of coefficients of the delta functions is consistently better for the positive relaxation. Thus,

both criteria eliminate the spurious minimum which indicates negative relaxation.

As a function of energy range, the depth of the minimum in the residual surface increases as the energy range increases. This can be due to two causes. First, as the energy range increases, the surface sensitivity decreases. Thus, the single scattering features in the spectrum above approximately 200 eV are insensitive to the position of the surface, and this range of the data is not useful in the determination of surface relaxation. Second, as the energy range increases, inaccuracies due to multiple scattering, the energy dependent α, and the Debye-Waller factor combine to degrade the ability of the convoluted Patterson function to fit the Patterson function of the data. Therefore, too large a data range is a hindrance to determining the degree of relaxation. On the other hand, a small data range does not seem to be acceptable either because strong multiple scattering structure could alter the solution. Therefore, we compromise by choosing in the analyzed data which follows the energy range which includes two Bragg peaks--surface (b) in this present case.

We now comment on the magnitude of the inner potential. For the kinematic results in Figs. 3 and 4, the correct solution has a value of the inner potential equal to that used to derive the I-V curve. For this case of tungsten, however, we obtain an inner potential of 41 eV, whereas the value used to calculate the I-V curve in the multiple scattering program of Van Hove and Tong (*15*) was V_o = 16 eV. The explanation for this is as follows. The inner potential in multiple scattering calculations and the inner potential in our single scattering theory are not the same physical quantity. In multiple scattering calculations, the inner potential shifts the energy scale and thereby accounts for the change in the wavelength of the electron.

In the kinematic calculations, the inner potential must do this and more. The wave function of an electron transmitted through a layer is a linear combination of an unscattered wave and a forward scattered wave. This combination results in a phase shifted wave whose optical path length is different from the geometric path length. In the kinematic theory used here the inner potential must be altered to take this difference into account. Only if the crystal scattering is dominated by single scattering events will the inner potentials for the two approaches be the same. Therefore, the fact that the determined inner potential is 41 eV for the (11) beam of W(110) is both acceptable and indicative of the fact that tungsten is a highly dynamic scatterer. Also, the determined inner potential may be different for different beams or for different angles of incidence of the same beam.

We will now discuss the method used for choosing the window function and the results of various different choices. In the work of Landman and Adams (*13*,*14*), the window function is calculated by carefully evaluating the first factor in Eq. (17). This requires much detailed information concerning the surface such as the scattering phase shifts, the Debye-Waller factor, the surface reflectivity and the Lorentz factor. Since these are only approximately known, Landman and Adams allow for a variation of the Debye temperature until an optimum deconvolution is performed. The resulting window function for the case of Al(100) is very similar to the envelope of the data (*14*).

In our approach, we delete this difficult step. The window function we use is a hand-drawn envelope of the data, touching or approaching the I-V curve at the positions where Bragg peaks may occur. This window has a degree of arbitrariness about it which we will show is not

important. The reason this drawn window is the desired window function [and not the calculated prefactor in Eq. (17)] can be understood when we consider what it is to accomplish. The Patterson function of the data contains spurious structure due to truncation effects which appear as high frequency oscillations in z-space. These high frequency features in z-space are due to the gross features of the intensity in S-space; in particular, the envelope of the data as well as the cut-off at a particular S. By making the window in S-space mimic the envelope of the data as well as the cut-off, we have the best chance of accounting for the extra peaks in the Patterson function.

As defined, the window function is somewhat arbitrary. Different workers will have different opinions as to the proper window function. However, we have found that, contrary to the results using Landman and Adams approach, our results are not sensitive to this choice. We illustrate this in Fig. 7. Four different choices of window functions and methods of manipulating the window function are shown. In Fig. 7a, we show the drawn window as used in Fig. 6b. In Fig. 7b, we show an extreme case of using a constant window. In Fig. 7c, the data is divided by the drawn window in Fig. 7a, and then a constant window is used. This has the effect of making all the Bragg features of equal magnitude (when they can be identified). Finally, in Fig. 7d, we show the case where both the data and the drawn window in Fig. 7a have been apodized in S-space. The apodizing function used is given by

$$A(S) = 1 - \cos 2\pi \frac{(S - S_1)}{(S_2 - S_1)} \tag{32}$$

where S_1 and S_2 are the limits of the data in S-space.

In all four cases, the residual surface as a function of t and V_o has two minima like those shown in Fig. 6b. The difference among all the

results is the depth of the minima. For the minimum at positive t, all four give the position at t = 11%, V_o = 41 eV with values of Δ = 84%, 35%, 74%, and 90% for the four windows, respectively. For the spurious minimum at negative t, the position varies slightly with the four choices and the depth in every case is approximately half of the value for the minima at positive t. This series of results demonstrates that the constant window is the poorest choice (although it still yields the proper answer), and the other three windows and manipulations all yield approximately the same results. Since the use of the drawn window alone involves less manipulation of the data than the windows in Figs. 7c and 7d, we have chosen to use that option in the results that follow.

Since the spurious minimum in the residual surface is at a negative value of t, we analyzed W(110) data appropriate for a negative relaxation. We show for comparison in Figs. 8a and 8b the I-V curves for the (11) beam for both relaxation outward and inward, respectively. The two curves are very similar in overall shape. Hence, it is not too surprising that the residual surface for the t = -9% I-V curve has the same general shape as that shown in Fig. 6b for t = +9%. There are two minima in the residual surface, one at t = 11%, V_o = 41 eV and one at t = -9%, V_o = 13 eV. The results for this I-V curve can be distinguished from the results in Fig. 6b by comparing the depth of the minimum and the set of delta function coefficients. In Figs. 8c - 8f, we show the coefficients for the two minima for each spectrum. For the spectrum in Fig. 8a, the deeper of the two minima is at t = 11% and V_o = 41 eV having a value of Δ = 84% (Fig. 8c) as compared to Δ = 44% for the minimum at t = -13% and V_o = 17 eV (Fig. 8e). The set of coefficients shown in Fig. 8c is also physically more realistic than the set in Fig. 8e leading to the choice of the positive relaxation as the correct solution. For the I-V

curve in Fig. 8b, however, the opposite is true. The deeper minimum occurs at t = -9% and V_o = 13 eV having a value of Δ = 67% (Fig. 8f) as compared to Δ = 57% for the minimum at t = 11% and V_o = 41 eV. In addition, the set of coefficients in Fig. 8f is more favorable. Thus, even though the intensities are surprisingly similar for t = +9% and t = -9%, the convolution-transform method does distinguish between them.

The other three beams for the W(110) surface calculated by Van Hove and Tong (*15*) have also been analyzed. In Fig. 9, we show the I-V curves for the (00), (20), and (02) beam for the case of both inward and outward relaxation by 9%. All curves are over the energy range appropriate to contain approximately two Bragg peaks. The curves for inward and outward relaxation are similar in shape, particularly for the (00) beam. In Table I, we summarize the results where we present the information regarding each of the minima which occurs in the residual surfaces. The table shows that both the (11) and the (20) beams clearly determine the correct structure, the (02) beam is ambiguous, and the (00) beam correctly determines the negative relaxation but is wrong concerning the positive relaxation.

If we are optimistic, we conclude that this method is capable of determining the surface geometry given the fact that many experimental I-V curves may be analyzed and the fact that some experimental I-V curves are more kinematic than others. If we are pessimistic, we conclude that whereas this method may not determine structures unambiguously, it strongly limits the number of possible structures which may have to be analyzed via multiple scattering calculations.

Finally, we turn to the case where the surface is not relaxed. In Fig. 10a, we show the I-V curve and window for the (11) beam for the case t = 0%. In Fig. 10b, we show the residual surface. The residual shows a

trough near V_o = 12 eV which is characteristic of an unrelaxed surface. There is also a deep minimum at V_o = 37 eV and t = 13%, but the set of coefficients for this minimum is very poor so that this solution may be eliminated. The trough does have a shallow minimum within it for negative values of t. An examination of the coefficients for the values at the bottom of the trough is shown in Fig. 10c. As the value of t is swept from +15% to -15%, the value of V_o is varied from 11 eV to 15 eV so as to stay at the bottom of the trough. The series of coefficients shows a trend similar to that in Fig. 5c in that coefficients appear at multiples of the bulk spacing for all assumed values of t. For negative values of t, the first doublet structure at z = d is fair, but the doublets at z = 2d and 3d are poor. The behavior shown in this figure, then, is indicative of an unrelaxed crystal surface.

The analysis of the other three beams for the case of an unrelaxed surface shows that each of the residual surfaces contains a trough. For the (20) beam it occurs at V_o = 12 eV, for the (02) beam at V_o = 22 eV, and for the (00) beam at V_o = 15 eV. Except for the (00) beam, each trough is quite pronounced. The structure of the residual surface, then, is qualitatively different for the unrelaxed crystal surface as compared to the case of relaxation by either positive or negative 9%.

VI. Conclusions

We have presented a new variation of the transform method which uses the Patterson function of LEED data to obtain structural information. The method is based upon single scattering concepts, but we have shown by example that highly dynamic data may also be analyzed. Since the method is kinematic, there must, of course, be kinematic features in the I-V curves which are analyzed. The reason that we can obtain structures even for spectra that are highly dynamic is due to the averaging properties of the Fourier transform. The Fourier transform of a function is large when the spacing between features is periodic (as is the case for kinematic features) and is small otherwise (as is the case for the aperiodic multiple scattering features). Thus, the Patterson function accentuates the single scattering structure and allows for the determination of the layer spacing.

The characteristics which make our approach different from that of Landman and Adams (*13*,*14*) are as follows: (i) Our procedure is a convolution procedure requiring a guess of the result rather than a deconvolution procedure; (ii) We constrain the allowed delta functions to be at physically meaningful positions; (iii) The inner potential is treated as a parameter to be determined by each I-V curve; (iv) Our choice of window function is determined by the data rather than calculated; (v) The method can tolerate a high degree of multiple scattering and still give meaningful results; (vi) We have shown by actual example that our method is capable of determining surface relaxation with data that is dynamic.

In favorable cases, where the experimental I-V curves are highly kinematic, our method can uniquely determine the surface relaxation. In unfavorable cases, where the I-V curves are dominated by multiple scattering structure, the method can strongly limit the possible solutions, thereby making the search using multiple scattering calculations more efficient.

Acknowledgments

We gratefully acknowledge M. Van Hove for very helpful discussions concerning the inner potential and who, along with S. Y. Tong, very graciously supplied us with computer cards of the calculated I-V curves for W(110). We are very thankful to G. L. Griffin for his very careful and imaginative work during the early stages of this project. Also, we acknowledge support for this work by the Army Research Office - Durham, Grant No. DAHCO4-75-0170, and the Ford Energy Research Program of the California Institute of Technology.

References

1. J. J. Lander and J. Morrison, J. Appl. Phys. 34, 3517 (1963); and J. J. Lander, Prog. Solid State Chem. 2, 26 (1965).

2. C. G. Darwin, Phil. Mag. 27, 315 (1914).

3. For example, see L. H. Germer and A. U. MacRae, J. Appl. Phys. 32, 2432 (1962), 33, 2923 (1962); E. G. McRae and C. W. Caldwell, Jr., Surface Sci. 2, 509 (1964); P. W. Palmberg and T. N. Rhodin, J. Chem. Phys. 49, 134, 147 (1968); R. L. Gerlach and T. N. Rhodin, Surface Sci. 10, 446 (1968).

4. P. W. Palmberg and W. T. Peria, Surface Sci. 6, 57 (1967)

5. Many review articles exist including J. B. Pendry, Low-Energy Electron Diffraction: The Theory and Its Application to Determination of Surface Structure, Academic Press, London, 1974; C. B. Duke, Adv. Chem. Phys. 27, 1 (1974); J. A. Strozier, D. W. Jepsen and F. Jona, in J. M. Blakely (Ed.) Surface Physics of Crystalline Materials, Academic Press, London, 1976; S. Y. Tong, Prog. Surf. Sci. 7, 1 (1975).

6. R. H. Tait, S. Y. Tong and T. N. Rhodin, Phys. Rev. Lett. 28, 553 (1972); M. A. Van Hove and S. Y. Tong, Phys. Rev. Lett. 35, 1092 (1975); S. Y. Tong, Solid State Commun. 16, 91 (1975).

7. M. B. Webb and M. G. Lagally, Solid State Phys. 28, 301 (1973); M. G. Lagally, T. C. Ngoc and M. B. Webb, Phys. Rev. Lett. 26, 1557 (1971); T. C. Ngoc, M. G. Lagally and M. B. Webb, Surface Sci. 35, 117 (1973).

8. J. M. Burkstrand, G. G. Kleiman and F. J. Arlinghaus, Surface Sci. 46, 43 (1974); G. G. Kleiman and J. M. Burkstrand, Surface Sci. 50, 493 (1975); J. M. Burkstrand, G. G. Kleiman, G. G. Tibbetts, and J. C. Tracy, J. Vac. Sci. Technol. 13, 291 (1976).

9. G. N. Ramachandran and R. Srinivasan, Fourier Methods in Crystallography, Wiley, New York, 1970.

10. T. A. Clarke, R. Mason and M. Tescari, Proc. Roy. Soc. London A331, 321 (1972); Surface Sci. 30, 553 (1972); 40, 1 (1973).

11. D. P. Woodruff, K. A. R. Mitchell and L. McDonnell, Surface Sci. 42, 355 (1974).

12. C. W. Tucker, Jr., Appl. Phys. Lett. 1, 34 (1962); Surface Sci. 2, 516 (1964); J. Appl. Phys. 35, 1897 (1964); 37, 3013, 4147 (1966); 38, 2696 (1967).

13. U. Landman and D. L. Adams, J. Vac. Sci. Technol. 11, 195 (1974); D. L. Adams and U. Landman, Phys. Rev. Lett. 33, 585 (1974).

14. U. Landman and D. L. Adams, J. Vac. Sci. Technol. 13, 363 (1976); D. L. Adams, U. Landman and J. C. Hamilton, J. Vac. Sci. Technol. 12, 260 (1975); U. Landman, Faraday Disc. Chem. Soc. 60, 230 (1975).

15. M. A. Van Hove and S. Y. Tong, Surface Sci. 54, 91 (1976).

16. M. G. Lagally and M. B. Webb, Phys. Rev. Lett. 21, 1388 (1968).

17. M. A. Van Hove and S. Y. Tong, private communication.

Table I. Summary of the results from analysis of the I-V curves for W(110) for both inward and outward relaxation.

Beam	(11)		(20)		(02)		(00)	
Data for t = +9%								
Range (eV)	24-144		24-130		64-188		24-168	
t(%)	11	-13	9	<-15	13	- 9	11	- 9
V_o(eV)	41	17	29	13	41	>45	21	41
Δ(%)	84	44	28	~40	48	~55	7	44
$\{g_i\}$	ok	bad	ok	bad	ok	ok	bad	ok
Data for t = -9%								
Range (eV)	24-130		24-120		64-168		24-160	
t(%)	9	- 9	9	-11	11	-11	9	- 9
V_o(eV)	41	17	37	13	>45	17	29	37
Δ(%)	58	67	43	64	~55	38	62	66
$\{g_i\}$	bad	ok	bad	ok	ok	ok	bad	ok

Figure Captions

Figure 1: View of the real lattice and reciprocal lattice appropriate for the (110) surface of a bcc material. For the top view, the square atoms are in the even number layers. For the side view, the shaded atoms are in a plane $a_2/2$ below the plane of the open atoms.

Figure 2: Schematic showing idealized intensities in momentum space along with the corresponding Fourier transforms in real space. (a) Interference function for 15% relaxation of the surface. (b) Fourier transform of (a) assuming the data extend to infinity. This shows the type of doublet structure expected for a relaxed surface. There is a single delta function at the origin of unit magnitude. (c)-(d) Schematic of window function limiting the data range along with its Fourier transform. (e)-(f) Appearance of a finite data set along with the Patterson function showing spurious features not associated with structure. Curve (e) is the product of (a) and (c). Curve (f) is therefore the convolution product of (b) and (d).

Figure 3: (a) Kinematic interference function and constant window function for surface relaxed 9% and V_o = 16 eV. (b) Plot of residual as a function of inner potential, V_o, and % relaxation, t. (c) Contour plot of part (b) showing minimum in the surface at t ~ 8% and V_o ~ 17 eV. All contours in this paper are separated by $\Delta R = 0.05$.

Figure 4: (a) Interference function, I_f, for W(110) assuming V_o = 16 eV and the surface is first relaxed inward by 9% and second unrelaxed. (b) Topographic plot of the residual as a function of V_o and t for the 9% relaxed surface I-V curve. (c) Same for the I-V

curve for the unrelaxed surface.

Figure 5: (a) Set of coefficients $\{g_i\}$ for the residual solution at V_o = 17 eV and t = -9% shown in Fig. 4c. (b) Same for the residual solution at V_o = 37 eV and t = 11%. The set shown in (a) is physically more realistic than the set in (b) which demonstrates that these coefficients can aid in distinguishing spurious minima in the residual surface. (c) Set of coefficients for the residual surface shown in Fig. 4d for V_o = 17 and for various values of t. All sets of coefficients are nearly identical implying that the surface is not relaxed. The carets below the axis show which coefficients are missing.

Figure 6: I-V curve and drawn window for the (11) beam of W(110) taken from ref. 15 for the case t = 9%. The four topographic plots are the residual surfaces for increasing ranges of data. (a) 24 - 74 eV, (b) 24 - 144 eV, (c) 24 - 214 eV, and (d) 24 - 296 eV.

Figure 7: Same data as used in Fig. 6b showing four different types of window functions: (a) drawn envelope window; (b) constant window; (c) effect of dividing data by drawn window in (a) and then using a constant window; and (d) apodizing both data and drawn window in (a). All four result in residual surfaces similar to those in Fig. 6 with the minima being of different depths.

Figure 8: (a) Same data as in Fig. 7a. (b) Data for same beam but for the case of the surface relaxed inward by 9%. Note the similarity of the two sets of data. (c) and (e) For the t = 9% curve, these are the sets of coefficients for the two minima that occur in the residual surface in Fig. 6b. (d) and (f) For the t = -9% curve, the sets of coefficients for the

two minima in the residual surface. Even though the data are similar and the residual surfaces are similar, the coefficient sets allow for a distinction between the correct minima and the spurious minima.

Figure 9: Data for W(110) from ref. 15 for the case of both inward relaxation of t = -9% and outward relaxation of t = 9%. (a) (00) beam (b) (20) beam, and (c) (02) beam. Note the very strong similarity between the (00) beams for the two cases.

Figure 10: (a) Data and window for (11) beam of W(110) from ref. 15 for the case of an unrelaxed surface. (b) Topographic plot of the residual surface as a function of V_o and t showing a trough at V_o = 12 eV which is the signature of an unrelaxed surface. The minimum at V_o = 37 eV is spurious as seen from the set of coefficients. (c) Sets of coefficients for various values of t and V_o which occur at the bottom of the trough.

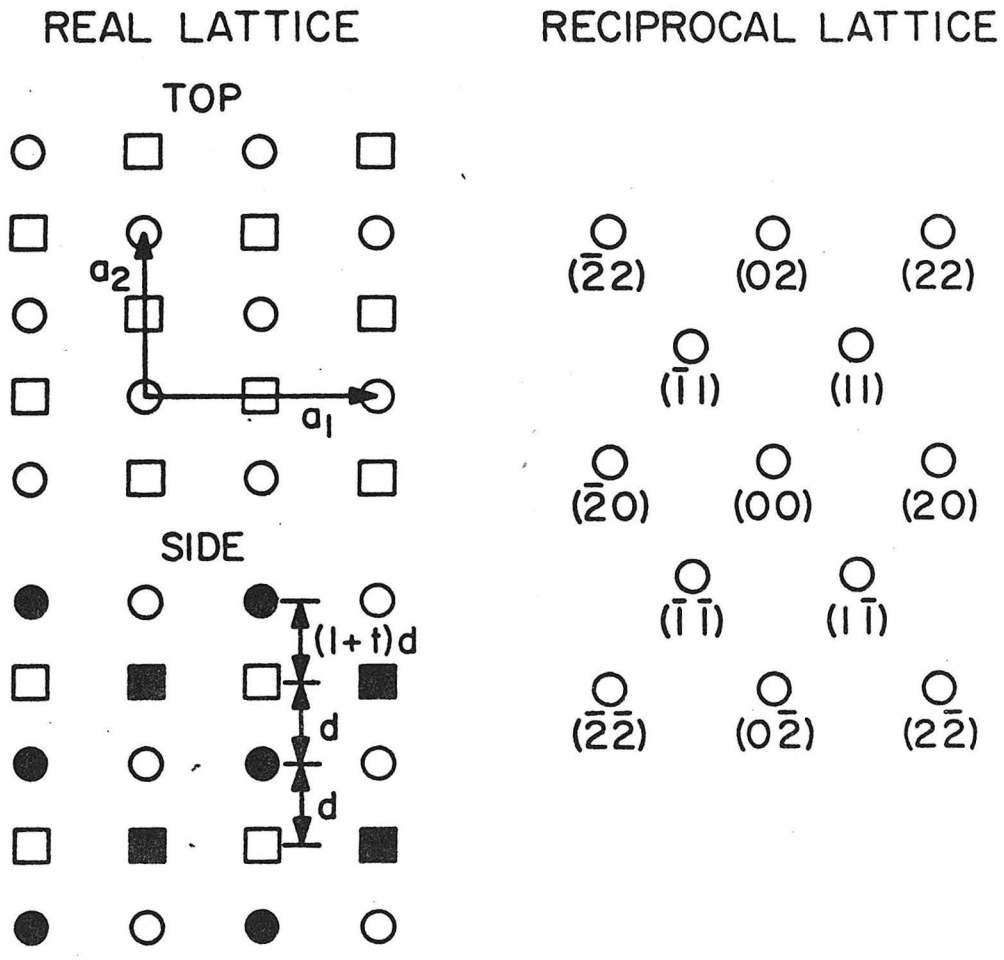
REAL LATTICE
RECIPROCAL LATTICE
TOP
a_2
a_1
SIDE
(1+t)d
d
d
$(\bar{2}2)$
(02)
(22)
$(\bar{1}1)$
(11)
$(\bar{2}0)$
(00)
(20)
$(\bar{1}\bar{1})$
$(1\bar{1})$
$(\bar{2}\bar{2})$
$(0\bar{2})$
$(2\bar{2})$

Figure 1

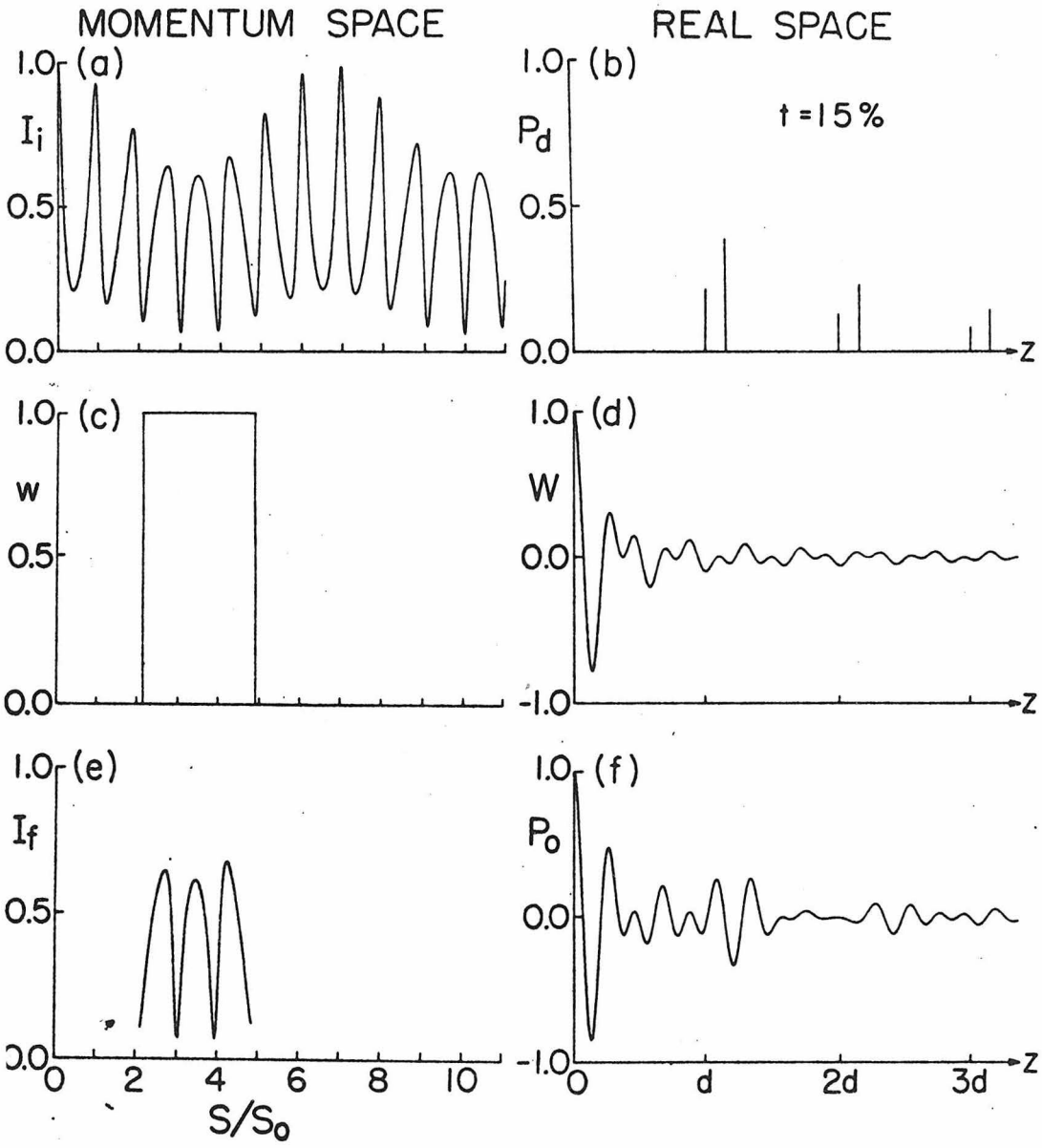
MOMENTUM SPACE
REAL SPACE
(a)
(b)
(c)
(d)
(e)
(f)
I_i
P_d
w
W
I_f
P_o
t = 15%
1.0
0.5
0.0
-1.0
z
0
2
4
6
8
10
S/S_o
d
2d
3d

Fig. 2

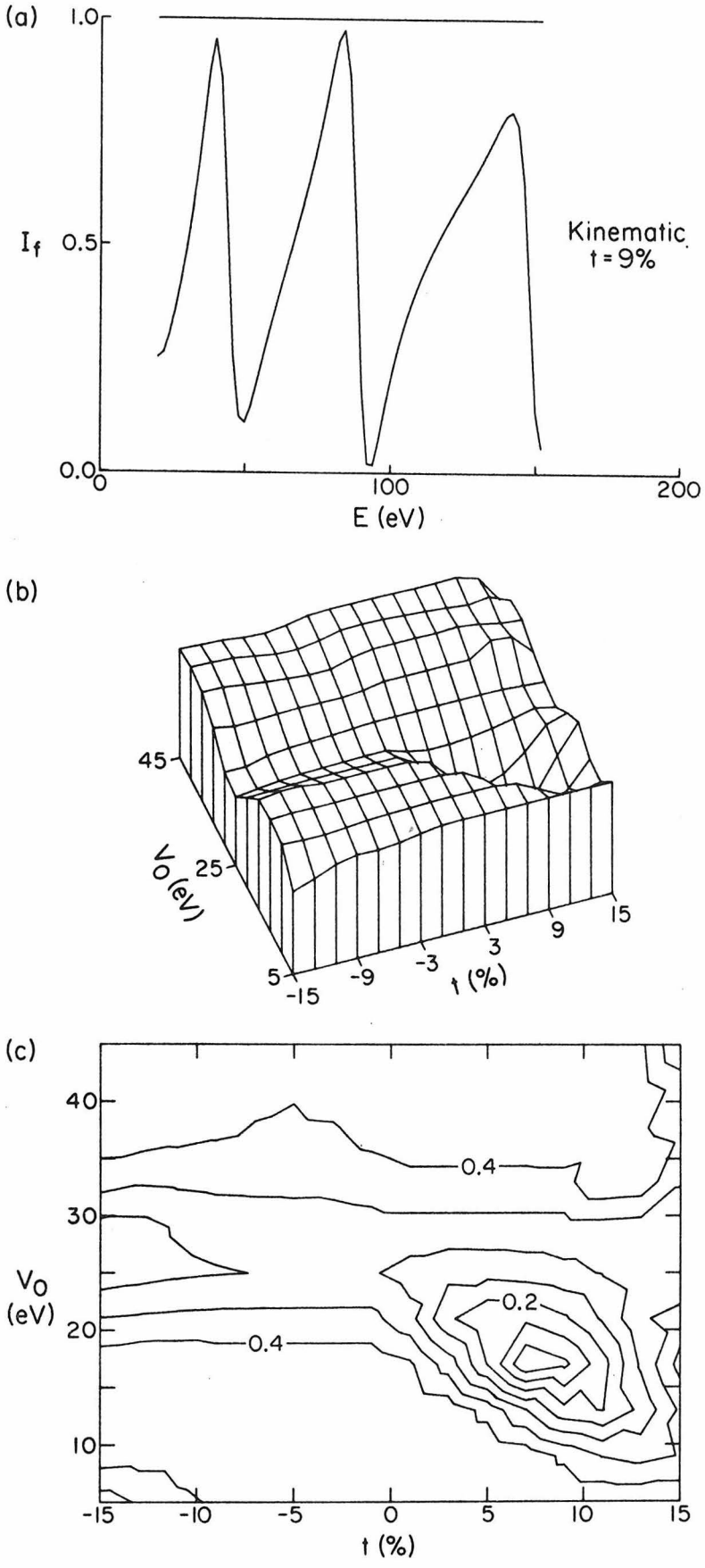
(a)
1.0
0.5
0.0
I_f
0
100
200
E (eV)
Kinematic
t = 9%
(b)
45
25
5
V_o (eV)
-15
-9
-3
3
9
15
t (%)
(c)
40
30
20
10
V_o
(eV)
0.4
0.2
0.4
-15
-10
-5
0
5
10
15
t (%)

Figure 3

KINEMATIC

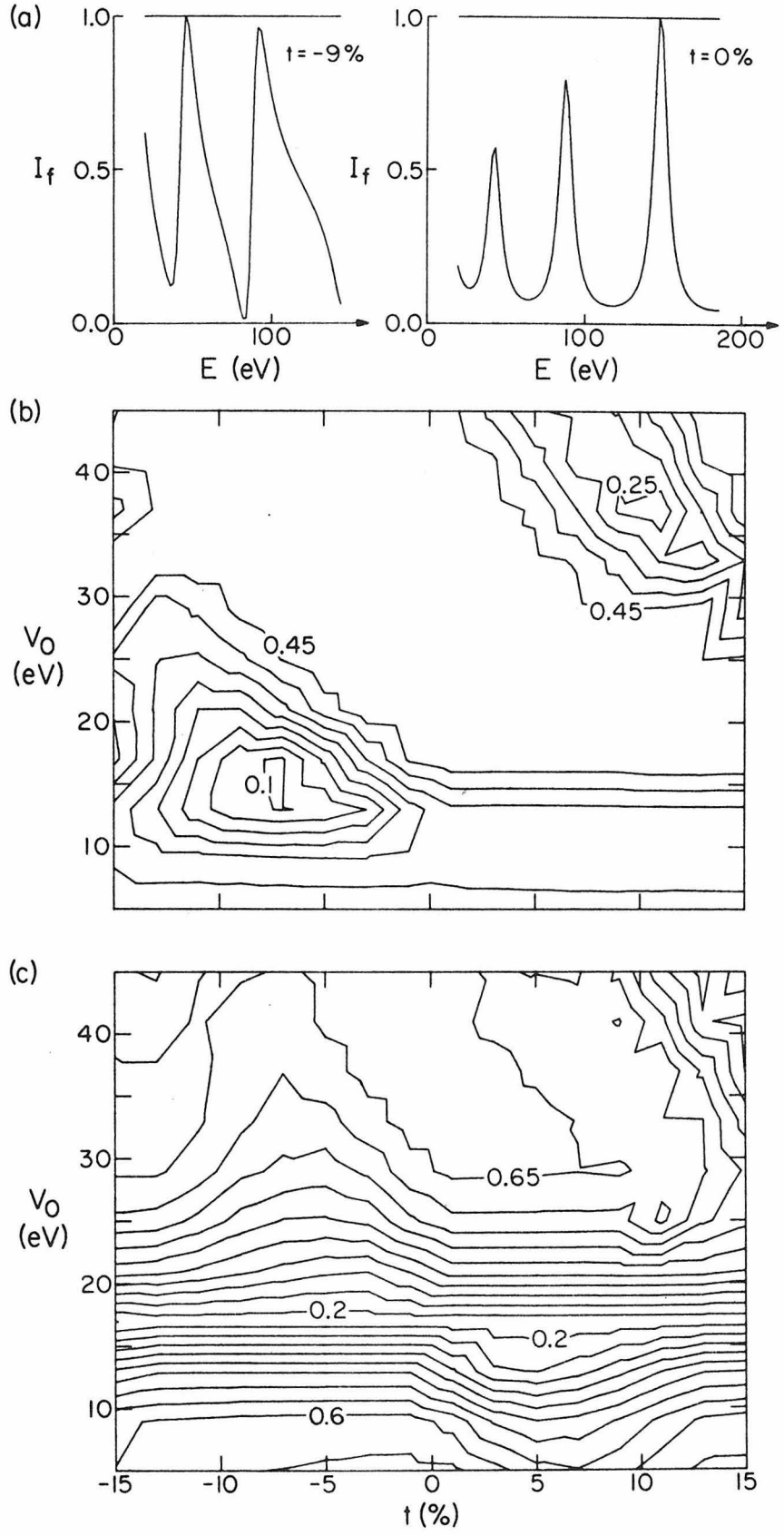

Figure 4

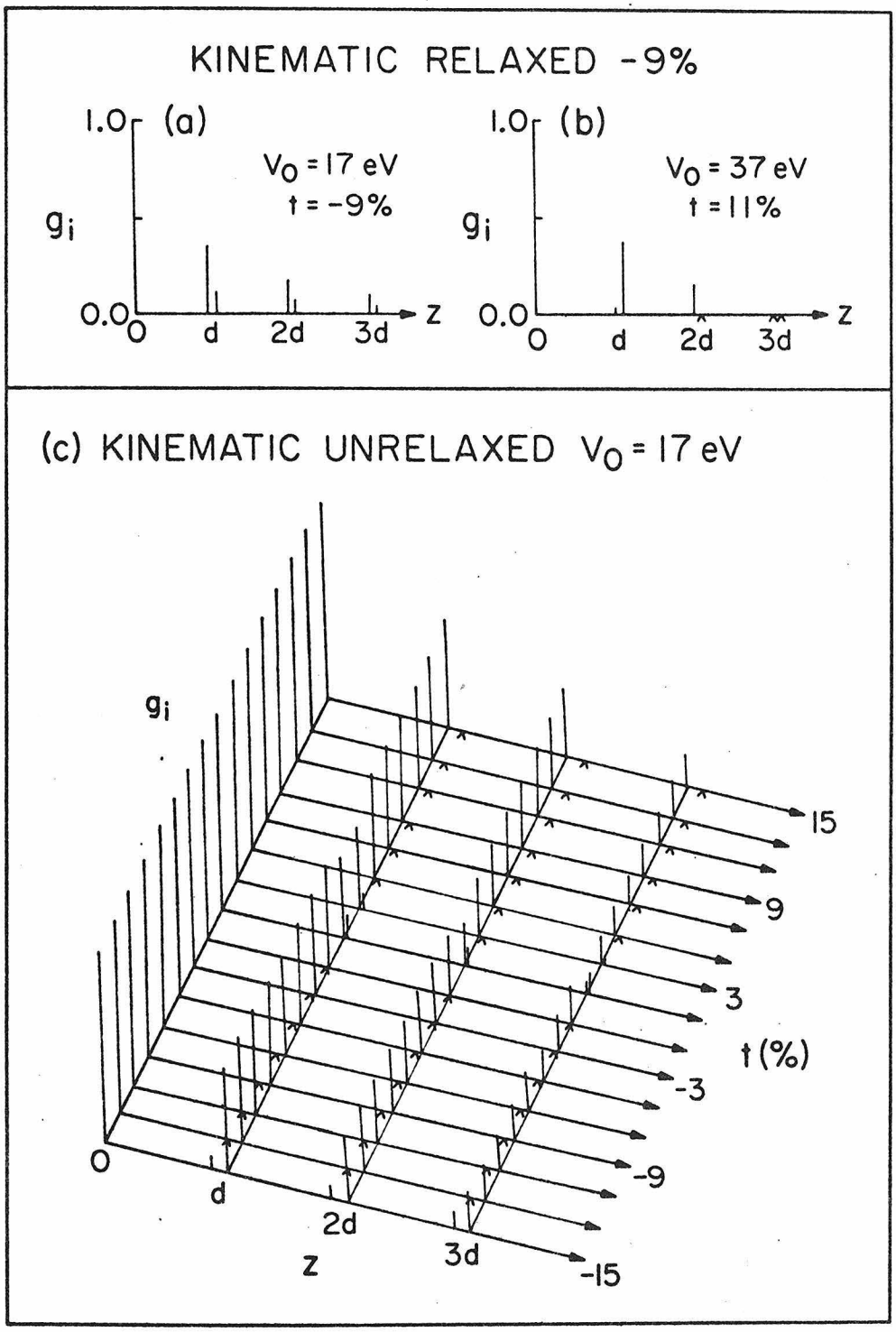
KINEMATIC RELAXED -9%
1.0
(a)
V_0 = 17 eV
t = -9%
g_i
0.0
0
d
2d
3d
z
1.0
(b)
V_0 = 37 eV
t = 11%
g_i
0.0
0
d
2d
3d
z
(c) KINEMATIC UNRELAXED V_0 = 17 eV
g_i
15
9
3
t (%)
-3
-9
-15
0
d
2d
3d
z

Figure 5

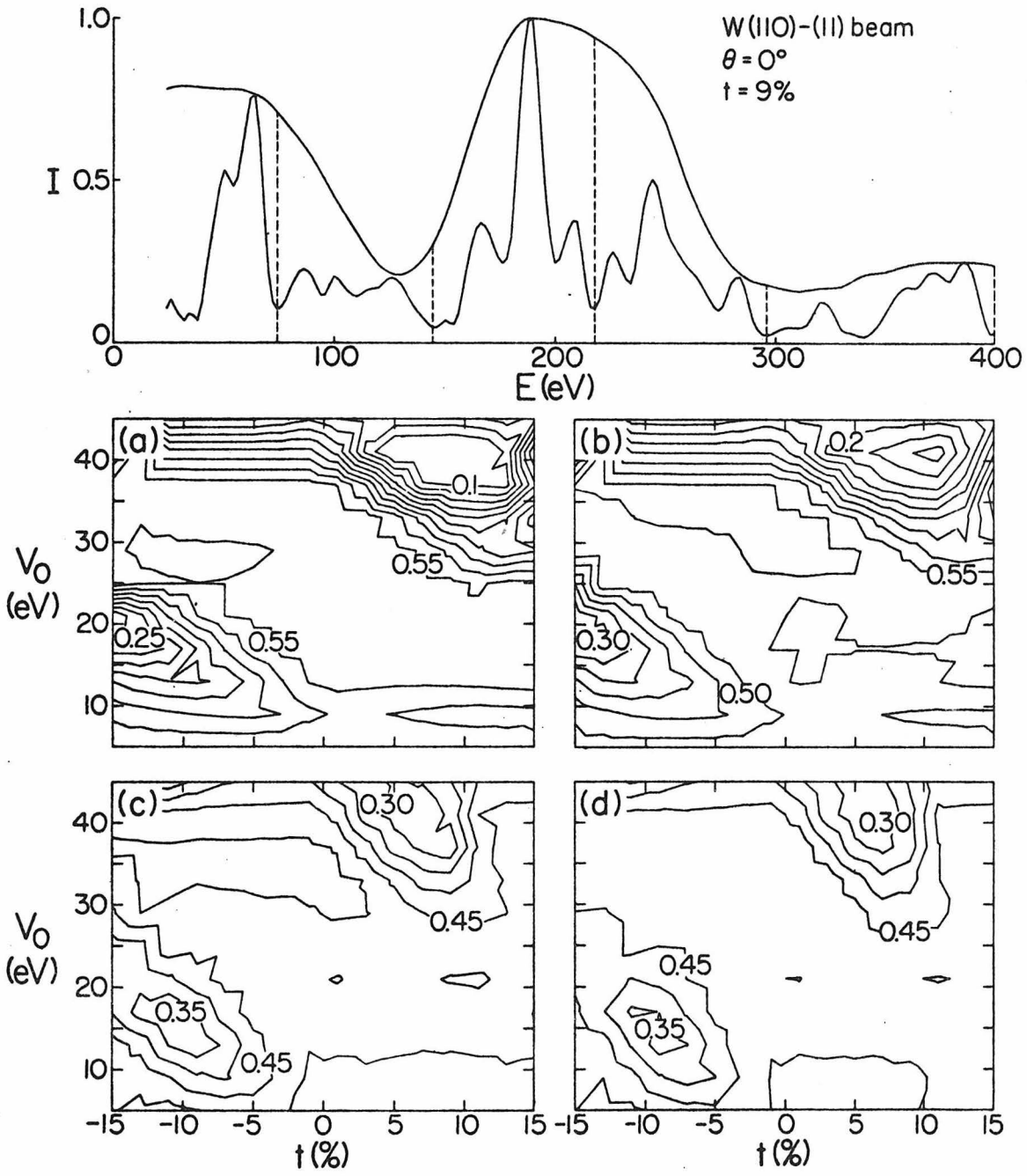

Figure 6

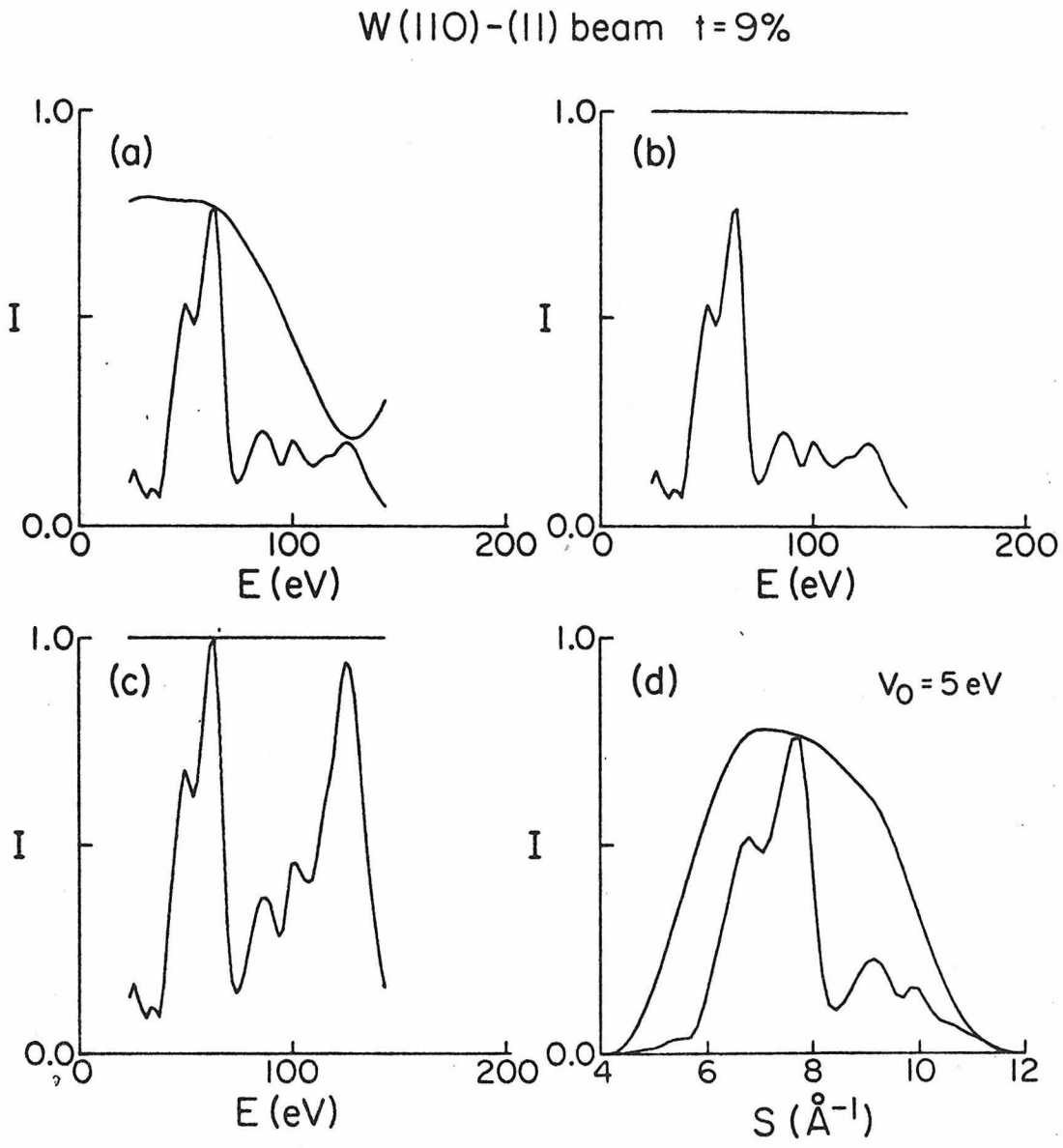

Figure 7

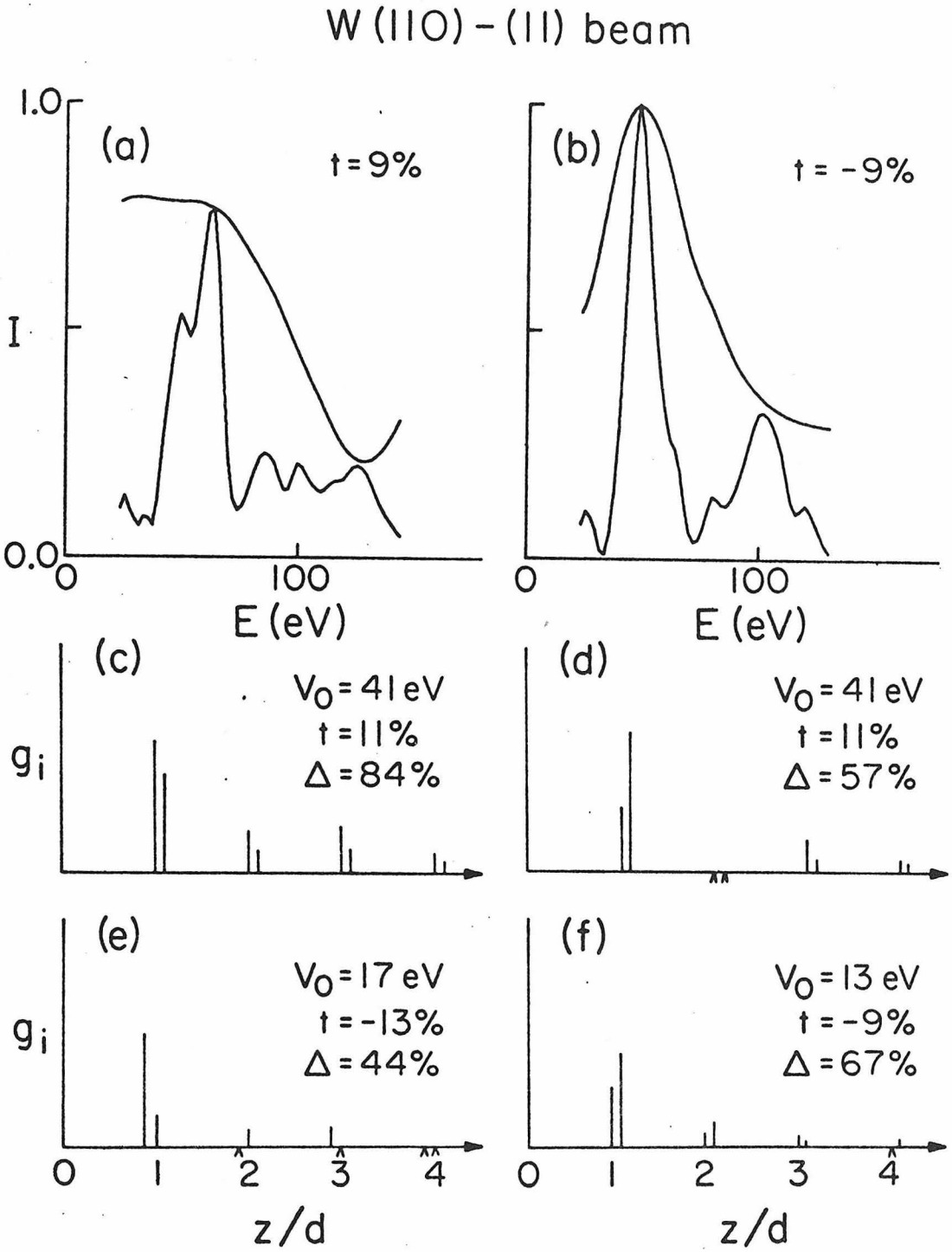
W (110) - (11) beam
1.0
0.0
I
(a)
t = 9%
(b)
t = -9%
0
100
E (eV)
(c)
V_0 = 41 eV
t = 11%
Δ = 84%
(d)
V_0 = 41 eV
t = 11%
Δ = 57%
g_i
(e)
V_0 = 17 eV
t = -13%
Δ = 44%
(f)
V_0 = 13 eV
t = -9%
Δ = 67%
0
1
2
3
4
z/d

Figure 8

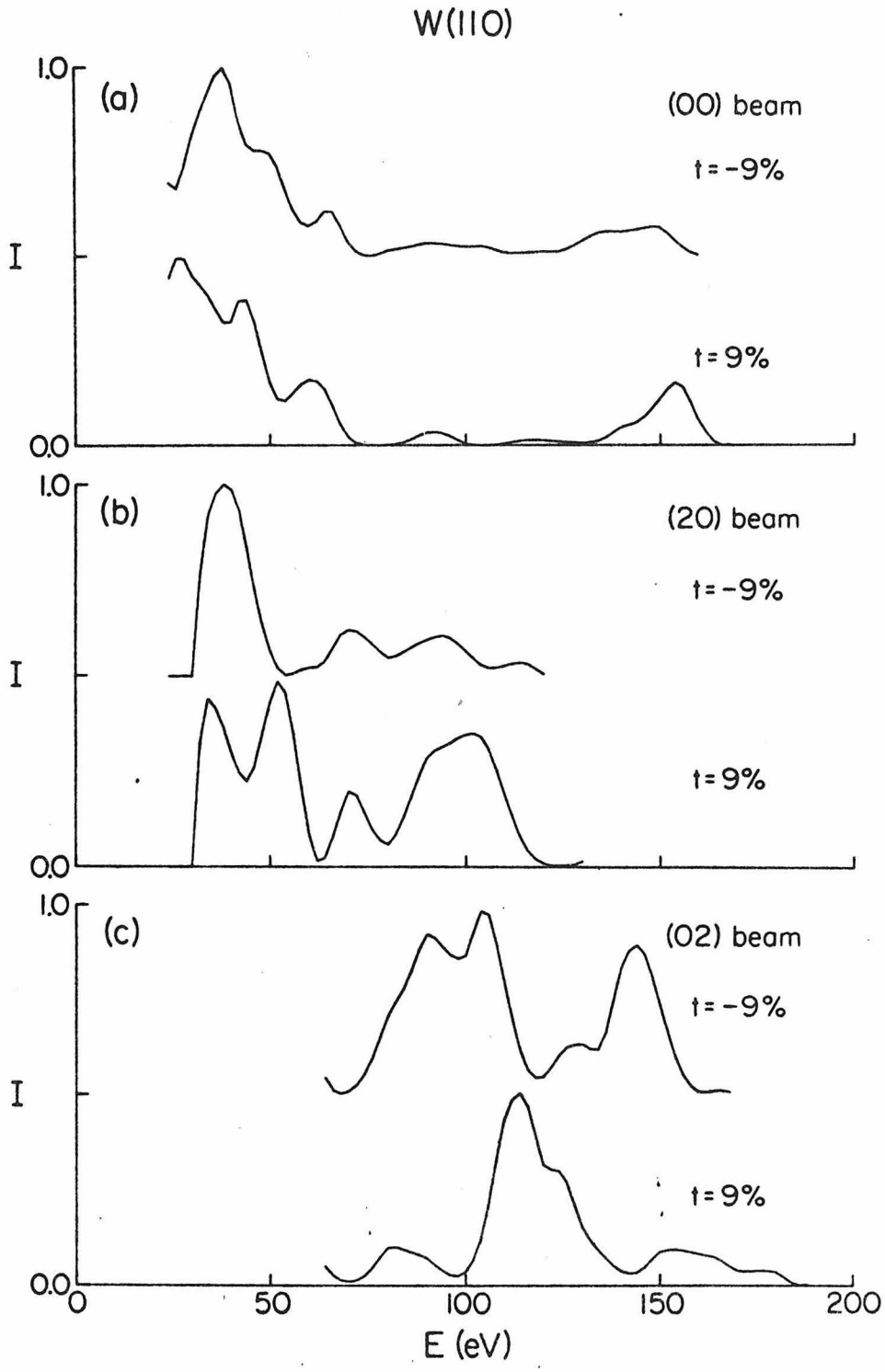
W(110)
1.0
(a)
(00) beam
t=-9%
I
t=9%
0.0
1.0
(b)
(20) beam
t=-9%
I
t=9%
0.0
1.0
(c)
(02) beam
t=-9%
I
t=9%
0.0
0
50
100
150
200
E (eV)

Figure 9

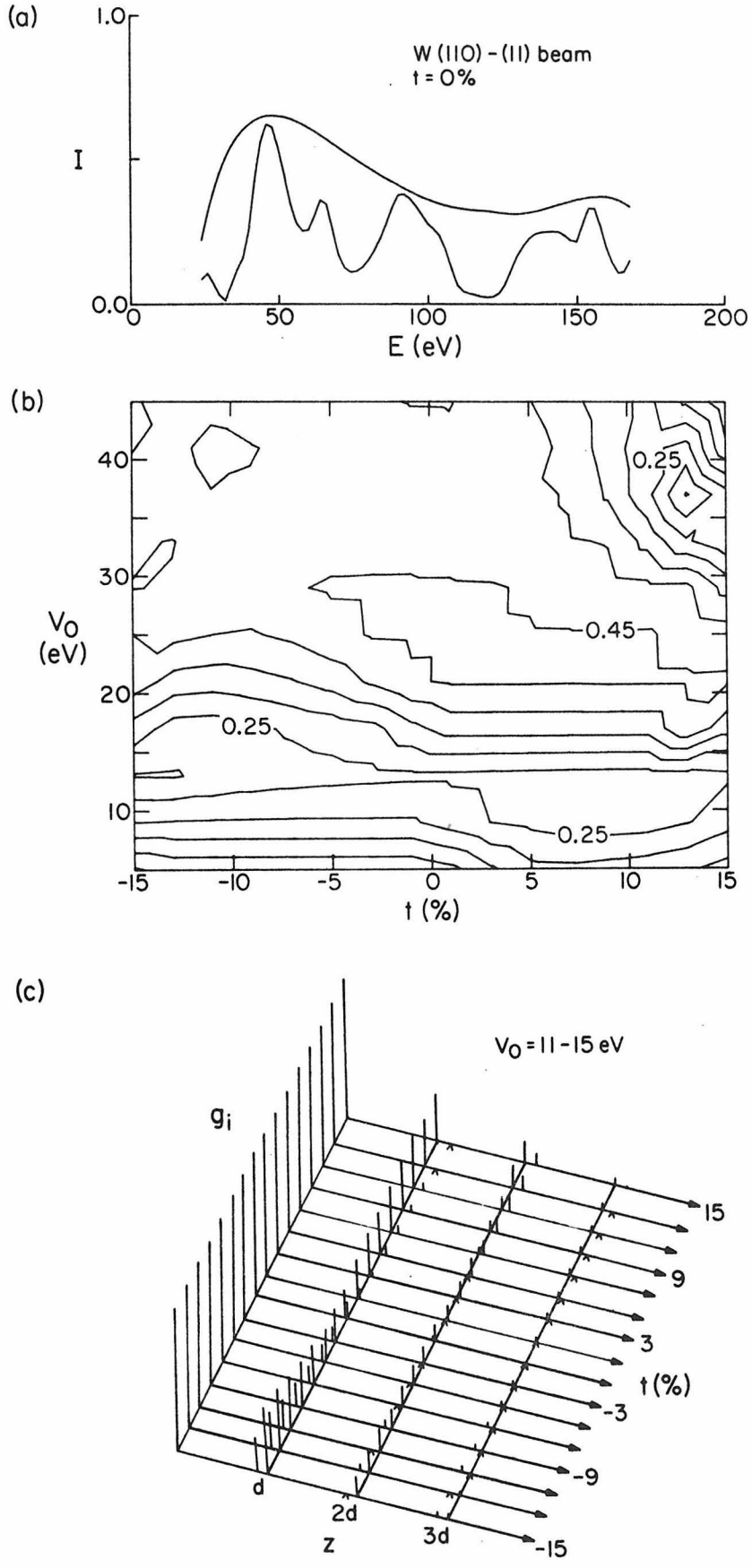
(a)
1.0
0.0
I
W (110) - (11) beam
t = 0%
0
50
100
150
200
E (eV)
(b)
40
30
20
10
V_0 (eV)
0.25
0.45
0.25
0.25
-15
-10
-5
0
5
10
15
t (%)
(c)
V_0 = 11 - 15 eV
g_i
15
9
3
t (%)
-3
-9
-15
d
2d
3d
z

Figure 10

Chapter 3

ANALYSIS OF THE STRUCTURE OF THE PLATINUM (111) SURFACE BY LOW-ENERGY ELECTRON DIFFRACTION: MULTIPLE SCATTERING AND CONVOLUTION-TRANSFORM

D. Dion, R. P. Merrill and D. Monroe
Department of Chemical Engineering
University of California
Berkeley, California 94720

and

C.-M. Chan, S. L. Cunningham, M. A. Van Hove and W. H. Weinberg
Division of Chemistry and Chemical Engineering
California Institute of Technology
Pasadena, California 91125

1. Introduction

We have made new measurements of low-energy electron diffraction (LEED) intensity-voltage (I-V) beam profiles using a Faraday cup collector in order to examine the relaxation of clean Pt(111) by two different, independent methods. These methods are a full multiple-scattering calculation (1) and convolution-transform calculation (2-4).

Dynamical calculations have been used successfully in the determination of the structure of numerous surfaces (1). Likewise, the convolution-transform method has been applied successfully in the determination of the structure of various clean metal surfaces yielding good agreement with results from dynamical calculations (2-4).

The structure of the clean Pt(111) surface has been investigated both by ion channeling experiments (5) and low-energy electron diffraction (6-7). Davis et al. (5) reported that the surface layer relaxes outward by 15% of the bulk spacing. However, they found the crystal was covered with one monolayer of oxygen and ~0.1 monolayer of carbon after the experiments. On the other hand, Kesmodel et al. found that the relaxation of the clean surface layer is less than $\pm$5% in their earlier work (6) and less than $\pm$2.5% in a more recent and more extensive analysis (7). Our work presents an independent structure determination by analyzing a new set of I-V beam profiles using three different methods as mentioned above. The consistent results obtained by these methods indicate that the outermost layer of the Pt(111) surface contracts by less than 5% of its bulk value.

Analysis by Dynamical Calculations

Using dynamical (i.e., multiple scattering) calculations, we have analyzed the LEED intensity-voltage spectra of Pt(111) for the (00) beam for three directions of incidence [$(\theta,\phi) = (6^{o}, -2^{o})$, $(12^{o},-2^{o})$ and $(15^{o}, 178^{o})$] as well as the (10), $(\bar{1}0)$ and $(\bar{2}0)$ beams at normal incidence. We use the following conventions: $\theta=0^{o}$ defines normal incidence, while $\phi=0^{o}$ defines the direction of the (10) beam (as in ref. 7).

The atomic potential for platinum comes from a self-consistent Hartree-Foch-Slater cluster calculation as described in Moruzzi et al. (8); no relativistic effects are included [as opposed to the potential used by Kesmodel et al. (6,7)]. A muffin-tin constant of -10 eV was used and found to be adequate (in Refs. 6 and 7, a value of -14.3 eV was found appropriate for the different potential). Damping is described by an energy-independent imaginary part of the electron self-energy of -3 eV (cf., -2.5 eV in Ref. 7, superseding -4 eV in Ref. 6). Room temperature applies, the atomic vibrations being characterized by a Debye temperature of 240K; but the mean-square vibrational amplitudes are increased arbitrarily by a factor of 1.4 to account for enchanced vibrations at the surface.

The perturbation scheme known as renormalized forward scattering (Ref. 1) was chosen for efficiency. Good convergence occurred despite the strong atomic scattering, as in the case of iridium in an earlier study (3).

The calculations ranged over relaxations of the topmost interlayer spacing from -5% (contraction) to +15% (expansion). Furthermore, a check was made concerning

the layer registries: the topmost layer was allowed to shift from an fcc arrangement (ABCABC...; surface at left) to an hcp arrangement (CBCABC...). The hcp arrangement gave no agreement with experiment, whatever the spacing. For the pure fcc surface, the comparison with experiment favored no relaxation with an uncertainty of about 5% of the bulk spacing, cf., Figs. 1 and 2. The level of agreement between theory and experiment obtained here is slightly inferior to that obtained in Ref. 7. This may be the result of neglecting relativistic effects in the construction of the atomic potential.

Analysis by the Convolution-Transform Method

The convolution-transform method has been described previously in detail (2-4). It is based on the concept of finding the best fit between the observed and calculated Patterson functions. The observed Patterson function, $P_o(z)$, is the Fourier transform of the intensity of an elastically reflected electron beam as a function of the momentum transfer perpendicular to crystal surface The Fourier transform of a finite range of data produces Gibbs oscillations in the observed Patterson function. To account for the Gibbs oscillations, a calculated Patterson function $P_c(z)$ is constructed by convoluting the Fourier transform of a window function with a set of delta functions which represents the layer spacings of the crystal. A simple and effective window function is the truncated envelope of the data as shown in Fig. 3. The purpose of the convolution procedure is to reproduce the Gibbs oscillations so that the features containing structural information in the observed and calculated Patterson functions can be compared.

The quality of the fit between $P_o(z)$ and $P_c(z)$ is given by a residual R defined as

$$R^2 \equiv \int_0^\infty \left[P_o(z) - P_c(z)\right]^2 dz \quad . \qquad (1)$$

The best fit is represented as a minimum in the two-dimensional residual surface obtained by plotting R as a function of both V_o (the effective inner potential) and t (the percent expansion of the surface layer with respect to the bulk spacing). The minimum is characterized by a parameter Δ, defined as

$$\Delta \equiv 100\ (R_{ave} - R_{min})/R_{ave}, \qquad (2)$$

where R_{ave} is the average value of R over all values of V_o and t examined, and R_{min} is the smallest value of the residual. In searching for the minimum, the value of t is varied from -20% to 20% and the value of V_o is varied from 0 to 40 eV.

The LEED I-V profiles for the (00) beam for six angles of incidence: $(\theta,\phi) = (6^o, -2^o)$, $(12^o, -2^o)$, $(15^o, 178^o)$, $(6^o, 268^o)$, $(12^o, 268^o)$ and $(27^o, 268^o)$ have been analyzed. These spectra are shown in Fig. 3. The energy range of the experimental data is from 10 eV to 500 eV. However, the energy range actually used in the convolution-transform calculation was from 40 eV to 180 eV (for reasons specified in Ref. 4). The low energy cut-off in the calculation was selected to occur at a minimum in the I-V curve. The high energy cut-off was somewhat arbitrary due to the low intensity. The energy range used initially for the curve for $(\theta,\phi) = (15^o, 178^o)$ was from 40 to 200 eV, but the residual surface obtained showed no minimum, probably due to the presence of multiple overlapping peaks in the energy range from 40 to 70 eV. A minimum in the residual surface was obtained however after the data below 70 eV were truncated.

The results of our calculations are summarized in Table 1. The surface relaxation obtained from different beams varies from -8% to 6%, and the inner potential varies from 0 to 26 eV. The average result from all beams analyzed

suggests a -2.3% relaxation (i.e. 2.3% contraction). However, as discussed in Ref. (4), it seems more reasonable to weight the results from different beams according to the quality of the fit between the observed and the calculated Patterson functions. To obtain the weighted average, we multiply the relaxation, t, by the corresponding values of Δ and normalize by the sum of the Δ's. The weighted average result gives a relaxation of -2.8%.

References:

1. J. B. Pendry, Low-Energy Electron Diffraction, Academic Press, London, 1974.
2. S. L. Cunningham, C.-M. Chan and W. H. Weinberg, Phys. Rev. B (in press).
3. C.-M. Chan, S. L. Cunningham, M. A. Van Hove, W. H. Weinberg and S. P. Withrow, Surface Sci. (in press).
4. C.-M. Chan, S. L. Cunningham, M. A. Van Hove, W. H. Weinberg, Surface Sci. (in press).
5. J. A. Davies, D. P. Jackson, J. B. Mitchell, P. R.Norton and R. L. Tapping, Phys. Letters 54 A, 239 (1975).
6. L. L. Kesmodel and G. A. Somorjai, Phys. Rev. B11, 630 (1975).
7. L. L. Kesmodel, P. C. Stair and G. A. Somorjai, Surface Sci. 64, 342 (1977).
8. V. L. Moruzzi, A. R. Williams and J. F. Janak, Calculated Electronic Properties of Metals, (to be published).

Table Captions

Table 1: Summary of convolution-transform results for Pt(111) surface. V_o is the effective inner potential and t is the percent relaxation of the surface layer with respect to the bulk for which a minimum occurs in the residual (t is positive for expansion, negative for contraction). The parameter Δ is a measure of the quality of the fit between theory and experiment: it can range from 0% for no fit to 100% for a perfect fit; typical values from previous experience are 10% for a bad fit and 50% for a good fit.
θ is the angle of incidence relative to the surface normal, and $\phi = 0^o$ defines the direction of the (10) beam.

Table 1

θ	φ	Energy Range (eV)	V_o (eV)	Δ%	t%
27	268	30-120	26	69	0
12	268	40-180	18	51	-4
6	268	36-140	20	41	-4
15	178	70-200	26	54	-8
12	-2	40-180	0	29	6
6	-2	36-160	20	40	-4

Figure Captions:

Figure 1: Experimental (dashed) and dynamically calculated (continuous lines) IV-curves for the (00) beam reflected from Pt(111) at three directions of incidence (θ,ϕ). The theoretical curves apply to three different top interlayer spacings: relaxed by -5% (contracted), 0% (unrelaxed) and 5% (expanded) relative to the bulk value. The intensity scales are arbitrary, but constant within each group of three theoretical curves at the same direction of incidence.

Figure 2: Same as Figure 1 for the (10), ($\bar{1}$0) and ($\bar{2}$0) beams at normal incidence. The theoretical curves correspond to an unrelaxed surface. The experimental ($\bar{1}$ 1) beam, symmetrical to the (10) beam at normal incidence, is included for comparison.

Figure 3: Experimental I-V spectra for (00) beam at 300^{o}K for various angles of incidence (θ,ϕ); drawn windows are included.

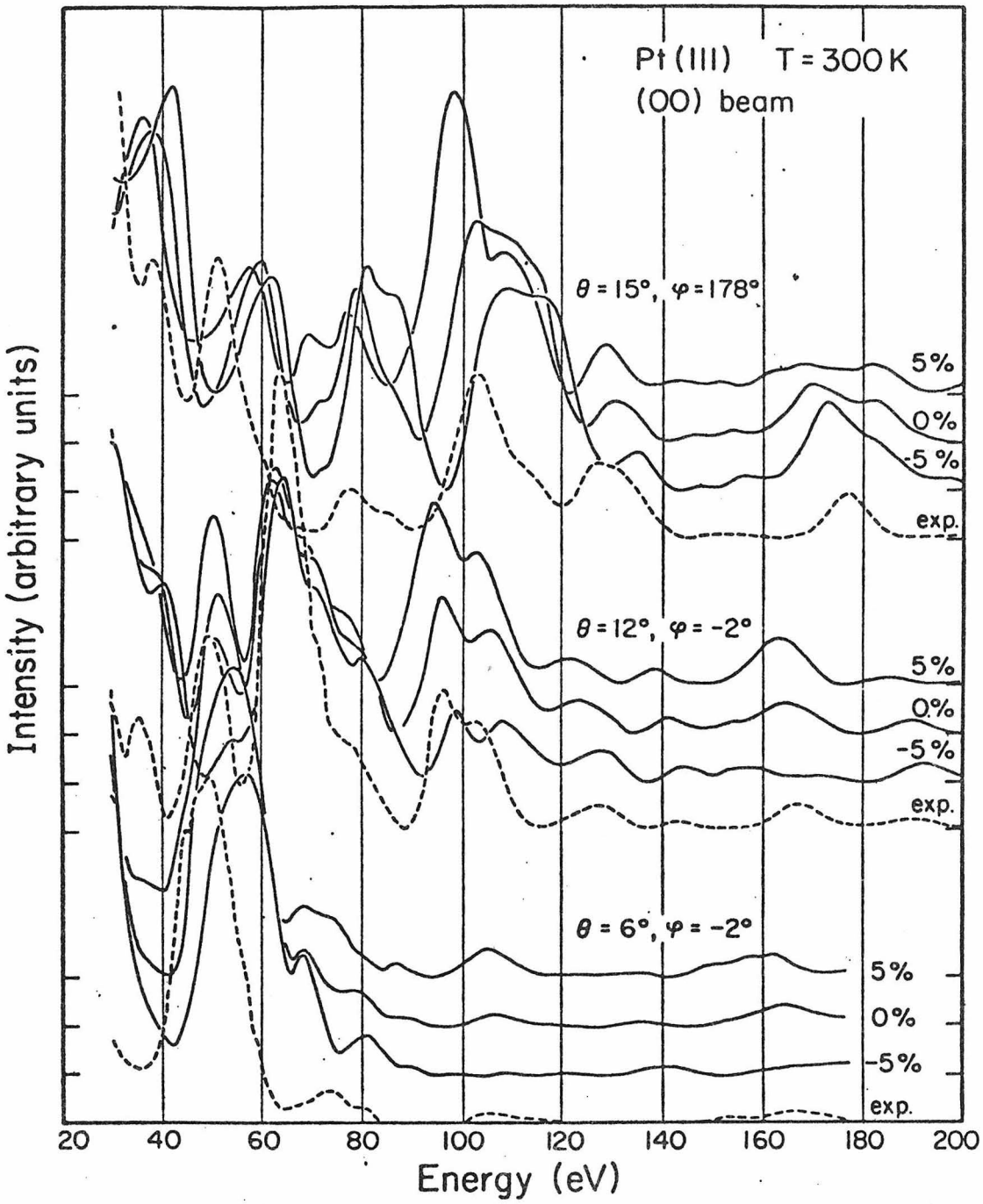
Pt (111) T = 300 K
(00) beam
θ = 15°, φ = 178°
5%
0%
-5%
exp.
θ = 12°, φ = -2°
5%
0%
-5%
exp.
θ = 6°, φ = -2°
5%
0%
-5%
exp.
Intensity (arbitrary units)
20
40
60
80
100
120
140
160
180
200
Energy (eV)

Fig. 1

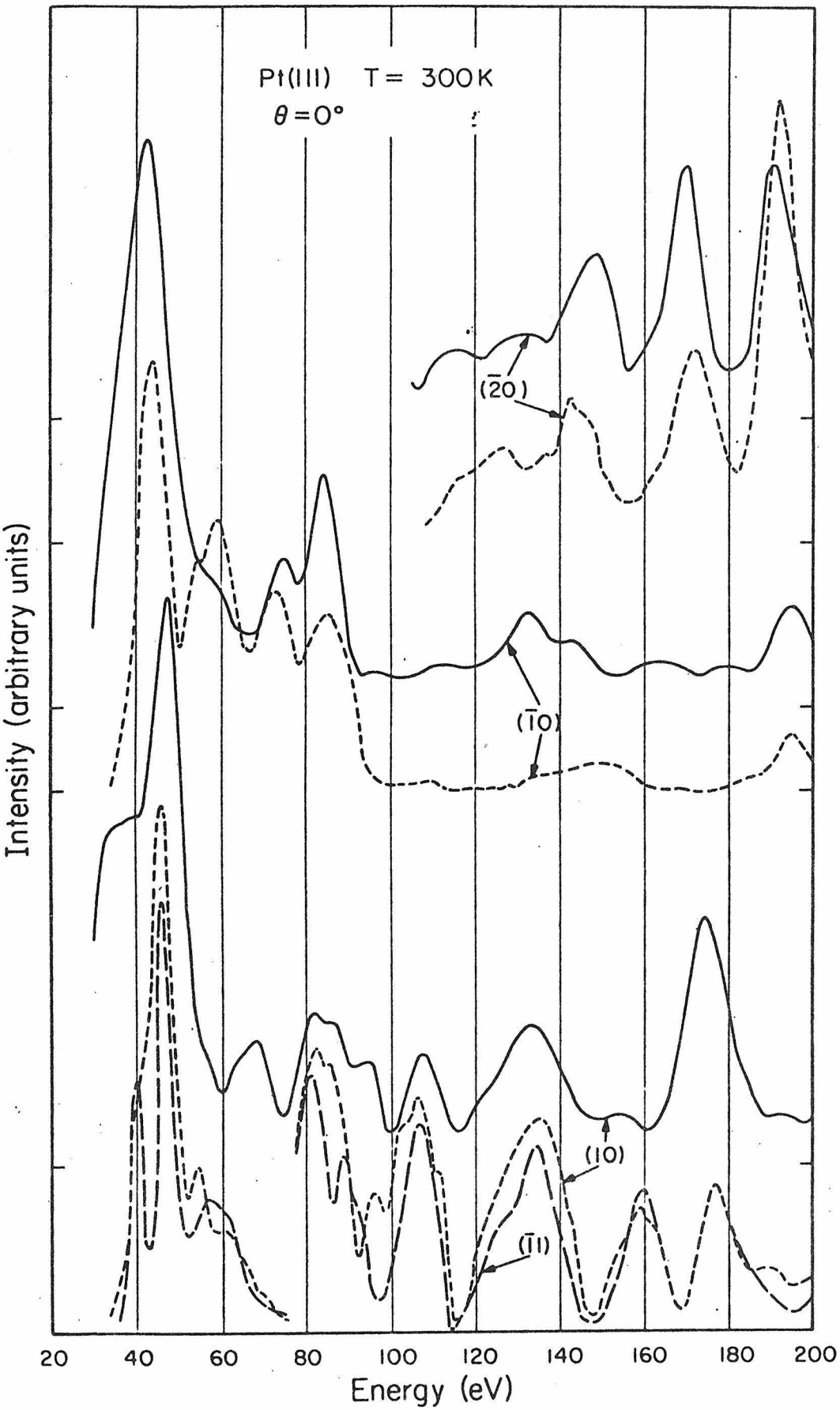
Pt(111) T = 300K
θ = 0°
(2̄0)
(1̄0)
(10)
(1̄1)
Intensity (arbitrary units)
20
40
60
80
100
120
140
160
180
200
Energy (eV)

Fig. 2

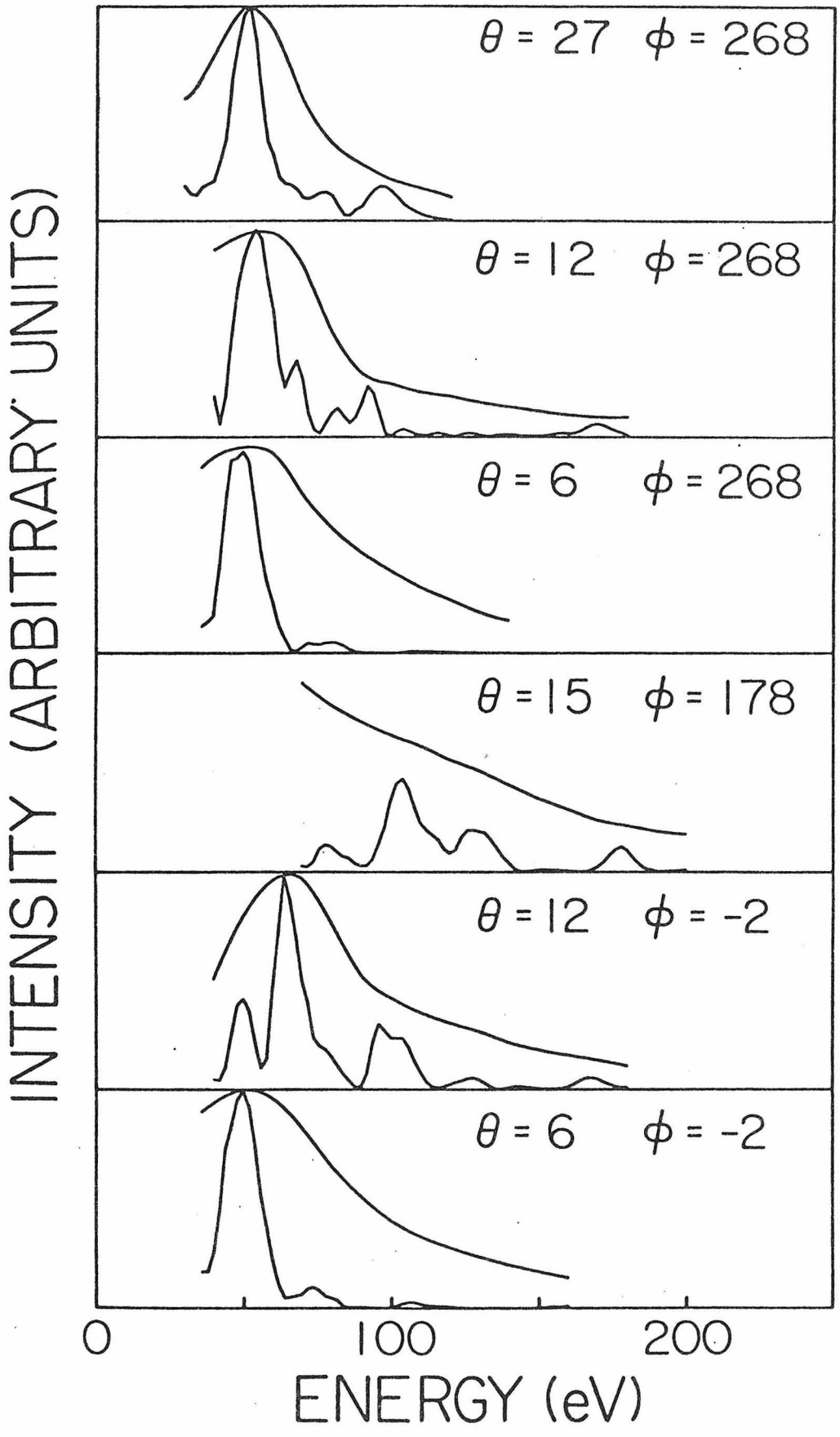
θ = 27 φ = 268
θ = 12 φ = 268
θ = 6 φ = 268
θ = 15 φ = 178
θ = 12 φ = -2
θ = 6 φ = -2
INTENSITY (ARBITRARY UNITS)
0
100
200
ENERGY (eV)

Fig. 3

Chapter 4

SURFACE RELAXATION OF Ni(110), Al(110) and Ag(110) DETERMINED BY THE CONVOLUTION-TRANSFORM METHOD

by

C.-M. Chan, S. L. Cunningham, M. A. Van Hove and W. H. Weinberg

Division of Chemistry and Chemical Engineering
California Institute of Technology
Pasadena, California 91125

Surface Science 67, 1-9 (1977)

Abstract

Experimental (LEED) intensity-voltage (I-V) beam profiles for clean Ni(110), Al(110) and Ag(110) have been analyzed by the convolution-transform method. Results indicate that the first layer spacing of Ni(110), Al(110) and Ag(110) is contracted by 5%, 4% and 7% of their bulk spacing, respectively. These results are in good agreement with the results obtained earlier using dynamical calculations.

1. Introduction

Previously, we have applied our convolution-transform method of surface structure determination to analyze both theoretical LEED I-V "data" for W(110) which were calculated by Van Hove and Tong (1) as well as experimental LEED I-V data for Ir(111) (2). For the case of the calculated I-V curves, the agreement between the results from the convolution-transform method and the dynamical calculations is excellent in the case of 9% contraction of the W(110) surface and good both for the case of 9% expansion and no relaxation of the surface layer of W(110). For the case of experimental I-V curves, both the convolution-transform method and dynamical calculations applied to the (00) beam from Ir(111) indicate that the contraction of the top layer spacing of the Ir(111) surface is no greater than 5% of the bulk spacing.

During the past five years, the (110) surfaces of Ni, Al and Ag have been the object of both experimental and theoretical investigations. Duke *et al.* (3), Jepsen *et al.* (4), and Martin *et al.* (5) have investigated the Al(110) surface and reported that the surface layer contracts by 10%, 10-15% and 10% of the bulk layer spacing, respectively. Demuth *et al.* (6) investigated the Ni(110) surface and found that the top layer of the surface contracts by 5%. Moritz (7) and Zanazzi *et al.* (8) investigated the Ag(110) surface and concluded that the surface layer contracts by 7-8% and 7%, respectively.

In this work, we have applied our convolution-transform method in order to determine the relaxation of these clean Ni(110), Al(110) and Ag(110) surfaces. This represents the first non-dynamical analysis of surfaces that are predicted by dynamical calculations to be relaxed. Consequently, our results will serve a dual purpose. First, the results of the convolution-transform method and the dynamical calculations may be compared quantitatively;

and second, the convolution-transform method of LEED analysis is extended to include a new class of experimental data, namely, data from clean contracted metal surfaces.

In Sec. 2, a brief description of the convolution-transform method is given. In Sec. 3, the results of our calculations are presented and discussed. Finally, our conclusions are listed in Sec. 4.

2. Theory

In earlier work, the convolution-transform method of LEED analysis has been described (1,9,10) and applied (2) to determine the spacing of the outermost layer of several clean metal surfaces. The convolution-transform method is based on the concept of fitting the Patterson function of the data with a calculated Patterson function as is done in X-ray crystallographic studies. The "observed" Patterson function, $P_o(z)$, which depends upon the real space coordinate z perpendicular to the surface, is the Fourier transform of the intensity of the LEED beam when plotted as a function of the change in momentum of the scattered electron (which is related to the square root of the electron energy when corrected by the inner potential V_o). The "calculated" Patterson function, $P_c(z)$, is constructed by convoluting the Fourier transform of a "window" function with a set of delta functions which represent the layer spacing of the crystal. The positions of the delta functions are defined completely by one parameter, t, the percent expansion of the surface layer spacing. The "window" function is somewhat arbitrary. As shown in ref. 1, the best fit between $P_o(z)$ and $P_c(z)$ occurs when the window is taken to be a smooth envelope of the data, although other choices can be used.

The quantities $P_o(z)$ and $P_c(z)$ are used to calculate a residual, R, given by

$$R^2 = \int_o^\infty \left[P_o(z) - P_c(z) \right]^2 \, dz. \qquad (1)$$

The two-dimensional mathematical surface of the function R plotted as a function of both V_o and t has a minimum. This minimum is characterized by the parameter Δ defined as

$$\Delta = 100\ (R_{min} - R_{ave})\ /\ R_{ave}, \qquad (2)$$

where R_{min} is the smallest value of the residual, and R_{ave} is the average value over the entire V_o and t parameter space examined. The position of the minimum gives the structure, and the depth of the minimum gives the "goodness" of the fit compared to the average of all fits. The convolution-transform method is described in detail in refs. (1) and (2).

Since we use a kinematic model for electron diffraction, the I-V spectra for this method of analysis should contain kinematic features, i.e., both identifiable Bragg peaks and an identifiable skewness of these peaks if the surface is relaxed. In addition, the energy range of the data has to be considered carefully. Bragg peaks at very low energies (~20 eV) provide the maximum surface sensitivity due to the short electron mean free path, but a severe drawback in using the very low energy peaks ($\lesssim$25 eV) is the uncertainty in the peak shapes caused by the rapidly changing normalization factor of the incident beam current. Another reason for not using the low energy peaks is that low energy electrons ($\lesssim$25 eV) are more sensitive to a number of effects that we neglect (e.g., the surface potential barrier). On the other hand, peaks at high energies (e.g., $\gtrsim$400 eV) have much less surface sensitivity due to the larger electron mean free path. Hence, the use of high energy data will result in a structure similar to that of the bulk. According to our past experience, the optimum energy range for this method

of analysis is from approximately 40 to 250 eV (for low index beams). In this energy range, an I-V spectrum contains approximately two or three Bragg peaks.

In the present case, the energy range of the existing experimental data is relatively short, especially for some spectra of the Ag(110) surface. In the same energy range, fcc(110) surfaces will produce fewer Bragg peaks than, for example, surfaces of W(110) and Ir(111) which we have treated previously. This is due to the fact that Bragg peaks for fcc(110) surfaces are more widely spaced, a manifestation of a smaller interlayer spacing. The short energy range used, especially if an individual I-V spectrum contains only one Bragg peak, will cause more uncertainty in the results. This is due to the fact that the fit between the observed and the calculated Patterson functions will be affected more strongly by the presence of extra structure caused by multiple scattering.

3. Results and Discussion

All the experimental I-V spectra used in this paper were obtained from previously published data (4,7,8,11,12). Due to the limited availability of existing experimental data in the literature, we have little flexibility in choosing I-V spectra with both strong kinematic character and a suitable energy range. Consequently, the results of this work would be expected to have a greater uncertainty than those obtained previously (1,2).

To obtain the best fit between the observed and the calculated Patterson functions, we vary t (the percentage relaxation of the surface layer with respect to the bulk spacing) from -20% to + 20% and V_o (the effective inner potential) from 0 to 40 eV. The lower bound on V_o is chosen to be zero since

we know of no physical effect, including multiple scattering, that could systematically shift all the Bragg peaks in an I-V curve to higher energies. The upper bound of 40 eV is more arbitrary, but past experience with other metals (W and Ir) suggests that this is adequate. We ascribe large values of the effective inner potential, when they occur, to multiple scattering effects. These are known from dynamical theory to shift Bragg peaks mainly to lower energies by approximately 10 eV. Whereas the surface structure (value of t) obtained from different beams should be the same, there may be no relation between the values of the inner potential for these different beams. This is due to the fact that the inner potential, as used in the convolution-transform method, takes account of many multiple scattering effects which vary from beam to beam (1).

A. Ni(110)

We have analyzed each of the eight Ni(110) I-V spectra (12) shown in Fig. 1. Of the eight spectra, only the (11) beam does not give a result inside the range of our searching parameters. Therefore, we exclude this spectrum from our analysis. The results of our calculations are summarized in Table I, wherein we present the values of V_o and t for which the minimum occurs in the residual as well as the value of Δ characterizing the depth of the minimum. The surface layer relaxation obtained from the several different beams varies from -8% to +2%, and the variation of the inner potential is from 30 eV to 10 eV. The scatter of the results is due to a number of factors including multiple scattering, variable mean free path and a limited flexibility in choosing spectra from the literature (e.g., a short energy range). However, an an average of the above results should be helpful in minimizing the seriousness of these effects and should provide a more reliable answer. The average result from all beams suggests a -4.6% relaxation (i.e., 4.6% contraction). However, rather than taking an unweighted average, it seems more reasonable to weight the results from the different beams according to the quality of the fit between their observed and calculated Patterson functions. To obtain the weighted average, we multiply the relaxation, t, by the corresponding weight, Δ, and normalize by the sum

of the Δ's. The weighted average of all beams yields a -5.1% relaxation. However, the arguments given above are correct only if the spectra considered have the same number of Bragg peaks. This is so by virtue of the fact that it is easier to match the Fourier transform of the experimental spectra which have a fewer number of Bragg peaks (assuming secondary peaks are absent) with the calculated Patterson function. Hence, we obtain an apparently more reliable fit (larger value of Δ) in the case of a spectrum having a fewer number of Bragg peaks. Of course, any dynamical effects will complicate these arguments further. Since not all the I-V spectra used in this analysis have the same number of Bragg peaks, the weighted average results are not so reliable as they might be.

B. Al(110)

Of the six I-V spectra (4,11) shown in Fig. 2 which were analyzed, two did not yield a solution within the prescribed range of parameters searched. Hence, these experimental data are excluded. A summary of the results of all beams is shown in Table II. The results vary from t = -12% to t = 0%, and V_o = 10 eV to V_o = 4 eV. Unweighted and weighted average relaxations of the surface layer based on the four usable spectra are -5% and -4%, respectively. The contraction of the top layer of Al(110), obtained by the convolution-transform method, is somewhat less than that obtained by dynamical calculations. The latter suggest a -10% (3), a -10 to -15% (5), and a -10% (4) relaxation. Since the quoted accuracy of the dynamical calculations is ±5%, the results using the convolution-transform method (which, of course, have an inherent uncertainty themselves) are in rough agreement with the earlier dynamical calculations.

C. Ag(110)

The unweighted and weighted results of the four experimental I-V spectra (7,8) shown in Fig. 3 (excluding the (01) beam) give a -1% and a -7.3% relaxation, respectively. Results from the individual beams are summarized in Table III. The energy range for most of these spectra is rather short, especially for the (00) and the (11) beams which contain only one Bragg peak. Hence, results using these beams are relatively less reliable.

A summary of the average results for these three surfaces as well as a comparison with results from dynamical calculations are shown in Table IV.

4. Conclusions

The convolution-transform method seems to be able to determine the degree of relaxation of clean metal surfaces. The results of the convolution-transform method are consistent with the results of dynamical calculations indicating that a relaxation of -5%, -4%, and -6% (i.e., contraction) occurs on the Ni(110), Al(110), and Ag(110) surfaces, respectively. By comparing the results between the convolution-transform method and the dynamical calculations in this present work as well as our earlier work, we estimate the accuracy of the results of the convolution-transform method to be approximately ±5%, an accuracy similar to that of dynamical calculations.

Acknowledgment

This work was supported by the Army Research Office (Durham) under Grant Number DAHC04-75-0170. Partial support was also obatined from the Donors of the Petroleum Research Fund administrated by the American Chemical Society (Grant Numbers 6809-AC5,7 and 9309-AC5,7).

References

1. S. L. Cunningham, C.-M. Chan and W. H. Weinberg, Phys. Rev. B (in press).

2. C.-M. Chan, S. L. Cunningham, M. A. Van Hove, W. H. Weinberg and S. P. Withrow, Surface Sci. 67, 000 (1977).

3. C. B. Duke, G. E. Laramore, B. W. Holland and A. M. Gibbons, Surface Sci. 27, 523 (1971); G. E. Laramore and C. B. Duke, Phys. Rev. B5, 267 (1972).

4. D. W. Jepsen, P. M. Marcus and F. Jona, Phys. Rev. B6, 3684 (1972).

5. M. R. Martin and G. A. Somorjai, Phys. Rev. B7, 3607 (1973).

6. J. E. Demuth, P. M. Marcus and D. W. Jepsen, Phys. Rev. B11, 1460 (1975).

7. W. Moritz, Ph.D. Thesis, University of Munich (1976); and M. Alff, Ph.D. Thesis, University of Munich (1976).

8. E. Zanazzi, F. Jona, D. W. Jepsen and P. M. Marcus, J. Phys. C: Solid State Phys. 10, 375 (1977).

9. G. L. Griffin, S. L. Cunningham and W. H. Weinberg, Bull. Am. Phys. Soc. 21, 320 (1976).

10. S. L. Cunningham, C.-M. Chan and W. H. Weinberg, J. Vacuum Sci. Technol. 14, 312 (1977).

11. F. Jona, IBM J. Res. Develop. 14, 444 (1970).

12. J. E. Demuth and T.N. Rhodin, Surface Sci. 42, 261 (1974).

Table Captions

Table I: Summary of the results for Ni(110) surface. V_o is the effective inner potential, and t is the % expansion of the surface layer with respect to the bulk for which a minimum occurs in the residual. The parameter Δ is the measure of the quality of the fit between the observed and the calculated Patterson functions. Data are from ref. (12); see Fig. 1.

Table II: Same as Table I for Al(110) surface. Data are from refs. (4) and (11); see Fig. 2.

Table III: Same as Table I for Ag(110) surface. Data are from refs. (7) and (8); see Fig. 3.

Table IV: Summary of both the average and the weighted average results for Ni(110), Al(110) and Ag(110) surfaces as well as comparisons with the results from dynamical calculations.

Table I

Ni(110)

Beam	θ	ϕ	Energy Range (eV)	V_o (eV)	Δ%	t%
(02)	0		98 - 242	10	19	+2
(11)	0		60 - 246	<0		
(10)	0		48 - 236	18	44	-8
(00)	12	90	30 - 226	30	12	-6
(00)	10	90	30 - 226	22	19	-2
(00)	8	90	30 - 226	28	26	-6
(00)	6	90	54 - 230	22	21	-6
(00)	6	0	54 - 220	22	15	-6

Table II

Al(110)

Beam	θ	ϕ	Energy Range (eV)	V_o (eV)	Δ%	t%
(11)	0		62 - 221	10	74	-4
(0-1)	0		48 - 221	<0		
(10)	5	90	21 - 134	8	29	-12
(01)	5	90	32 - 131	<0		
(00)	5	90	42 - 230	4	59	0
(00)	5	0	42 - 192	6	45	-4

Table III

Ag(110)

Beam	θ	ϕ	Energy Range (eV)	V_o (eV)	Δ%	t%
(21)	0		85 - 190	32	21	-16
(11)	0		65 - 168	6	59	0
(01)	0		35 - 140	<0		
(10)	0		45 - 145	8	26	-14
(00)	10	53.5	40 - 110	36	11	-14

Table IV

	Average (t%)	Weighted Average (t%)	Dynamical Calculation (t%)	
Ni(110)	-5	-5	-5	(6)
Al(110)	-5	-4	-10	(3)
			-10 to -15	(5)
			-10	(4)
Ag(110)	-11	-7	-7	(7)
			-7 to -8	(8)

Figure Captions

Figure 1: I-V spectra and drawn windows for the Ni(110) surface. θ is the angle of incidence relative to the surface normal, and ϕ is the azimuthal angle with respect to the x-axis. The longer side of the unit cell in real space was chosen to be along the y direction. Curves are taken from ref. (12).

Figure 2: Same as Fig. 1 for Al(110) surface. Curves are taken from refs. (4) and (11).

Figure 3: Same as Fig. 1 for Ag(110) surface. Curves are taken from refs. (7) and (8). The azimuthal angle is defined according to the convention adopted in ref. (8).

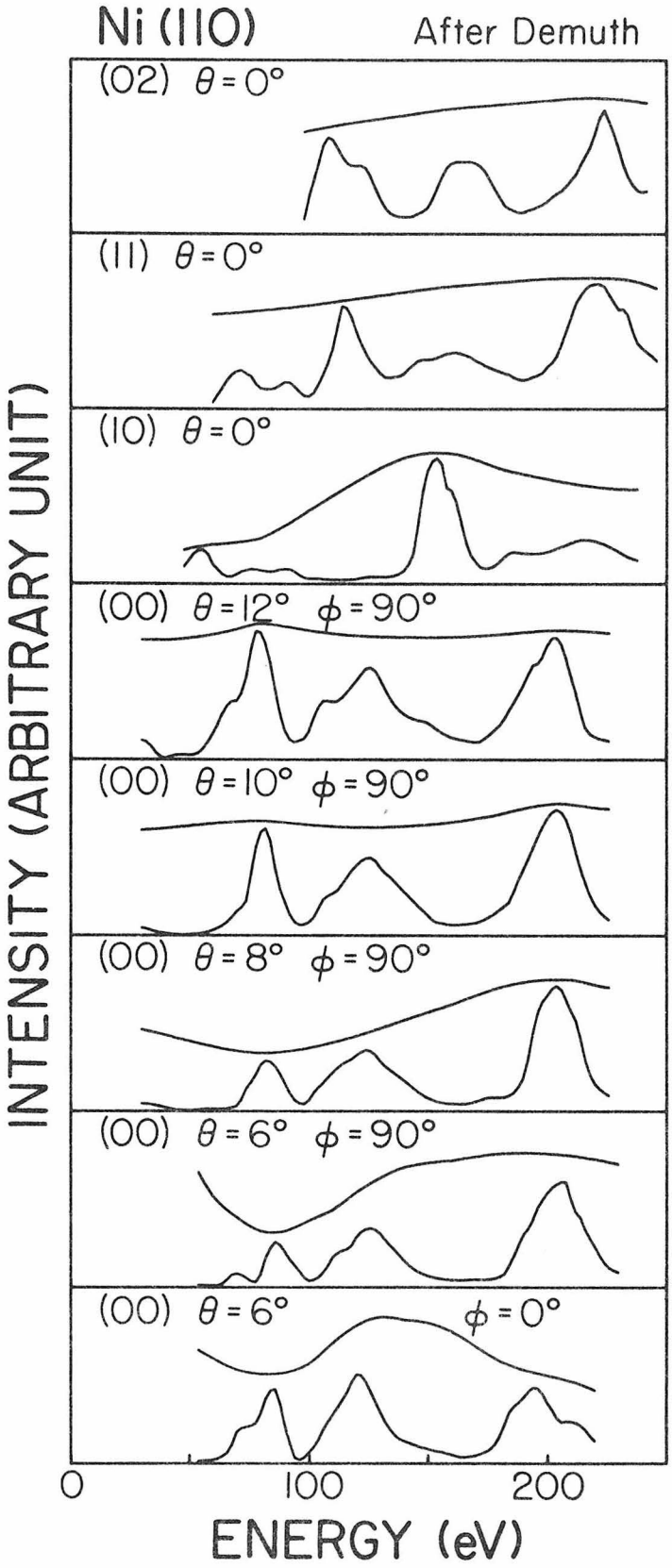
Ni (110)
After Demuth
(02) θ = 0°
(11) θ = 0°
(10) θ = 0°
(00) θ = 12° φ = 90°
(00) θ = 10° φ = 90°
(00) θ = 8° φ = 90°
(00) θ = 6° φ = 90°
(00) θ = 6° φ = 0°
INTENSITY (ARBITRARY UNIT)
0
100
200
ENERGY (eV)

Fig. 1

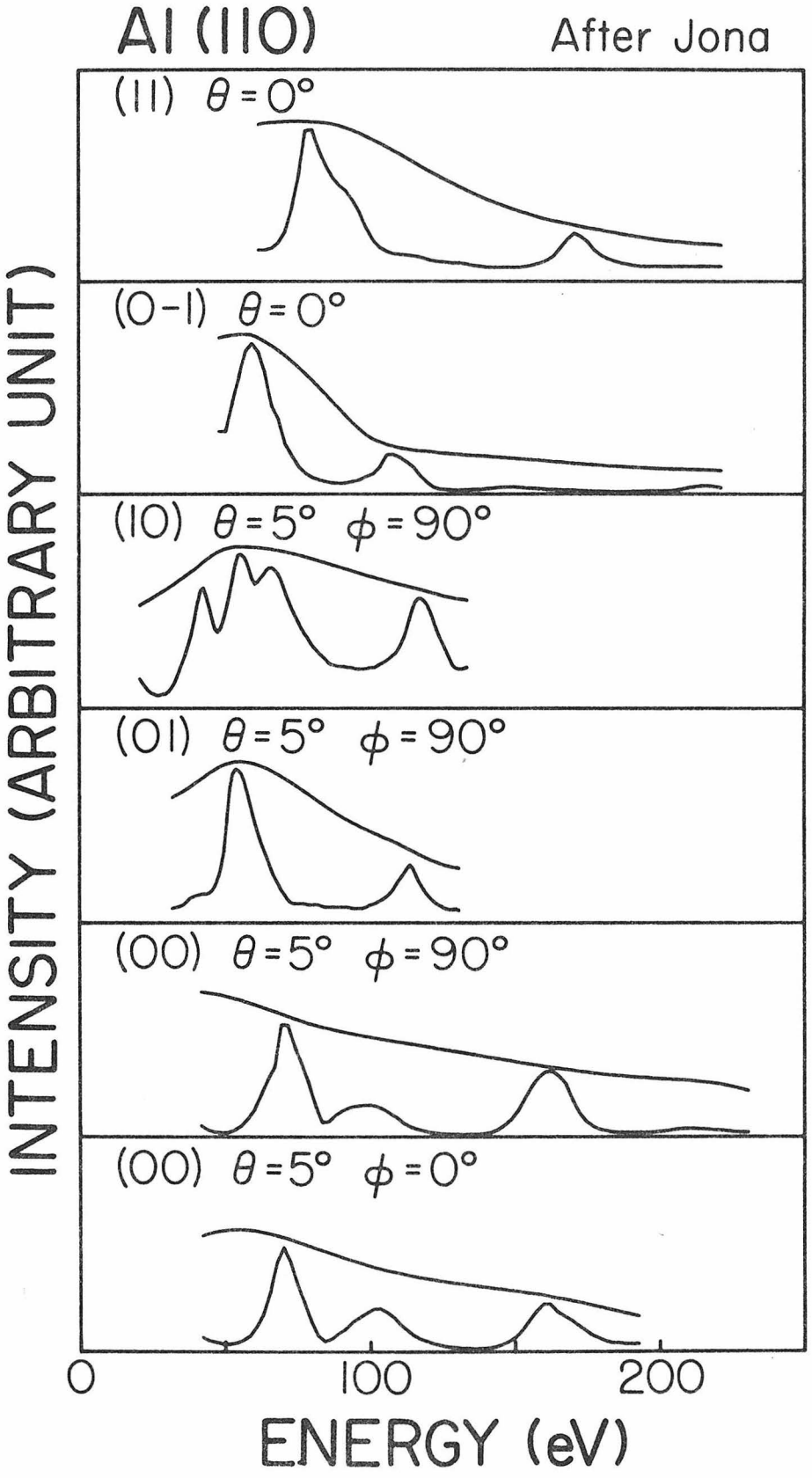
Al (110)
After Jona
(11) θ=0°
(0-1) θ=0°
(10) θ=5° φ=90°
(01) θ=5° φ=90°
(00) θ=5° φ=90°
(00) θ=5° φ=0°
INTENSITY (ARBITRARY UNIT)
0
100
200
ENERGY (eV)

Fig.2

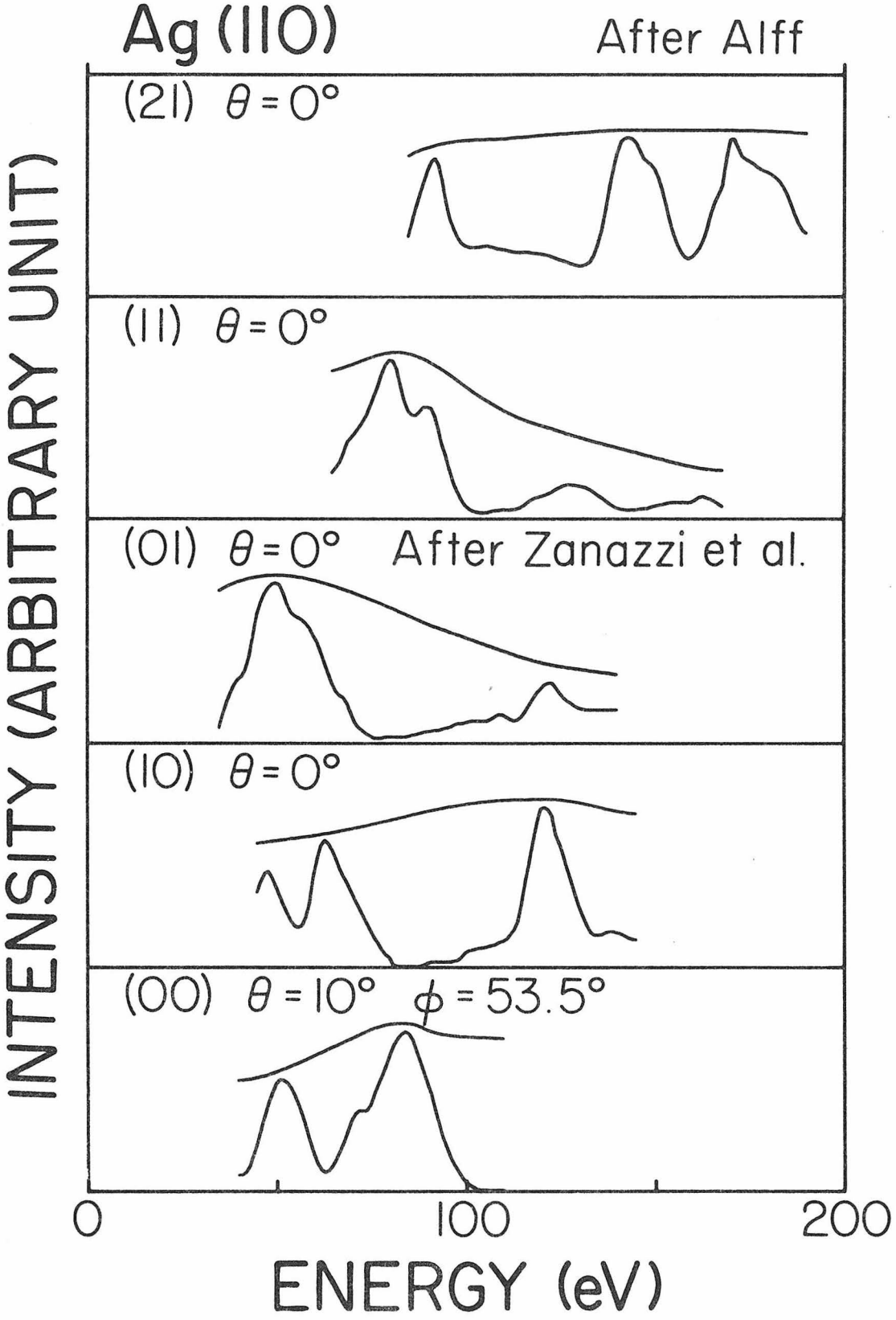
Ag (110)
After Alff
(21) θ = 0°
(11) θ = 0°
(01) θ = 0°
After Zanazzi et al.
(10) θ = 0°
(00) θ = 10° φ = 53.5°
INTENSITY (ARBITRARY UNIT)
0
100
200
ENERGY (eV)

Fig.3

Chapter 5

THE GEOMETRICAL AND VIBRATIONAL PROPERTIES OF THE Rh(111) SURFACE

by

Chi-Ming Chan, Patricia A. Thiel, John T. Yates, Jr.
and W. Henry Weinberg

Division of Chemistry and Chemical Engineering
California Institute of Technology
Pasadena, California 91125

Surface Science 76, 296-310 (1978)

Abstract

Low-energy electron diffraction (LEED) data have been used to characterize the clean Rh(111) surface. The surface geometry, the degree of surface relaxation, and the Debye temperature have been determined. In the Debye temperature measurement, specular LEED beam intensities were monitored as a function of temperature over a range of electron energies from approximately 30 eV to 1000 eV. It was found that the bulk Debye temperature is 380 ± 23 K, and the normal component of the Debye temperature at the lowest electron energy used is 197 ± 12 K. The Rh(111) surface relaxation has been determined both by a convolution-transform analysis and by dynamical calculations. Within experimental error, neither expansion nor contraction of the topmost layer has been detected. The results of the convolution-transform analysis of specular beams at two angles of incidence and of a nonspecular beam at normal incidence suggest an expansion of the topmost layer of 3 ± 5% of the bulk layer spacing. In agreement with this, comparisons between the results of the dynamical calculation and experimental data for five nonspecular beams at normal incidence suggest that the surface layer relaxes by 0 ± 5%. In addition, the dynamical calculations indicate that the topmost layer maintains an fcc structure.

1. Introduction

Because of their importance as industrial catalysts, the Group VIII transition metals have been the object of extensive studies. Rhodium, one of the members of this group, is an important catalyst for a number of important types of catalytic reactions. In this paper, we report the results of a study of the surface vibrational and surface structural properties of the close-packed Rh(111) plane.

Castner et al. (1) have studied small molecules chemisorbed on the Rh(111) and (100) surfaces by low-energy electron diffraction (LEED) and thermal desorption mass spectrometry. Mitchell et al. (2) have found from LEED data that the topmost layers of Rh(111) and (110) surfaces are relaxed outward by 0 ± 5% and by 3 ± 5%, respectively. There are no reports in the literature concerning measurements of the Debye temperature, θ_D, on the clean Rh(111) surface from LEED data.

We have studied the Debye temperatures for Rh(111) as a function of incident electron energies ranging approximately from 30 eV to 1000 eV. We also report new measurements of LEED intensity-voltage (I-V) beam profiles. These have been used to determine the surface relaxation of clean Rh(111) by both the convolution-transform method and dynamical calculations.

In Section 2, the experimental procedures and apparatus are described. In Section 3, a brief formalism and a discussion of the results of the Debye temperature measurement are presented. In Sections 4 and 5, the results of the convolution-transform analysis and the dynamical calculations are presented. The conclusions of our work are summarized in Section 6.

2. Experimental Details

A. Apparatus

The experiments were done in an ion-pumped stainless steel ultra high vacuum system equipped with Ti sublimation pumping. The base pressure following bakeout was $< 1 \times 10^{-10}$ torr. The system was equipped with a four grid LEED display apparatus containing a movable Faraday cup for beam intensity measurements. The Faraday cup aperture subtended an angle of 4.6×10^{-3} steradians. The system also contained a quadrupole mass spectrometer, a cylindrical mirror single pass Auger spectrometer, and an ion gun for Ar^+ bombardment of the crystal for cleaning. Two pairs of Helmholtz coils were used to compensate the magnetic field of the earth inside the chamber during LEED measurements.

B. Crystal Preparation

The Rh(111) single crystal disk was cut by means of an abrasive loaded stainless steel string saw from a Marz grade Rh single crystal rod (Materials Research Corporation, nominally 99.99% pure). The disk was ground and polished on both faces to within 0.3^{o} of the Rh(111) plane using one micron diamond paste as the final polishing compound. At this point Laue back-reflection X-ray photographs indicated the presence of some surface disorder; this was removed by electropolishing the crystal surface in 50% aqueous HCl solution for 30 minutes at a d.c. current density of approximately $2 \times 10^{-2} A/cm^2$. The average diameter of the crystal was 0.6 cm and its final thickness was 0.05 cm. The polished crystal was welded to two parallel 0.025 cm diameter Ta heating wires which were clamped in a Cu holder which was part of a rotary manipulator assembly. A thermocouple consisting of 5% Re/95% W and 26% Re/74% W wires (.0075 cm dia.) was welded

to short sections of (0.25 cm dia.) thermocouple leads which were welded together on the crystal face to make the junction. The Rh(111) crystal could be cooled to 85 K using liquid N_2 refrigeration, and it could be electrically heated to above 1400 K. The thermocouple calibration of Sandstrom and Withrow (3) was used below 273 K.

Cleaning of the Rh(111) crystal was accomplished by a combination of Ar^+ bombardment (~ 10μA, 1 kv, 60 min, 5 x 10^{-5}torr Ar, gettered with freshly deposited Ti) and high temperature O_2 treatment at 5 x 10^{-7}torr, followed by flashing in vacuum to 1250 K. The Auger spectrum shown in Fig. 1 is typical of our Rh(111) surface following this cleaning procedure. The seven Rh Auger features indicated in the figure are the same as those reported by Grant and Haas (4). Small features at ~ 160 eV(S) and at ~ 130 eV(P?) may be removed to the levels shown in Fig. 1 by heating in O_2 or by ion bombardment. As reported by others (1,2,5), a major surface contaminant is boron (185 eV) which diffuses from the bulk to the surface upon heating. To alleviate this problem, the bulk was partially depleted of B by heating and ion bombardment; a final condition was reached where diffusion to the surface was not detectable by Auger spectroscopy on heating the Rh(111) to 1250 K. Low levels of B and C contamination were easily removed by heating in O_2. The impurities in our Rh(111) crystal and the cleaning procedures used were similar to those of other workers (1,2,5).

It should be noted that O_2 treatment leaves behind a small broad O-Auger feature near 515 eV. The intensity of this feature could be reduced to 0.3-0.5% of the peak-to-peak intensity of the strong Rh Auger feature at 303 eV by heating the O_2 treated crystal in vacuum to 1250 K. Other small features at 406 eV, 441 eV and 458 eV were essentially invariant with O_2 or

Ar^+ cleaning procedures following annealing and may be characteristic of clean Rh surfaces. Similar low level Auger features have been seen on Ru(001) surfaces (6,7). Examination of the Auger spectrum up to 2000 eV at highest sensitivity failed to reveal additional features.

C. Measurement of Debye-Waller Factor

The crystal was tilted such that the specular beam was reflected at angles as high as 24^o from the normal. To measure this angle the procedure of Cunningham and Weinberg (8) was employed. Essentially, this procedure involves photographing the diffraction pattern at an unknown angle of incidence. Measurement of the angle between the line joining the (00) spot and the center of the LEED screen and the lines joining other diffraction spots permits an accurate calculation of the angle of incidence with respect to the surface normal and the azimuthal angle. Since a number of diffracted beams are employed, the crystal angle and the azimuthal angle may be determined rather accurately. The estimated errors in the determination of the angle of incidence and the azimuthal angle using on the order of ten beams for each of the three orientations are approximately 0.3^o and 1^o, respectively.

Measurements of the dependence of the specular beam intensity on crystal temperature were made using the Faraday cup to monitor beam intensity as the crystal cooled slowly from an initial temperature of ~1100 K to ~ 300 K, as monitored with the thermocouple. The specular beam intensity was continuously plotted against thermocouple potential during cooling.

D. Measurement of LEED Intensities as a Function of Electron Energy

In Fig. 2 is shown a schematic diagram of the first order diffraction pattern from Rh(111) with the scheme for indexing beams and for definition of the azimuthal angle indicated.

Intensity-voltage curves for five non-equivalent diffracted beams were measured at 2 eV intervals, and these are shown in Figs. 7-11. The measured intensity has been corrected for variation in the primary electron beam current (collected by the crystal) as the voltage was changed. In Fig. 3 is shown the comparison of the I-V curves obtained for two equivalent first order beams. The satisfactory agreement obtained is indicative of small systematic errors which may exist due to inaccuracy of crystal positioning, residual magnetic fields, etc.

3. Debye-Waller Factor Measurement

The Debye temperature is related to the root-mean-square displacements of atoms from their equilibrium positions in the lattice and may be measured by studying the variation of the LEED beam intensity as a function of temperature. In the kinematic approximation, the intensity of the back scattered electrons, I, may be written as

$$I = I_0 e^{-2M} , \tag{1}$$

where 2M is the Debye-Waller factor. For the specular beam, the Debye-Waller factor is given as

$$2M = |\Delta k_\perp|^2 \langle u_\perp^2 \rangle , \tag{2}$$

where $\Delta k_\perp$ is the normal momentum transfer of the electron and $\langle u_\perp \rangle$ is the root-mean-square displacement of the surface atom perpendicular to the crystal surface. In the case of the specular beam, the perpendicular momentum transfer of the electron is determined by the energy of the electron and the angle of incidence of the electron beam with respect to the surface normal. It is

given by

$$|\Delta k_{\perp}|^2 = \frac{8m_e}{\hbar^2} (E \cos^2\theta + V_o), \tag{3}$$

where m_e is the mass of the electron, $2\pi\hbar$ is Planck's constant, E is the energy of the electron, θ is the angle of incidence with respect to the surface normal, and V_o is the inner potential. In the high temperature limit, the perpendicular mean-square displacement of an atom in a solid is given by

$$\langle u_{\perp}^2 \rangle = \frac{3\hbar^2 T}{m_a k (\theta_{D\perp}^{EFF})^2} , \tag{4}$$

where m_a is the mass of the atom, k is the Boltzmann constant, and $\theta_{D\perp}^{EFF}$ is the perpendicular component of the effective Debye temperature.

Combining Eqs. (2), (3) and (4) gives

$$2M = \frac{24m_e(E \cos^2\theta + V_o)T}{m_a k (\theta_{D\perp}^{EFF})^2} . \tag{5}$$

Thus, from the slope of a plot of $\ln(I/I_o)$ versus temperature, $\theta_{D\perp}^{EFF}$ can be evaluated. To obtain the correct effective Debye temperature from Eq. (1), however, the background intensity of scattered electrons must be subtracted from the experimentally measured intensity. This background intensity results from thermal diffuse scattering. Hence, Eq. (1) should be written as

$$I - I_{bk} = I_o e^{-2M} , \tag{6}$$

where I_{bk} is the background intensity. An accurate background intensity is very difficult to determine experimentally, especially at high electron beam energies (E>500 eV) where the diffraction spots are closely spaced. Therefore, rather than using an experimentally measured background intensity, we have treated the background intensity as a variable in a least squares fitting procedure for the plot of $\ln(I-I_{bk})$ versus T. If I_{bk} is determined correctly, the plot of $\ln(I-I_{bk})$ versus T should be a straight line; hence, we allow the value of

I_{bk} to vary within physically reasonable limits until the best straight line for $\ln(I-I_{bk})$ as a function of T is obtained. In the least squares fitting procedure, the values of $\ln(I-I_{bk})$ are weighted according to the experimentally measured intensities, causing the values of $\ln(I-I_{bk})$ at lower temperature to be weighted more heavily than the values of $\ln(I-I_{bk})$ at high temperatures. This is justified by the fact that the intensities at low temperatures can be measured more accurately and are less sensitive to the variation of the background intensity. The value of $\theta_{D\perp}^{EFF}$ is determined from the slope of the best straight line in the plot of $\ln(I-I_{bk})$ versus T with appropriate weighting factors in the least squares fitting procedure. We have shown that use of different weighting schemes, such as weighting the values of $\ln(I-I_{bk})$ according to the squares of the experimentally measured intensities, does not change the result by more than a few percent.

Figure 4 shows several plots of our experimental curves of $\ln(I-I_{bk})$ versus T, using the best numerically determined I_{bk}. In the calculation of the Debye temperature, a value of 10 eV was used for the inner potential, V_o. This value of V_o was used also in the dynamical calculations discussed in Section 5. Figure 5 shows values of $\theta_{D\perp}^{EFF}$ as a function of $\Delta k_\perp$ for the (00) beam at three different angles of incidence: $\theta = 10.5^o$, $\theta = 14.9^o$, and $\theta = 23.9^o$. The solid line in Figure 5 is a second degree least squares polynomial fit to all the data points. The value of $\theta_{D\perp}^{EFF}$ at the lowest value of $\Delta k_\perp$ is taken as the surface $\theta_{D\perp}$, although it is realized that even at this low value of $\Delta k_\perp$ we are sampling several atomic layers of the Rh crystal.

From these data, this value is 197 ± 12 K. The high-energy asymptote of the curve of the polynomial fit to the data points gives a value for the bulk θ_D of 380 ± 23 K. The errors were estimated from the standard deviation of the measured data. The values for the bulk θ_D given in Ref. (9) are 315 K, calculated from the melting point formula of Lindemann, and 370 K, deduced from the electrical conductivity. A value of 325 K has also been determined from heat capacity data (11). Another value for the bulk θ_D given in Ref. (10) is 480 K. Our bulk θ_D is in good agreement with the value of θ_D deduced from the electrical conductivity.

It would also be appropriate to use LEED to determine $\theta_{D||}^{EFF}$ using non-specular LEED beams. Unfortunately, as pointed out by Farrell and Somorjai (12), one must work at high angles of incidence to obtain sufficient accuracy in $\theta_{D||}^{EFF}$. The present geometry of our apparatus precluded this measurement.

4. Convolution-Transform Method

In earlier work, the convolution-transform method of LEED analysis has been described and used to determine the spacing of the outermost layer of several clean metal surfaces (13-17). In the convolution-transform method, a least squares fit is made between the Patterson function of the data (the observed Patterson function) and the "calculated" Patterson function. The observed Patterson function $P_o(z)$ is the Fourier transform of the intensity from momentum space into real space. The "calculated" Patterson function $P_c(z)$ is constructed by convoluting the Fourier transform of a "window" function with a set of delta functions which represent the layer spacings of the crystal. The "window" function is chosen somewhat arbitrarily to define the energy range of the I-V spectrum and is taken to be a smooth

envelope of the data. The best fit between the observed and the "calculated" Patterson functions is found by searching for the minimum in a parameter termed the residual as a function of both V_o, the effective inner potential, and t, the percentage relaxation of the topmost layer. The inner potential is different from the one used in dynamical calculations. As discussed in detail elsewhere (15-17), it should be considered as an adjustable parameter in the convolution-transform method. The square of the residual is given by

$$R^2 = \int_0^\infty \left[P_o(z) - P_c(z)\right]^2 dz \ . \tag{13}$$

This minimum is characterized by a parameter Δ, defined as

$$\Delta = 100\ (R_{ave} - R_{min})/R_{ave} \ , \tag{14}$$

where R_{min} is the smallest value of the residual and R_{ave} is the average value of the residual. The position of the minimum gives the structure, and the value of Δ defines the goodness of fit.

Three Rh(111) I-V spectra with their window functions are shown in Fig. 6. The results of our calculations are summarized in Table 1. The results vary from t = +1% to t = +7% and V_o = 3 eV to V_o = 15 eV. The weighted average of all beams, obtained by multiplying the relaxation t by the corresponding value of Δ and normalizing by the sum of Δ's, is 3 ± 5%.

5. Multiple-Scattering Analysis

The computational method of analysis is very similar to that described previously (15). Renormalized forward scattering (18) was used for rapid and good convergence. The LEED I-V spectra for Rh(111) were calculated at a normal angle of incidence for five non-specular beams, namely, the (01),

(10), (11), (02) and (20) beams.

The potential used for rhodium is a band structure potential which we obtained by scaling the relativistic Hartree-Fock-Slater potential of Rh with respect to Ir. This is possible since a band structure potential is available for Ir (19) as well as atomic potentials for Ir and Rh (20). Eight phase shifts were used, properly modified for atomic vibrations. An assumed value of 15 eV was used for the real part of the inner potential (the muffin-tin zero). For the comparison between the theoretical and the experimental I-V spectra, the inner potential was allowed to change by a rigid shift of the energy scale. An energy-independent imaginary part of the inner potential of 5 eV was used to represent all inelastic processes. The crystal temperature was 350 K, the nominal bulk Debye temperature used in the calculation was 300 K, and an enhancement factor of 1.43 was chosen for the surface mean-square vibrational amplitudes. Twenty-seven beams were used in the calculations.

In the calculations, the outermost layer of the Rh(111) surface was allowed to relax from -15% (contraction) to +10% (expansion) in steps of 5%. It was found from the comparisons between the theoretical and experimental I-V spectra for the five chosen beams, the unrelaxed surface agrees best with an inner potential of 10 eV. Figures 7-11 show the comparison between the theoretical I-V spectra modified with an inner potential of 10 eV and the experimental I-V spectra.

The good agreement between experiment and theory indicates that a lateral shift of the top atomic layer to an hcp configuration is highly unlikely; hence, calculations for such a shift were not undertaken. Based on the results of these comparisons between theory and experiment, we conclude that the topmost layer of Rh(111) exhibits a relaxation of $0 \pm 5\%$.

6. Conclusions

Our major conclusions may be summarized as follows:

(1) The normal component of the Rh(111) surface Debye temperature is 197 ± 12 K, and the bulk Debye temperature of Rh is 380 ± 23 K. Our data indicate that $\theta_{D\perp}^{EFF}$ is a rather smooth function of $\Delta k_{\perp}$. For an accurate determination of $\theta_{D\parallel}^{EFF}$, the measurements of I-V peak intensities as a function of temperature must be done at a very large angle of incidence.

(2) The results of a convolution-transform analysis indicate that the topmost layer of Rh(111) surface is expanded outward by 3 ± 5%.

(3) The results of dynamical calculations indicate that the topmost layer of the Rh(111) surface is relaxed by 0 ± 5%.

(4) The dynamical calculations indicate that the first layer of the Rh(111) surface does not shift to an hcp configuration but maintains an fcc structure.

7. Acknowledgments

We gratefully acknowledge the help of Dr S. L. Cunningham and M. A. Van Hove for setting up the programs for the dynamical calculations. One of us (J.T.Y.) acknowledges partial support of equipment facilities from the Division of Physical Research, Department of Energy.

References

1. D. G. Castner, B. A. Sexton and G. A. Somorjai, Surface Sci. (submitted).

2. K. A. R. Mitchell, F. R. Shepherd, P. R. Watson and D. C. Frost, Surface Sci. 64, 737 (1977);
D. C. Frost, K. A. R. Mitchell, F. R. Shepherd and P. R. Watson, Proc. 7th Intern. Vac. Congr. and 3rd Intern. Conf. Solid Surfaces, Vienna, 1977, p. A-2725.

3. D. R. Sandstrom and S. P. Withrow, J. Vac. Sci. Technol. 14, 748 (1977).

4. J. T. Grant and T. W. Haas, Surface Sci. 21, 76 (1970).

5. R. A. Marbrow and R. M. Lambert, Surface Sci. 67, 489 (1977).

6. T. E. Madey, H. A. Engelhardt and D. Menzel, Surface Sci. 48, 304 (1975).

7. D. W. Goodman, T. E. Madey, M. Ono and J. T. Yates, Jr., J. Catal. 50, 279 (1977).

8. S. L. Cunningham and W. H. Weinberg, Rev. Sci. Instrum. (in press).

9. N. F. Mott and H. Jones, The Theory of the Properties of Metals and Alloys, Oxford Press, London, p. 14, 1936.

10. G. V. Samsonov, Handbook of Physicochemical Properties of the Elements, Plenum Press, N.Y., p. 284, 1968.

11. G. T. Furukawa, M. L. Reilly and J. S. Gallagher, J. Phys. Chem. Ref. Data 3, 175 (1974).

12. G. A. Somorjai and H. H. Farrell, Advan. Chem. Phys. 20, 215 (1971).

13. S. L. Cunningham, C.-M. Chan and W. H. Weinberg, J. Vac. Sci. Technol. 14, 312 (1977).

14. C.-M. Chan, S. L. Cunningham and W. H. Weinberg, Bull. Am. Phys. Soc. 22, 357 (1977).

15. C.-M. Chan, S. L. Cunningham, M. A. Van Hove, W. H. Weinberg and S. P. Withrow, Surface Sci., 66 394 (1977).

16. C.-M. Chan, S. L. Cunningham, M. A. Van Hove and W. H. Weinberg, Surface Sci. 67, 1 (1977).

17. S. L. Cunningham, C.-M. Chan and W. H. Weinberg, Phys. Rev. B (in press).

18. J. B. Pendry, Low-Energy Electron Diffraction, Academic Press, London, 1974.

19. G. O. Arbman and S. Hörnfelt, J. Phys. F2, 1033 (1972).

20. C. C. Lu, T. A. Carlson, F. B. Malik, T. C. Tucker and C. W. Nestor, Jr., Atomic Data 3, 50 (1971).

Table 1. Summary of Convolution-Transform Results

Beam	θ(deg)	φ(deg)	Energy Range (eV)	V_o(eV)	Δ(%)	t(%)
(00)	10.4	-76.5	46-220	3	30	+1
(00)	23.9	-76.5	60-234	9	15	+1
(11)	0		94-254	15	25	+7

V_o = Effective inner potential.

Δ = Measure of quality of fit between observed and calculated Patterson functions.

t = % Expansion of the surface layer with respect to the bulk interlayer spacing of 2.196 Å for which a minimum occurs in the residual.

Figure Captions

Fig. 1: A typical Auger spectrum of the Rh(111) surface following the cleaning procedure described in the text.

Fig. 2: (a) The (111) crystal surface for $\phi = -90^{o}$. a_1 and a_2 are the lattice vectors.

(b) The reciprocal space of Fig. 2(a).

(c) The reciprocal space for a (111) surface for $\phi = 0^{o}$.

Fig. 3: Experimental I-V curves for two beams which should be equivalent at normal incidence.

Fig. 4: Plots of representative experimental curves of $\ln(I-I_{bk})$ versus T, using the best numerically determined I_{bk}. The curves are vertically displaced with respect to each other for ease of presentation.

Fig. 5: Values of $\theta_{D\perp}^{EFF}$ as a function of $\Delta k_{\perp}$ for the (00) beam at three different angles of incidence: $\theta = 10.5^{o}$, $\theta = 14.9^{o}$ and $\theta = 23.9^{o}$. The solid line in the figure is a second degree least squares polynomial fit to all the data points. Ref. A = Ref. 9; Ref. B = Ref. 10; Ref. C = Ref. 11.

Fig. 6: I-V spectra and drawn window for the Rh(111) surface. θ is the angle of incidence relative to the surface normal, and ϕ is the azimuthmal angle with respect to the crystal x-axis.

Fig. 7: Comparison between the theoretical I-V spectra modified with an inner potential of 10 eV and the experimental I-V spectrum the (01) beam. The % parameter refers to expansion (+) or contraction (-) of the Rh interlayer spacing.

Fig. 8: Comparison between the theoretical I-V spectra modified with an inner potential of 10 eV and the experimental I-V spectrum for the (10) beam. The % parameter refers to expansion (+) or contraction (-) of the Rh interlayer spacing.

Fig. 9: Comparison between the theoretical I-V spectra modified with an inner potential of 10 eV and the experimental I-V spectrum for the (11) beam. The % parameter refers to expansion (+) or contraction (-) of the Rh interlayer spacing.

Fig. 10: Comparison between the theoretical I-V spectra modified with an inner potential of 10 eV and the experimental I-V spectrum for the (02) beam. The % parameter refers to expansion (+) or contraction (-) of the Rh interlayer spacing.

Fig. 11: Comparison between the theoretical I-V spectra modified with an inner potential of 10 eV and the experimental I-V spectrum for the (20) beam. The % parameter refers to expansion (+) or contraction (-) of the Rh interlayer spacing.

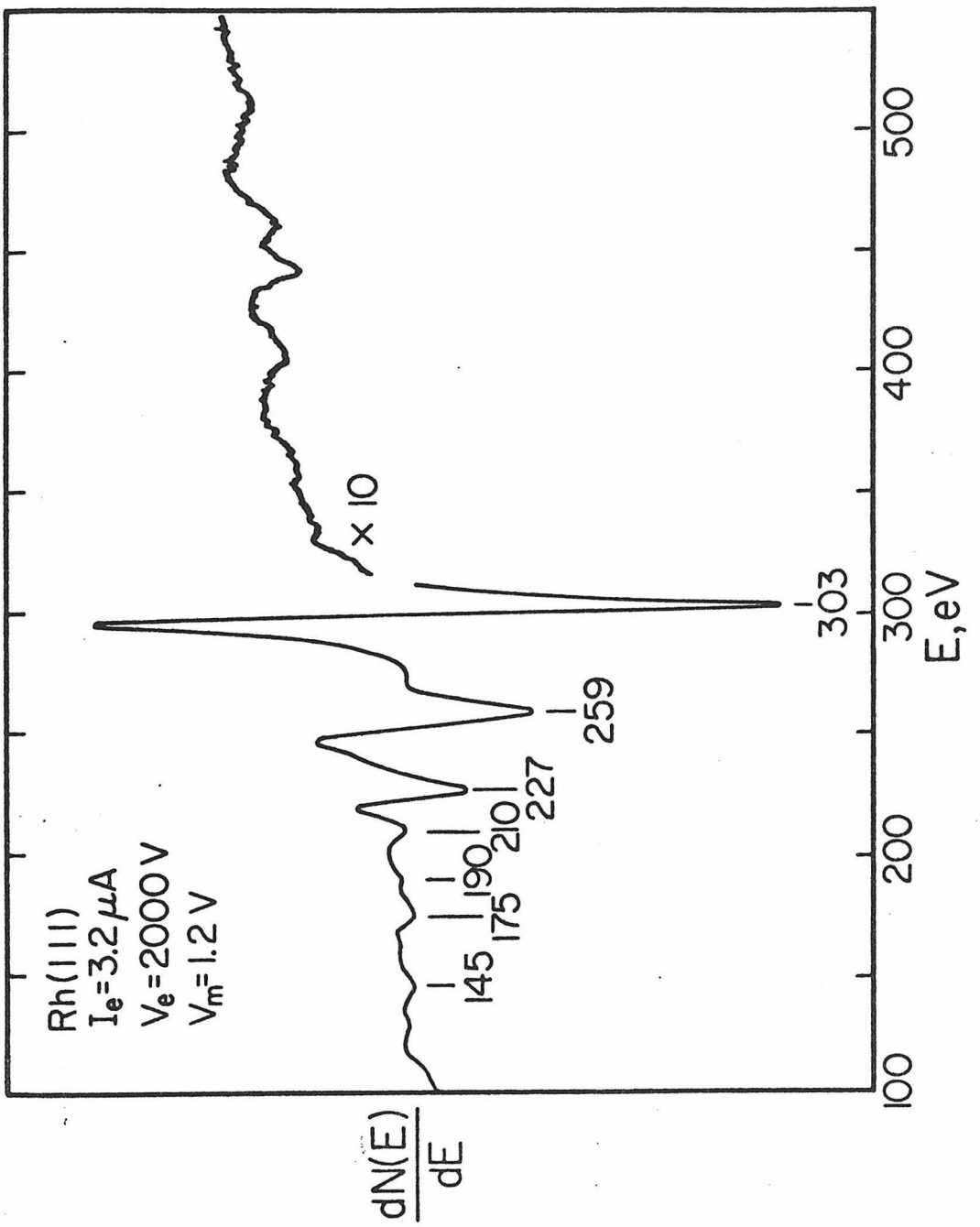
Rh(111)
I_e=3.2 μA
V_e=2000 V
V_m=1.2 V
× 10
145
175
190
210
227
259
303
100
200
300
400
500
E, eV
dN(E)/dE

Fig. 1

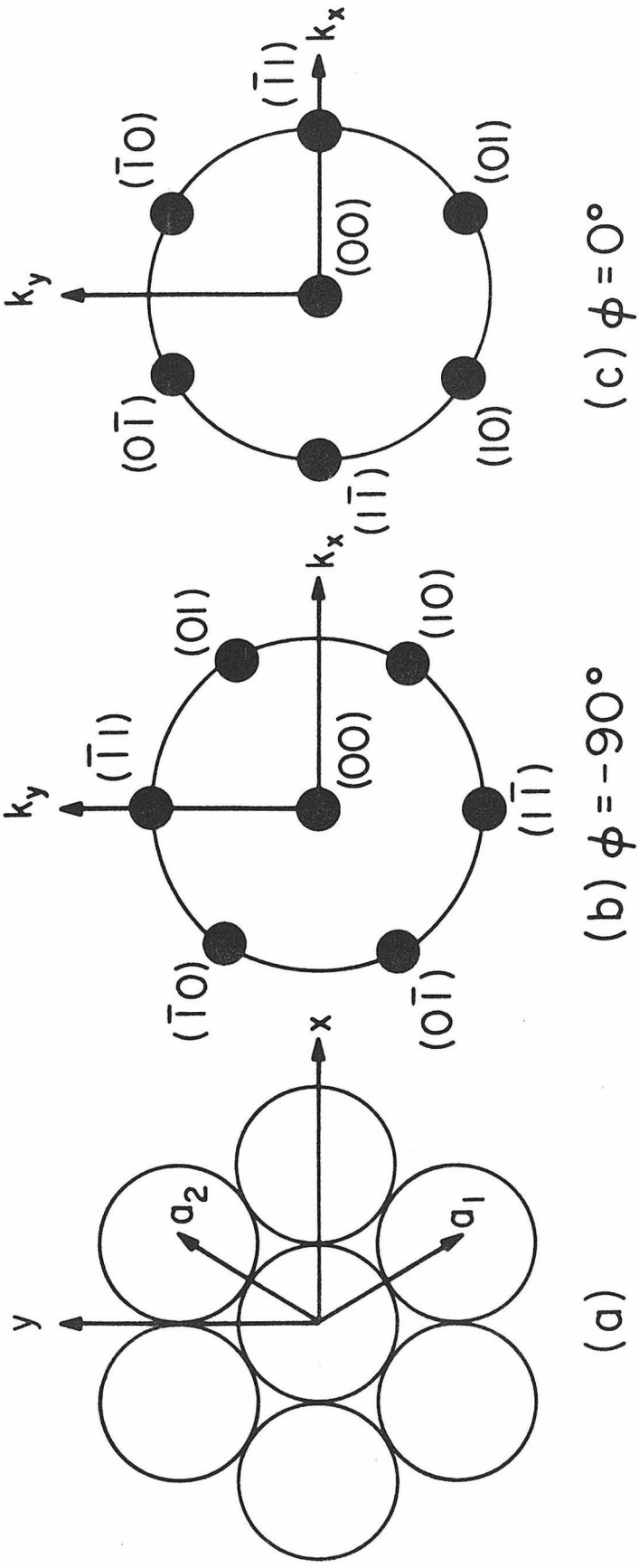
x
y
a_2
a_1
(a)
k_x
k_y
$(\bar{1}0)$
$(0\bar{1})$
(01)
(10)
$(\bar{1}1)$
$(1\bar{1})$
(00)
(b) $\phi = -90°$
k_x
k_y
$(\bar{1}\bar{1})$
$(\bar{1}0)$
$(0\bar{1})$
(01)
(10)
$(1\bar{1})$
(00)
(c) $\phi = 0°$

Fig. 2

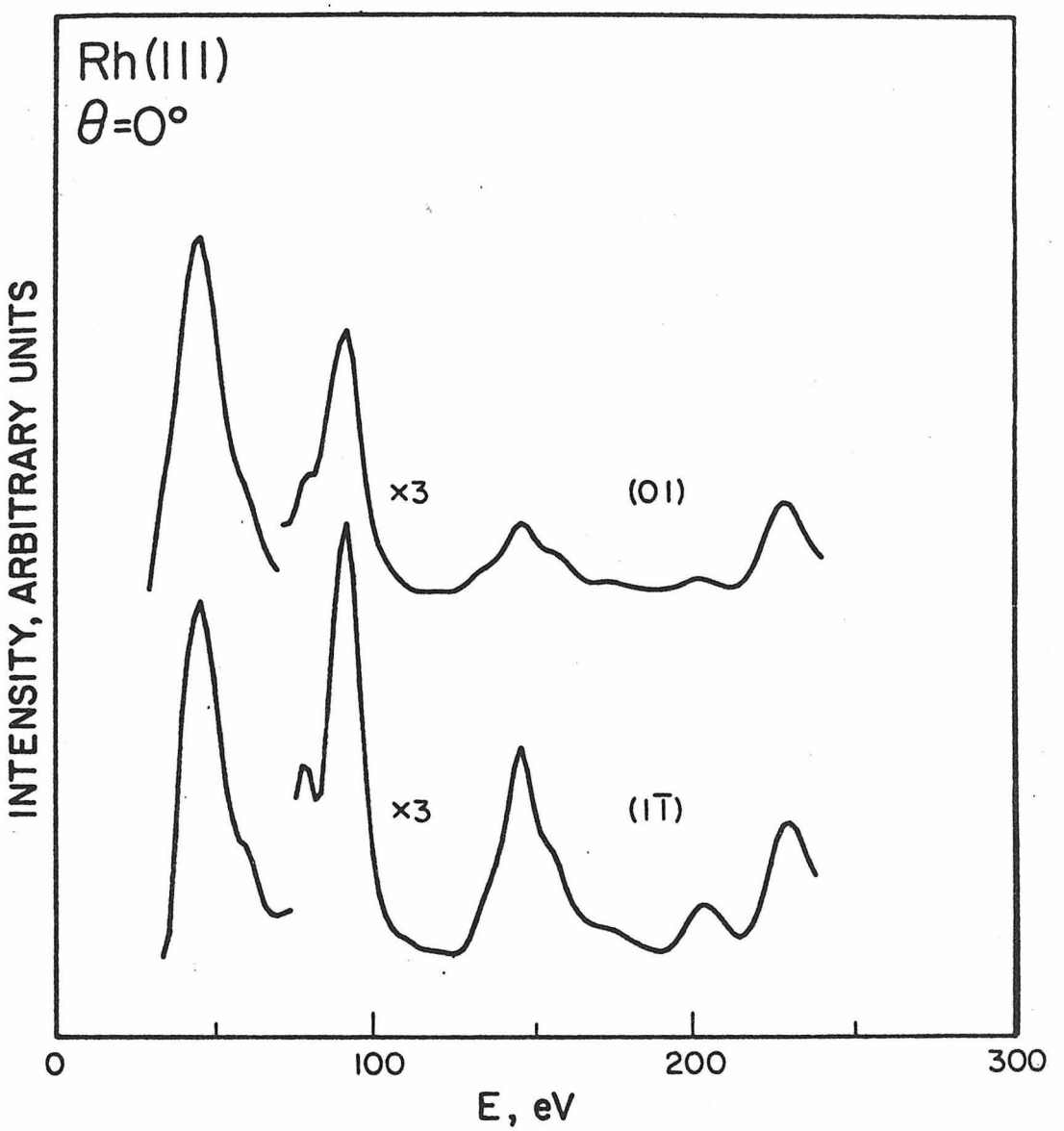
Rh(111)
θ=0°
INTENSITY, ARBITRARY UNITS
×3
(01)
×3
(1$\bar{1}$)
0
100
200
300
E, eV

Fig. 3

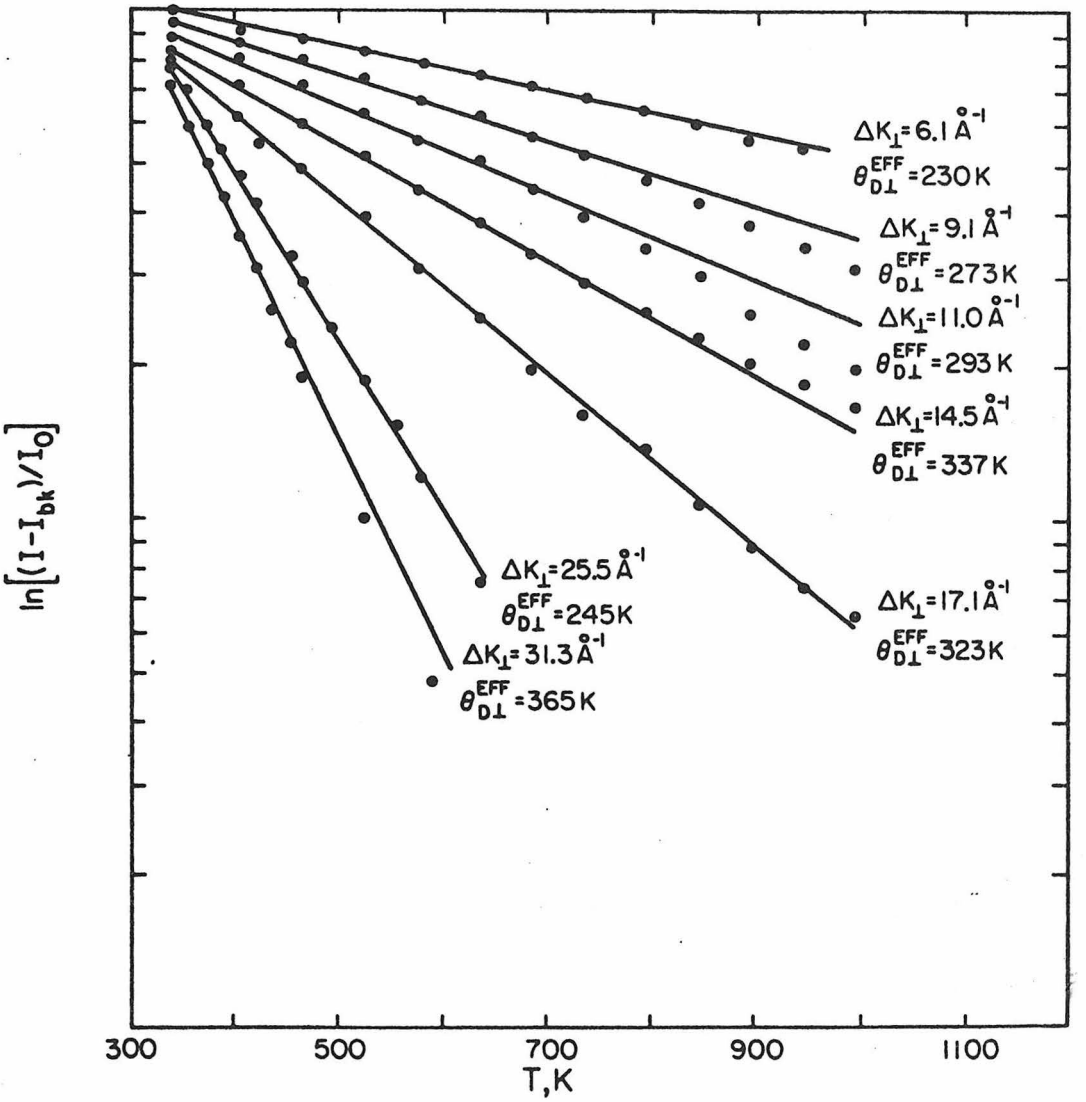
$\ln[(I-I_{bk})/I_0]$
$\Delta K_\perp = 6.1\,\text{Å}^{-1}$
$\theta_{D\perp}^{EFF} = 230\,K$
$\Delta K_\perp = 9.1\,\text{Å}^{-1}$
$\theta_{D\perp}^{EFF} = 273\,K$
$\Delta K_\perp = 11.0\,\text{Å}^{-1}$
$\theta_{D\perp}^{EFF} = 293\,K$
$\Delta K_\perp = 14.5\,\text{Å}^{-1}$
$\theta_{D\perp}^{EFF} = 337\,K$
$\Delta K_\perp = 17.1\,\text{Å}^{-1}$
$\theta_{D\perp}^{EFF} = 323\,K$
$\Delta K_\perp = 25.5\,\text{Å}^{-1}$
$\theta_{D\perp}^{EFF} = 245\,K$
$\Delta K_\perp = 31.3\,\text{Å}^{-1}$
$\theta_{D\perp}^{EFF} = 365\,K$
300
500
700
900
1100
T,K

Fig. 4

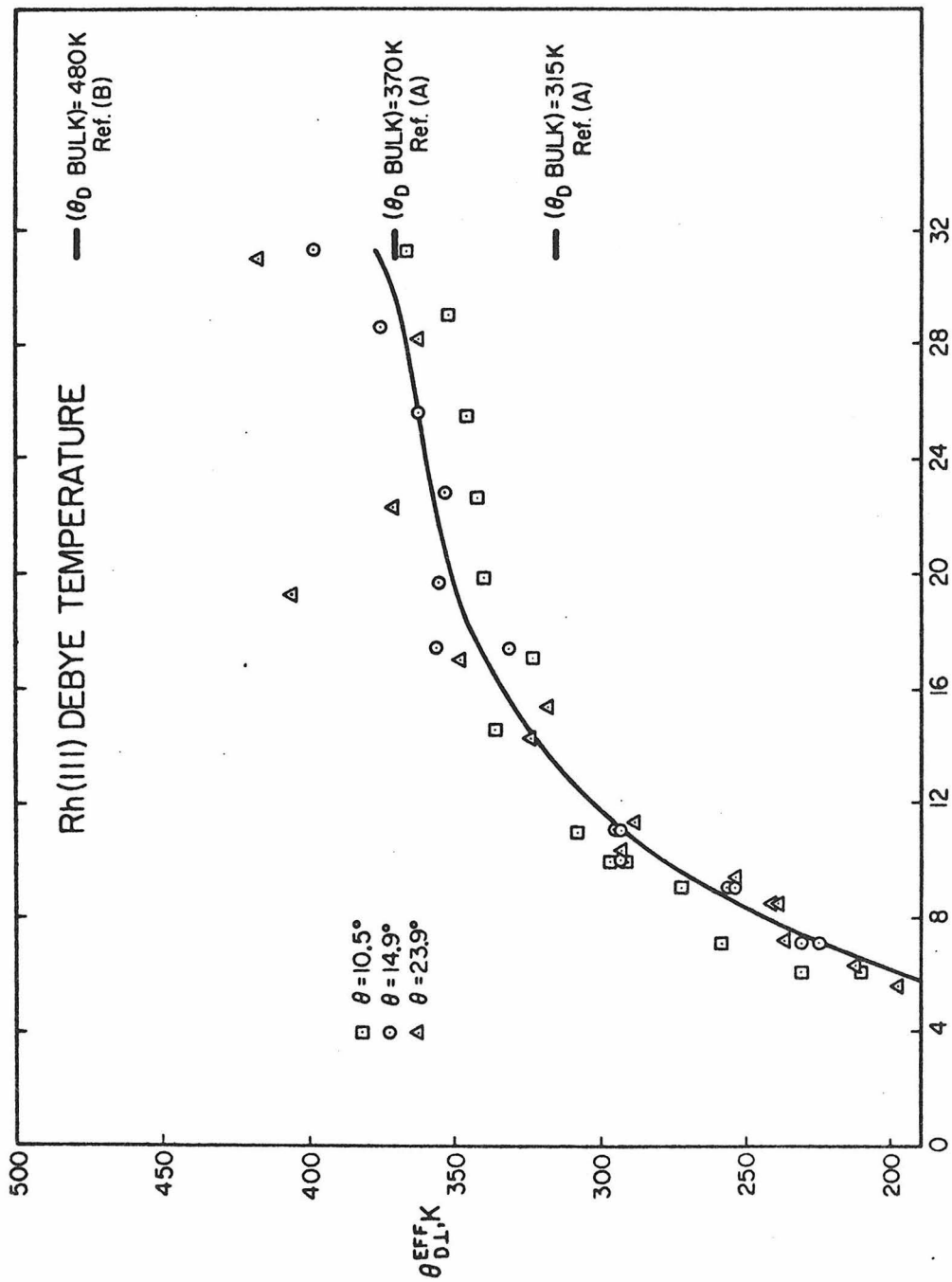
Rh(111) DEBYE TEMPERATURE
(θD BULK)= 480K
Ref. (B)
(θD BULK)=370K
Ref. (A)
(θD BULK)=315K
Ref. (A)
θ =10.5°
θ =14.9°
θ =23.9°
θ⊥EFF,K
ΔK⊥,Å-1
500
450
400
350
300
250
200
0
4
8
12
16
20
24
28
32

Fig. 5

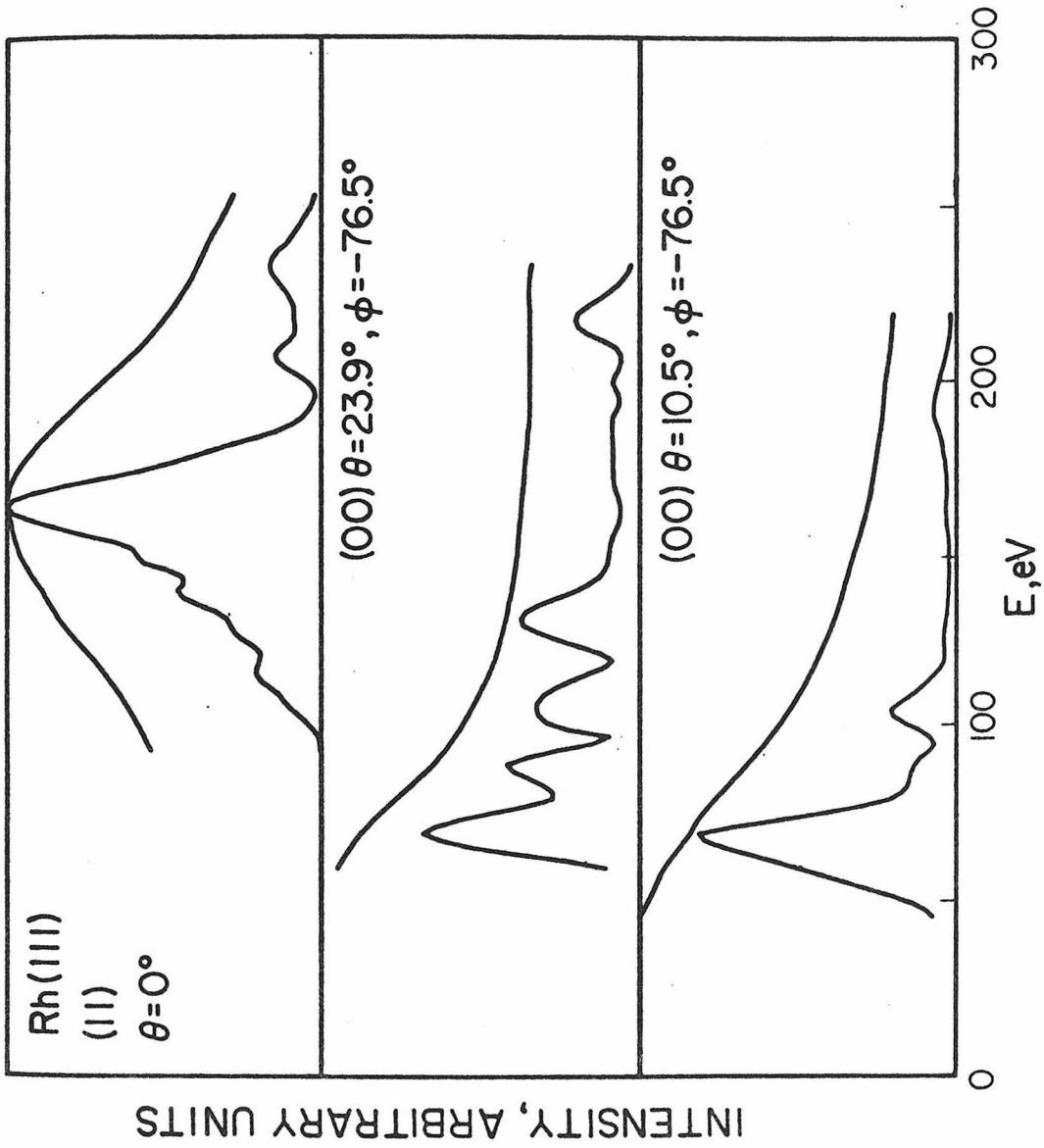
Rh(111)
(11)
θ=0°
(00) θ=23.9°, φ=-76.5°
(00) θ=10.5°, φ=-76.5°
0
100
200
300
E,eV
INTENSITY, ARBITRARY UNITS

Fig. 6

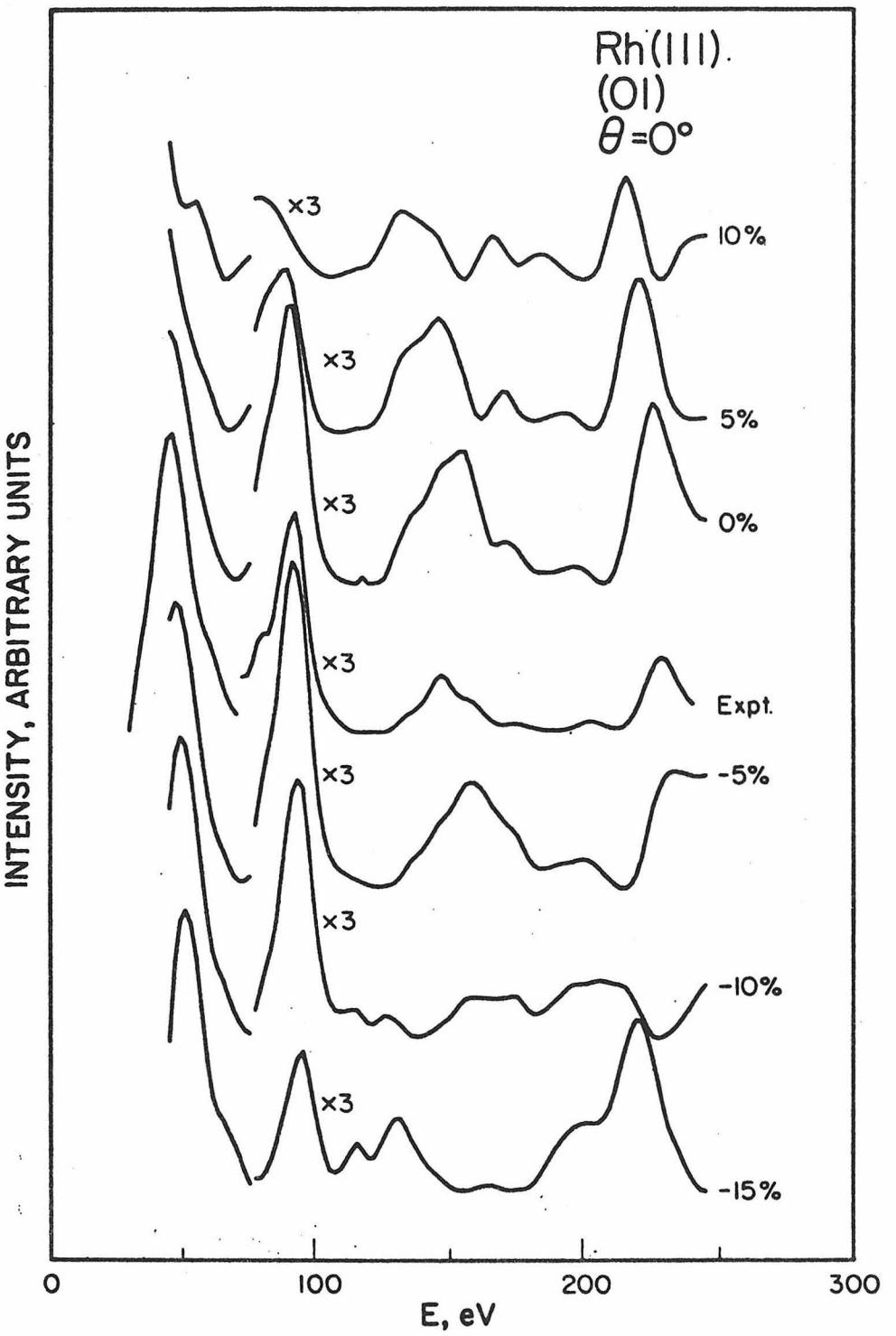
Rh(111).
(01)
θ=0°
×3
10%
×3
5%
×3
0%
×3
Expt.
×3
-5%
×3
-10%
×3
-15%
INTENSITY, ARBITRARY UNITS
0
100
200
300
E, eV

Fig. 7

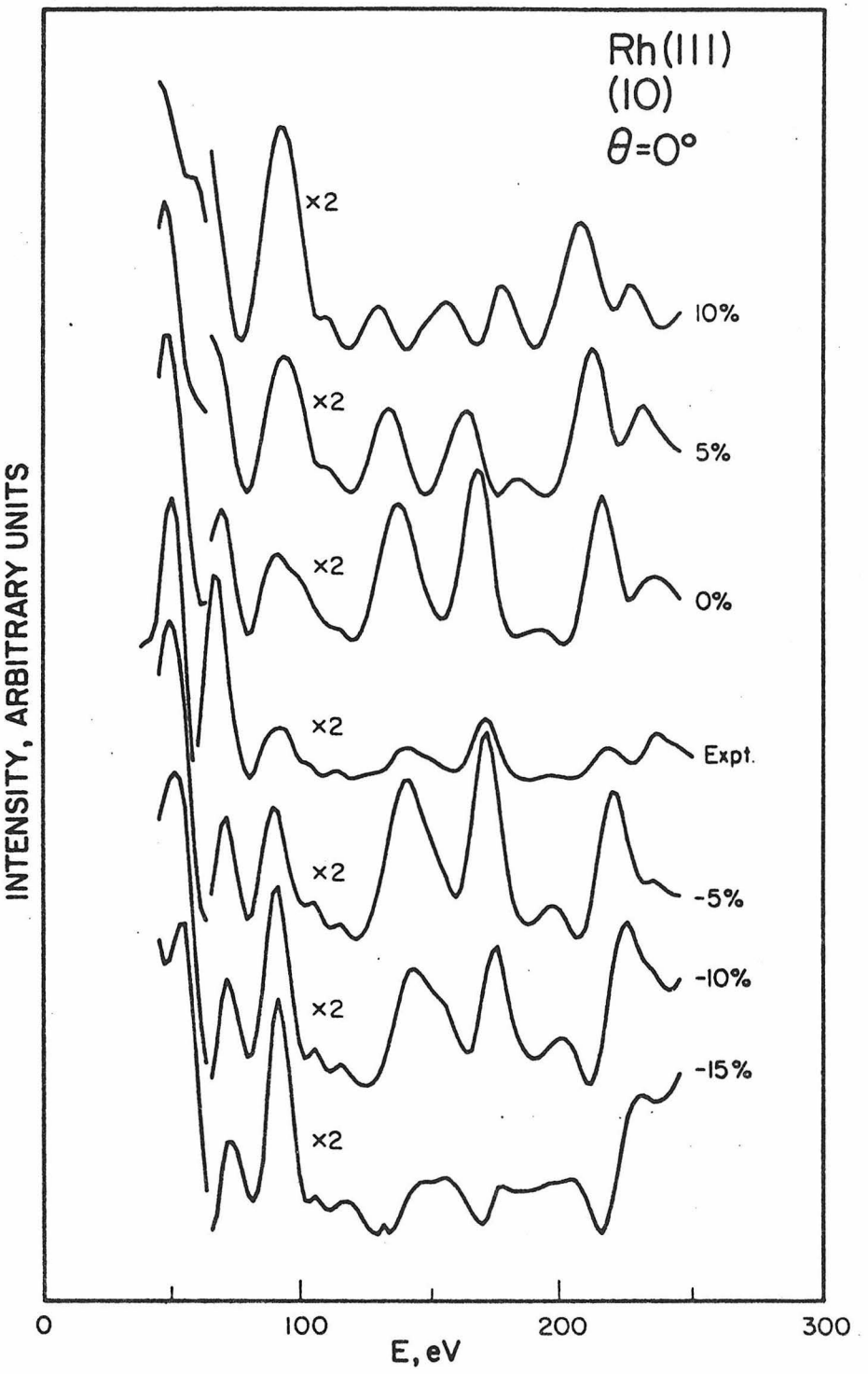
Rh(111)
(10)
θ=0°
×2
10%
5%
0%
Expt.
-5%
-10%
-15%
INTENSITY, ARBITRARY UNITS
0
100
200
300
E, eV

Fig. 8

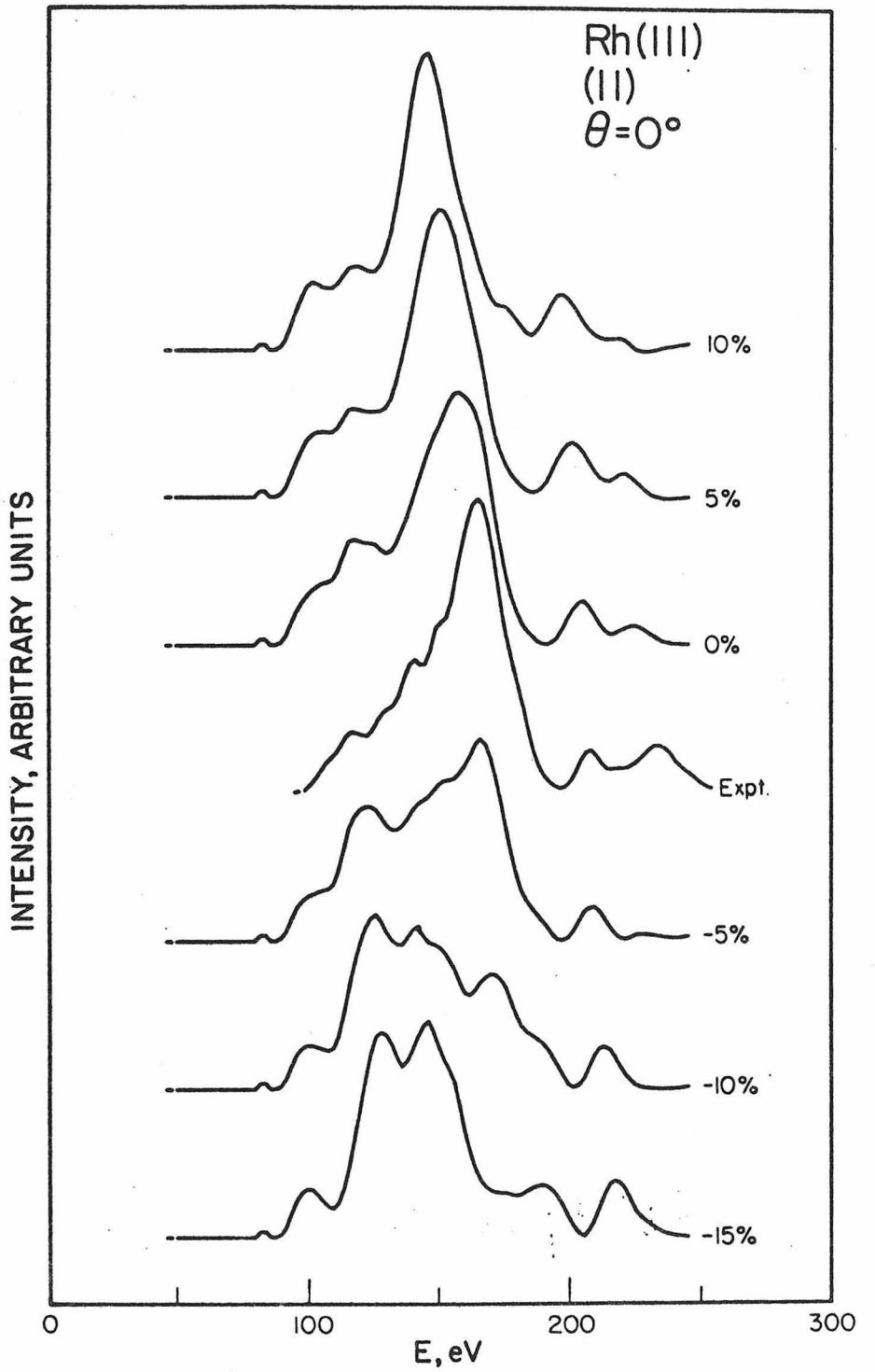
Rh(111)
(11)
θ=0°
10%
5%
0%
Expt.
-5%
-10%
-15%
INTENSITY, ARBITRARY UNITS
0
100
200
300
E, eV

Fig. 9

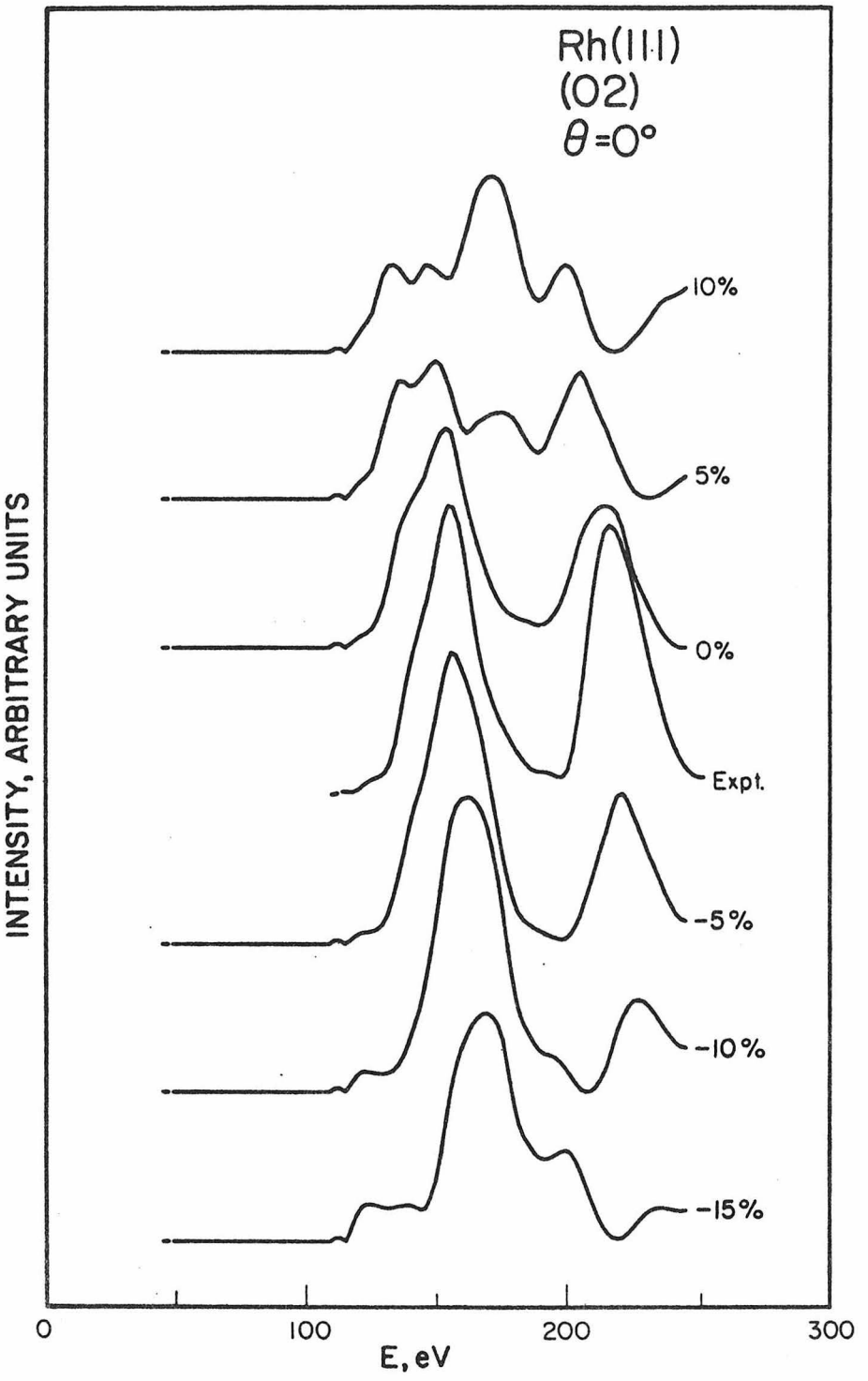
Rh(111)
(02)
θ=0°
10%
5%
0%
Expt.
-5%
-10%
-15%
INTENSITY, ARBITRARY UNITS
0
100
200
300
E, eV

Fig. 10

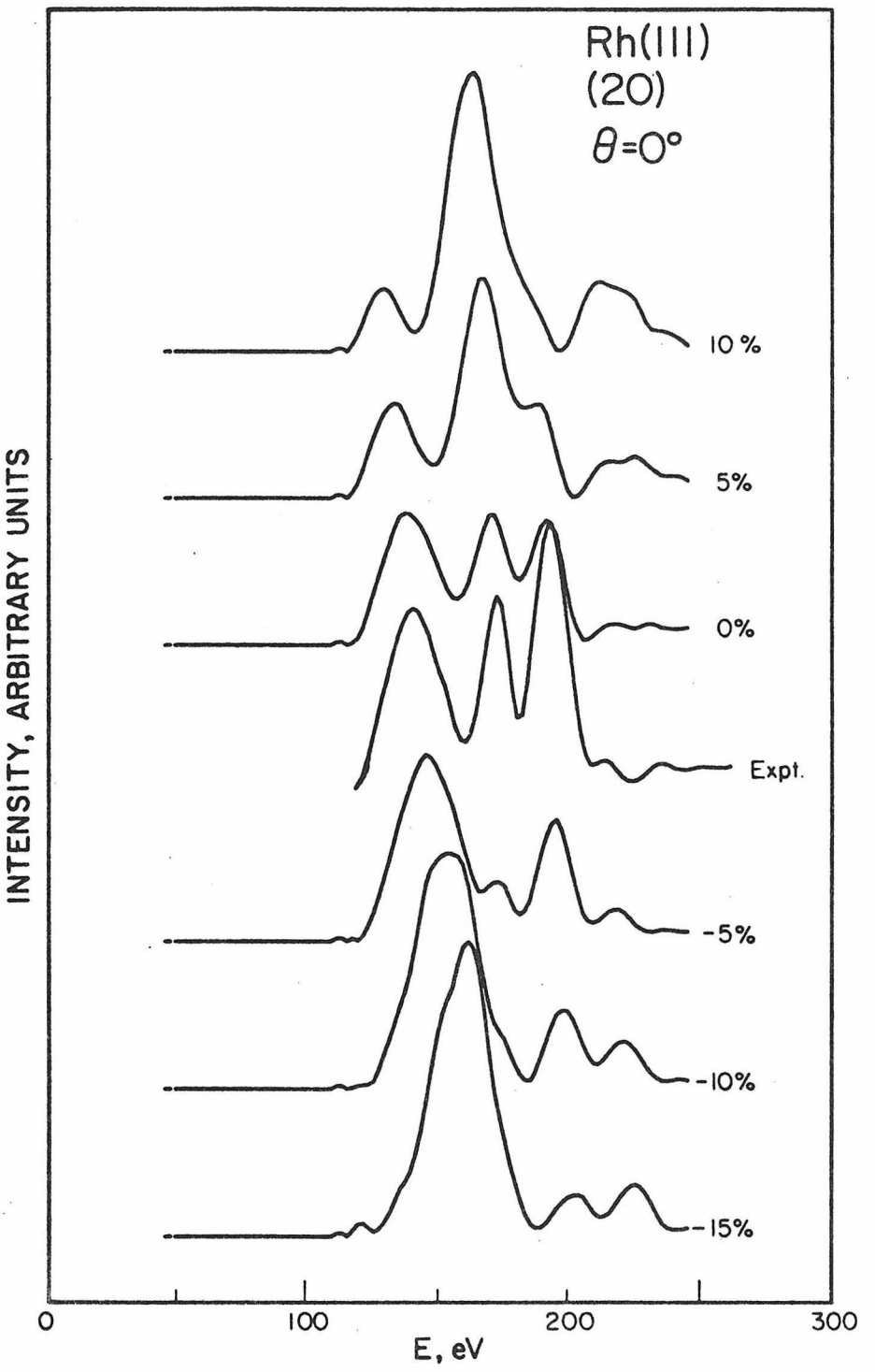
Rh(111)
(20)
θ=0°
10 %
5%
0%
Expt.
-5%
-10%
-15%
INTENSITY, ARBITRARY UNITS
0
100
200
300
E, eV

Fig. 11

Part III

Studies of Iridium (110) and (111) Surfaces by Low-Energy Electron Diffraction

Chapter 1

STRUCTURAL STUDY OF THE RECONSTRUTED Ir(110)-(1x2) SURFACE BY LOW-ENERGY ELECTRON DIFFRACTION

by

C.-M. Chan, M. A. Van Hove,
W. H. Weinberg, and Ellen D. Williams

Division of Chemistry and Chemical Engineering
California Institute of Technology
Pasadena, California 91125

Solid State Communications 29, 47-49 (1979)

ABSTRACT

The structure of the reconstructed Ir(110) - (1x2) surface has been analyzed by low-energy electron diffraction. Three models proposed for the reconstructed Ir(110) - (1x2) surface--the missing row model, the paired row model and the buckled surface model--were tested. Based on a comparison between experimental data consisting of intensity-voltage profiles for ten half-order beams and eight integral-order beams and the calculated curves, the missing row model with a topmost interlayer spacing of 1.22 ± 0.07 Å is the preferred structure.

This Communication reports the first structural analysis, by low-energy electron diffraction (LEED), of an irreversibly reconstructed clean metal surface. Very recently, a preliminary analysis of the low temperature (below room temperature) c(2x2) structure of the W(100) surface has been carried out (1). However, the limited number of beams examined (five) and the equivocal agreement between theory and experiment did not permit a definitive "structural determination" of this reconstructed surface. It has been known for some time from LEED studies that a clean Ir(110) surface displays a (1x2) structure, illustrated schematically in Fig. 1, indicating a reconstructed surface superlattice with a y-dimension twice that of the bulk lattice (2). Different models for this reconstructed surface have been proposed. The three most common and simplest ones are the missing row model, the paired row model and the buckled surface model.

In the missing row model, alternate rows of atoms are absent on the surface. The paired row model suggests that every two adjacent rows of first layer atoms are paired to form one row. In the buckled surface model, adjacent rows of the first layer are relaxed in opposite directions perpendicular to the crystal surface. Fig. 2 shows schematic hard-sphere drawings of these three models proposed for the reconstructed Ir(110) - (1x2) surface. Previous investigations of the unreconstructed Ir(110) surface (3) suggest that the transformation of the impurity-stabilized (1x1) structure to the (1x2) structure involves an extensive atomic rearrangement of the surface. A priori, this evidence makes the missing row model a highly possible candidate for the reconstructed surface since

its formation would involve movement of entire rows of atoms.

The Ir sample, a randomly oriented single crystal rod, was aligned within $\frac{1^{\circ}}{2}$ of the (110) orientation by the back-reflection Laue X-ray method and was cut and polished mechanically using standard techniques (3). After Ar^{+} bombardment and a series of treatments in 5 x 10^{-8} torr oxygen at 800 K, followed by brief annealing in vacuum at 1600 K, the surface was shown to contain less than 2 atomic % carbon which was shown not to influence the surface structure [the intensity-voltage (I-V) beam profiles were unchanged when occasionally more and/or less carbon was present on the surface] and no other impurities detectable by Auger electron spectroscopy. The clean (110) surface, after further annealing at 1600 K in vacuum, exhibited a (1x2) superstructure.

Eighteen LEED I-V spectra consisting of ten half-order beams and eight integral-order beams were collected with a rotatable Faraday cup at approximately 2 eV intervals. In all cases, the incident electron beam was normal to the surface. The achievement of normal incidence was verified by the satisfactory agreement between equivalent non-specular beams. To confirm that the data are reproducible, ten spectra were retaken after repolishing the Ir crystal. The agreement between these two independent sets of data is excellent.

A convergent perturbative scheme known as the layer-doubling method (4) was used for the theoretical calculations. The atomic potential used for Ir is a band structure potential (5) and includes full Slater exchange. Symmetry properties of the beams at normal incidence were exploited in the calculations. Eight phase shifts and an equivalent of a maximum of 170 beams were used. The real part of the inner potential (the muffin-tin-zero) was assumed to be 15 eV, and this quantity was allowed to vary by a

rigid shift of the energy scale in the comparison between theoretical and experimental I-V spectra. A constant inelastic damping of 5 eV was used.

Comparisons between the experimental data and the results of the calculations using the missing row model, the paired row model and the buckled surface model show that the missing row model is the best one considered. In the calculations of the LEED I-V spectra for the missing row model, the topmost layer spacing of the Ir(110) surface was allowed to relax from -15% (percentage contraction of the bulk interlayer spacing of 1.385 Å) to +5% (expansion) in steps of 5%. The comparisons between the experimental I-V spectra and the theoretical I-V spectra obtained from the missing row model calculations with a topmost interlayer spacing of 1.22 Å (-10%), modified with an inner potential of 10 eV are displayed in Figs. 3 and 4 for the integral-order beams and the half-order beams, respectively.

Of the eight integral-order beams, six show very good agreement between theory and experiment; whereas two, the (11) and the (21) beams, agree less well from 70 to 100 eV and from 180 to 210 eV, respectively. Among the ten half-order beams, eight exhibit very good correspondence with experiment, but the (0 3/2) beam exhibits only mediocre agreement, while the calculated (1 1/2) beam shows some minor disagreement with the experimental data. The minor disagreement between theory and experiment for these beams may be due to roughness of the (110) surface (6, 7). However, the missing row model, with a topmost interlayer spacing of 1.22 ± 0.07 Å, is certainly the most probable structure for the (1x2) reconstructed surface of those tested, based on the agreement between experiment and theory for the majority of the beams.

A detailed R-factor analysis, developed by Zanazzi and Jona (8), will be used to determine quantitatively the level of agreement between theory and experiment for the different models considered (9). Work is in progress also to include a slight movement (row pairing) of the second layer within the framework of the missing row model (9).

This work was supported by the Army Research Office (Durham) under Grant No. DAHC04-75-0170, and by the Donors of the Petroleum Research Fund administered by the American Chemical Society (Grant No. 9309-AC5,7).

References

1. R. A. Barker, P. J. Estrup, F. Jona and P. M. Marcus, Solid State Commun. 25, 375 (1978).

2. K. Christmann and G. Ertl, Z. Naturforsch. 28a, 1144 (1973).

3. C.-M. Chan, S. L. Cunningham, K. L. Luke, W. H. Weinberg and S. P. Withrow, Surface Sci. 78, 15 (1978).

4. J. B. Pendry, Low-Energy Electron Diffraction, Academic, London, 1974.

5. G. O. Arbman and S. Hornfelt, J. Phys. F2, 1033 (1972).

6. E. Zanazzi, F. Jona, D. W. Jepsen and P. M. Marcus, J. Phys. C10, 375 (1977).

7. M. Maglietta, E. Zanazzi, F. Jona, D. W. Jepsen and P. M. Marcus, J. Phys. C10, 3287 (1977).

8. E. Zanazzi and F. Jona, Surface Sci. 62, 61 (1977).

9. C.-M. Chan, M. A. Van Hove, W. H. Weinberg and E. D. Williams (in preparation).

Figure Captions

Figure 1. Schematic Ir(110) - (1x2) LEED pattern.

Figure 2. Top views of a hard-spheres representation of (a) the paired row model; (b) the buckled surface model; and (c) the missing row model. The x- and y-directions are in the plane of the crystal surface. The corresponding side views are shown in (d) - (f), respectively. The z-direction is perpendicular to the crystal surface.

Figure 3. Comparison between the theoretical I-V spectra for the missing row model (with a modified inner potential of 10 eV and a topmost interlayer spacing of 1.22 Å) and the experimental I-V spectra of integral-order beams from the Ir(110) - (1x2) surface. $\theta = 0$ corresponds to normal incidence.

Figure 4. As in Fig. 3, except for half-order beams.

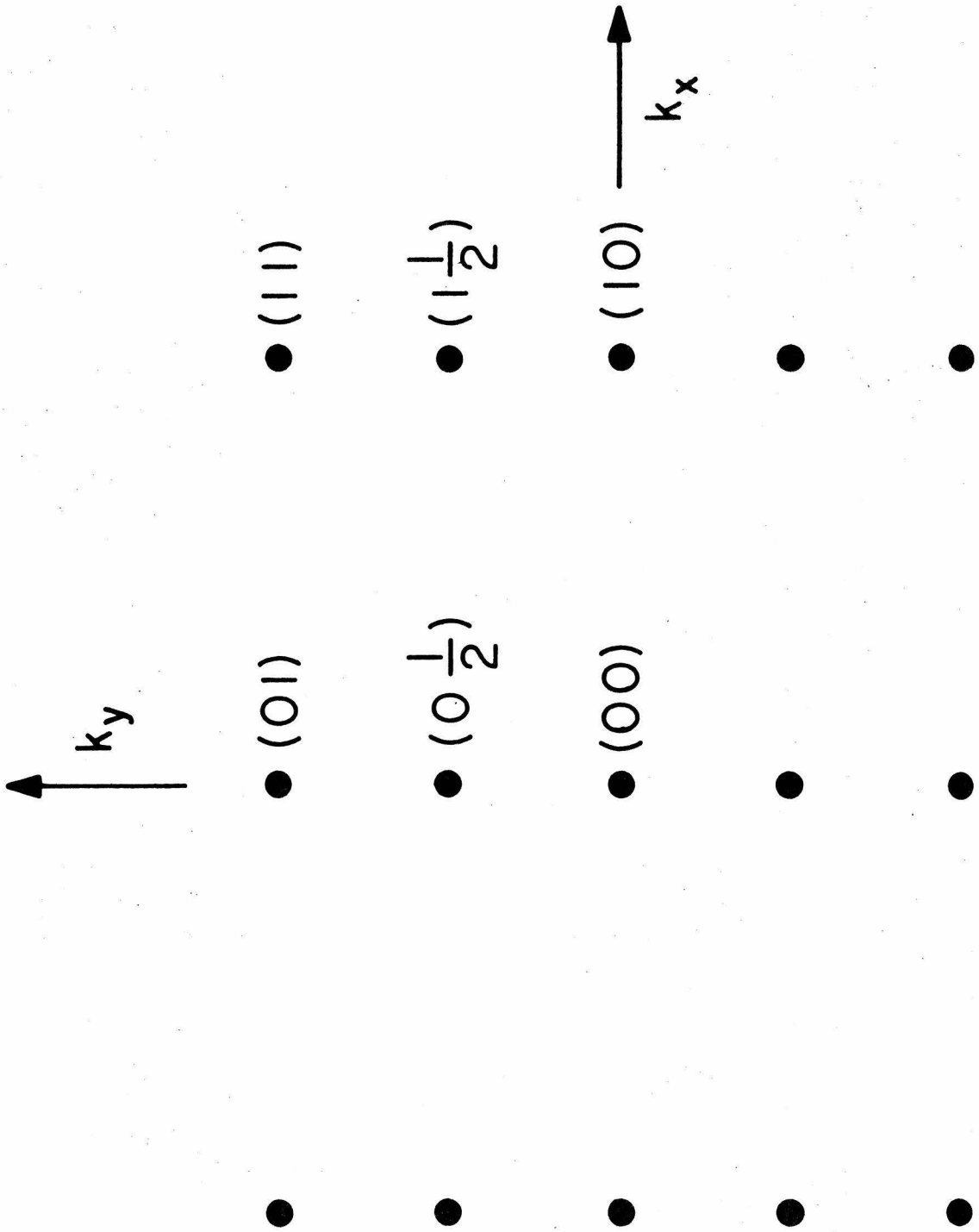

Fig. 1

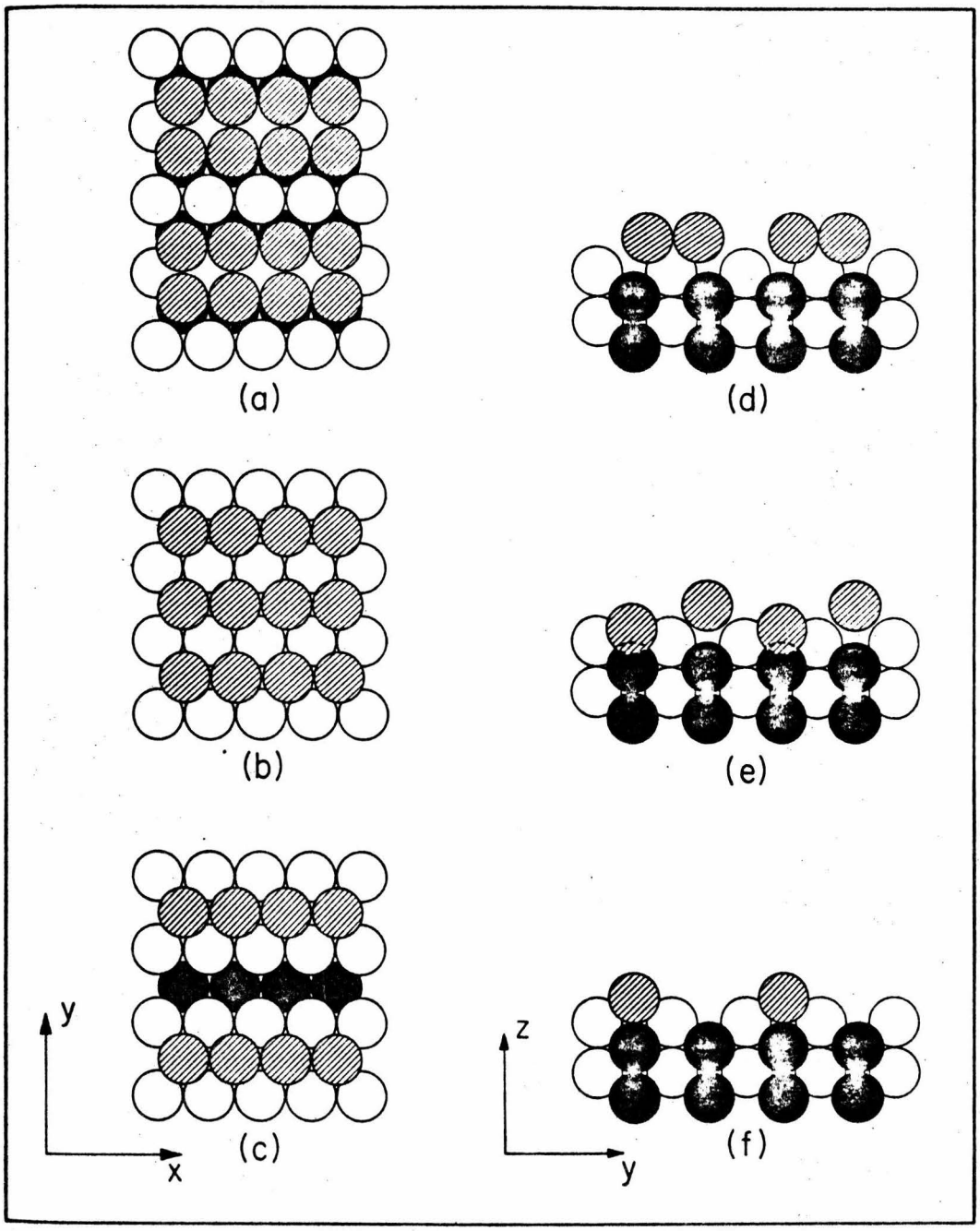

Fig. 2

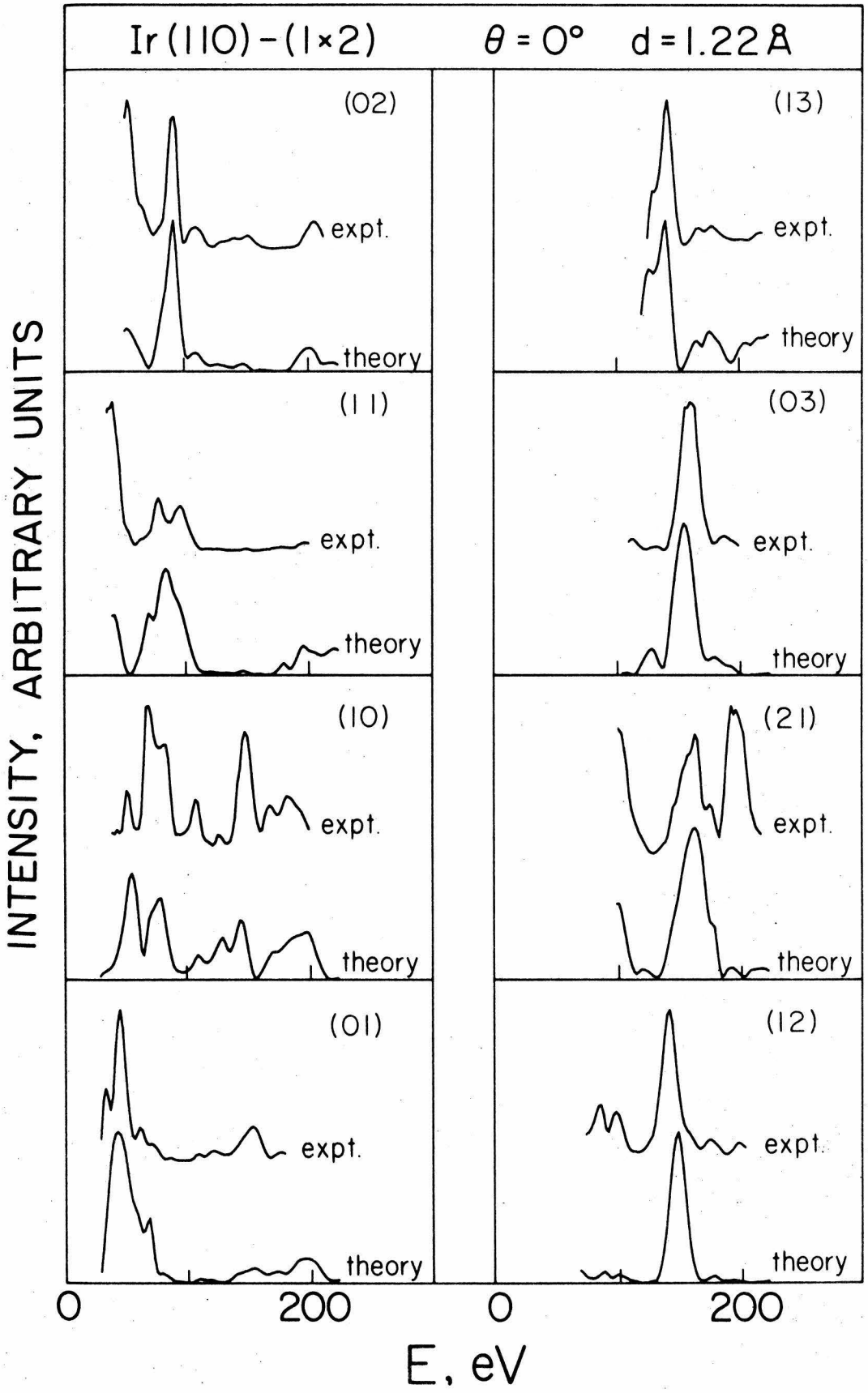
Ir(110)-(1×2)
θ = 0°
d = 1.22 Å
(02)
(13)
(11)
(03)
(10)
(21)
(01)
(12)
expt.
theory
INTENSITY, ARBITRARY UNITS
0
200
E, eV

Fig. 3

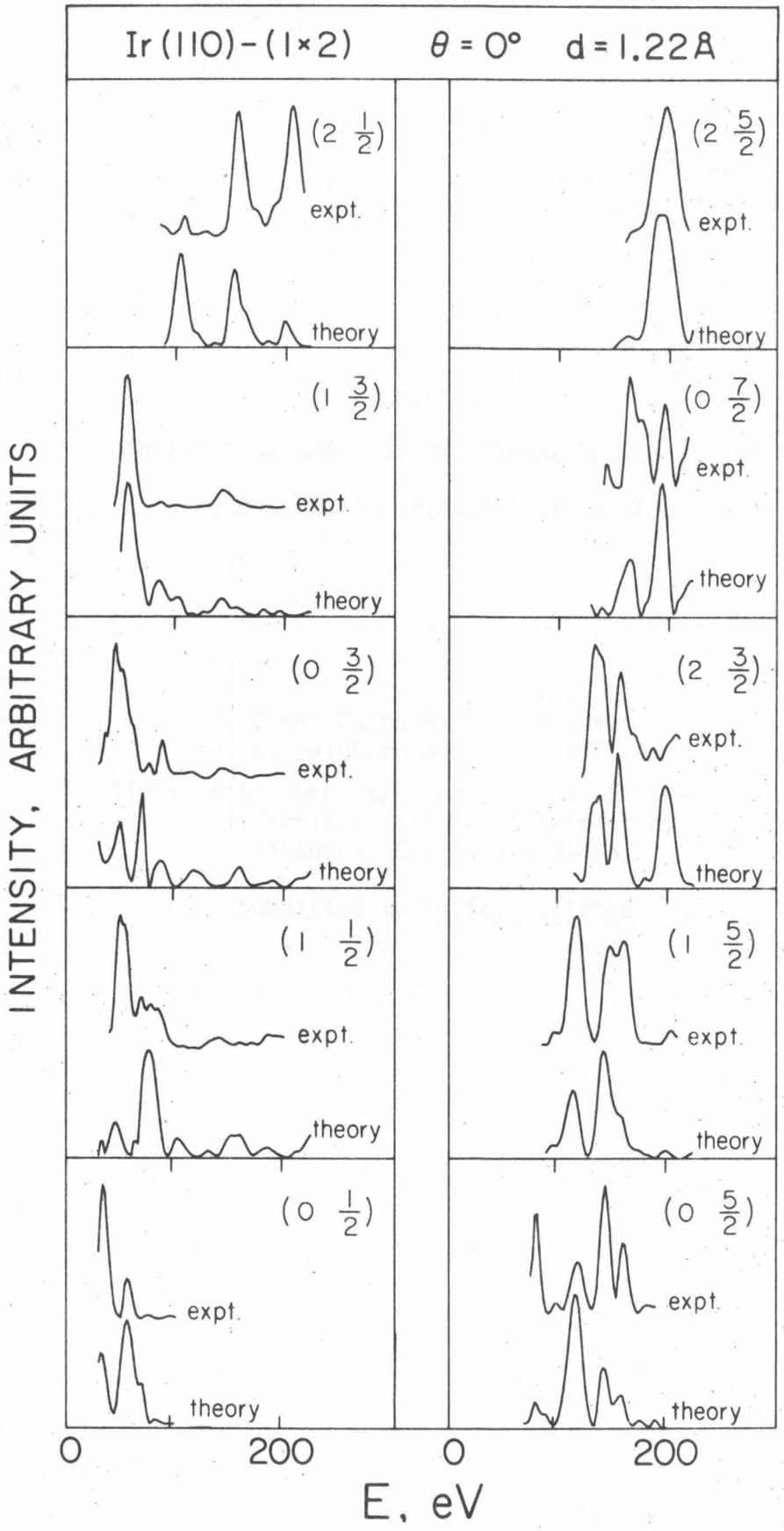
Ir(110)-(1×2) θ = 0° d = 1.22 Å
(2 1/2)
expt.
theory
(2 5/2)
expt.
theory
(1 3/2)
expt.
theory
(0 7/2)
expt.
theory
(0 3/2)
expt.
theory
(2 3/2)
expt.
theory
(1 1/2)
expt.
theory
(1 5/2)
expt.
theory
(0 1/2)
expt.
theory
(0 5/2)
expt.
theory
INTENSITY, ARBITRARY UNITS
0
200
0
200
E, eV

Fig. 4

Chapter 2

AN R-FACTOR ANALYSIS OF SEVERAL MODELS OF THE RECONSTRUCTED Ir(110)-(1x2) SURFACE

by

C.-M. Chan, M. A. Van Hove
W. H. Weinberg and E. D. Williams

Division of Chemistry and Chemical Engineering
California Institute of Technology
Pasadena, California 91125

Submitted to Surface Science

Abstract

The structure of the reconstructed Ir(110)-(1x2) surface has been analyzed by low-energy electron diffraction. The reliability (R)-factor analysis, proposed by Zanazzi and Jona, has been applied to determine quantitatively the level of agreement between the experimental and calculated beam intensities for different models proposed for the (1x2) structure. The models tested were the following: (1) The missing row model, (2) The missing row model with a slight movement of the second layer, (3) The paired-rows model, and (4) The buckled surface model. Based on the results of the R-factor analysis, the missing row model with a topmost layer spacing of 1.16 ± 0.07 Å, which corresponds to approximately 15% contraction of the bulk interlayer spacing of 1.36 Å, is the preferred structure.

1. Introduction

The reconstruction of clean surfaces is one of the more important current problems of structural analysis by low-energy electron diffraction (LEED). Examples of recent attempts to solve such problems are the following: Au(110)-(1x2) (1), Si(001)-(2x1) (2,3), Si(111)-(2x1) (4) and W(100)-c(2x2) (5). The absence of any completely successful result reflects the difficulty involved in such an analysis.

It has been known for some time from LEED studies that the clean (110) surfaces of Ir, Pt and Au display a (1x2) LEED pattern, as illustrated in Fig. 1. In previous studies (6,7), our results indicated that the missing row model, with a topmost interlayer spacing of 1.22 ± 0.07 Å, is the preferred structure for the Ir(110) surface. These results also corroborated our postulate that the transformation of the (1x2) structure to the impurity stabilized (1x1) structure involves an extensive atomic rearrangement on the surface (6,8). In this paper, as an extension of the results presented previously (7), a slight movement (row-pairing) of the second layer within the framework of the missing row model is considered, and the results of an R-factor analysis for all the models tested are presented.

2. Experimental Procedure

The experiments were performed in an UHV chamber which has a base pressure of approximately 5×10^{-11} torr. The Ir sample was cut from a single crystal and aligned within $\frac{1}{2}^{o}$ of the (110) orientation by the back-reflection Laue X-ray method. Both sides of the crystal were polished mechanically using standard techniques. A crystal temperature up to 1600 K could be achieved by resistive heating. The crystal

temperature was measured with a 5%Re/95%W-26%Re/74%W thermocouple which was spotwelded to the back of the crystal. After Ar^+ bombardment and a series of treatments in 5 x 10^{-8} torr oxygen at 800 K, followed by brief annealing in vacuum at 1600 K, the surface was shown to contain less than 2 atomic % carbon and no other impurities by Auger electron spectroscopy. The clean (110) surface, after further annealing at 1600 K in vacuum, exhibited a (1x2) superstructure.

Eighteen LEED intensity-voltage (I-V) spectra consisting of ten half-order beams and eight integral-order beams were collected with a rotatable Faraday cup at approximately 2 eV intervals. To confirm that the data are reproducible, ten spectra were retaken after repolishing the Ir crystal. The agreement between these two independent sets of data is excellent. The beams are indexed so that the longer side of the real space unit cell is the y-direction.

3. Analysis

A convergent perturbative scheme known as the Layer-Doubling method (9), supplemented by a Reverse Scattering Perturbation formalism (10) when small interlayer spacings occurred, was used for the theoretical calculations. The scattering potential used for the Ir atoms is due to Arbman and Hornfelt (11). It has been used successfully in our previous analyses (6 - 8,12,13). Symmetry properties of the beams at normal incidence were exploited in the calculations. Eight phase shifts were used. The real part of the inner potential (V_0) was assumed to be 15 eV, and this quantity was allowed to vary by a rigid shift of the energy scale for the comparison between theoretical and experimental I-V spectra.

A constant inelastic damping of 5 eV was used. The bulk Debye temperature used in the calculation was 280 K, and an enhancement factor of 1.4 was chosen for the surface mean-square vibrational amplitudes.

The three most common and simplest models proposed for the (1x2) reconstructed surface are the missing row model, the paired-rows model, and the buckled surface model. In the missing row model, alternate rows of surface atoms are absent. The paired-rows model suggests that every two adjacent rows of first layer atoms are paired to form one row. In the buckled surface model, adjacent rows of the first layer are relaxed in opposite directions perpendicular to the crystal surface. Figure 2 shows schematic hard-sphere drawings of these three models proposed for the reconstructed Ir(110)-(1x2) surface. Of these three models, the analysis indicates that the missing row model represents the most probable structure (6,7). Hence, the missing row model is extended by including a slight movement of the second layer (row pairing). A complete summary of all the models considered with the ranges of geometrical parameters used for each is listed in Table 1. In Fig. 3, detailed schematic drawings showing the geometrical parameters used in the different models are presented.

4. Results

A comparison between experimentally measured LEED I-V spectra and the best (lowest R-factor) calculated set of I-V spectra for each of the four different models is shown in Figs. 4 - 11 for four integral-order and four half-order beams. A visual inspection of Figs. 4 - 11 indicates that the missing row model is the preferred structure for the (1x2) surface. This

qualitative evaluation is confirmed by an R-factor analysis as shown below. Figs. 12 and 13 summarize the comparison between experimental I-V spectra and calculated spectra for the missing row model with $d_1 = 1.16$ Å and $V_o = 11$ eV for the integral-order beams and the half-order beams, respectively.

As is particularly evident in Figs. 7, 9 and 11, the calculated spectra are quite sensitive to even a small movement in the second layer. The sensitivity of the calculated spectra to a variation in geometrical parameters is an important ingredient in the success of any LEED structural analysis. This sensitivity of the calculated spectra enhances the credibility of the results of the analysis.

The reliability (R)-factor analysis suggested by Zanazzi and Jona (14) was used to determine quantitatively the level of agreement between experimental spectra and calculated spectra for all the different models considered. The interpretation of the value of the R-factor is as follows: a value near approximately 0.2 indicates high reliability of the proposed model, one near 0.35 indicates a possibly correct structure, while one above approximately 0.5 indicates an incorrect structure (14,15). Thus, a comparison of the R-factors calculated for the different models discriminates among the various models quantitatively.

R-factors were calculated for the sets of I-V curves corresponding to each trial structure listed in Table 1. The R-factors for the optimum structure within each model are presented in Table 2. The missing row model with an R-factor of 0.24 is the most probable model among those tested. The two missing row models with row pairing, and the paired-rows model having R-factors of 0.28, 0.27 and 0.29, respectively, could be regarded

as possibly correct structures.

The R-factor for the missing row model that is the preferred structure is 0.24, which is slightly higher than the proposed value of 0.2 for a structure of high reliability. This minor disagreement between experiment and theory may be due to roughness of the (110) surface (16,17). However, the missing row model with a topmost interlayer spacing of 1.16 ± 0.07 Å is the most probable structure for the (1x2) reconstructed surface based on the results of both a visual inspection and an R-factor analysis.

5. Synopsis

Based on the totality of the experiment and theoretical LEED results, of the various surface structures tested (the missing row model, the missing row model with row pairing, the paired-rows model, and the buckled surface model), the missing row model with a topmost interlayer spacing of 1.16 ± 0.07 Å is the most probable structure for the (1x2) reconstructed surface of Ir(110).

References

1. J. R. Noonan and H. R. Davis, J. Vacuum Sci. Technol. 16, 000 (1979).
2. F. Jona, H. D. Shih, A. Ignatiev, D. W. Jepsen and P. M. Marcus, J. Phys. C10, L67 (1977).
3. A. Ignatiev, F. Jona, M. Debe, D. E. Johnson, S. J. White and D. P. Woodruff, J. Phys. C10, 1109 (1977).
4. P. Mark, J. D. Levine and S. H. McFarlane, Phys. Rev. Letters 38, 1408 (1977).
5. R. A. Barker, P. J. Estrup, F. Jona and P. M. Marcus, Solid State Commun. 25, 375 (1978).
6. C.-M. Chan, M. A. Van Hove, W. H. Weinberg and E. D. Williams, J. Vacuum Sci. Technol. 16, 000 (1979).
7. C.-M. Chan, M. A. Van Hove, W. H. Weinberg and E. D. Williams, Solid State Commun. 29, 000 (1979).
8. C.-M. Chan, S. L. Cunningham, K. L. Luke, W. H. Weinberg and S. P. Withrow, Surface Sci. 78, 15 (1978).
9. J. B. Pendry, Low-Energy Electron Diffraction, Academic Press, London, 1974.
10. S. Y. Tong and M. A. Van Hove, Phys. Rev. B16, 1459 (1977).
11. G. O. Arbman and S. Hornfelt, J. Phys. F2, 1033 (1972).
12. C.-M. Chan, K. L. Luke, M. A. Van Hove, W. H. Weinberg and S. P. Withrow, Surface Sci. 78, 386 (1978).
13. C.-M. Chan, S. L. Cunningham, M. A. Van Hove, W. H. Weinberg and S. P. Withrow, Surface Sci. 66, 394 (1977).
14. E. Zanazzi and F. Jona, Surface Sci. 62, 61 (1977).
15. F. Jona, J. Phys. C11, 4271 (1978).

16. E. Zanazzi, F. Jona, D. W. Jepsen and P. M. Marcus, J. Phys. C10, 375 (1977).

17. M. Maglietta, E. Zanazzi, F. Jona, D. W. Jepsen and P. M. Marcus, J. Phys. C10, 3287 (1977).

Table 1. Summary of the Geometrical Parameters used in Different Models. For explanation of the symbols, see Fig. 3.

Model	Range* of Geometrical Variables, Å	Increment in the Variables, Å
Paired-rows model	d_1 = 1.21 to 1.81	0.15
	σ = 2.95 to 3.55	0.30
Buckled surface model	d_δ = 1.06 to 1.51	0.15
	2δ = 0.20 to 0.80	0.20
Missing row model	d_1 = 0.91 to 1.46	0.05
Missing row model with row pairing	d_1 = 0.76 to 1.56	0.20
	d_2 = 1.16 to 1.76	0.20
	β = 3.25 to 3.55	0.30

*Where more than one parameter is listed, all combinations of the values indicated were evaluated.

Table 2. Results of an R-Factor Analysis

Model	Inner Potential, eV	Geometrical Parameters, Å	R-Factor
Paired-rows model	13	$d_1 = 1.21$ $\sigma = 3.55$	0.29
Buckled surface model	13	$d_\delta = 1.11$ $2\delta = 0.20$	0.32
Missing row model	11	$d_1 = 1.16$	0.24
Missing row model with row pairing	13	$d_1 = 1.16$ $d_2 = 1.16$ $\beta = 3.55$	0.28
	13	$d_1 = 1.16$ $d_2 = 1.16$ $\beta = 3.25$	0.27

Figure Captions

Fig. 1. Schematic Ir(110)-(1x2) LEED pattern.

Fig. 2. Top views of a hard spheres representation of (a) the paired-rows model; (b) the buckled surface model; and (c) the missing row model. The corresponding side views are shown in (d) - (f), respectively. The z-direction is perpendicular to the crystal surface.

Fig. 3. The geometrical parameters used in different models where $a = 3.58$ Å is the normal spacing between adjacent rows of atoms in the (001) crystallographic direction.

The paired-rows model: d_1 is the interlayer spacing between the first and second layers of atoms; and σ is the spacing between the adjacent close-packed top rows of atoms which have moved toward each other.

The buckled surface model: 2δ is the spacing between the two topmost layers of atoms which are relaxed in opposite directions perpendicular to the crystal surface; and d_δ is interlayer spacing between the average distance of the buckled, top layers of atoms and the second layer of atoms.

The missing row model with row pairing: d_1 is the interlayer spacing between the top and second layers of atoms; d_2 is the interlayer spacing between the second and the third layers of atoms; and β is the spacing between the adjacent rows of atoms in the second layer in the (001) crystallographic direction. This becomes the missing row model when $\beta = a$ with d_2 equal to the interlayer spacing.

Fig. 4. Comparison between experimental I-V spectra and optimized calculated spectra for each model for the (01) beam where $\theta = 0^{o}$ defines normal incidence.

(a), the paired-rows model with V_o = 13 eV;

(b), the buckled surface model with V_o = 13 eV;

(c) and (d), the missing row model with row pairing and with V_o = 13 eV;

(e), the missing row model with V_o = 11 eV; and

(f), the experimental I-V spectrum.

Fig. 5. As in Fig. 4, except the (0 2) beam.

Fig. 6. As in Fig. 4, except the (2 1) beam.

Fig. 7. As in Fig. 4, except the (1 3) beam.

Fig. 8. As in Fig. 4, except the $(0\ \frac{1}{2})$ beam.

Fig. 9. As in Fig. 4, except the $(1\ \frac{3}{2})$ beam.

Fig. 10. As in Fig. 4, except the $(1\ \frac{5}{2})$ beam.

Fig. 11. As in Fig. 4, except the $(2\ \frac{1}{2})$ beam.

Fig. 12. Comparison between the theoretical I-V spectra for the missing row model (with V_o = 11 eV and d_1 = 1.16 Å) and the experimental I-V spectra of eight integral-order beams where $\theta = 0^{o}$ defines normal incidence.

Fig. 13. As in Fig. 12, except for ten nonintegral-order beams.

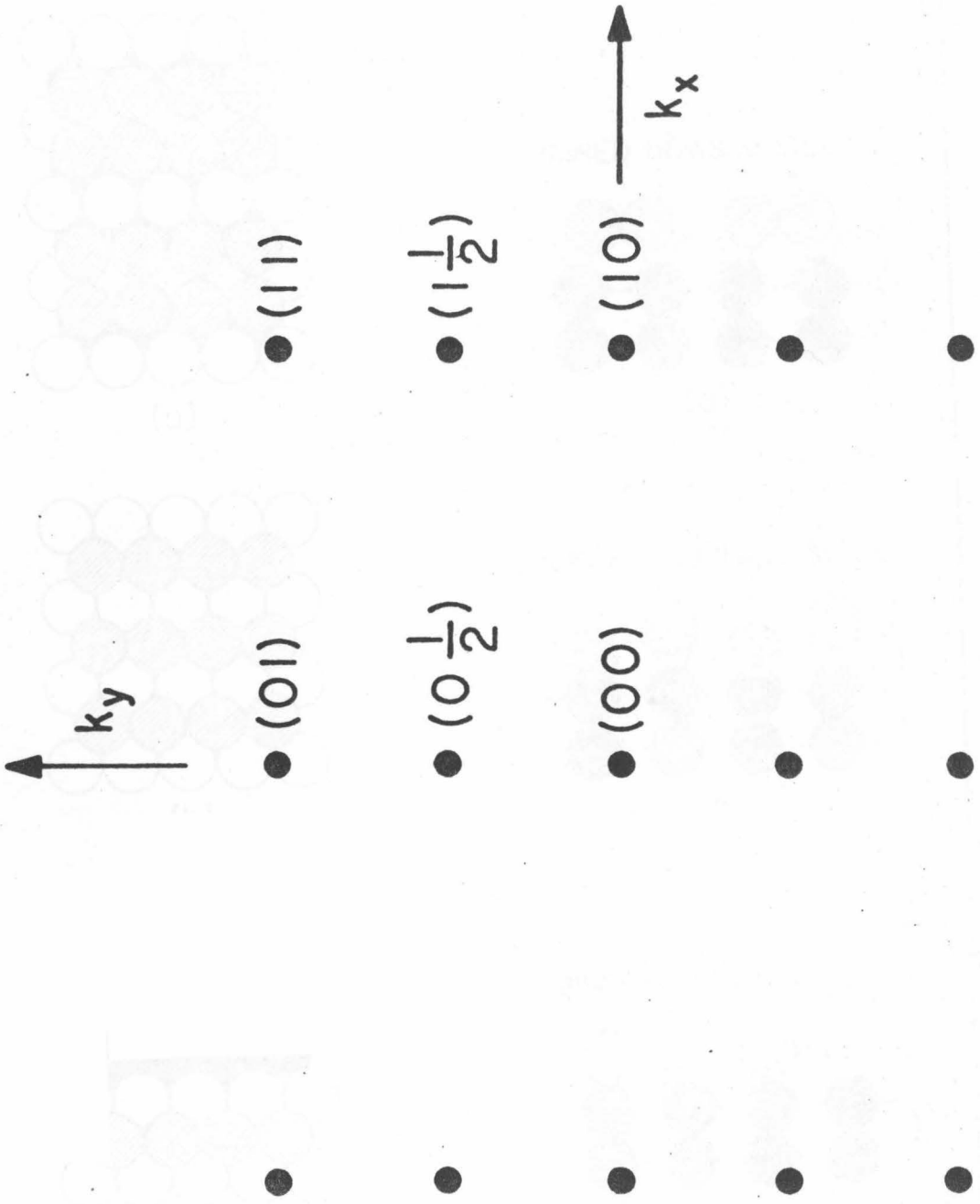

Fig. 1

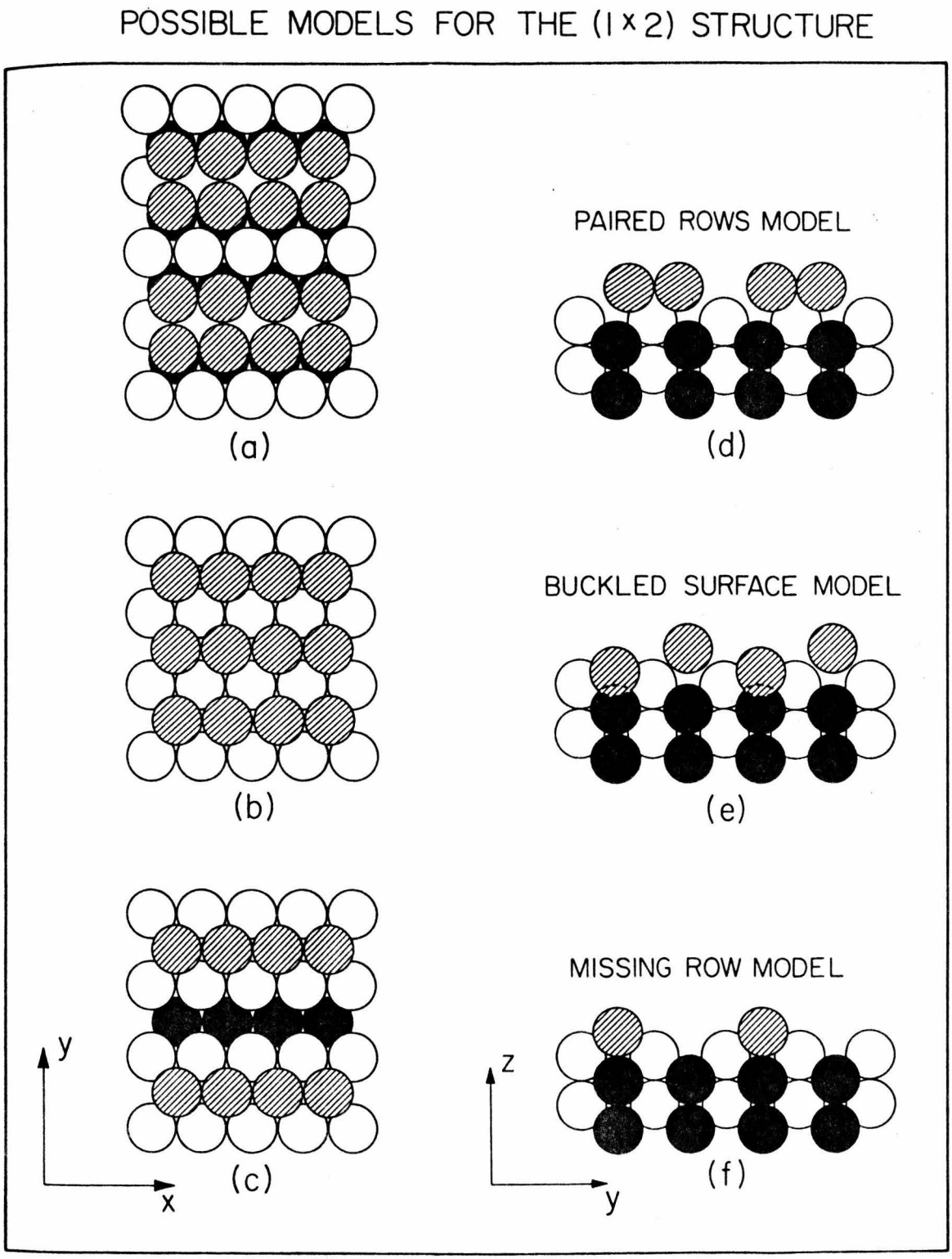
POSSIBLE MODELS FOR THE (1 x 2) STRUCTURE
(a)
PAIRED ROWS MODEL
(d)
(b)
BUCKLED SURFACE MODEL
(e)
y
x
(c)
MISSING ROW MODEL
z
y
(f)

Fig. 2

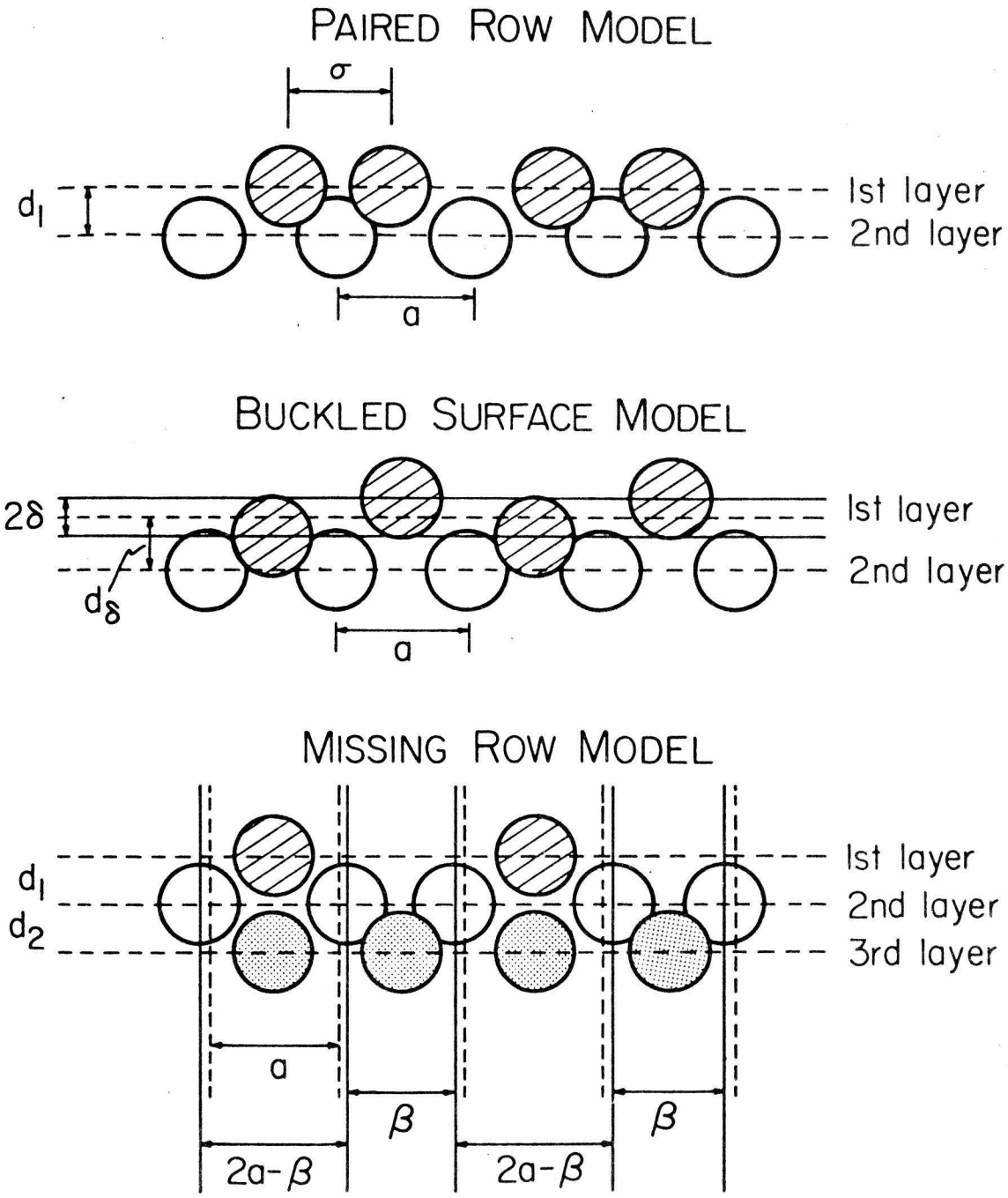
PAIRED ROW MODEL
σ
d1
1st layer
2nd layer
a
BUCKLED SURFACE MODEL
2δ
dδ
1st layer
2nd layer
a
MISSING ROW MODEL
d1
d2
1st layer
2nd layer
3rd layer
a
β
β
2a-β
2a-β

Fig. 3

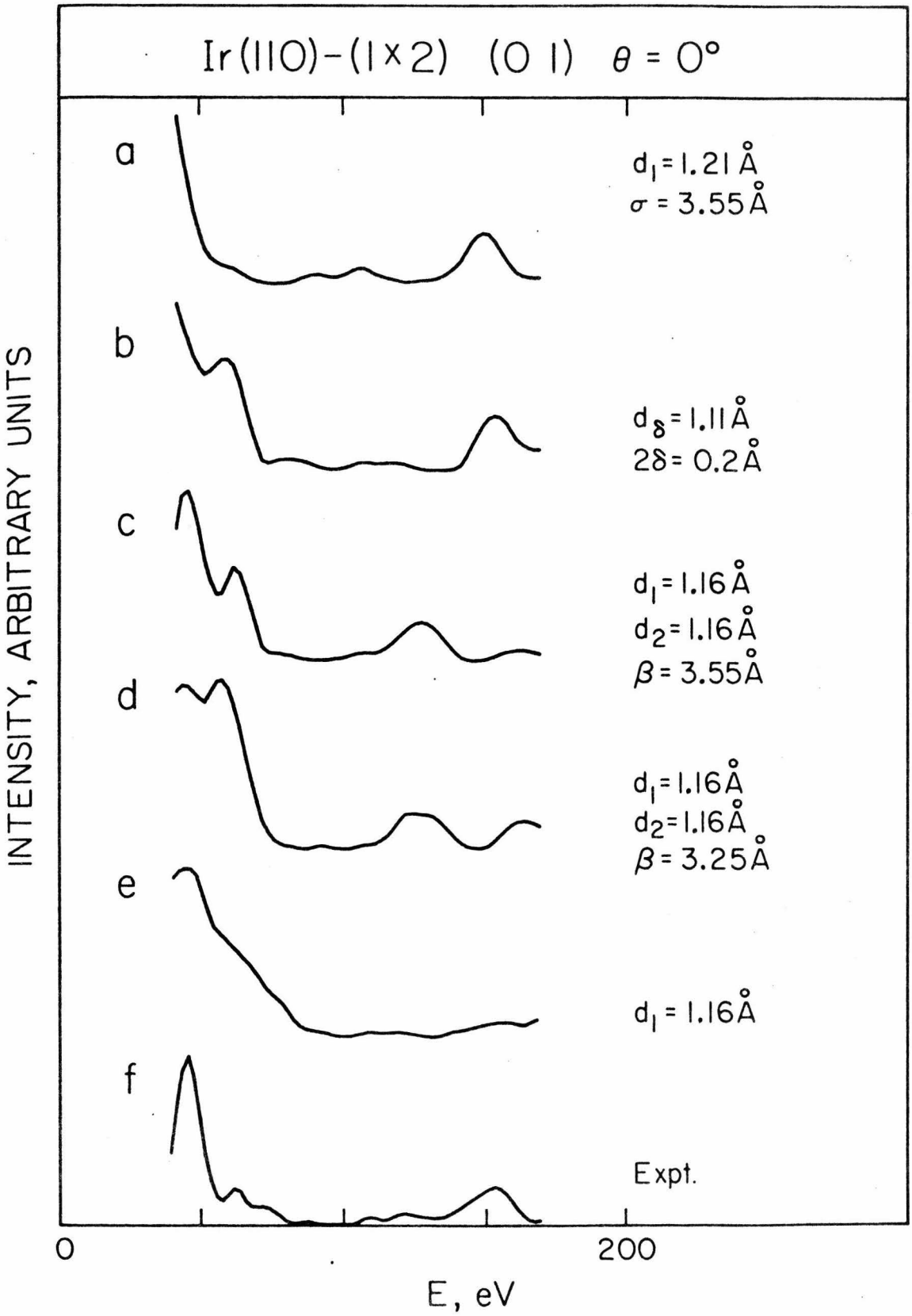
Ir(110)-(1×2) (0 1) θ = 0°
a
d1 = 1.21 Å
σ = 3.55 Å
b
dδ = 1.11 Å
2δ = 0.2 Å
c
d1 = 1.16 Å
d2 = 1.16 Å
β = 3.55 Å
d
d1 = 1.16 Å
d2 = 1.16 Å
β = 3.25 Å
e
d1 = 1.16 Å
f
Expt.
INTENSITY, ARBITRARY UNITS
0
200
E, eV

Fig. 4

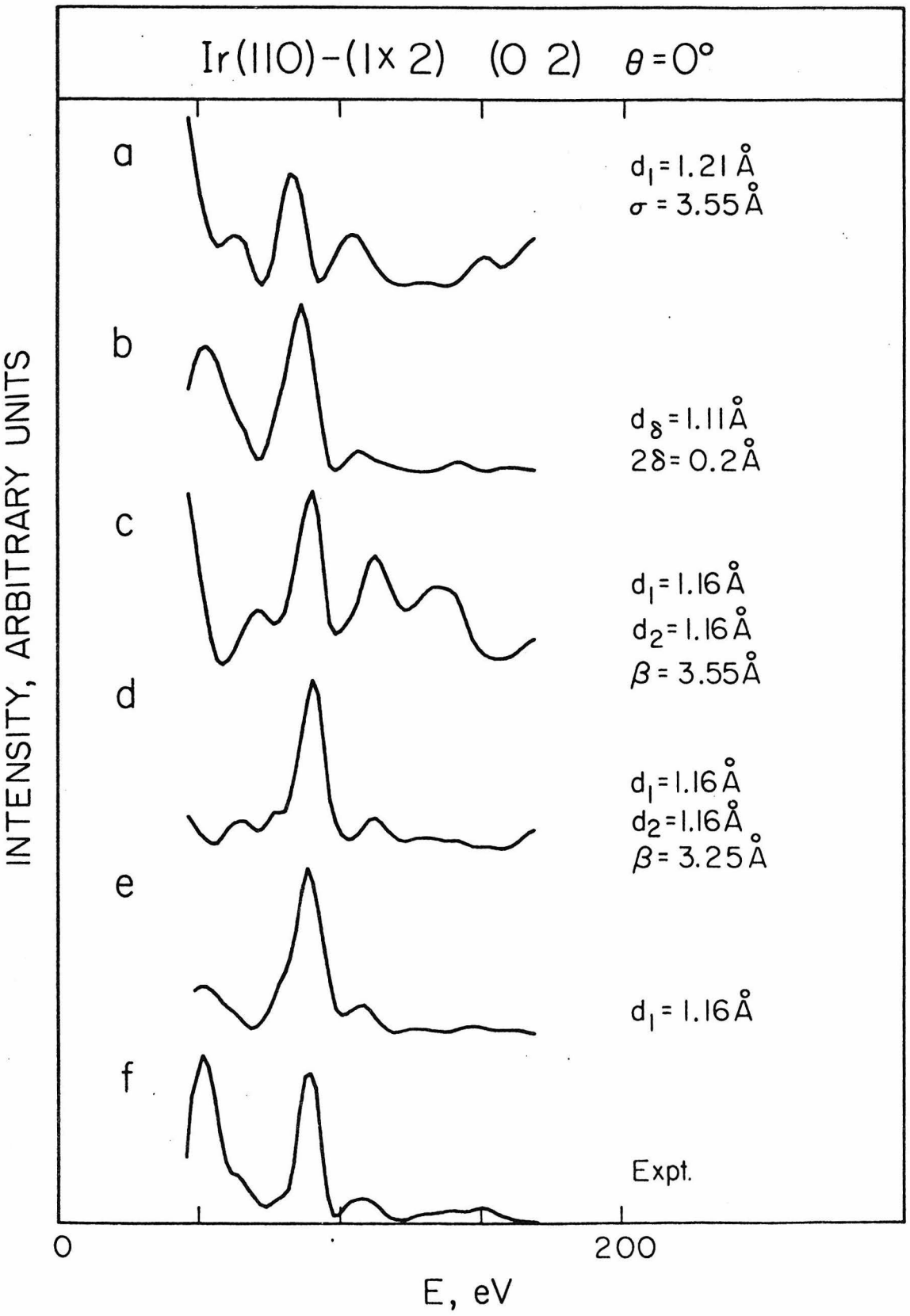
Ir(110)-(1x 2) (0 2) θ=0°
a
d1 = 1.21 Å
σ = 3.55 Å
b
dδ = 1.11 Å
2δ = 0.2 Å
c
d1 = 1.16 Å
d2 = 1.16 Å
β = 3.55 Å
d
d1 = 1.16 Å
d2 = 1.16 Å
β = 3.25 Å
e
d1 = 1.16 Å
f
Expt.
INTENSITY, ARBITRARY UNITS
0
200
E, eV

Fig. 5

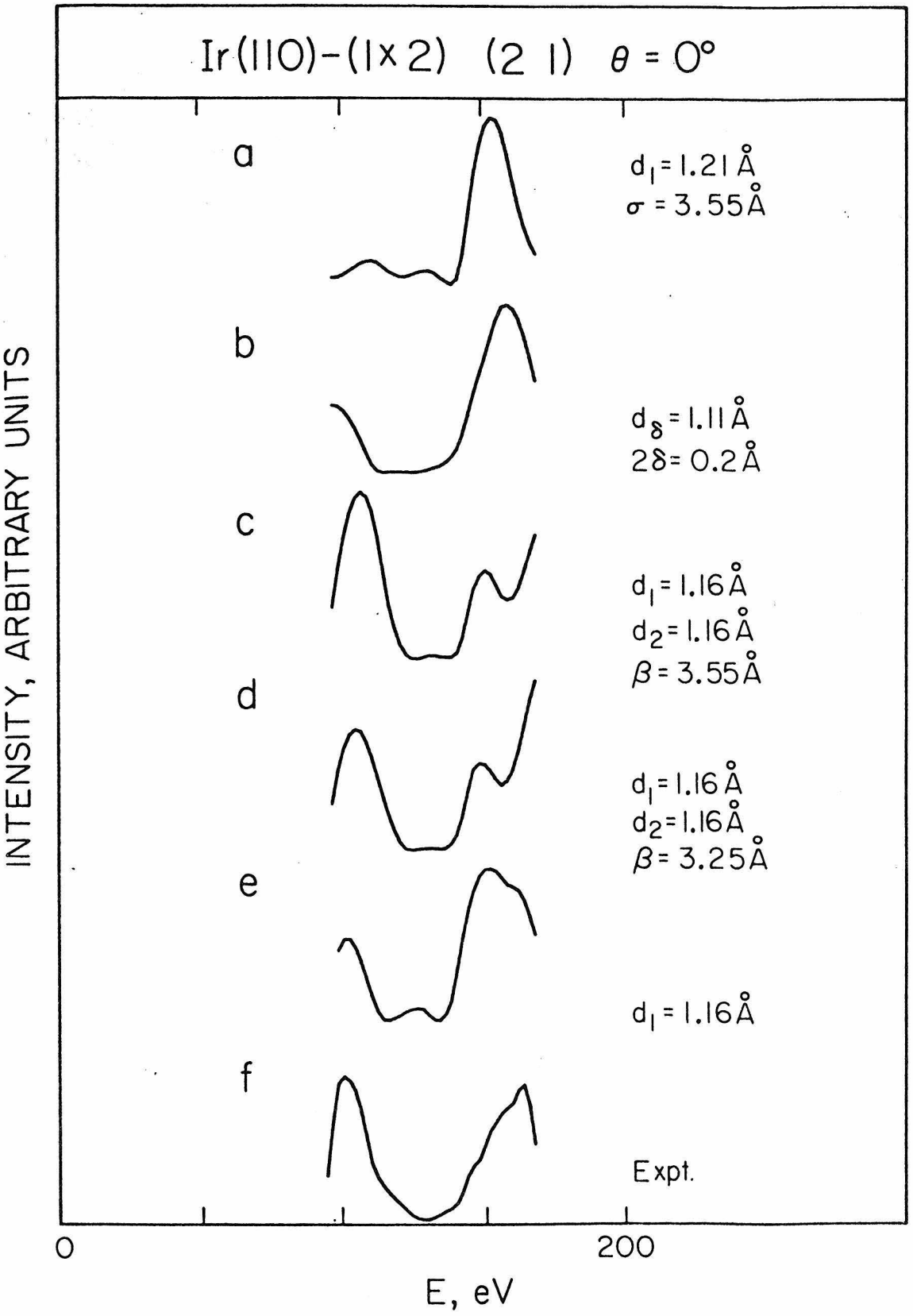
Ir(110)-(1x2) (2 1) θ = 0°
a
d1 = 1.21 Å
σ = 3.55Å
b
dδ = 1.11 Å
2δ = 0.2 Å
c
d1 = 1.16 Å
d2 = 1.16 Å
β = 3.55 Å
d
d1 = 1.16 Å
d2 = 1.16 Å
β = 3.25 Å
e
d1 = 1.16 Å
f
Expt.
INTENSITY, ARBITRARY UNITS
0
200
E, eV

Fig. 6

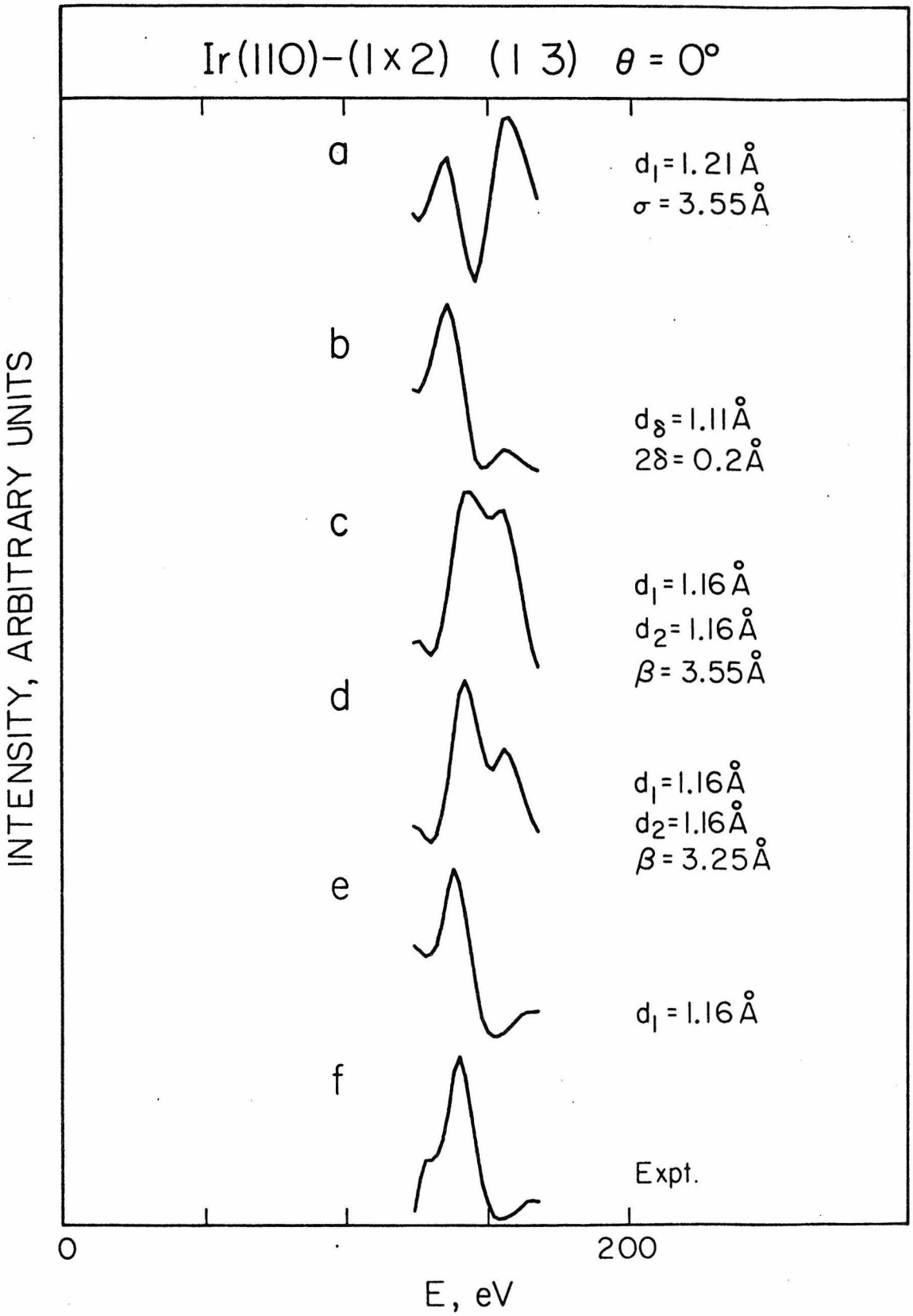
Ir(110)-(1x2) (1 3) θ = 0°
a
d1 = 1.21 Å
σ = 3.55 Å
b
dδ = 1.11 Å
2δ = 0.2 Å
c
d1 = 1.16 Å
d2 = 1.16 Å
β = 3.55 Å
d
d1 = 1.16 Å
d2 = 1.16 Å
β = 3.25 Å
e
d1 = 1.16 Å
f
Expt.
INTENSITY, ARBITRARY UNITS
0
200
E, eV

Fig. 7

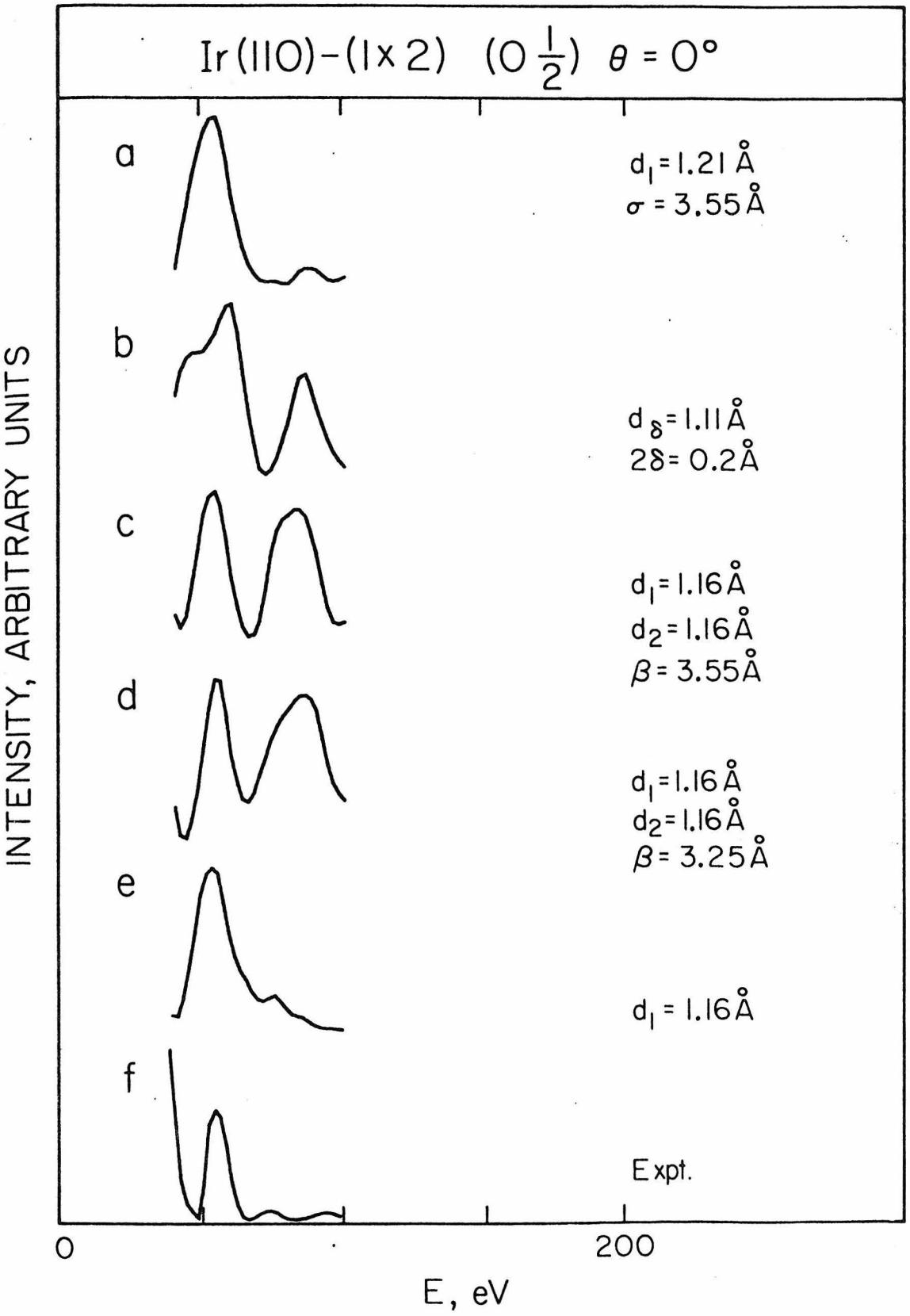
Ir(110)-(1x2) (0 1/2) θ = 0°
a
d1 = 1.21 Å
σ = 3.55 Å
b
dδ = 1.11 Å
2δ = 0.2 Å
c
d1 = 1.16 Å
d2 = 1.16 Å
β = 3.55 Å
d
d1 = 1.16 Å
d2 = 1.16 Å
β = 3.25 Å
e
d1 = 1.16 Å
f
Expt.
INTENSITY, ARBITRARY UNITS
0
200
E, eV

Fig. 8

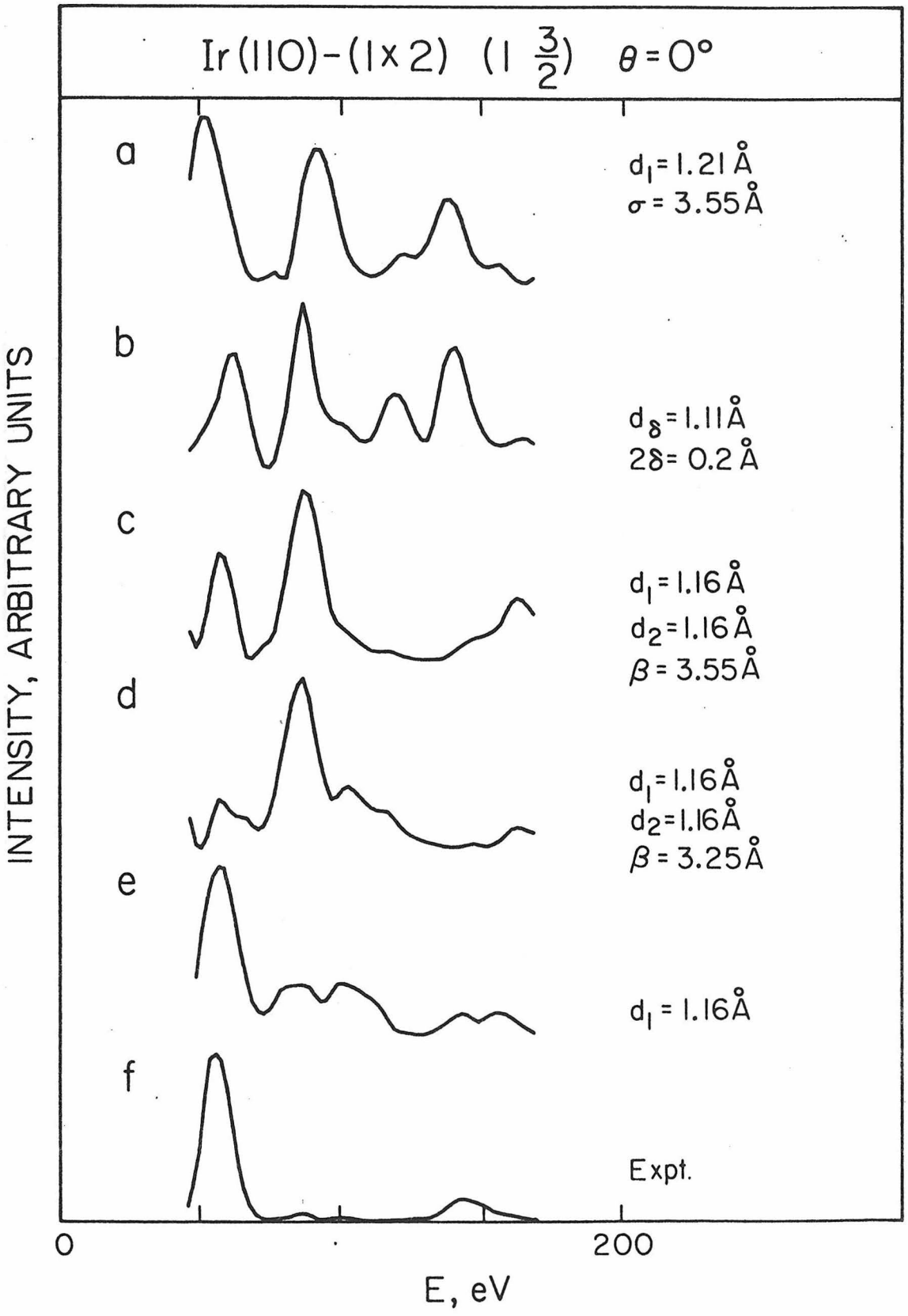
Ir(110)-(1x2) (1 3/2) θ=0°
a
d1= 1.21 Å
σ = 3.55Å
b
dδ= 1.11Å
2δ= 0.2 Å
c
d1= 1.16 Å
d2= 1.16 Å
β = 3.55Å
d
d1= 1.16Å
d2= 1.16Å
β = 3.25Å
e
d1 = 1.16Å
f
Expt.
INTENSITY, ARBITRARY UNITS
0
200
E, eV

Fig. 9

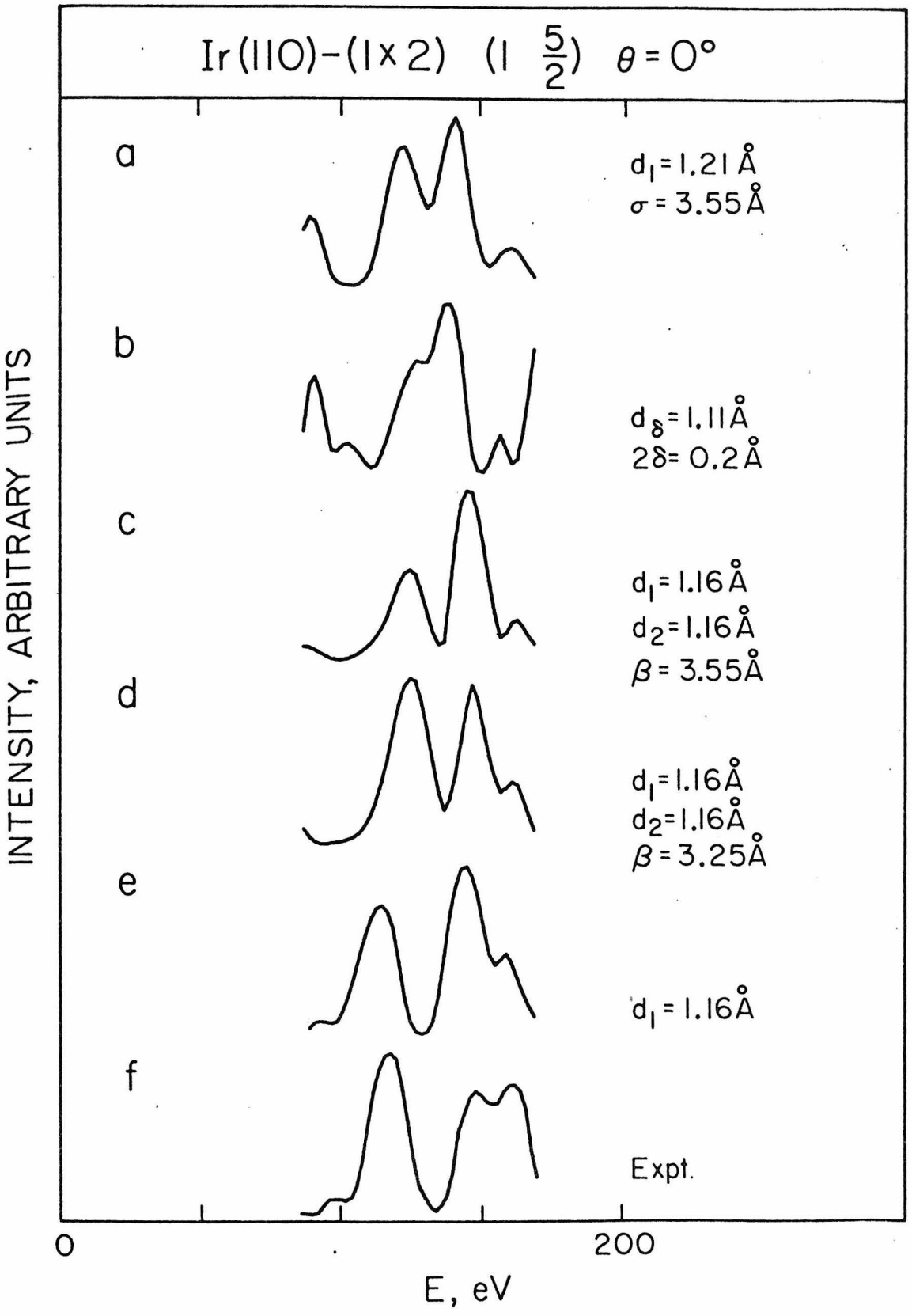
Ir(110)-(1×2) (1 5/2) θ = 0°
a
d1 = 1.21 Å
σ = 3.55 Å
b
dδ = 1.11 Å
2δ = 0.2 Å
c
d1 = 1.16 Å
d2 = 1.16 Å
β = 3.55 Å
d
d1 = 1.16 Å
d2 = 1.16 Å
β = 3.25 Å
e
d1 = 1.16 Å
f
Expt.
INTENSITY, ARBITRARY UNITS
0
200
E, eV

Fig. 10

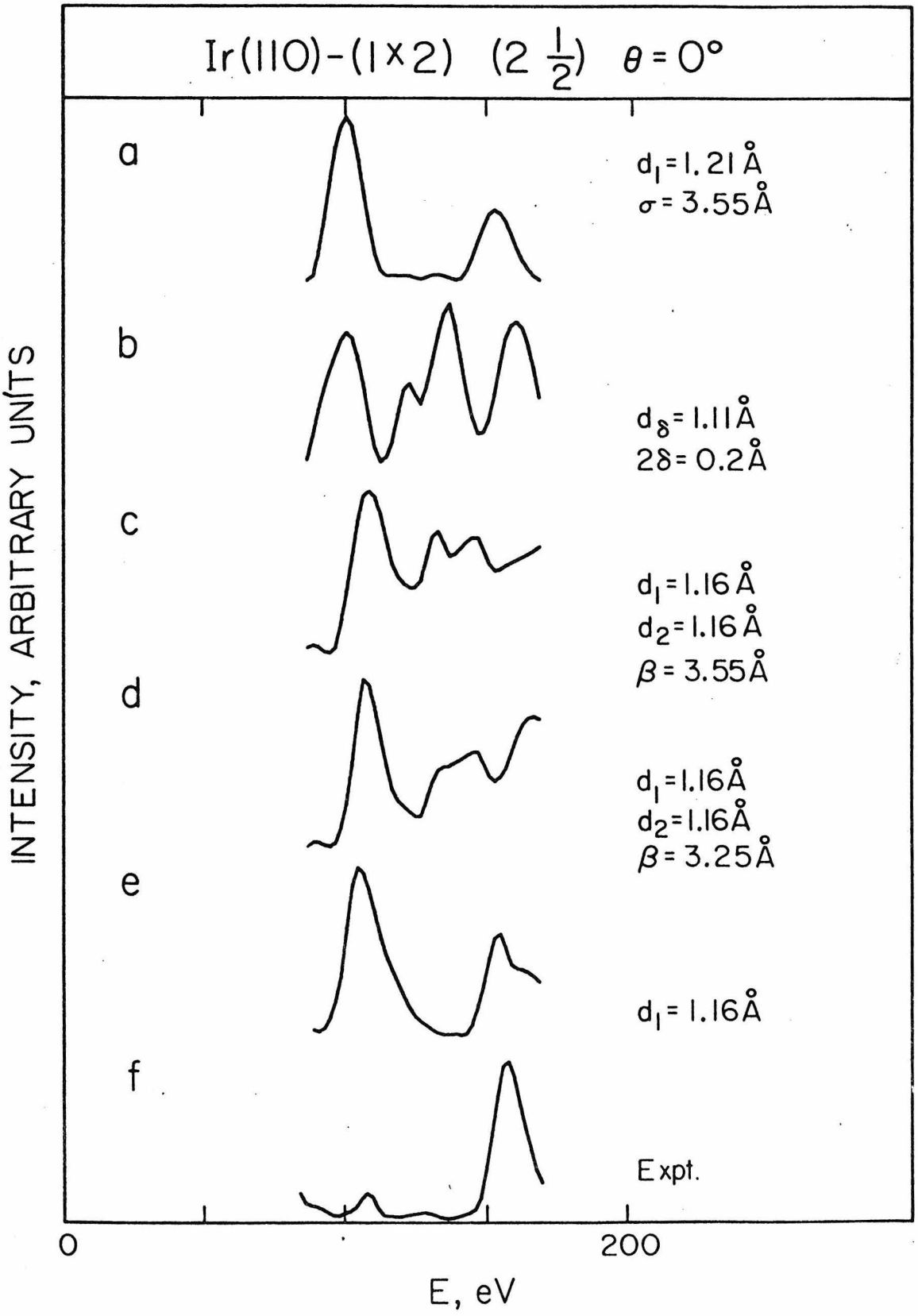
Ir(110)-(1×2) (2 1/2) θ = 0°
a
d1 = 1.21 Å
σ = 3.55 Å
b
dδ = 1.11 Å
2δ = 0.2 Å
c
d1 = 1.16 Å
d2 = 1.16 Å
β = 3.55 Å
d
d1 = 1.16 Å
d2 = 1.16 Å
β = 3.25 Å
e
d1 = 1.16 Å
f
Expt.
INTENSITY, ARBITRARY UNITS
0
200
E, eV

Fig. 11

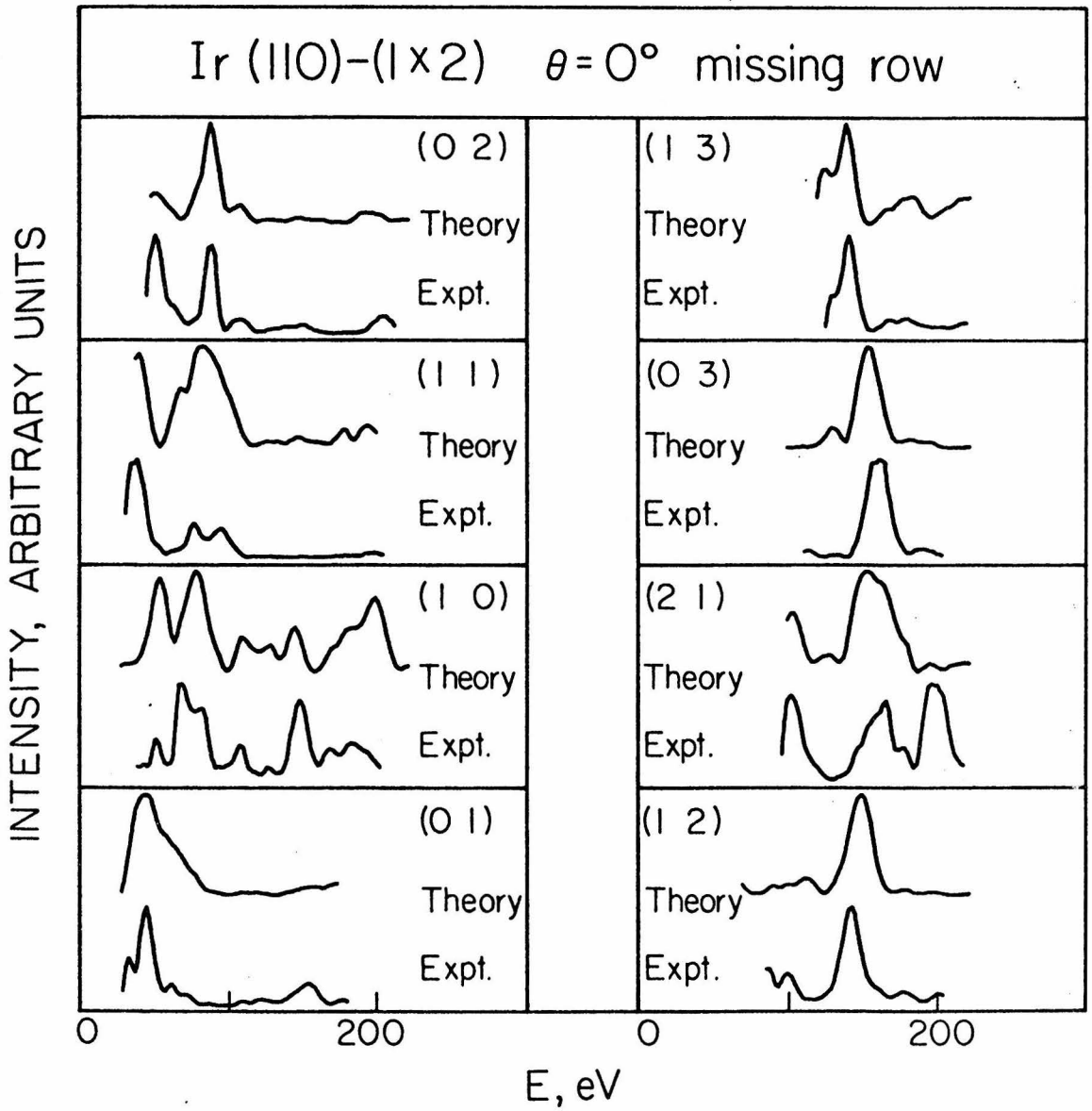
Ir (110)-(1 x 2) θ = 0° missing row
(0 2)
Theory
Expt.
(1 3)
Theory
Expt.
(1 1)
Theory
Expt.
(0 3)
Theory
Expt.
(1 0)
Theory
Expt.
(2 1)
Theory
Expt.
(0 1)
Theory
Expt.
(1 2)
Theory
Expt.
INTENSITY, ARBITRARY UNITS
0
200
0
200
E, eV

Fig. 12

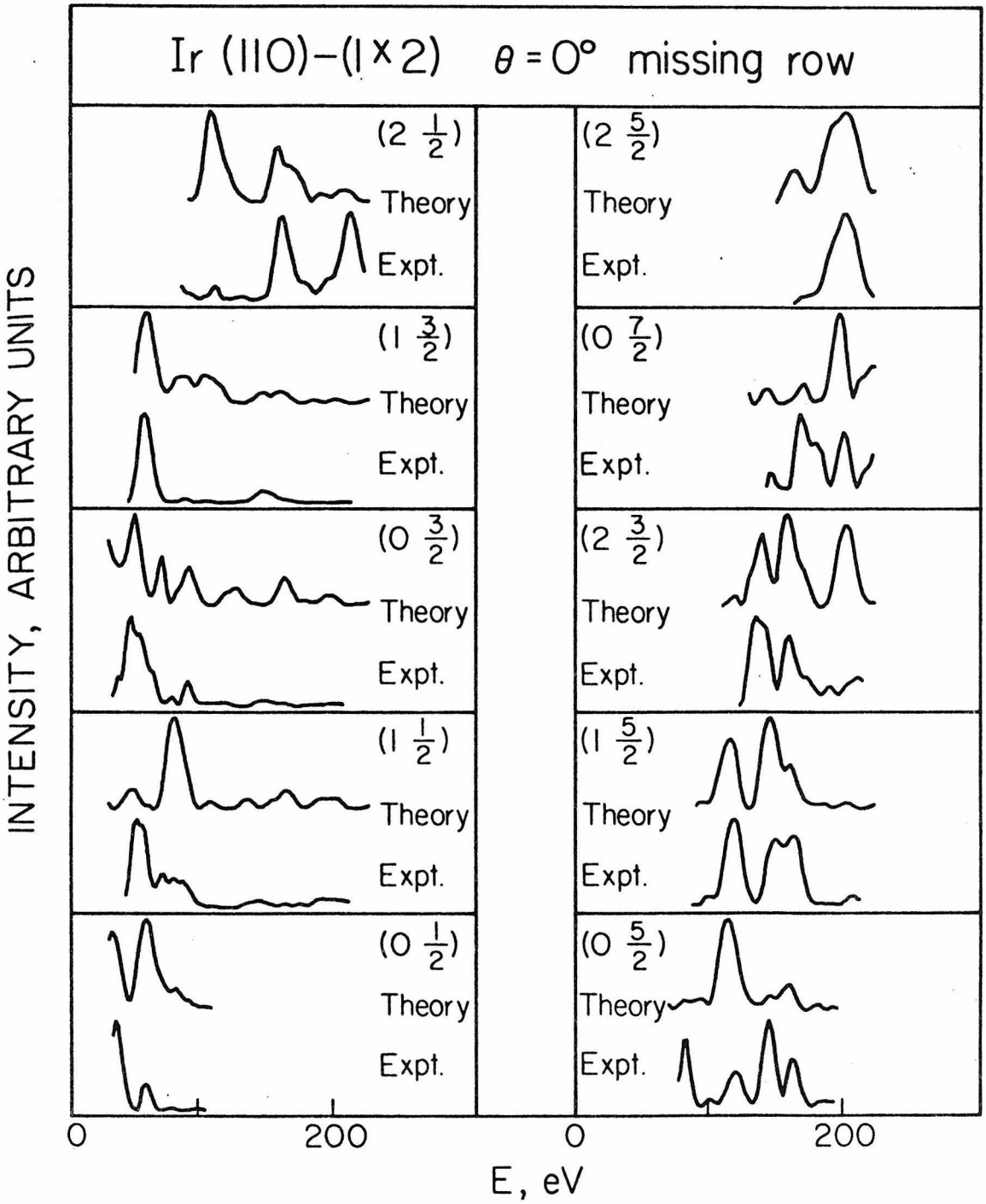
Ir (110)–(1×2) θ = 0° missing row
INTENSITY, ARBITRARY UNITS
(2 1/2)
Theory
Expt.
(2 5/2)
Theory
Expt.
(1 3/2)
Theory
Expt.
(0 7/2)
Theory
Expt.
(0 3/2)
Theory
Expt.
(2 3/2)
Theory
Expt.
(1 1/2)
Theory
Expt.
(1 5/2)
Theory
Expt.
(0 1/2)
Theory
Expt.
(0 5/2)
Theory
Expt.
0
200
0
200
E, eV

Fig. 13

Chapter 3

DETERMINATION OF THE ATOMIC ARRANGEMENT OF THE UNRECONSTRUCTED Ir(110) SURFACE BY LOW-ENERGY ELECTRON DIFFRACTION

by

C.-M. Chan, S. L. Cunningham, K. L. Luke,
W. H. Weinberg and S. P. Withrow

Division of Chemistry and Chemical Engineering
California Institute of Technology
Pasadena, California 91125

Surface Science 78, 15-23 (1978)

Abstract

An Ir(110) - (1x1) surface structure has been prepared by adsorbing ¼ monolayer of oxygen at 850 K on a clean, reconstructed (1x2) surface. Results of the low-energy electron diffraction structure analysis reveal that the oxygen is probably distributed randomly over the crystal surface, and the (1x1) structure is the same as a clean unreconstructed (1x1) structure, with a topmost interlayer Ir spacing of 1.26 ± 0.05 Å. This is equivalent to a contraction of approximately 7.5% of the bulk interlayer spacing of 1.36 Å.

1. Introduction

A microscopic understanding of the atomic structure of reconstructed surfaces presents a very important and interesting problem in the study of solid surfaces. It has been long known that many surfaces have atomic structures different from that obtained by terminating the bulk structure. Examples are the (100) and (111) surfaces of Si, and the (100) and (110) surfaces of Ir, Pt and Au. It has been found that the deposition of impurities on some of the reconstructed surfaces permits a relaxation of the reconstructed structure back to the (1x1) structure, e.g., H on Si (100) (1), and Te on Si (111) (2).

The purpose of the present work is to study, by LEED, the atomic arrangement of the Ir(110) - (1x1) surface structure resulting from oxygen deposition on the reconstructed (1x2) clean surface. The results from the analysis of the (1x1) structure will provide some useful insights concerning the atomic structure of the clean reconstructed (1x2) surface.

The experimental procedures are described in Sec. 2; the results are presented in Sec. 3; the analysis in Sec. 4; and the discussion in Sec. 5. A brief synopsis is presented in Sec. 6.

2. Experimental Procedure

The experiments were performed in a UHV chamber which has a base pressure less than 1×10^{-10} torr. The chamber is equipped with a four-grid, post acceleration display LEED system containing a rotatable Faraday cup for beam intensity measurements. The chemical composition of the crystal surface is determined by Auger spectroscopy using a single pass cylindrical mirror electron energy analyzer. Two sets of Helmholtz coils were used to reduce the effect of the earth's magnetic field on the electron beam during LEED measurements. Crystal temperatures up to 1600 K could be achieved by resistive heating. The crystal temperature was measured with a 5% Re/95% W and 26% Re/74% W thermocouple which was spotwelded to the back of the crystal.

Intensity-voltage (I-V) profiles for eight different non-specular beams at normal incidence were measured at approximately 2 eV intervals. All I-V beam profiles have been normalized to unit incident beam current. The achievement of normal incidence was verified by the satisfactory agreement between equivalent non-specular beams, as shown in Fig. 1. The beams are indexed so that the longer side of the real space unit cell is the x direction as shown explicitly in Fig. 2.

3. Results

It has been shown that a clean Ir(110) surface exhibits a reconstructed (1x2) surface structure (3), the real space unit cell and the LEED pattern of which are shown in Figs. 2a and 3a, respectively, assuming a missing row model. The (1x2) structure was prepared in the same way as that described elsewhere (4). When the crystal was heated in 5 x 10^{-8} torr of O_2 at 850 K for approximately two minutes, a (1x1) surface structure was formed, the unit cell and LEED pattern of which are shown in Figs. 2b and 3b, respectively. The formation of the (1x1) structure is more rapid at higher temperatures. Upon subsequent cooling to room temperature, streaks in the [001] direction (between rows) appeared as shown in Fig. 3c. This is thought to be caused by an excess amount of oxygen on the surface. A stable and sharp (1x1) structure was obtained by subjecting the surface to several Langmuirs (1L≡10^{-6} torr-sec) of CO and flashing the crystal to 575 K. This (1x1) structure is stable to about 1125 K in vacuum, and it is stable to 675 K in 5 x 10^{-8} torr of CO. Streaks in the [001] direction (between spots), as shown in Fig. 3d, were observed to appear after the crystal was heated above 1125 K in vacuum or above 675 K in 5 x 10^{-8} torr of CO for one to two minutes.

The amount of surface oxygen which was required to form the (1x1) structure from a clean (1x2) structure was estimated using Auger electron spectroscopy. The peak-to-peak amplitude of the differentiated Auger line (in the dN(E)/dE curve) of the oxygen KLL transition on the (1x1) surface is about four times less than that of a (1x2) surface fully saturated with oxygen to monolayer coverage. A monolayer coverage of oxygen is obtained by exposing the clean (1x2) surface to approximately 30 L of oxygen (5). Hence, approximately ¼ monolayer of oxygen is required for the formation of a (1x1)

structure from a clean (1x2) structure. This conclusion is also in agreement with independent contact potential difference measurements performed in this laboratory (5). Consequently, randomly adsorbed oxygen atoms stabilize the formation of an unreconstructed Ir(110) - (1x1) surface which is amenable to a structural analysis by LEED.

4. Analysis

A perturbation scheme termed the layer doubling method (6) is used for the calculation of LEED I-V spectra. The oxygen atoms are assumed to be randomly and evenly distributed over the surface. Within the framework of this assumption, the presence of oxygen on the surface would not give any contribution to the structure of the I-V spectra but could possibly modulate the intensities of the experimental I-V spectra. Hence, the presence of oxygen on the surface was neglected in the calculations of the I-V spectra, and the calculations were performed as for a clean, unreconstructed Ir(110) - (1x1) surface structure. The LEED I-V spectra for the Ir(110)-(1x1) structure were calculated at a normal angle of incidence for eight non-specular beams, namely, the (01), (10), (11), (02), (20), (12), (21) and (22) beams.

The atomic potential for Ir is a band structure potential obtained from Arbman and Hörnfelt (7) and includes full Slater exchange. The calculations were carried out with eight phase shifts, properly modified for vibrations. The real part of the inner potential (the muffin tin zero) was assumed to be 15 eV, and this quantity was allowed to change by a rigid shift of the energy scale for the comparison between theoretical and experimental I-V spectra. An energy-independent imaginary part of the inner potential of 5 eV was used to represent all inelastic processes. The bulk Debye temperature used in the calculations was 280 K, and an enhancement factor of 1.4 was chosen for the surface mean-square vibrational amplitudes. The crystal temperature was 300 K. The calculations were initiated at 40 eV and were continued in increments of 5 eV up to 240 eV. Symmetry properties of the beams at normal incidence were exploited in the calculations, e.g., at 190 eV, an equivalent of 40 beams was used in the calculations.

The topmost layer of the Ir(110) surface was allowed to relax from -15% (% contraction of the bulk interlayer spacing) to +15% (expansion) in steps of 5%. It was found that the experimental I-V spectra have the best agreement with the theoretical I-V spectra at a 5 to 10% contraction with an inner potential of 8 eV. The latter is in agreement with the value found previously (8). Figs. 4-11 show comparisons between the theoretical I-V spectra modified with an inner potential of 8 eV and the experimental I-V spectra. Based on the above comparisons, it may be concluded that the topmost layer of an unreconstructed Ir(110) - (1x1) structure is contracted by 7.5 ± 5%.

5. Discussion

The generally good agreement between theoretical and experimental I-V spectra, and the fact that only ¼ monolayer of oxygen is present on the surface rule out the possibility of the formation of any kind of oxide of iridium exhibiting a (1x1) structure. This agreement, assuming a clean unreconstructed (1x1) structure having 5-10% contraction, also strongly supports the assumption that oxygen atoms are randomly and evenly distributed over the surface, stabilizing the (1x1) structure.

Upon acceptance of such a model, it is possible to discuss a kinetically activated process for the formation of the (1x1) structure from a clean (1x2) structure. The fact that the formation of the (1x1) structure occurs at about 850 K or above indicates that thermal energy is needed for the motion of iridium atoms. The presence of the oxygen atoms on the surface must favor the formation of the (1x1) structure due to a reduction of the Gibbs energy of the surface.

At temperatures of 850 K, the formation of the (1x1) structure still takes approximately two minutes, which is a long time for atomic rearrangements. Upon removing oxygen by CO at about 675 K, or increasing the temperature of the crystal to 1125 K, the (1x1) structure does not revert to the (1x2) structure. Rather, the LEED pattern shows the formation of streaks between spots along the [001] direction as in Fig. 3d. Annealing at temperatures higher than 1600 K is required for the streaky (1x1) structure to resume the (1x2) structure. This fact may indicate that a substantial atomic rearrangement has occurred in the transformation of the (1x2) structure to the (1x1) structure. Different atomic models have been suggested for the atomic arrangement of

an fcc (110) reconstructed surface. The three most common and simple ones are the missing row model, the paired rows model, and the buckled surface model. In the missing row model, alternate rows of atoms are absent on the surface. The paired rows model suggests every two adjacent rows of first layer atoms pair up to form one row. In the buckled surface model, adjacent rows of first layer atoms are relaxed in opposite directions along the direction perpendicular to the crystal surface. Based on the available experimental evidence, the missing row model or the paired rows model would seem more likely as describing the atomic arrangement of the clean (1x2)structure compared to the buckled surface model. The former two models involve a more extensive atomic rearrangement for the transformation of the (1x2) structure to the (1x1) structure. Work is in progress to determine the structure of the reconstructed (1x2) surface.

6. Synopsis

The Ir(110) - (1x1) structure formed by the deposition of ¼ monolayer of oxygen on a clean, reconstructed Ir(110) - (1x2) structure is found to have a structure which is the same as the bulk structure, with a topmost interlayer spacing of 1.26 ± 0.05 Å. This is equivalent to a contraction of approximately 7.5% of the bulk interlayer spacing of 1.36 Å. The presence of the oxygen atoms on the surface stabilizes the formation of an unreconstructed (1x1) structure. Experimental evidence indicates that the transformation of the (1x2) structure to the (1x1) structure may involve an extensive atomic arrangement on the surface.

Acknowledgments

We gratefully acknowledge the assistance of Dr. M. A. Van Hove in setting up the computer programs for the dynamical calculations, and the financial support of this research by the Army Research Office.

References

1. S. J. White and D. P. Woodruff, Surface Sci. 63, 254 (1977).
2. H. D. Shih, F. Jona, D. W. Jepsen and P. M. Marcus, Phys. Rev. Letters 37, 1622 (1976).
3. K. Christmann and G. Ertl, Zeitschrift fur Naturforschung 28a, 1144 (1973).
4. C.-M. Chan, S. L. Cunningham, E. D. Williams, M. A. Van Hove and W. H. Weinberg (in preparation).
5. J. L. Taylor, D. E. Ibbotson and W. H. Weinberg (to be published).
6. J. B. Pendry, Low-Energy Electron Diffraction, Academic, London, 1974.
7. G. O. Arbman and S. Hornfelt, J. Phys. F 2, 1033 (1972).
8. C.-M. Chan, S. L. Cunningham, M. A. Van Hove, W. H. Weinberg and S. P. Withrow, Surface Sci. 66, 394 (1977).

Figure Captions

Fig. 1 Experimental I-V spectra for two sets of beams which should be equivalent at normal incidence on the Ir(110) - (1x1) surface.

Fig. 2(a) Schematic hard-sphere model of the unreconstructed Ir(110)-(1x2) structure assuming the missing row model.

(b) Schematic hard-sphere model of the unreconstructed Ir(110)-(1x1) structure.

Fig. 3(a) The reciprocal space lattice of Fig. 2a.

(b) The reciprocal space lattice of Fig. 2b.

(c) The reciprocal space lattice of Fig. 2b with streaks between rows in the [001] direction.

(d) The reciprocal space lattice of Fig. 2b with streaks between spots in the [001] direction.

Fig. 4 Comparison between the theoretical I-V spectra modified with an inner potential of 8 eV for the topmost layer spacing ranging from a -15% (contraction) to a +15% (expansion) compared to the bulk spacing, and the experimental I-V spectrum of the (01) beam from the Ir(110)-(1x1) surface. $\theta = 0^{o}$ corresponds to normal incidence.

Fig. 5 As in Fig. 2 except the (10) beam.

Fig. 6 As in Fig. 2 except the (11) beam.

Fig. 7 As in Fig. 2 except the (02) beam.

Fig. 8 As in Fig. 2 except the (20) beam.

Fig. 9 As in Fig. 2 except the (12) beam.

Fig.10 As in Fig. 2 except the (21) beam.

Fig.11 As in Fig. 2 except the (22) beam.

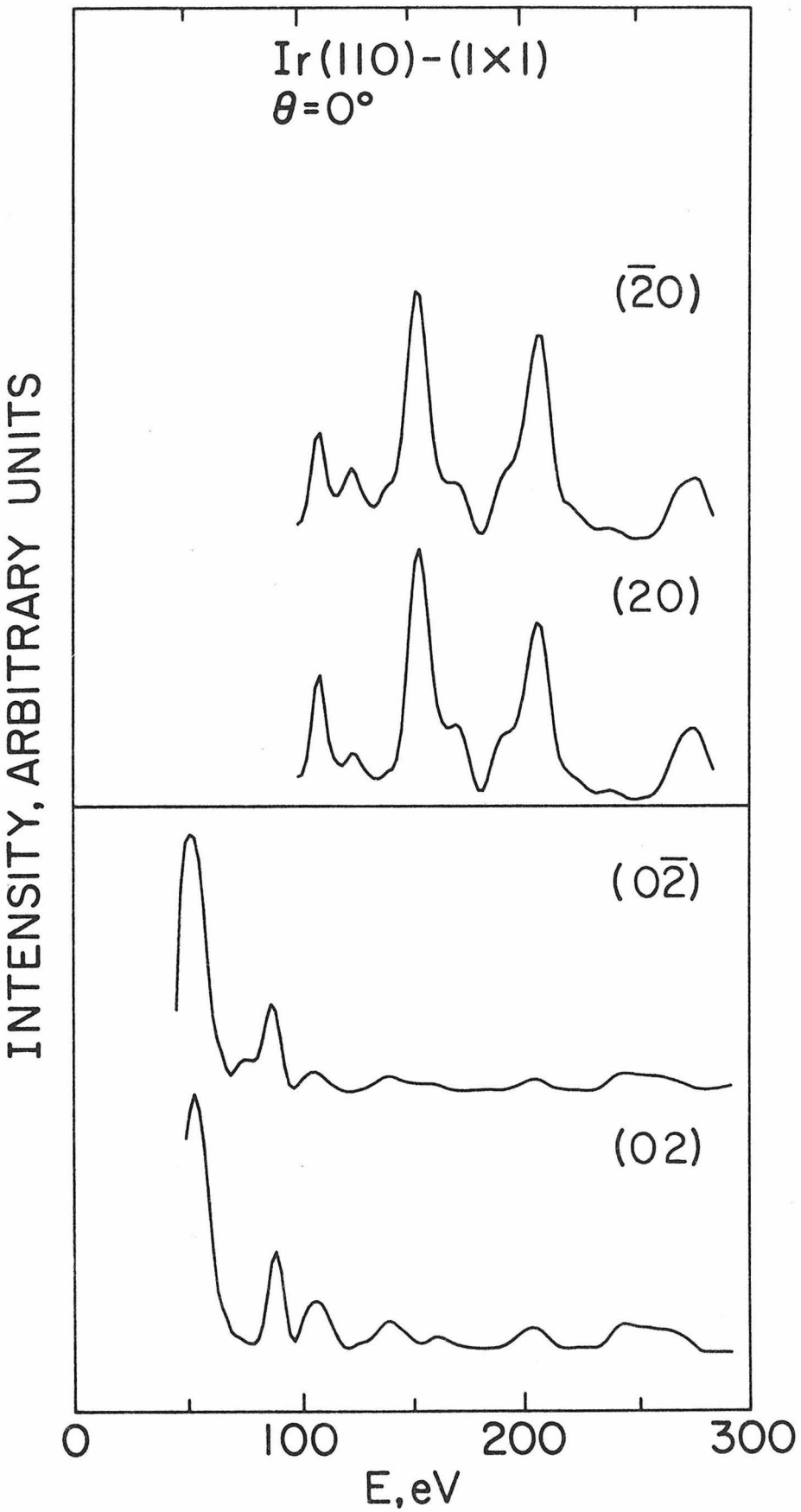
Ir(110)-(1×1)
θ=0°
(2̄0)
(20)
(02̄)
(02)
INTENSITY, ARBITRARY UNITS
0
100
200
300
E, eV

Fig. 1

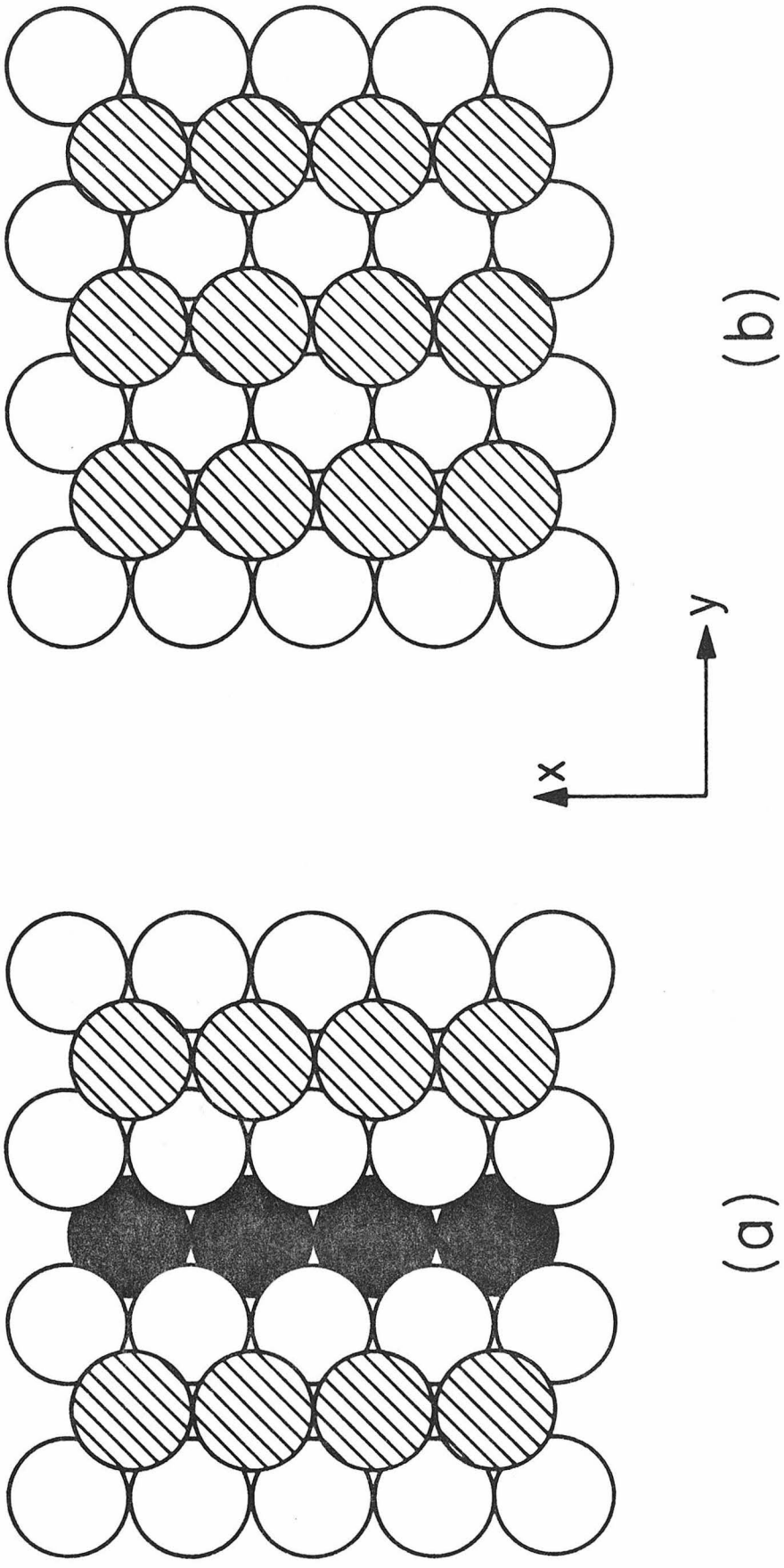

Fig. 2

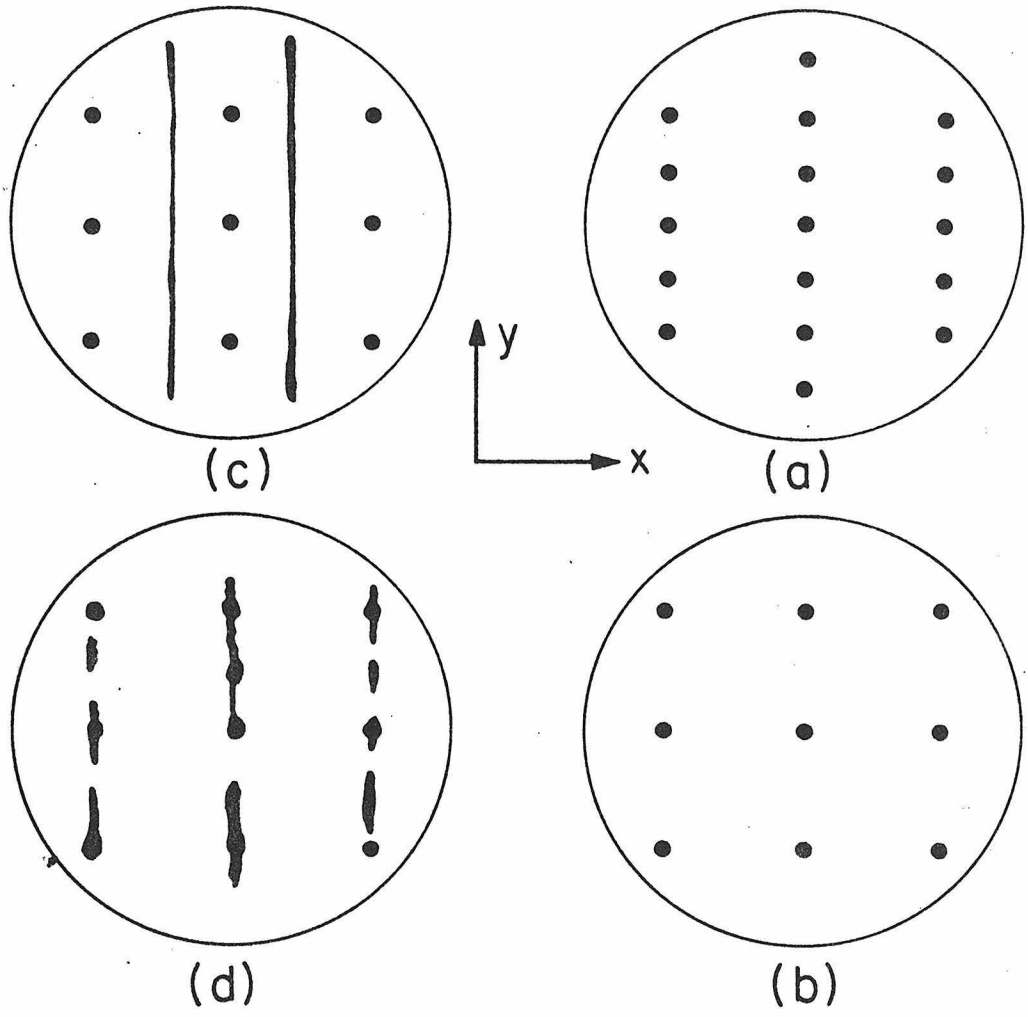

Fig. 3

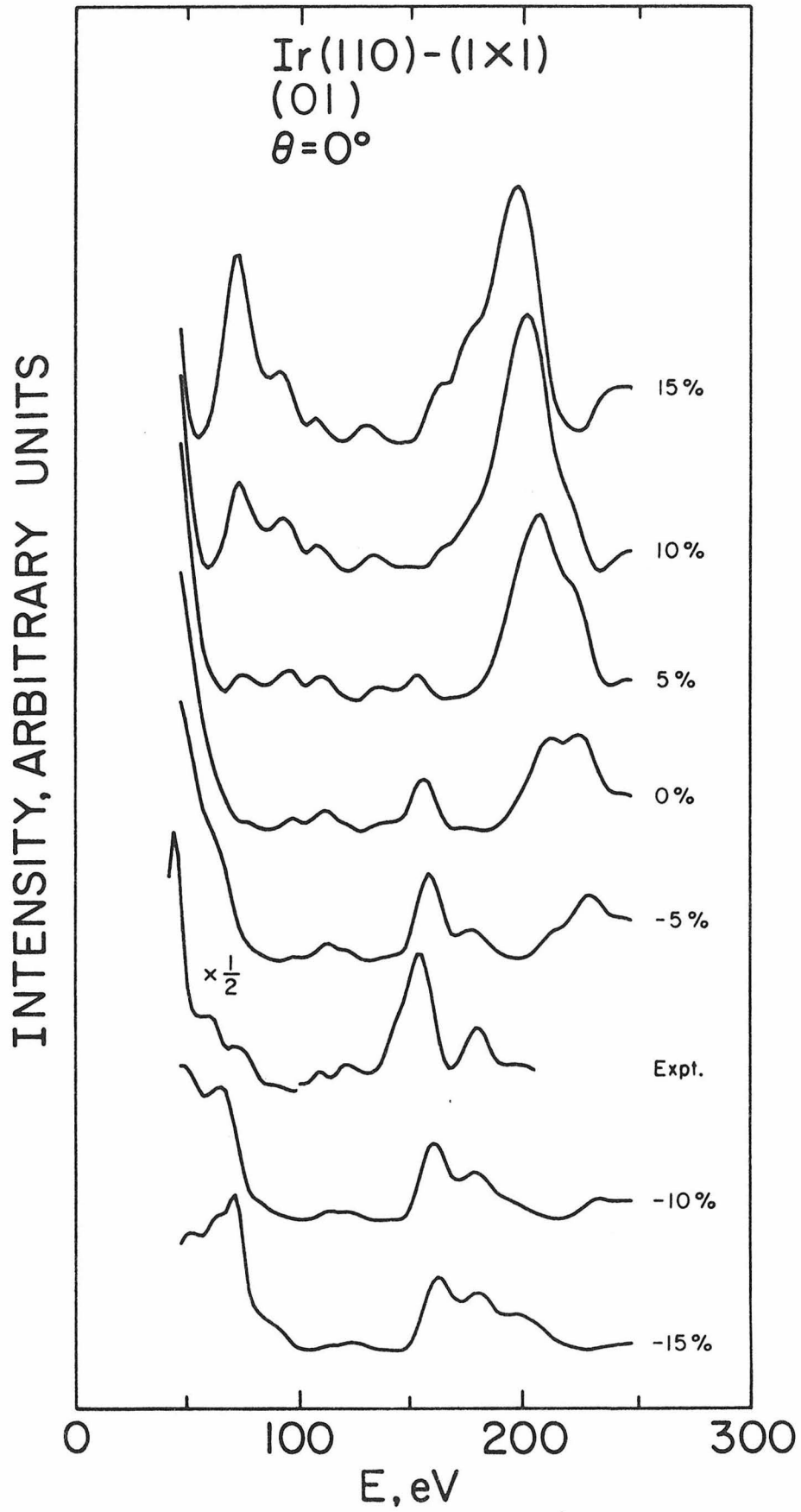
Ir(110)-(1×1)
(01)
θ=0°
INTENSITY, ARBITRARY UNITS
15%
10%
5%
0%
-5%
×1/2
Expt.
-10%
-15%
0
100
200
300
E, eV

Fig. 4

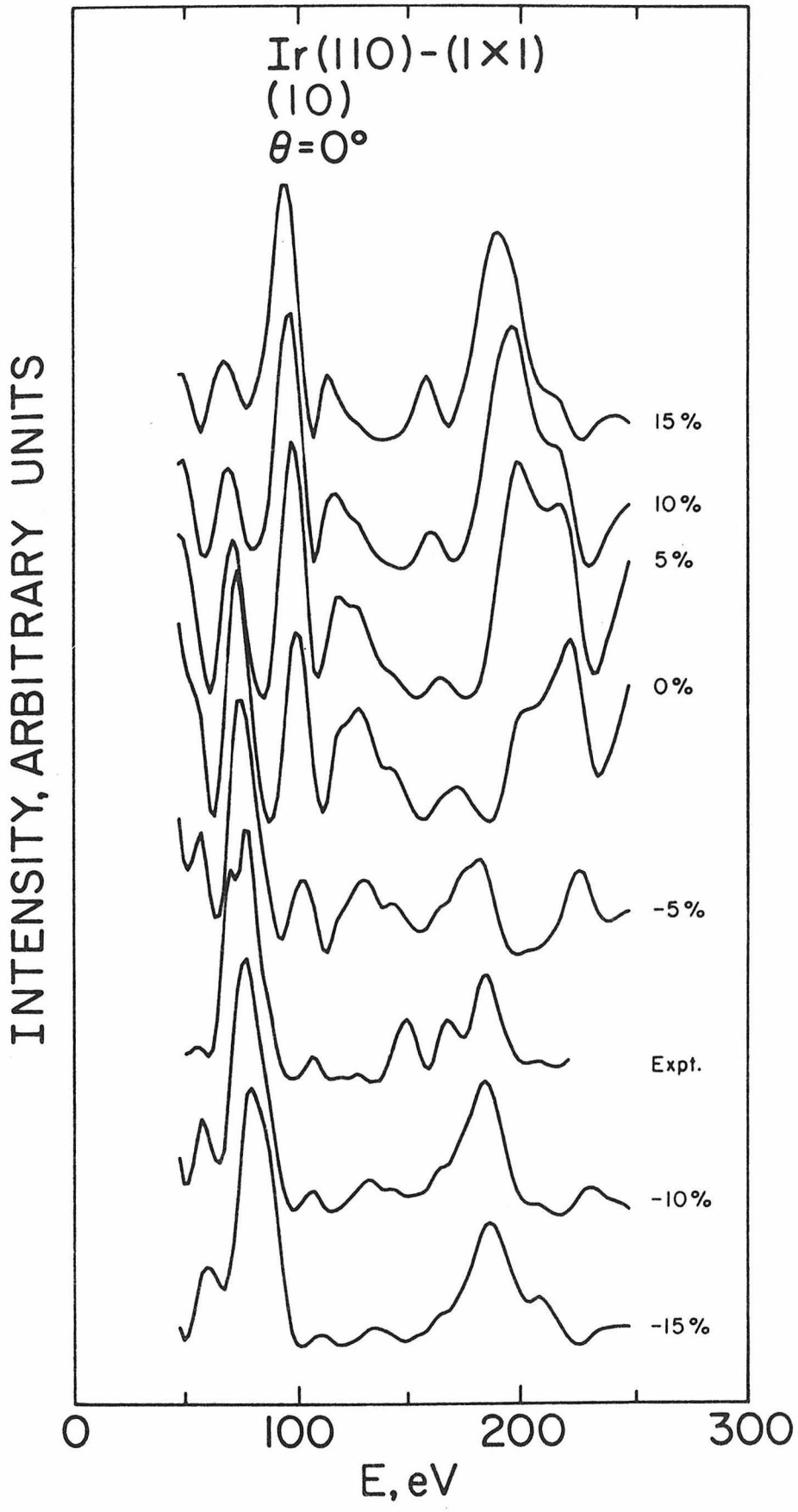
Ir(110)-(1×1)
(10)
θ=0°
INTENSITY, ARBITRARY UNITS
15%
10%
5%
0%
-5%
Expt.
-10%
-15%
0
100
200
300
E, eV

Fig. 5

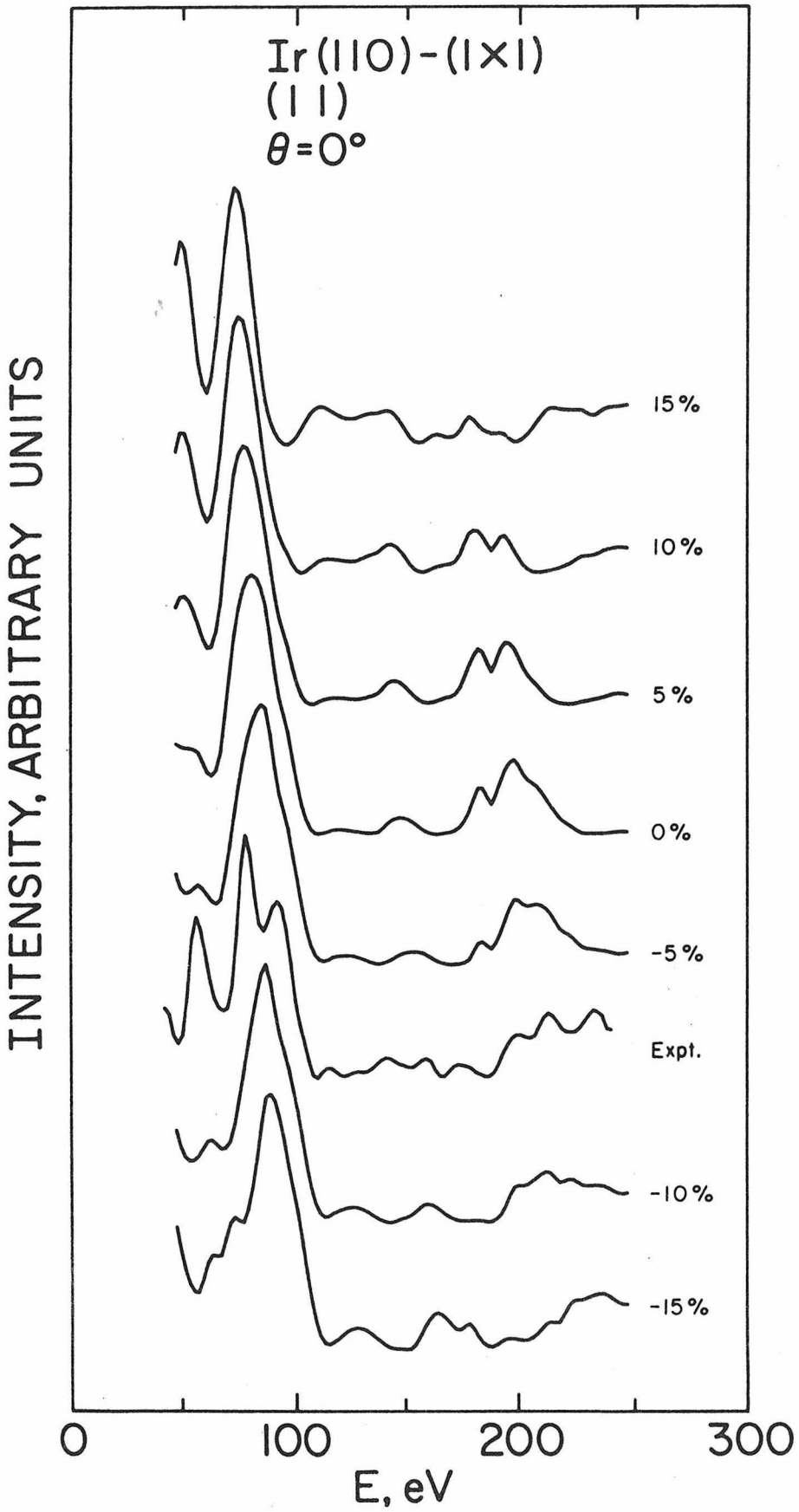
Ir(110)-(1×1)
(1 1)
θ=0°
15%
10%
5%
0%
-5%
Expt.
-10%
-15%
INTENSITY, ARBITRARY UNITS
0
100
200
300
E, eV

Fig. 6

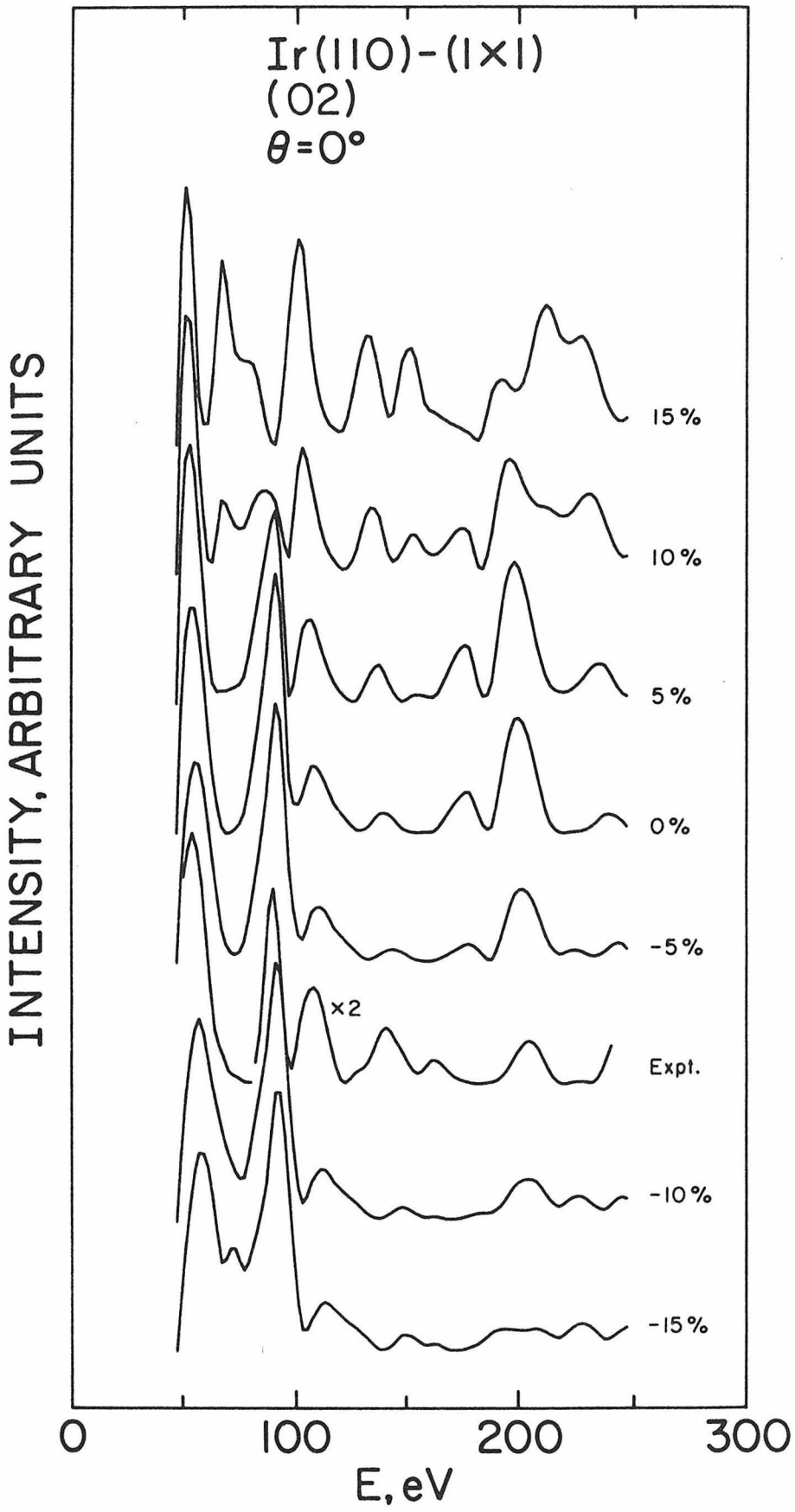
Ir(110)-(1×1)
(02)
θ=0°
15%
10%
5%
0%
-5%
×2
Expt.
-10%
-15%
INTENSITY, ARBITRARY UNITS
0
100
200
300
E, eV

Fig. 7

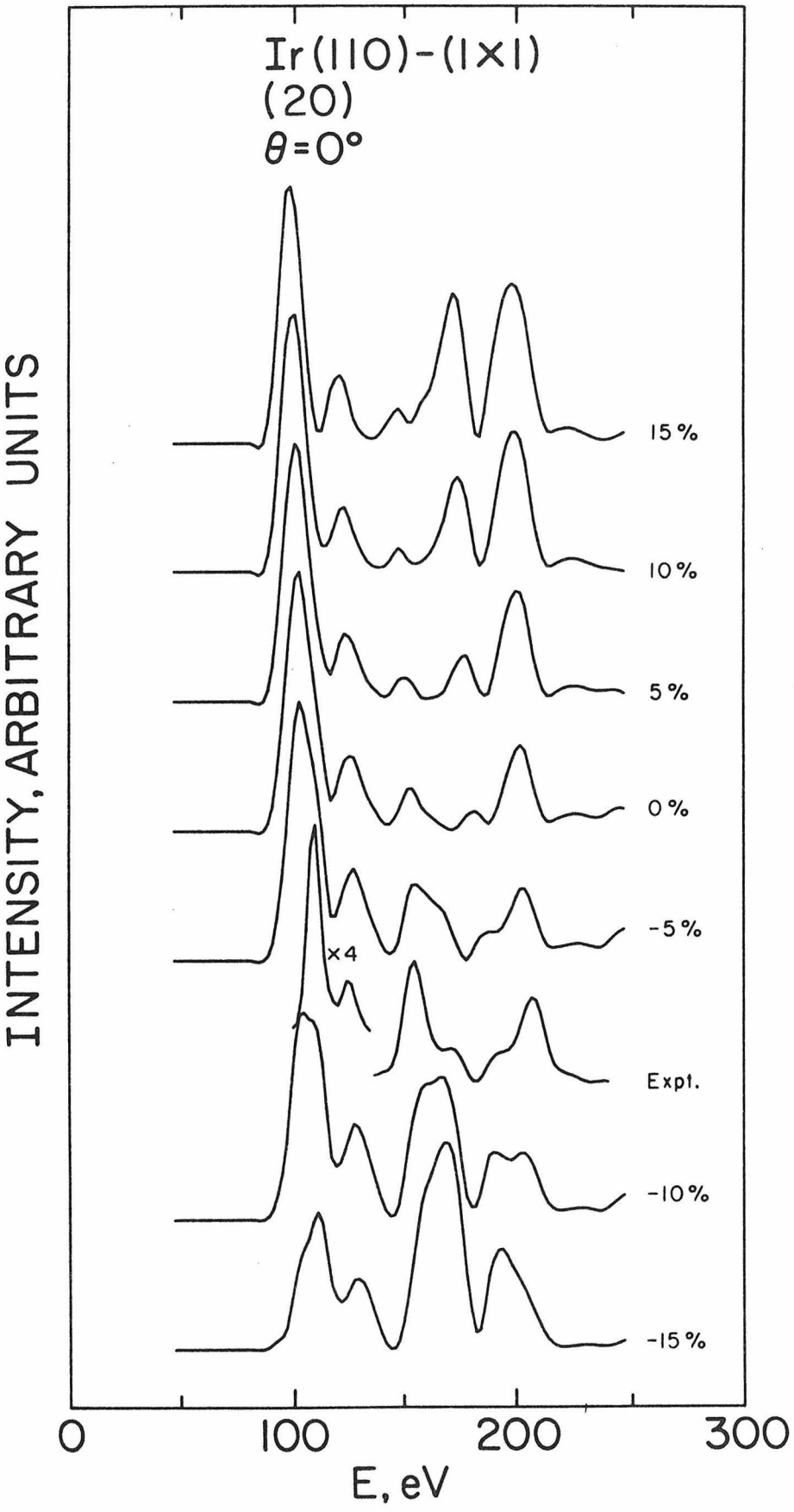
Ir(110)-(1×1)
(20)
θ=0°
INTENSITY, ARBITRARY UNITS
15%
10%
5%
0%
-5%
×4
Expt.
-10%
-15%
0
100
200
300
E, eV

Fig. 8

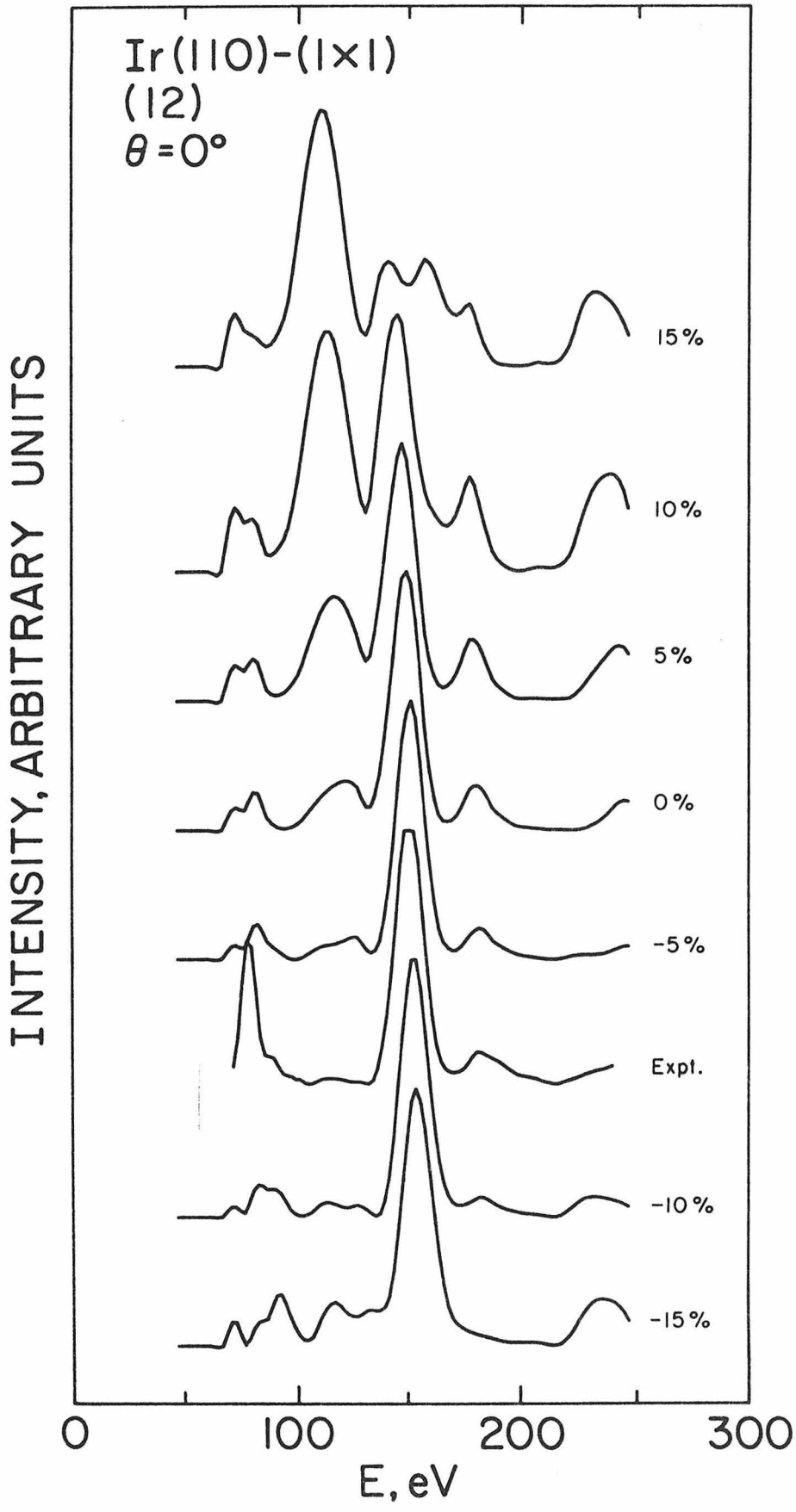
Ir(110)-(1×1)
(12)
θ = 0°
15%
10%
5%
0%
-5%
Expt.
-10%
-15%
INTENSITY, ARBITRARY UNITS
0
100
200
300
E, eV

Fig. 9

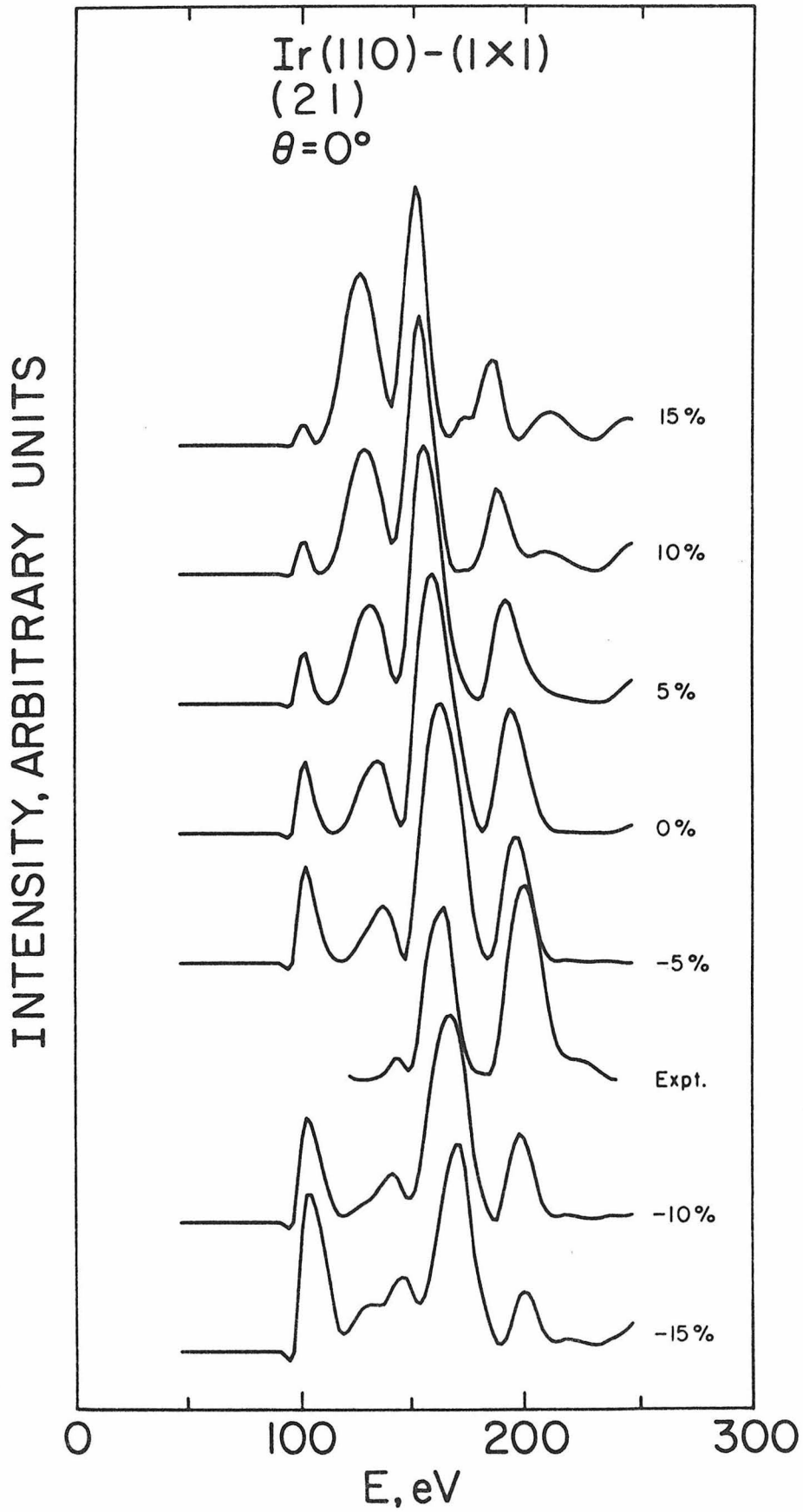
Ir(110)-(1×1)
(21)
θ=0°
INTENSITY, ARBITRARY UNITS
15%
10%
5%
0%
-5%
Expt.
-10%
-15%
0
100
200
300
E, eV

Fig. 10

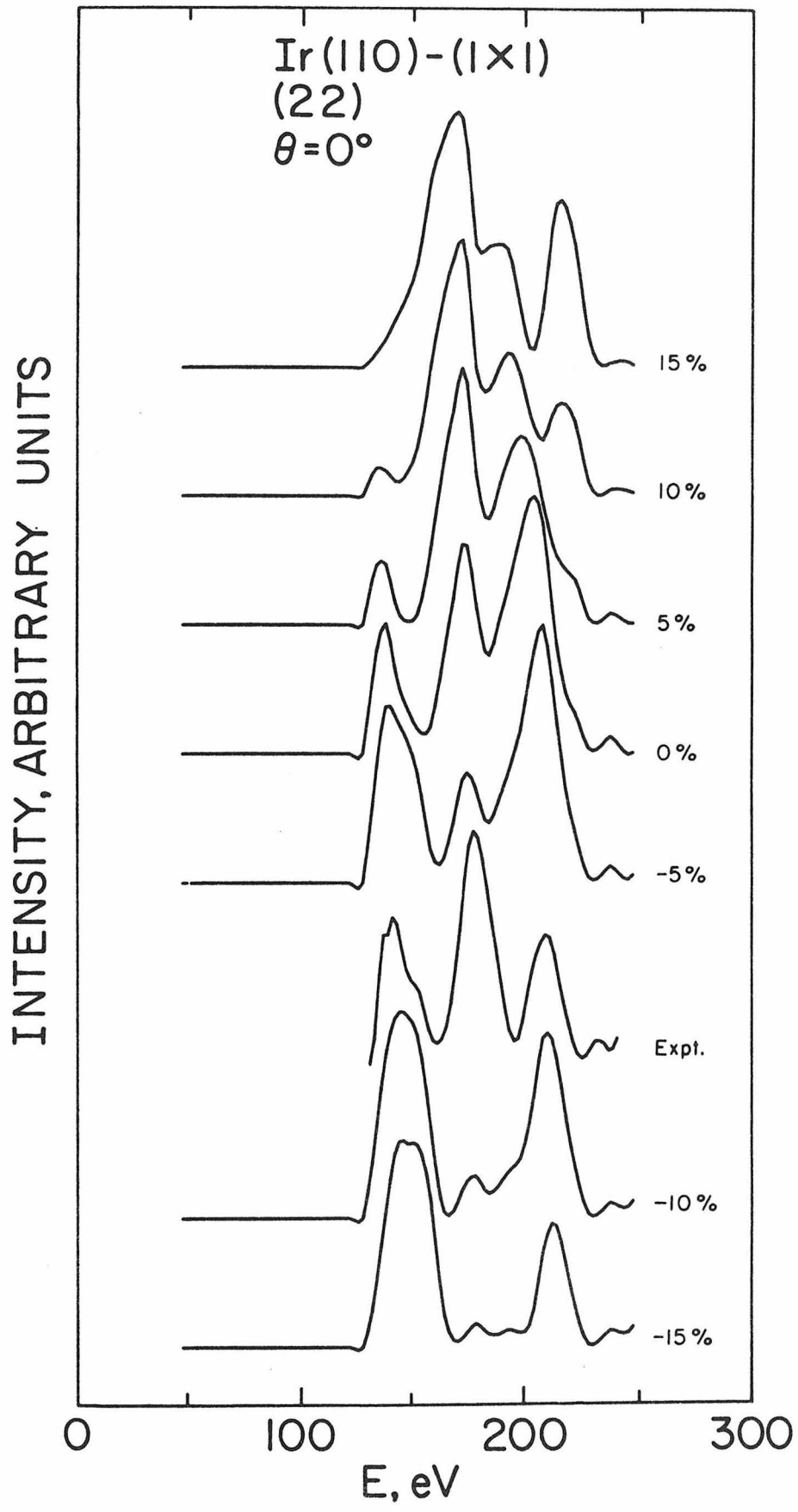
Ir(110)-(1×1)
(22)
θ=0°
INTENSITY, ARBITRARY UNITS
15%
10%
5%
0%
-5%
Expt.
-10%
-15%
0
100
200
300
E, eV

Fig. 11

Chapter 4

A STRUCTURAL DETERMINATION OF THE UNRECONSTRUCTED AND THE RECONSTRUCTED (110) SURFACES OF IRIDIUM

by

C.-M. Chan, K. L. Luke, M. A. Van Hove,
W. H. Weinberg and E. D. Williams

Division of Chemistry and Chemical Engineering
California Institute of Technology
Pasadena, California 91125

Journal of Science and Vacuum Technology 16, 000 (1979)

Abstract

An Ir(110)-(1x1) surface has been prepared by adsorbing 1/4 monolayer of oxygen at 850 K on a clean, reconstructed (1x2) surface. Good agreement was achieved between theoretical and experimental intensity-voltage (I-V) spectra for a surface model in which the oxygen is randomly and uniformly distributed over the crystal surface, and the (1x1) structure is the same as for a clean unreconstructed (1x1) surface with a topmost interlayer spacing of 1.26 ± 0.05 Å. Three different models have been tested for the reconstructed Ir(110)-(1x2) surface, namely, the missing row model, the paired rows model and the buckled surface model. Based on the comparison between experimental data (consisting of ten half-order beams and eight integral-order beams) and the theoretical calculations, the missing row model with a topmost interlayer spacing of 1.22 ± 0.07 Å is the most satisfactory model tested.

1. Introduction

Surface reconstruction presents a very important and interesting problem in the study of solid surfaces. Many surfaces have an atomic structure different from that obtained simply by terminating the bulk structure. Various studies have failed heretofore to determine the structure of any reconstructed surface.

The purpose of the present work is to study, by LEED, the atomic arrangements of both the Ir(110)-(1x1) surface resulting from oxygen deposition on the reconstructed (1x2) clean surface as well as the reconstructed (1x2) clean surface.

2. Experimental Procedure

The experiments were performed in a UHV chamber which has a base pressure less than 1×10^{-10} torr. The chamber is equipped with several probes for surface analysis, including LEED optics, a quadrupole mass spectrometer and a single pass cylindrical mirror energy analyzer for Auger spectroscopy. Two sets of Helmholtz coils were used to reduce the effect of the earth's magnetic field on the electron beam during LEED measurements. Crystal temperatures up to 1600 K could be achieved by resistive heating. The crystal temperature was measured with a 5% Re/95% W and 26% Re/74% W thermocouple which was spotwelded to the back of the crystal.

The Ir sample was cut from a single crystal and aligned within $\frac{1}{2}^{\circ}$ of the (110) orientation by the back-reflection Laue X-ray method. Both sides of the crystal were polished mechanically using standard techniques. After

Ar^+ bombardment and a series of treatments in 5 x 10^{-8} torr oxygen at 800 K, followed by brief annealing in vacuum at 1600 K, the surface was shown to contain less than 2% carbon and no other impurities detectable by Auger electron spectroscopy. The clean (110) surface, after further annealing at 1600 K in vacuum, exhibited a (1x2) superstructure with no detectable impurities present.

I-V beam profiles were measured at normal incidence at approximately 2 eV intervals using a rotatable Faraday cup collector. All I-V beam profiles have been normalized to unit incident beam current. The achievement of normal incidence was verified by the satisfactory agreement between equivalent non-specular beams. The beams are indexed so that the longer side of the real space unit cell is the y-direction. The real space unit cell and the LEED pattern of both the (1x1) and (1x2) structures are shown in Fig. 1.

3. Ir(110)-(1x1) Surface

When the clean reconstructed (1x2) surface of Ir(110) is heated in 5 x 10^{-8} torr oxygen at 850 K for approximately two minutes, a (1x1) surface structure is formed (1). The amount of surface oxygen required to form the (1x1) structure from a clean (1x2) structure was estimated using Auger electron spectroscopy to be 1/4 monolayer. This conclusion is in agreement with independent contact potential difference measurements performed in this laboratory (2). Intensity-voltage profiles for eight different non-specular beams of the (1x1) surface structure were measured at normal incidence at approximately 2 eV intervals.

A convergent perturbative scheme (3) known as the layer-doubling method was used to calculate LEED intensity-voltage spectra for the Ir(110)-(1x1) structure at normal incidence for the eight non-specular beams. The oxygen atoms were assumed to be distributed randomly and uniformly over the surface, so that the presence of oxygen on the surface would not contribute to the structure of the I-V spectra but could possibly modulate the spectral intensities. Hence, the presence of oxygen on the surface was neglected in the calculations of the I-V spectra, and the calculations were performed as for a clean, unreconstructed Ir(110)-(1x1) surface structure. The atomic potential used for Ir is a band structure potential (4) and includes full Slater exchange. The real part of the inner potential was assumed to be 15 eV, and this quantity was allowed to change by a rigid shift of the energy scale for the comparisons between theoretical and experimental I-V spectra. A constant inelastic damping of 5 eV was used. Symmetry properties of the beams at normal incidence were exploited in the calculations. LEED I-V spectra were calculated for topmost layer spacings of the Ir(110)-(1x1) surface which were varied from - 15% (% contraction of the bulk interlayer spacing of 1.36 Å) to + 15% (expansion) in steps of 5%.

Comparisons between theory and experiment show that the best agreement occurs with a 5 to 10% contraction and a modified inner potential of 8 eV. The experimental and calculated spectra are shown in Fig. 2. The good agreement between the experiment and theory further justifies the assumption that the oxygen atoms are distributed randomly and uniformly over the surface, stabilizing the (1x1) structure.

4. Ir(110)-(1x2) Surface

It has been shown that a clean Ir(110) surface displays a (1x2) structure (5,6). Different models for this reconstructed surface have been proposed. The three simplest and most common ones are the missing row model, the paired rows model, and the buckled surface model. Fig. 3 shows schematic hard-sphere drawings of these three models proposed for the reconstructed Ir(110)-(1x2) surface. In the missing row model, alternate rows of atoms are absent on the surface. The paired rows model suggests that every two adjacent rows of first layer atoms are paired to form one row. In the buckled surface model, adjacent rows of first layer atoms are relaxed in opposite directions perpendicular to the crystal surface. Previous investigations of the unreconstructed Ir(110)-(1x1) surface (1) indicate that the transformation of the (1x2) structure to the (1x1) structure occurs at a temperature of 850 K in 5×10^{-8} torr oxygen and takes approximately two minutes, which is a long time for atomic rearrangements. This fact indicates that a substantial atomic rearrangement has occurred in the transformation of the (1x2) structure to the (1x1) structure. A priori, this evidence makes the missing row model a highly possible candidate for the reconstructed surface since its formation would involve movement of entire rows of atoms.

Eighteen LEED I-V spectra consisting of ten half-order beams and eight integral order beams were collected for the (1x2) surface structure. To confirm that the data are reproducible, ten spectra were retaken after repolishing the Ir crystal. The agreement between the two independent sets of data is excellent.

The calculations for the theoretical I-V spectra were performed as

described in the previous section. Comparisons between the experimental data and the results of the calculations using the missing row model, the paired rows model, and the buckled surface model show that the missing row model is the most likely one considered. In the calculations of the LEED I-V spectra for the missing row model, the topmost interlayer spacing of the Ir(110) surface was allowed to relax from - 15% to + 5% in steps of 5%. The best agreement between the theoretical and experimental I-V spectra was obtained for the missing row model with a topmost interlayer spacing of 1.22 Å (- 10%) modified with an inner potential of 10 eV. Figs. 4 and 5 show the comparisons between experiment and theory for the integral order beams and the half-order beams, respectively.

Among the 18 experimental I-V spectra displayed in Figs. 4 and 5, fourteen show good correspondence between theory and experiment; whereas two integral order beams, the (11) and the (21), as well as two half-order beams, the (0 3/2) and the (1 1/2), exhibit only mediocre agreement. The minor disagreement between experiment and theory is probably due to roughness of the (110) surface (7,8). However, the missing row model, with a topmost interlayer spacing of 1.22 ± 0.07 Å, is certainly the most probable structure for the (1x2) reconstructed surface based on the good agreement between experiment and theory for the majority of beams.

A detailed R-factor analysis developed by Zanazzi and Jona (9) will be used to determine quantitatively the level of agreement between theory and experiment for the different models considered (10). Work is in progress also to include a slight movement (row pairing) of the second layer within the framework of the missing row model (10).

5. Conclusions

(1) The Ir(110)-(1x1) Surface.

Results of the LEED analysis indicate that the Ir(110)-(1x1) structure formed by the depositon of 1/4 monolayer of oxygen on a clean, reconstructed Ir(110)-(1x2) structure is the same as the bulk structure, with a topmost interlayer spacing of 1.26 ± 0.05 Å. These results corroborate our assumption that the oxygen atoms are randomly and uniformly distributed over the cyrstal surface, stabilizing the (1x1) structure. The transformation of the (1x2) structure to the (1x1) may involve an extensive atomic rearrangement on the surface.

(2) The Ir(110)-(1x2) surface.

Based on the good agreement between experiment and theory for the majority of the LEED beams examined, the missing row model, with a topmost interlayer spacing of 1.22 ± 0.07 Å is the most probable structure for the (1x2) reconstructed surface.

References

1. C.-M. Chan, S. L. Cunningham, K. L. Luke, W. H. Weinberg and S. P. Withrow, Surface Sci. (in press).
2. J. L. Taylor, D. E. Ibbotson and W. H. Weinberg, Surface Sci. (in press).
3. J. B. Pendry, Low-Energy Electron Diffraction, Academic Press, London, 1974.
4. G. O. Arbman and S. Hornfelt, J. Phys. F2, 1033 (1972).
5. K. Christmann and G. Ertl, Z. Naturforsch. 28a, 1144 (1973).
6. C.-M. Chan, M. A. Van Hove, W. H. Weinberg and E. D. Williams, Phys. Rev. Letters (submitted).
7. E. Zanazzi, F. Jona, D. W. Jepsen and P. M. Marcus, J. Phys. C10, 875 (1977).
8. M. Maglietta, E. Zanazzi, F. Jona, D. W. Jepsen and P. M. Marcus, J. Phys. C10, 3287 (1977).
9. E. Zanazzi and F. Jona, Surface Sci. 62, 61 (1977).
10. C.-M. Chan, M. A. Van Hove, W. H. Weinberg and E. D. Williams (in preparation).

Figure Captions

Fig. 1(a). Schematic hard sphere model of the unreconstructed Ir(110)-(1x1) surface.

(b). The reciprocal space representation of (a).

(c). Schematic hard sphere model of the reconstructed Ir(110)-(1x2) surface for the missing row model.

(d). The reciprocal space representation of (c).

Fig. 2. Comparison between experimental I-V spectra modified with an inner potential of 8 eV for a topmost layer spacing ranging from - 10% to - 5% and the experimental I-V spectra from the Ir(110)-(1x1) surface. $\theta = 0^{o}$ corresponds to normal incidence.

Fig. 3. Top views of a hard-spheres representation of (a) the paired rows model; (b) the buckled surface model; and (c) the missing row model. The corresponding side views are shown in (d) - (f), respectively. The x- and y-directions are in the plane of the crystal surface. The z-direction is perpendicular to the crystal surface.

Fig. 4. Comparison between the theoretical I-V spectra for the missing row model (with a modified inner potential of 10 eV and a topmost interlayer spacing of 1.22 $\mathring{A}$) and the experimental I-V spectra of integral-order beams from the Ir(110)-(1x2) surface.

Fig. 5. As in Fig. 4, except for half-order beams.

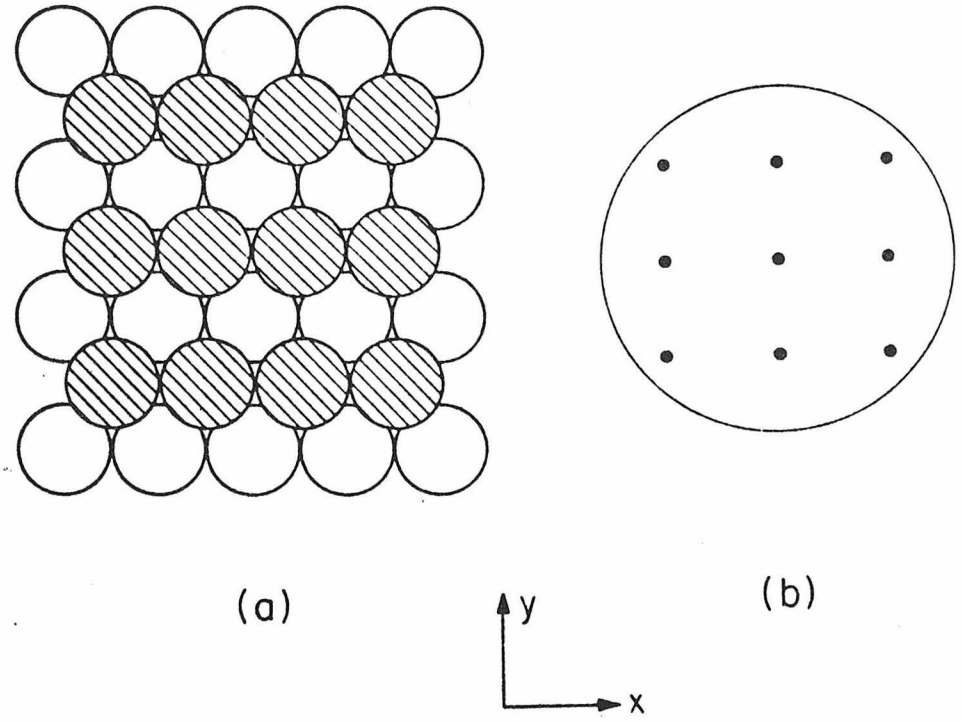

Fig. 1

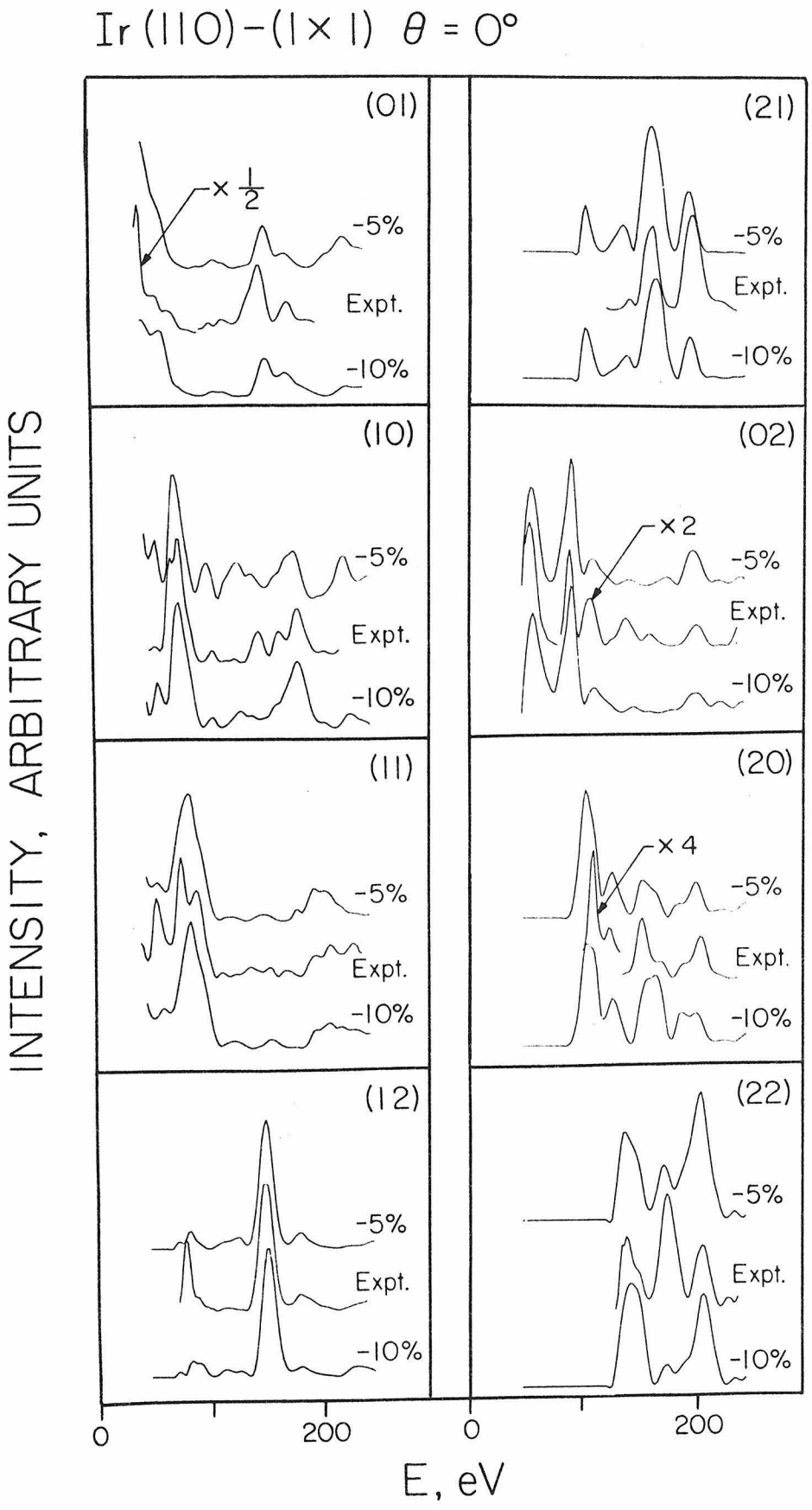
Ir (110)-(1 × 1) θ = 0°
(01)
× 1/2
-5%
Expt.
-10%
(21)
-5%
Expt.
-10%
(10)
-5%
Expt.
-10%
(02)
× 2
-5%
Expt.
-10%
(11)
-5%
Expt.
-10%
(20)
× 4
-5%
Expt.
-10%
(12)
-5%
Expt.
-10%
(22)
-5%
Expt.
-10%
INTENSITY, ARBITRARY UNITS
0
200
0
200
E, eV

Fig. 2

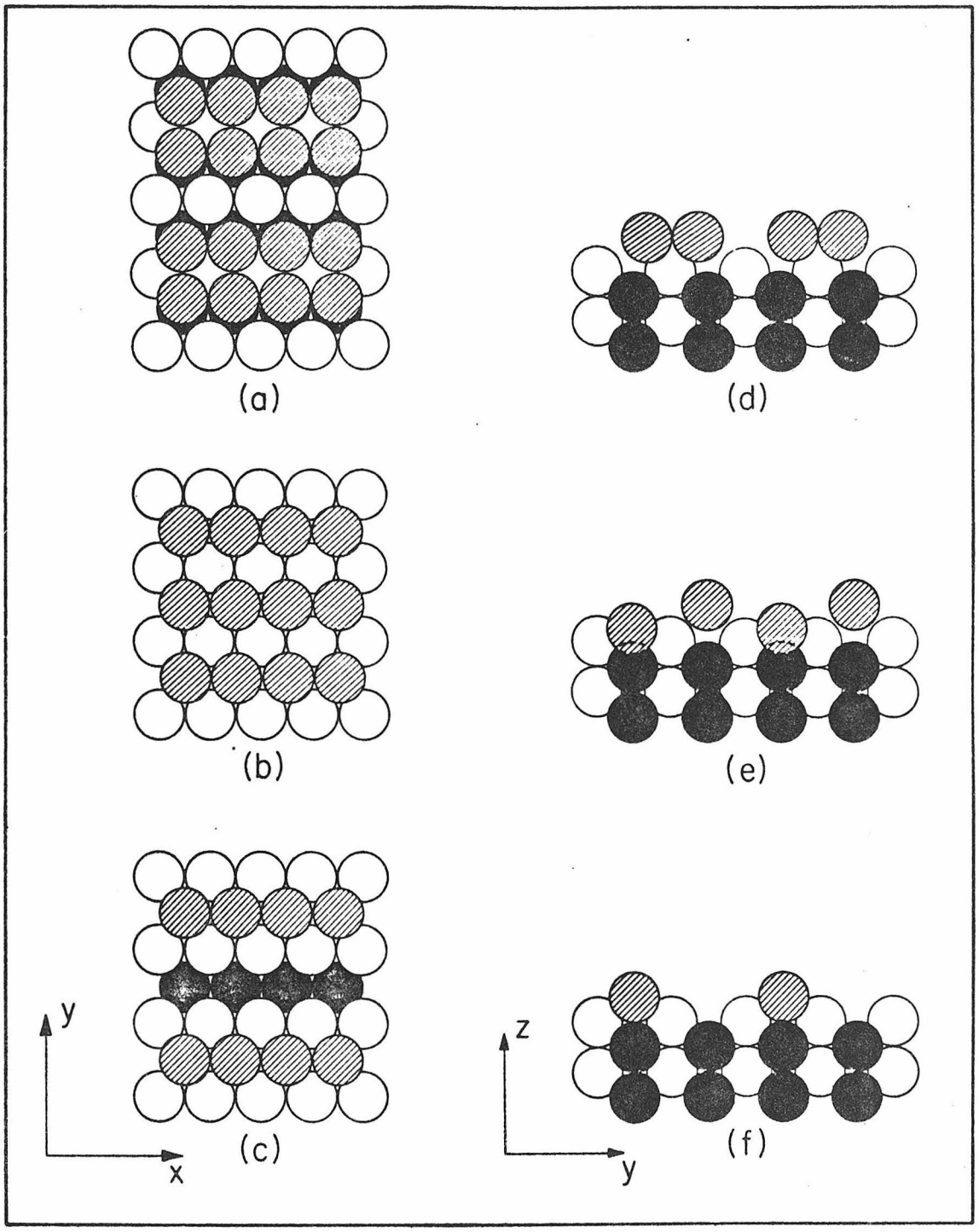

Fig. 3

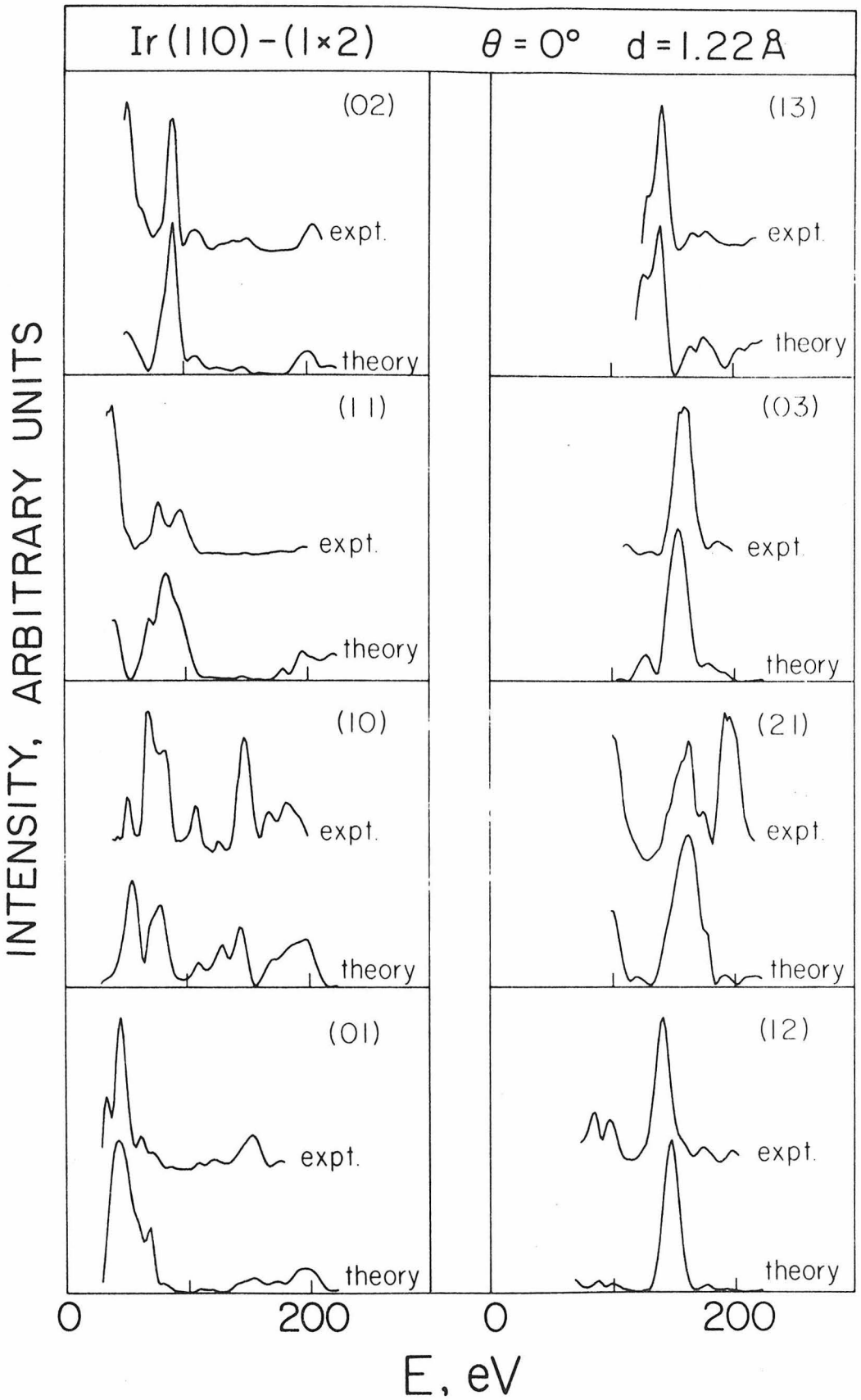
Ir(110)-(1×2) θ = 0° d = 1.22 Å
(02)
(13)
(11)
(03)
(10)
(21)
(01)
(12)
expt.
theory
INTENSITY, ARBITRARY UNITS
0
200
E, eV

Fig. 4

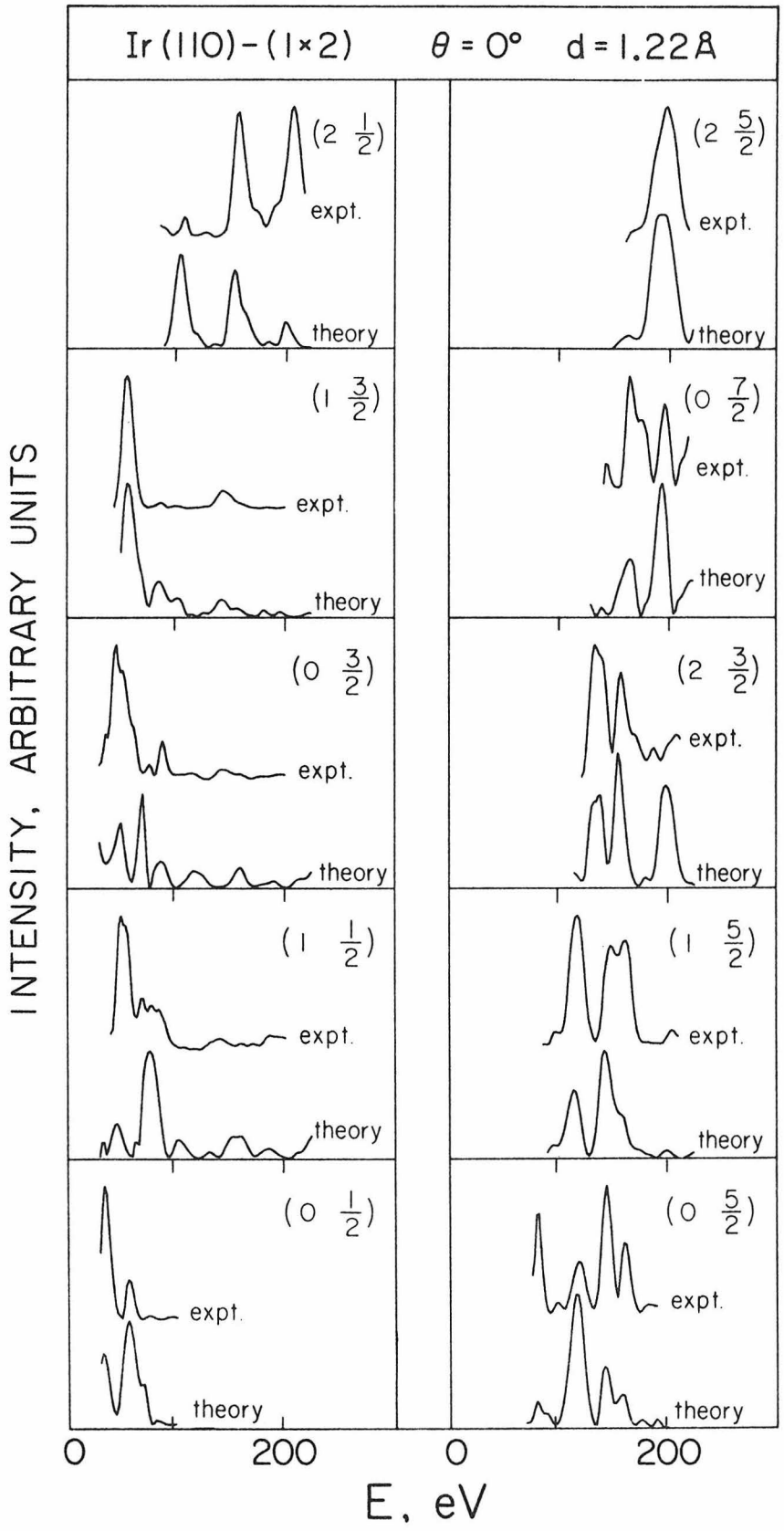
Ir (110) - (1×2) θ = 0° d = 1.22 Å
(2 1/2)
expt.
theory
(2 5/2)
expt.
theory
(1 3/2)
expt.
theory
(0 7/2)
expt.
theory
(0 3/2)
expt.
theory
(2 3/2)
expt.
theory
(1 1/2)
expt.
theory
(1 5/2)
expt.
theory
(0 1/2)
expt.
theory
(0 5/2)
expt.
theory
INTENSITY, ARBITRARY UNITS
0
200
0
200
E, eV

Fig. 5

Chapter 5

THE STRUCTURE OF THE c(2x2) OXYGEN OVERLAYER ON THE UNRECONSTRUCTED (110) SURFACE OF IRIDIUM

by

C.-M. Chan, K. L. Luke, M. A. Van Hove,
W. H. Weinberg and S. P. Withrow

Division of Chemistry and Chemical Engineering
California Institute of Technology
Pasadena, California 91125

Surface Science 78, 386-96 (1978)

Abstract

An Ir(110)-c(2x2)O structure has been prepared by adsorbing a half-monolayer of oxygen at room temperature on an unreconstructed (1x1) Ir surface stabilized by a quarter-monolayer of randomly adsorbed oxygen. Results of the low-energy electron diffraction structural analysis indicate that the ordered oxygen atoms are residing on the short-bridged sites on the (110) surface. The Ir-O interlayer spacing is 1.37 ± 0.05 Å, and the bond length is 1.93 ± 0.07 Å. The topmost substrate interlayer spacing is found to be 1.33 ± 0.07 Å rather than 1.26 ± 0.07 Å which is the topmost interlayer spacing of the unreconstructed (1x1) Ir surface.

1. Introduction

Previously, we have determined the structure of an unreconstructed Ir(110)-(1x1) surface (1) which is prepared by the deposition of a quarter-monolayer of oxygen on a clean, reconstructed (1x2) surface (2). The structure of the unreconstructed Ir(110)-(1x1) surface was found to be the same as the bulk structure, with a topmost interlayer spacing of 1.26 ± 0.07 Å which is equivalent to a contraction of approximately 7.5% of the bulk interlayer spacing of 1.36 Å. It was found that a c(2x2) structure was formed by the adsorption of an additional half-monolayer of oxygen on the (1x1) surface. The purpose of this work is to present the first structural determination of a superstructure on an impurity-stabilized unreconstructed metallic surface.

Demuth (3) has found that oxygen forms a (2x1) structure on a clean Ni(110) surface. The oxygen atoms were shown to reside on the short-bridged sites of this surface as defined in Fig. 1. However, it is certainly not clear, *à priori*, that the ordered oxygen on the impurity-stabilized Ir(110)-(1x1) surface will reside in similar sites. The fact that a quarter-monolayer of randomly adsorbed oxygen is needed for the formation of the (1x1) surface may have a strong effect on the binding sites of the ordered oxygen atoms forming the c(2x2) structure. Moreover, the c(2x2) symmetry of oxygen on Ir(110) is different from the (2x1) symmetry on the Ni(110) surface. Finally, it is interesting to determine whether the additional half-monolayer of ordered oxygen has any effect on the interlayer spacing of the topmost layer of the impurity-stabilized Ir(110)-(1x1) substrate. The latter has been shown to be contracted by approximately 7.5% relative to the bulk interlayer spacing (1).

2. Experimental Procedure

The experimental apparatus is identical to that described previously (1). An Ir(110)-(1x1) surface structure has been prepared by adsorbing a quarter-monolayer of oxygen at 850 K on a clean, reconstructed (1x2) surface (1). A well-ordered c(2x2) superstructure was observed when the (1x1) surface was exposed to 2L (1L=1 Langmuir$\equiv 10^{-6}$ torr-sec) of oxygen at room temperature. It was found that the intensity of the (1/2 1/2) diffraction beam reaches a maximum after an exposure of 2L of oxygen. The intensity is nearly maintained up to an exposure of 5L of oxygen, and then decreases more markedly upon further exposure of oxygen. A (1x1) structure was observed after the surface was exposed to 14L of oxygen.

Intensity-voltage (I-V) profiles for four integral and four half-order beams were measured at approximately 2 eV intervals. These beams are the following: (10), (11), (02), (20), (1/2 1/2), (1/2 3/2), (3/2 1/2) and (3/2 3/2). All I-V beam profiles have been normalized to unit incident beam current. The beams are indexed so that the longer side of the unit cell in real space is the y-direction as shown in Fig. 1.

3. Results

We have found that a clean Ir(110) surface exhibits a reconstructed (1x2) structure (2). A (1x1) structure appears when a quarter-monolayer of oxygen is deposited on the clean, reconstructed (1x2) surface (1). When the (1x1) surface is exposed to 2L of oxygen at room temperature, a c(2x2) superstructure is observed as shown in Fig. 1. The oxygen was found to be adsorbed dissociatively on the (1x1) surface (4).

A c(2x2) structure on the Ir(110)-(1x1) surface requires a half-monolayer of oxygen associated with the superstructure. This coverage of oxygen on the surface was verified by Auger electron spectroscopy. The peak-to-peak amplitude of the oxygen KLL transition for the surface on which the c(2x2) structure exists is approximately 3/4 of that of a (1x2) reconstructed surface which has been exposed to approximately 30L of oxygen. The latter exposure results in a coverage that is approximately equivalent to one monolayer of oxygen (4). Hence, a total of approximately 3/4 of a monolayer of oxygen is required for the formation of the c(2x2) structure on a clean, reconstructed (1x2) Ir surface. Upon subtraction of the amount of oxygen which is required for the formation of the (1x1) structure, approximately a half-monolayer of oxygen is needed for the formation of the c(2x2) structure on the (1x1) Ir surface. This conclusion is also in agreement with independent contact potential difference measurements made in this laboratory (4).

4. Analysis

Using the layer-doubling method (5), LEED intensity-voltage profiles for the (10), (11), (02), (20), (1/2 1/2), (1/2 3/2), (3/2 1/2) and (3/2 3/2) beams were calculated for various assumed surface geometries. Symmetry properties of the beams at normal incidence were exploited in the calculations, e.g., at 150 eV, an equivalent of 120 beams was included in the calculations. For the Ir substrate, a band structure potential which includes full Slater exchange was used (6). A superposition potential obtained by overlapping atomic charge densities (7) was used for the oxygen overlayer. Eight phase shifts were used for both the Ir substrate and the oxygen overlayer. An assumed inner potential (muffin-tin zero) of 15 eV was used for both the overlayer and substrate. The imaginary part of the inner potential (optical potential), which represents all inelastic processes, was set proportional to $E^{1/3}$. This optical potential is 3.8 eV when the incident energy is 105 eV. The optical potential for the overlayer was set equal to that of the substrate. The Debye temperature for the substrate and the overlayer were taken to be 280 K and 840 K, respectively. Enhancement factors of 1.4 and 2.0 were chosen for the surface mean-square vibrational amplitudes of the substrate and the overlayer, respectively. The crystal temperature was 300 K.

The most common (highest symmetry) models for an overlayer of adsorbed atoms forming a c(2x2) structure on a substrate with a rectangular unit cell are the four-fold, the on-top, the short-bridged and the long-bridged sites as shown schematically in Fig. 1. Calculations have been performed for the Ir(110)-c(2x2)O structure for the on-top, the short-bridged, and the long-bridged sites with various physically realistic interlayer spacings between the substrate

and the overlayer. Comparisons between experimental I-V spectra and the best theoretical I-V spectra for each model, obtained with a modified inner potential of 10 eV, are shown in Figs. 2-5. Comparisons between theory and experiment indicate that the short-bridged site model is the best one considered. For certain beams, the agreement between experiment and theory for the on-top model is acceptable, but the best overall agreement is obtained for the short-bridged site model. The long-bridged site model is clearly ruled out by the poor quality of agreement between theory and experiment in almost all cases.

It was found that the topmost interlayer spacing of the unreconstructed Ir(110)-(1x1) structure is contracted by approximately 7.5% of the bulk interlayer spacing (1). Therefore, calculations were performed for the short-bridged site model in which the topmost interlayer spacing of the substrate (d_1) varies from 1.22 Å (-10%) to 1.43 Å (+5%) in increments of 0.07 Å (5%), while the interlayer spacing between the substrate and the overlayer (d_2) varies from 1.20 Å to 1.50 Å in increments of 0.05 Å. Comparisons between experimental I-V spectra and theoretical I-V spectra for d_1 equal to 1.36 Å and 1.29 Å, and for d_2 varying between 1.35 Å and 1.50 Å are shown in Figs. 6-13. The results of the calculations indicate that the best agreement is found for values of d_1 and d_2 equal to 1.33 ± 0.07 Å and 1.37 ± 0.05 Å, respectively.

5. Discussion

The results of this study, which indicate that the oxygen atoms in the c(2x2) structure on Ir(110) are residing on the short-bridged sites, are in agreement with the bonding geometry found for the (2x1) oxygen overlayer on Ni(110) (3). The choice of the short-bridged site over the long-bridged site, the four-fold site, or the on-top site by the oxygen both on the Ni(110) and the Ir(110) surface is in agreement with the results of generalized valence bond calculations for oxygen chemisorption on metal clusters (8). If the oxygen atom is located in the on-top site or in the four-fold site on Ni(110) and/or Ir(110), the chemical bonding will be similar to the bonding between one oxygen atom and one Ni or Ir atom. It was found theoretically that the chemical bond formed between an oxygen atom and two Ni atoms, resembling the short-bridged site, is stronger by 10 kcal/mole than the chemical bond formed between one oxygen atom and one Ni atom, simulating the on-top or the four-fold site (8). By analogy, on the extended (110) surface, the short-bridged site should be preferred over the four-fold site and the on-top site due to the formation of stronger chemical bonding.

Moreover, it is known that most X_2O compounds have X-O-X bond angles of approximately 105^o, e.g., bond angles for H_2O, F_2O and Cl_2O are 105^o, 103^o and 111^o, respectively (9). Within the framework of a hard-spheres model, the bond angles for the short-bridged site and the long-bridged site on the Ir(110) surface are approximately 86^o and 148^o, respectively, as is shown in Fig. 14. Hence, the bonding of oxygen to Ir(110) in the long-bridged site is unfavorable due to the formation of a large Ir-O-Ir bond angle compared to the bond angles found in most X-O-X molecules. Indeed, our LEED calculations indicate that for the short-bridged site model, the interlayer

spacing between the oxygen and the Ir atoms is 1.37 Å. This spacing should be compared to 1.47 Å which is calculated from a hard-spheres model assuming a bond length of 2.00 Å, i.e., the sum of the convalent radii of the oxygen and Ir atoms. The actual bond length of oxygen on Ir(110), therefore, is 1.93 Å rather than 2.00 Å, and the bond angle is approximately 90^{o} rather than 86^{o}. Hence, a contraction of the interlayer spacing between the substrate and the overlayer is reasonable from the point of view of the formation of a more favorable Ir-O-Ir bond angle.

The I-V spectra of the integral order beams from the c(2x2) structure have a very close resemblance to those of the unreconstructed Ir(110)-(1x1) surface. This indicates that a half-monolayer of ordered oxygen does not affect the integral order beams significantly. The presence of a quarter-monolayer of disordered oxygen has an even smaller effect. This conclusion further justifies the assumption, made previously (1), that the presence of a disordered quarter-monolayer of oxygen does not contribute significantly to the structure of the I-V spectra.

6. Synopsis

The oxygen atoms in a c(2x2) overlayer structure were found to reside on the short-bridged sites of the unreconstructed Ir(110)-(1x1) surface which is stabilized by a quarter-monolayer of randomly adsorbed oxygen. The interlayer spacing between the oxygen and Ir atoms is 1.37 ± 0.05 Å. The Ir-O bond length is therefore 1.93 ± 0.07 Å. The topmost substrate interlayer spacing is 1.33 ± 0.07 Å, a contraction of 2 ± 5% compared to the bulk interlayer spacing. However, the clean, reconstructed Ir(110)-(1x1) surface is contracted by 7.5 ± 5% so that the oxygen overlayer causes a slight expansion of the top Ir-Ir interlayer spacing. The driving force for this expansion may be thought of in terms of the formation of a more favorable Ir-O-Ir bond angle leading to a strengthening of the local chemical bond between the oxygen and the Ir surface.

Acknowledgment

This research was supported by the Army Research Office (Durham) under Grant No. DAHCO-75-0170. Additonal support was derived from the American Vacuum Society, the Alfred P. Sloan Foundation, and the Camille and Henry Dreyfus Foundation.

References

1. C.-M. Chan, S. L. Cunningham, K. L. Luke, W. H. Weinberg and S. P. Withrow, Surface Sci. (submitted).

2. C.-M. Chan, M. A. Van Hove, W. H. Weinberg and Ellen D. Williams (in preparation).

3. J. E. Demuth, J. Colloid Interface Sci. 58, 184 (1977).

4. J. L. Taylor, D. E. Ibbotson and W. H. Weinberg, Surface Sci. (submitted).

5. J. B. Pendry, Low-Energy Electron Diffraction, Academic Press, London, 1974.

6. G. O. Arbman and S. Hörnfelt, J. Phys. F2, 1033 (1972).

7. M. A. Van Hove and S. Y. Tong, Phys. Rev. Letters 35, 1092 (1975).

8. W. A. Goddard III, S. P. Walch, A. K. Rappé and T. H. Upton, J. Vac. Sci. Technol. 14, 416 (1977).

9. L. Pauling, The Nature of the Chemical Bond, 3rd ed., Cornell University Press, Ithaca, New York, 1960.

Figure Captions

Fig. 1: Possible structures of the Ir(110)-c(2x2)O overlayer. Large circles denote iridium atoms, and small shaded circles denote oxygen atoms.

(a) on-top site

(b) short-bridged site

(c) four-fold site

(d) long-bridged site

(e) reciprocal space lattice of Ir(110)-c(2x2)O structure

Fig. 2: Comparison between the theoretical I-V spectra, modified with an inner potential of 10 eV for each model considered, and the experimental I-V spectrum of the (1/2 1/2) beam from the Ir(110)-c(2x2)O surface.

$\theta=0^{o}$ corresponds to normal incidence.

d_2 is the interlayer spacing between the substrate and the overlayer.

Fig. 3: As in Fig. 2, except the (1/2 3/2) beam.

Fig. 4: As in Fig. 2, except the (3/2 1/2) beam.

Fig. 5: As in Fig. 2, except the (3/2 3/2) beam.

Fig. 6: Comparison between theoretical I-V spectra, modified with an inner potential of 10 eV for the short-bridged site model for d_1 (the topmost interlayer spacing of the substrate) equal to 1.36 $\mathring{A}$ and 1.29 $\mathring{A}$ and for d_2 (the interlayer spacing between the substrate and the overlayer) ranging from 1.35 $\mathring{A}$ to 1.5 $\mathring{A}$, and the experimental I-V spectrum of the (10) beam from the Ir(110)-c(2x2)O surface. SBS denotes short-bridged site.

Fig. 7: As in Fig. 6, except the (11) beam.

Fig. 8: As in Fig. 6, except the (02) beam.

Fig. 9: As in Fig. 6, except the (20) beam.

Fig.10: As in Fig. 6, except the (1/2 1/2) beam.

Fig.11: As in Fig. 6, except the (1/2 3/2) beam.

Fig.12: As in Fig. 6, except the (3/2 1/2) beam.

Fig.13: As in Fig. 6, except the (3/2 3/2) beam.

Fig.14:(a) Schematic hard-spheres model showing a side view of the short-bridged site through the (001) surface. SBS denotes short-bridged site.

(b) Schematic hard-spheres model showing a side view of the long-bridged site through the $(1\bar{1}0)$ surface. LBS denotes long-bridged site.

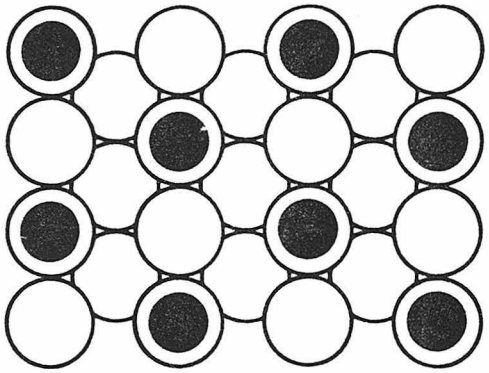

ON-TOP SITE
(a)

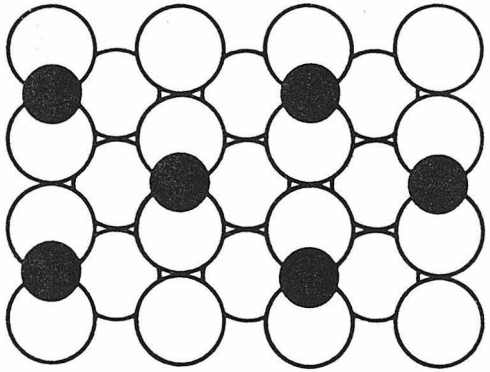

SHORT-BRIDGED SITE
(b)

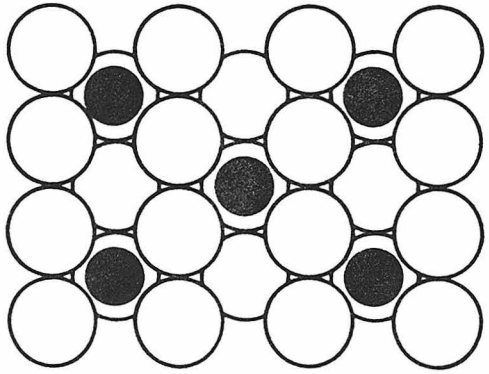

FOUR-FOLD SITE
(c)

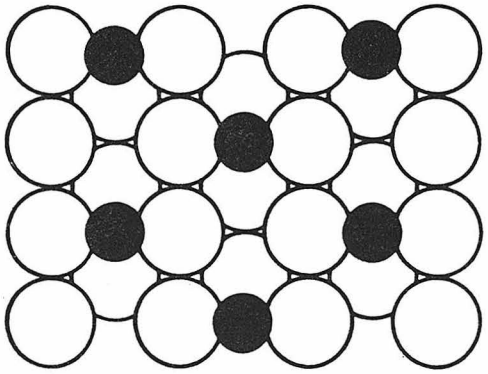

LONG-BRIDGED SITE
(d)

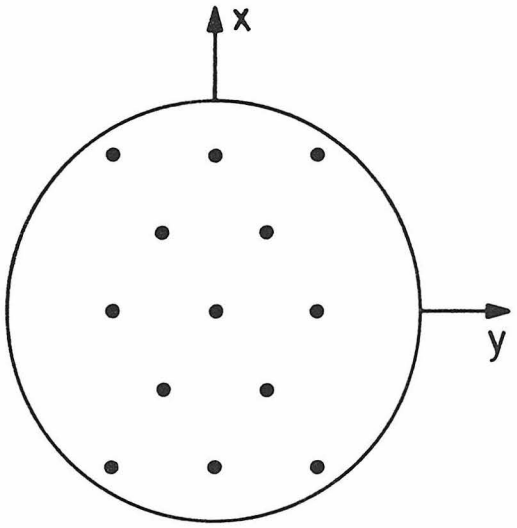

RECIPROCAL LATTICE
OF Ir(110)-c(2×2)O
(e)

Fig. 1

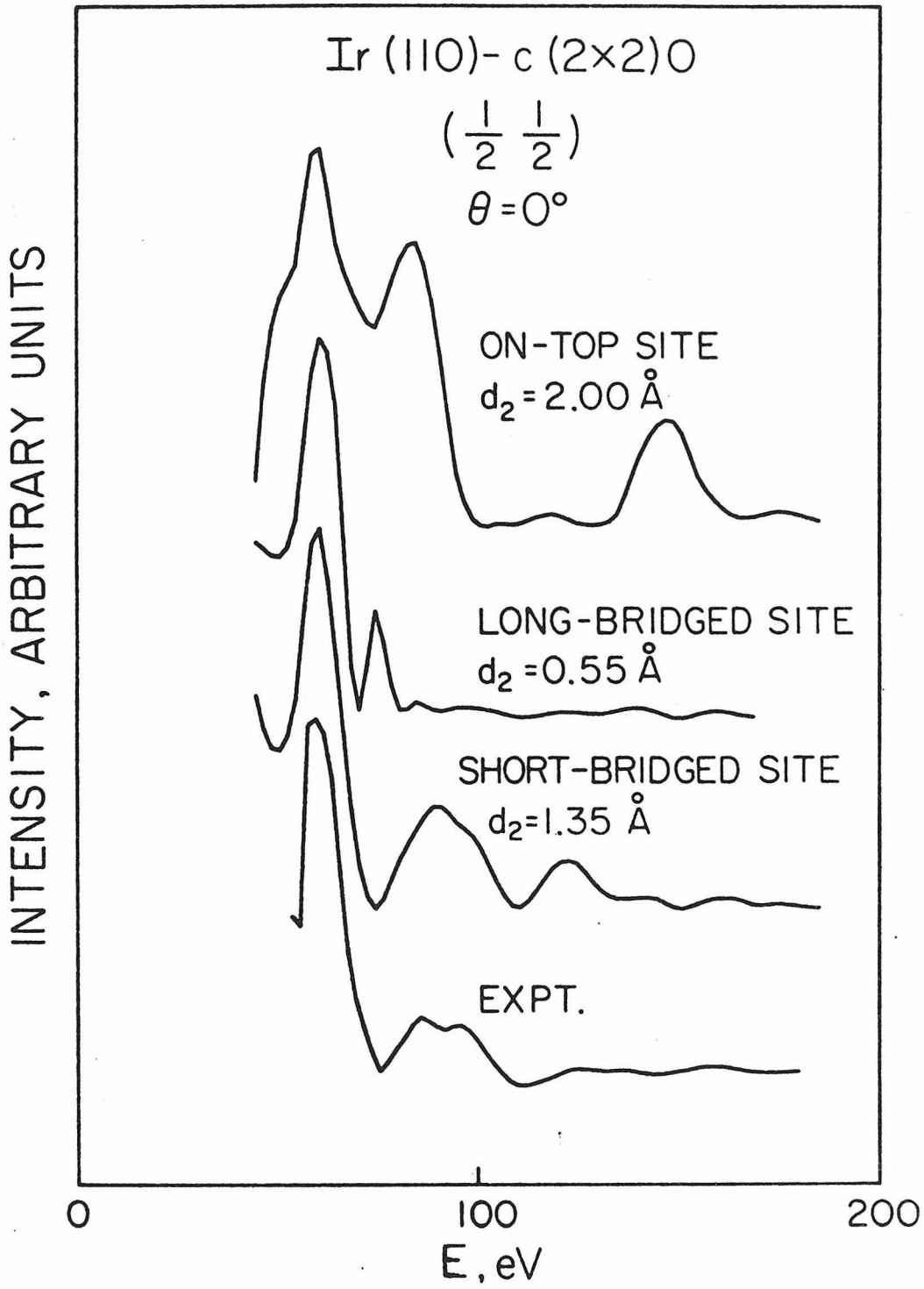
Ir (110)- c (2×2)O
(1/2 1/2)
θ = 0°
ON-TOP SITE
d2 = 2.00 Å
LONG-BRIDGED SITE
d2 = 0.55 Å
SHORT-BRIDGED SITE
d2 = 1.35 Å
EXPT.
INTENSITY, ARBITRARY UNITS
0
100
200
E, eV

Fig. 2

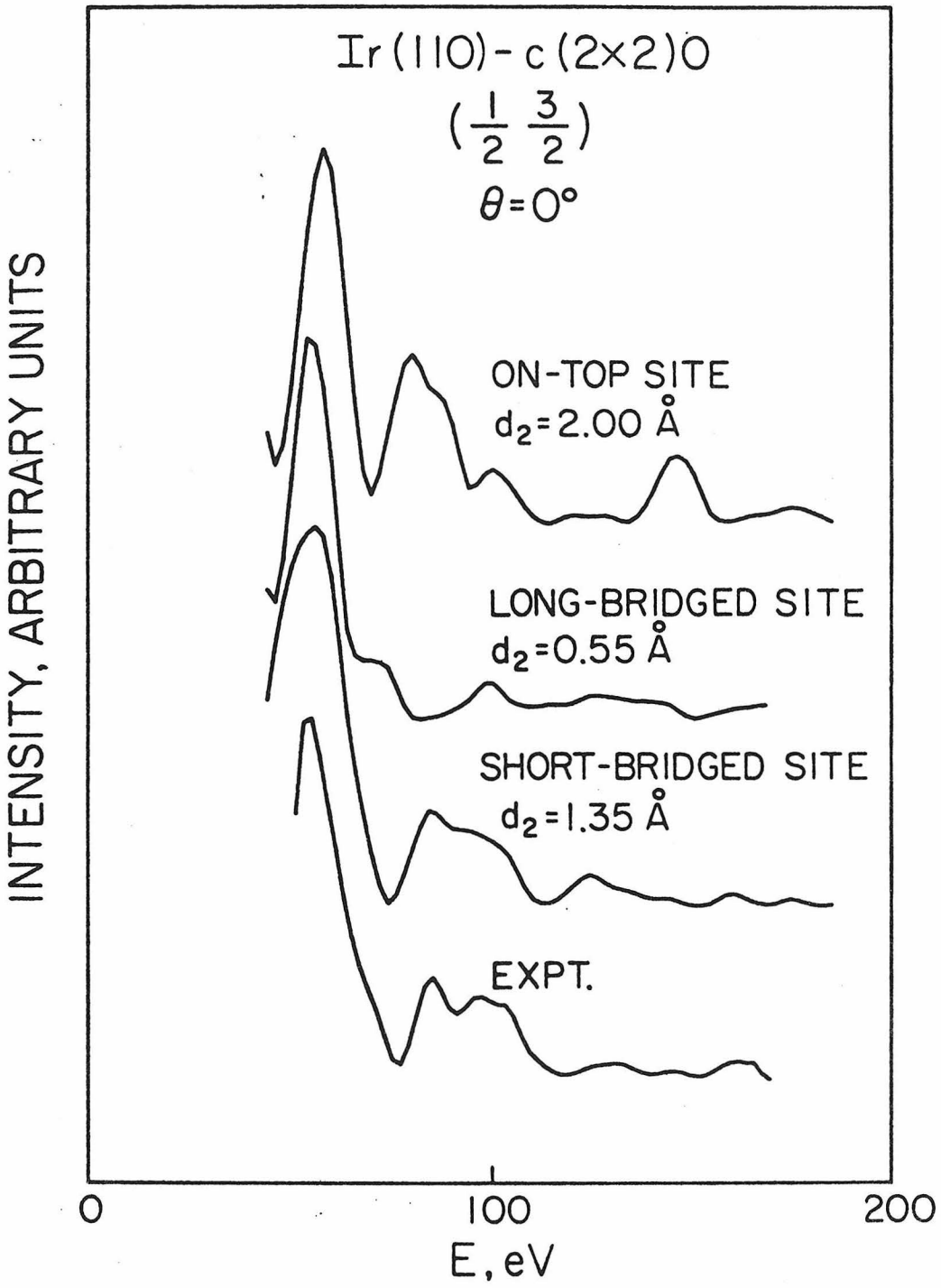
Ir(110)-c(2×2)O
(1/2 3/2)
θ=0°
ON-TOP SITE
d2=2.00 Å
LONG-BRIDGED SITE
d2=0.55 Å
SHORT-BRIDGED SITE
d2=1.35 Å
EXPT.
INTENSITY, ARBITRARY UNITS
0
100
200
E, eV

Fig. 3

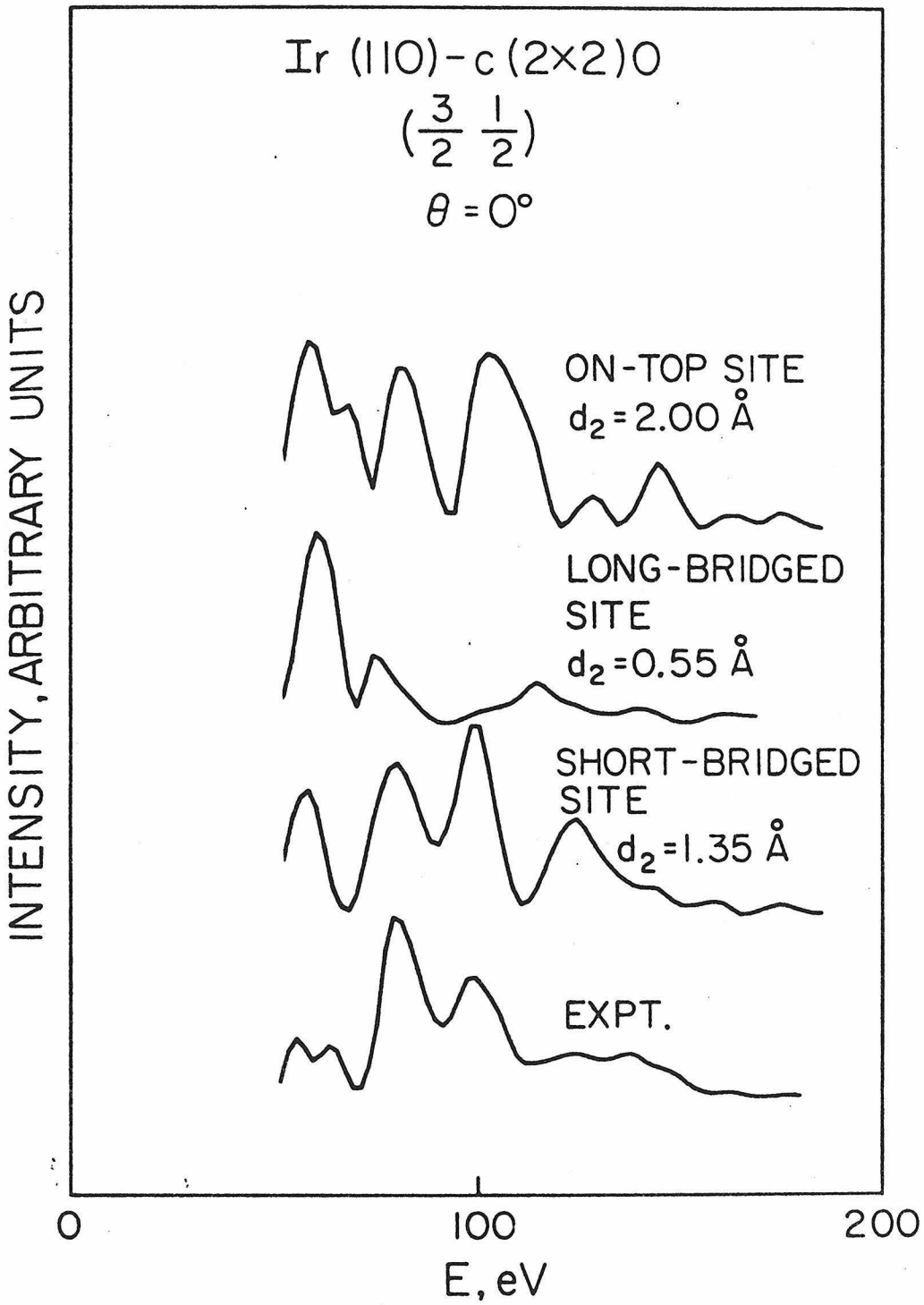
Ir (110)-c(2×2)O
(3/2 1/2)
θ = 0°
ON-TOP SITE
d2 = 2.00 Å
LONG-BRIDGED
SITE
d2 = 0.55 Å
SHORT-BRIDGED
SITE
d2 = 1.35 Å
EXPT.
INTENSITY, ARBITRARY UNITS
0
100
200
E, eV

Fig. 4

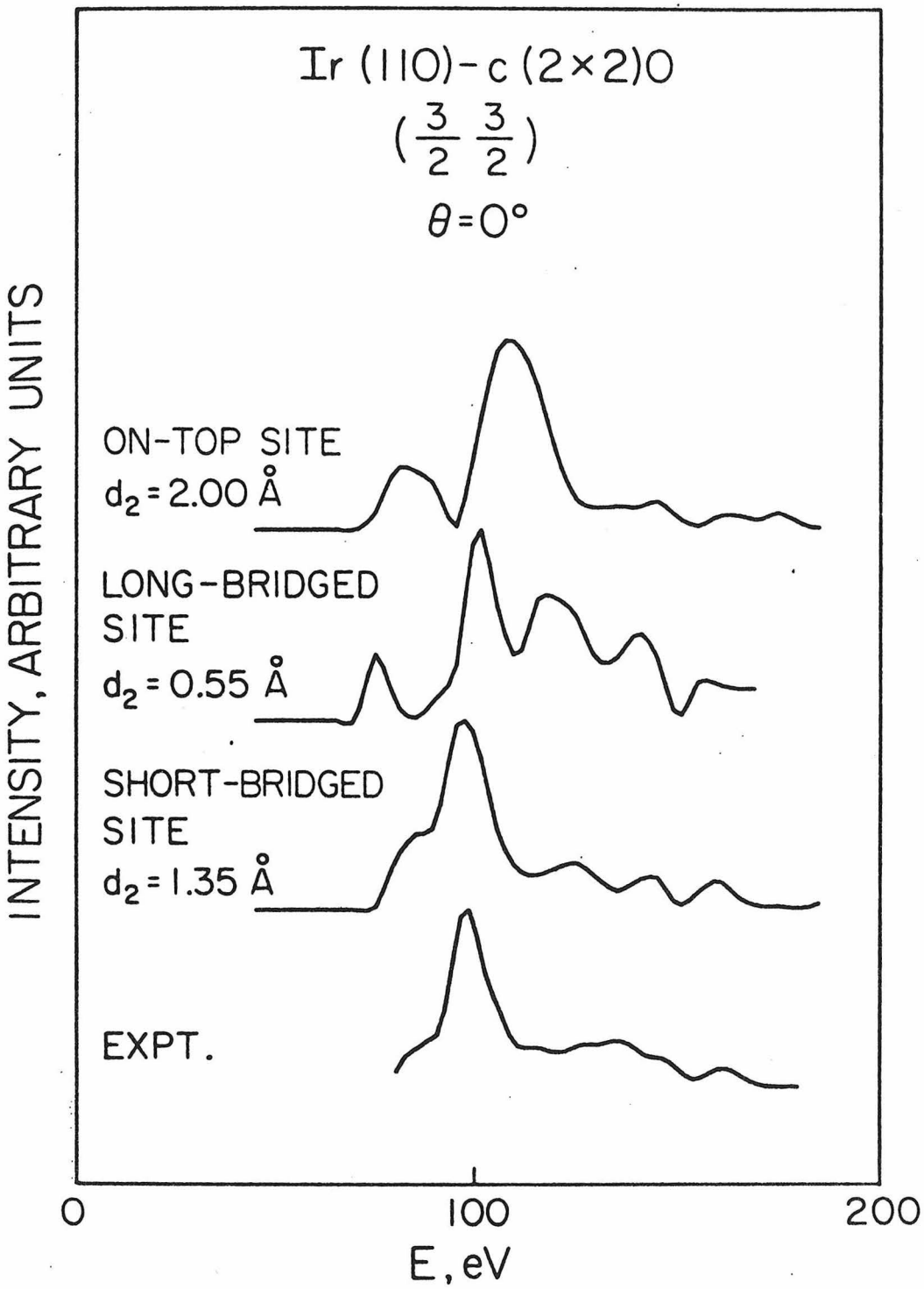
Ir (110)-c (2×2)O
(3/2 3/2)
θ=0°
ON-TOP SITE
d2 = 2.00 Å
LONG-BRIDGED SITE
d2 = 0.55 Å
SHORT-BRIDGED SITE
d2 = 1.35 Å
EXPT.
INTENSITY, ARBITRARY UNITS
0
100
200
E, eV

Fig. 5

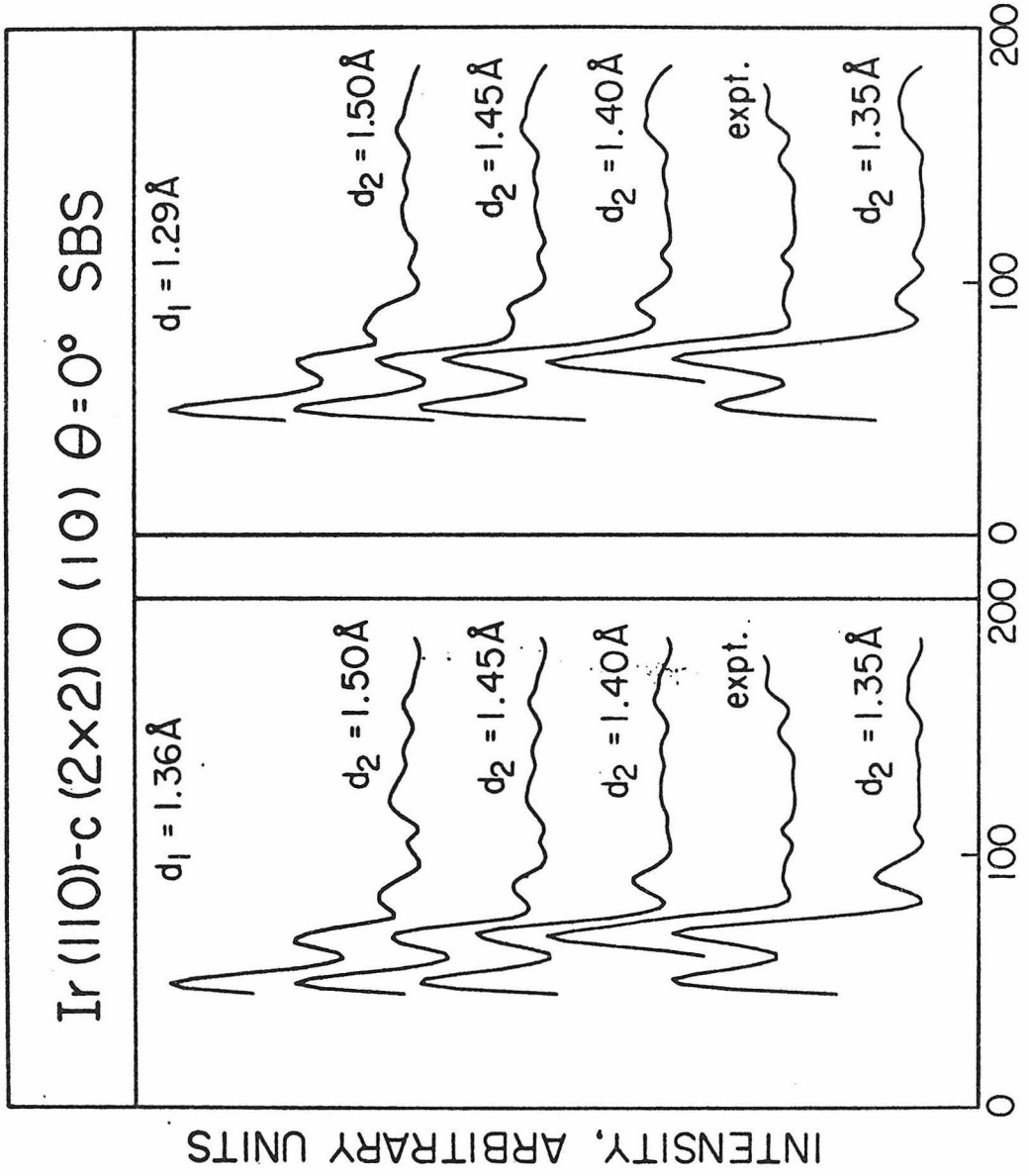
Ir (110)-c (2×2)O (10) θ=0° SBS
d1 = 1.36Å
d2 = 1.50Å
d2 = 1.45Å
d2 = 1.40Å
expt.
d2 = 1.35Å
d1 = 1.29Å
d2 = 1.50Å
d2 = 1.45Å
d2 = 1.40Å
expt.
d2 = 1.35Å
INTENSITY, ARBITRARY UNITS
0
100
200
0
100
200
E, eV

Fig. 6

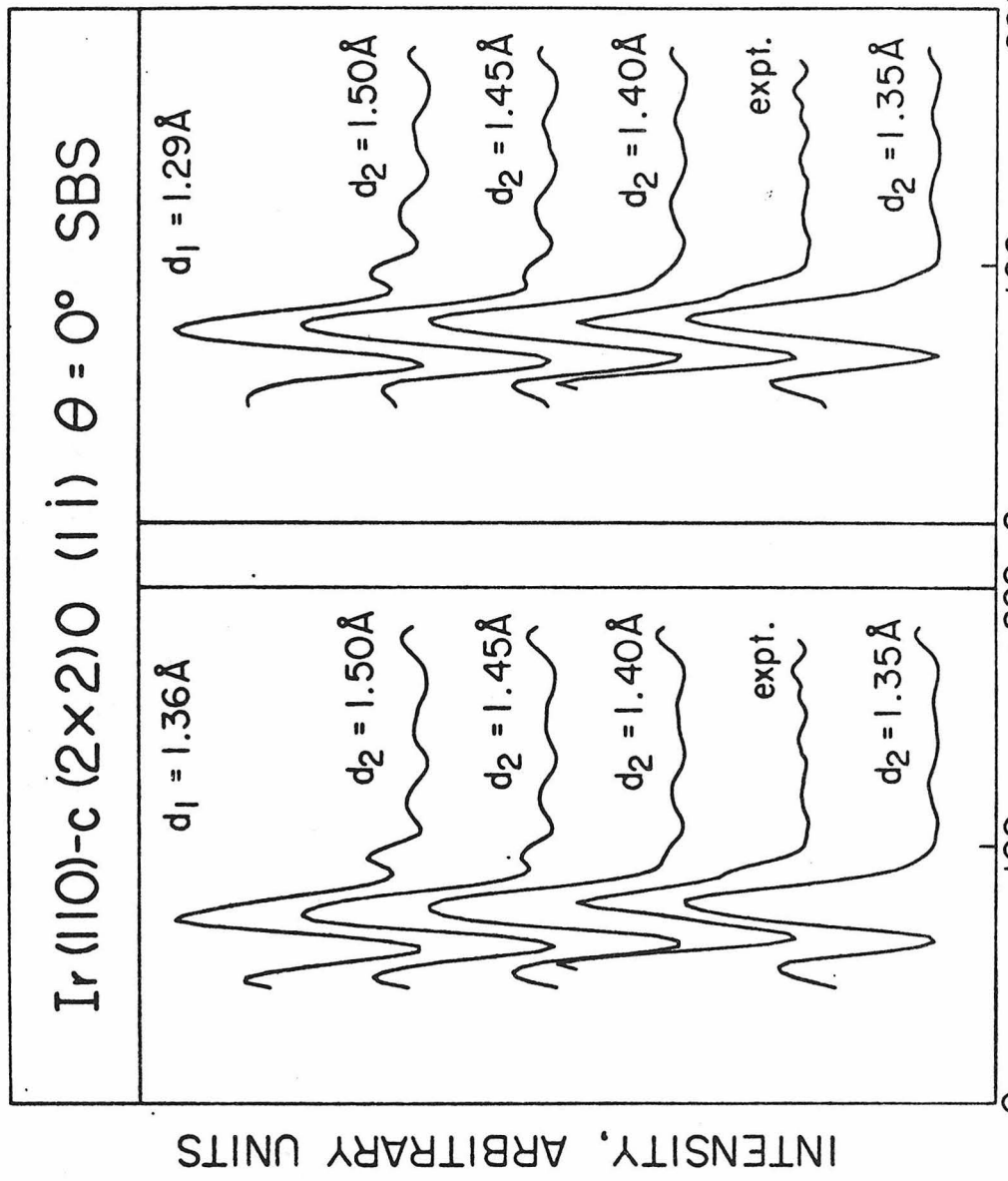
Ir (110)-c (2×2)O (1 1) θ = 0° SBS
d1 = 1.36Å
d2 = 1.50Å
d2 = 1.45Å
d2 = 1.40Å
expt.
d2 = 1.35Å
d1 = 1.29Å
d2 = 1.50Å
d2 = 1.45Å
d2 = 1.40Å
expt.
d2 = 1.35Å
0
100
200
0
100
200
E, eV
INTENSITY, ARBITRARY UNITS

Fig. 7

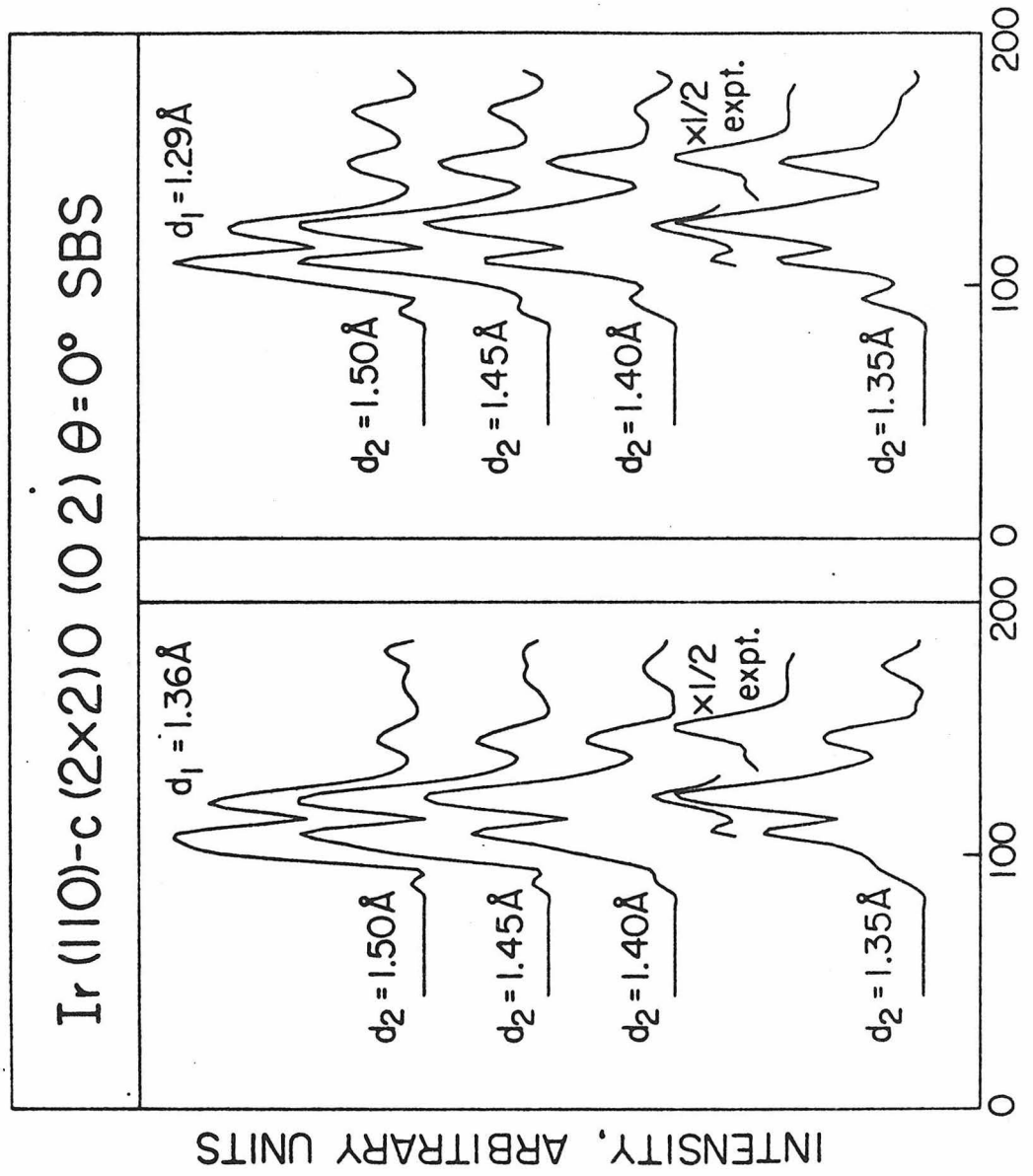
Ir (110)-c (2x2)O (0 2) θ=0° SBS
d1 = 1.36Å
d2 = 1.50Å
d2 = 1.45Å
d2 = 1.40Å
x1/2 expt.
d2 = 1.35Å
d1 = 1.29Å
d2 = 1.50Å
d2 = 1.45Å
d2 = 1.40Å
x1/2 expt.
d2 = 1.35Å
0
100
200
200
0
100
200
E, eV
INTENSITY, ARBITRARY UNITS

Fig. 8

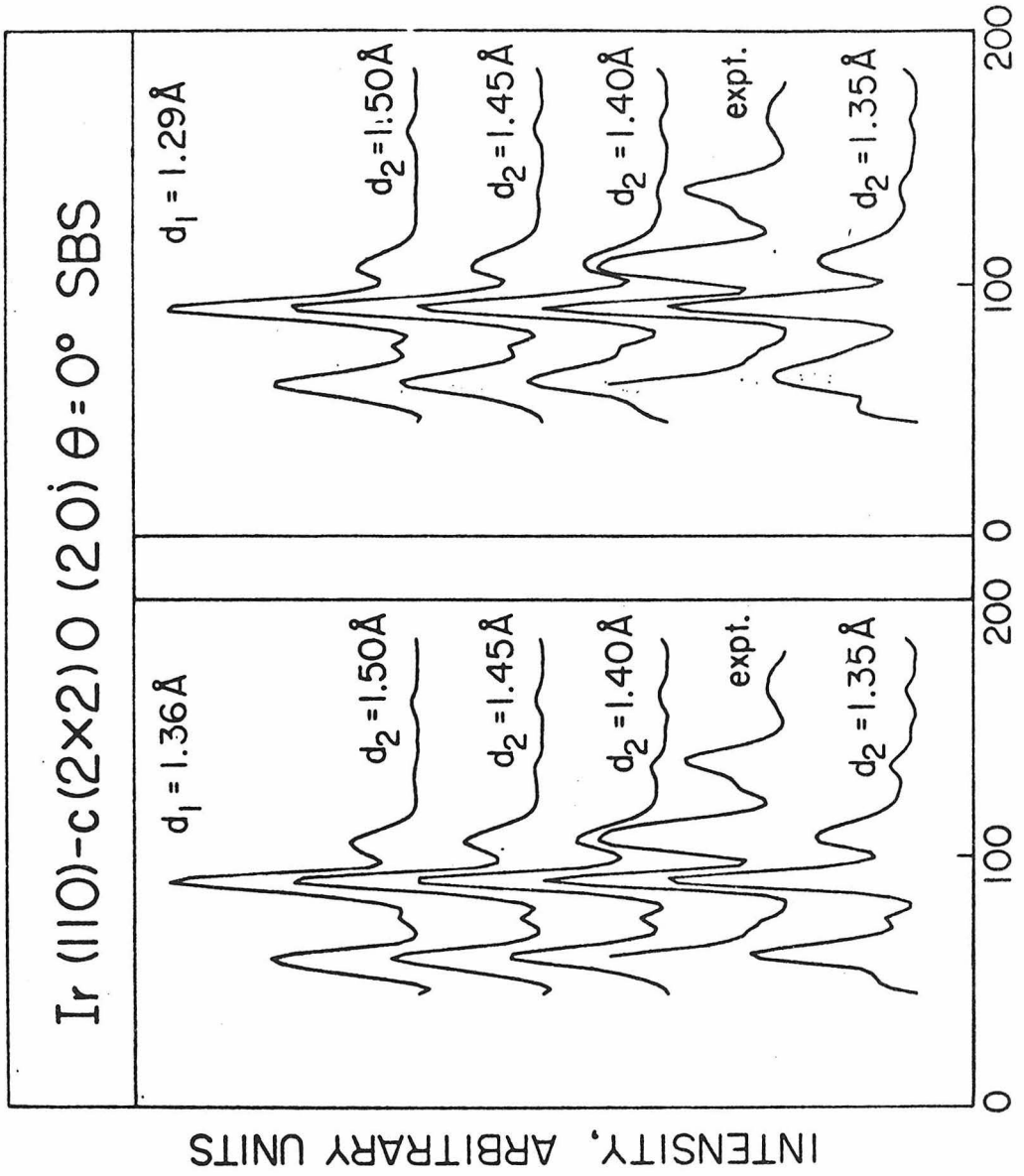
Ir (110)-c(2×2)O (2Oi) θ=0° SBS
d_1 = 1.36Å
d_2=1.50Å
d_2=1.45Å
d_2=1.40Å
expt.
d_2=1.35Å
d_1 = 1.29Å
d_2=1.50Å
d_2=1.45Å
d_2=1.40Å
expt.
d_2=1.35Å
0
100
200
200
100
0
E, eV
INTENSITY, ARBITRARY UNITS

Fig. 9

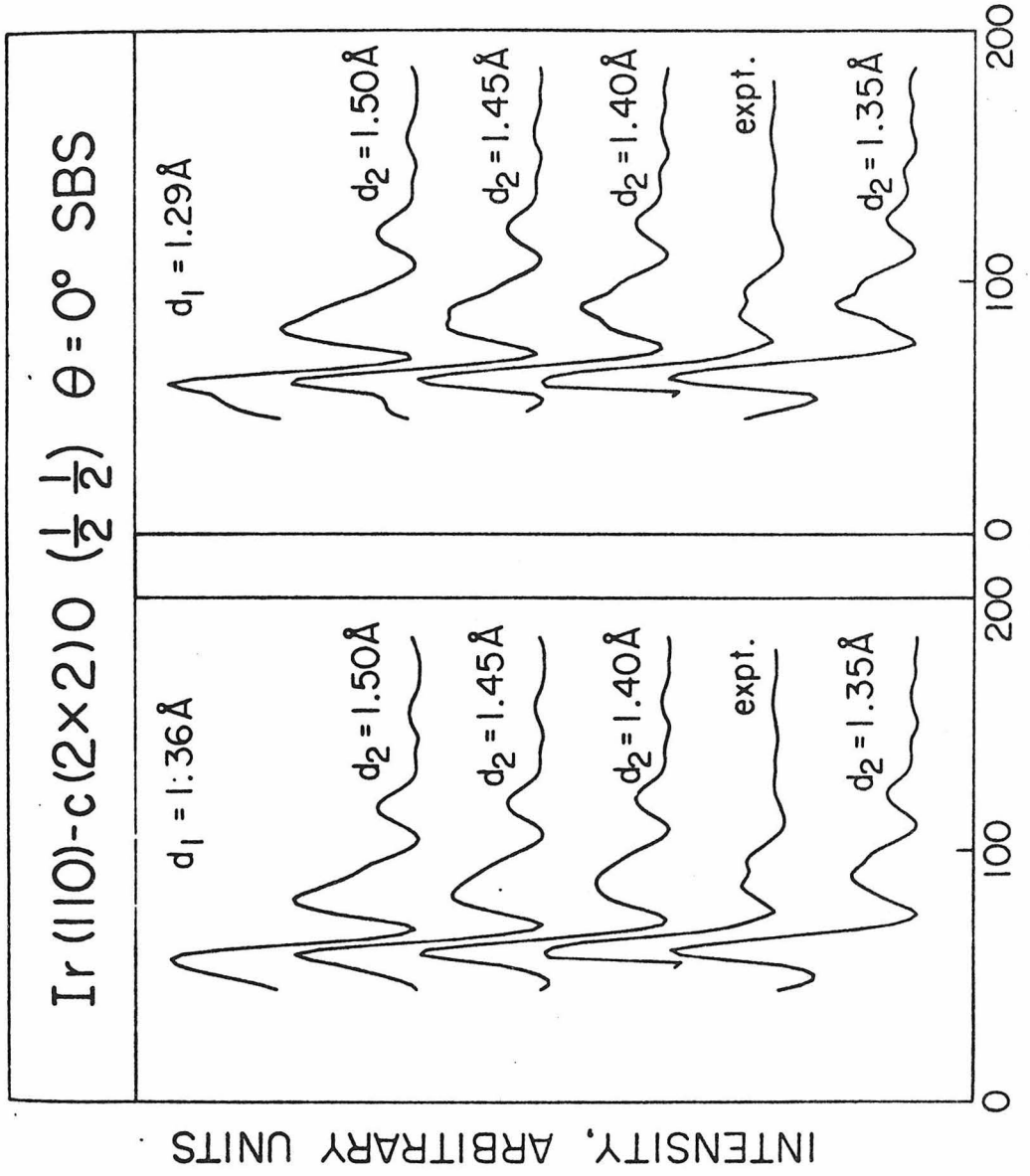
Ir (110)-c(2×2)O $(\frac{1}{2}\ \frac{1}{2})$ θ=0° SBS
d_1 = 1.36Å
d_2 = 1.50Å
d_2 = 1.45Å
d_2 = 1.40Å
expt.
d_2 = 1.35Å
d_1 = 1.29Å
d_2 = 1.50Å
d_2 = 1.45Å
d_2 = 1.40Å
expt.
d_2 = 1.35Å
0
100
200
200
100
0
E, eV
INTENSITY, ARBITRARY UNITS

Fig. 10

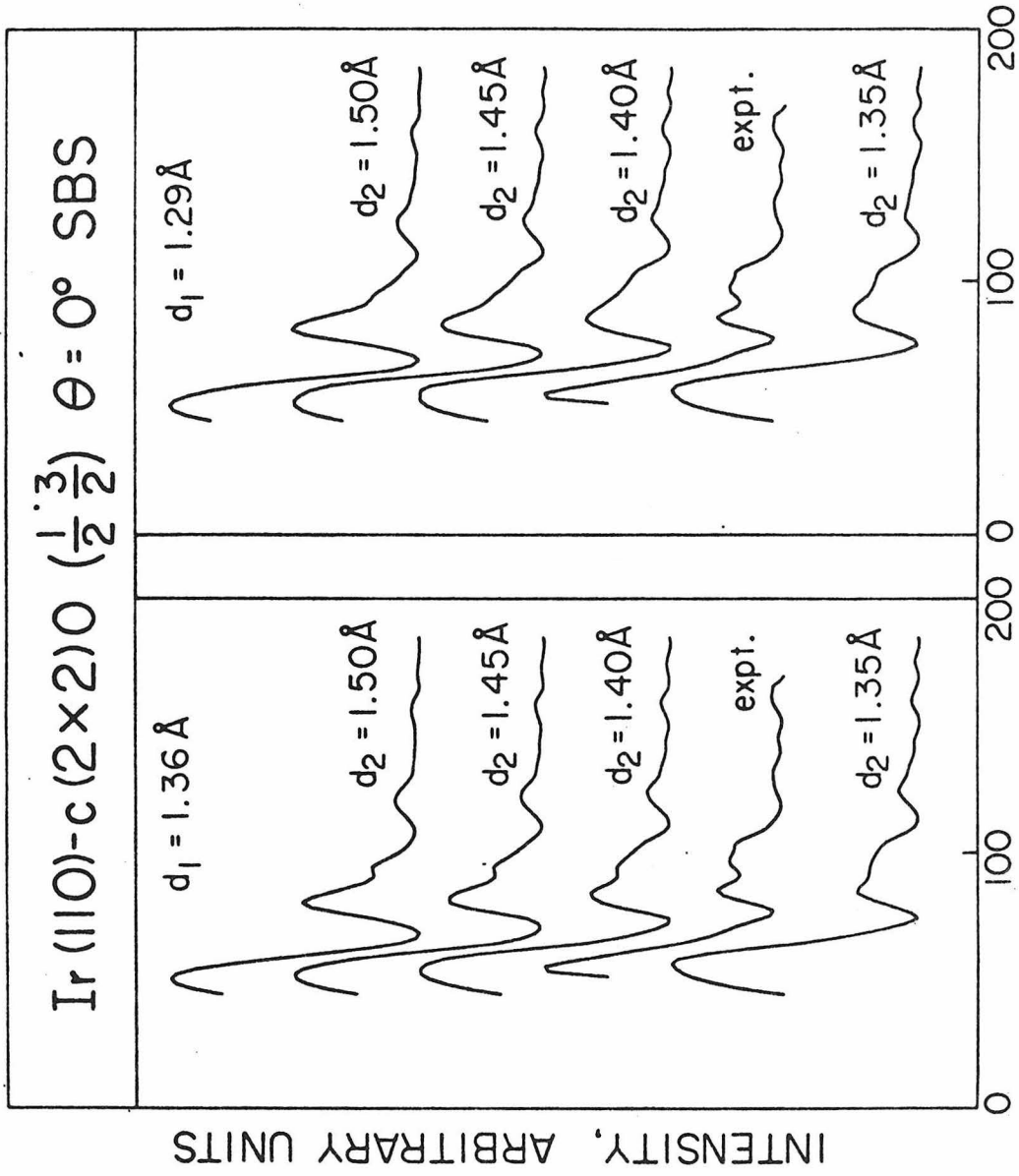
Ir (110)-c (2×2)O $(\frac{1}{2}\cdot\frac{3}{2})$ θ = 0° SBS
d_1 = 1.36 Å
d_2 = 1.50Å
d_2 = 1.45Å
d_2 = 1.40Å
expt.
d_2 = 1.35Å
d_1 = 1.29Å
d_2 = 1.50Å
d_2 = 1.45Å
d_2 = 1.40Å
expt.
d_2 = 1.35Å
0
100
200
200
100
0
E, eV
INTENSITY, ARBITRARY UNITS

Fig. 11

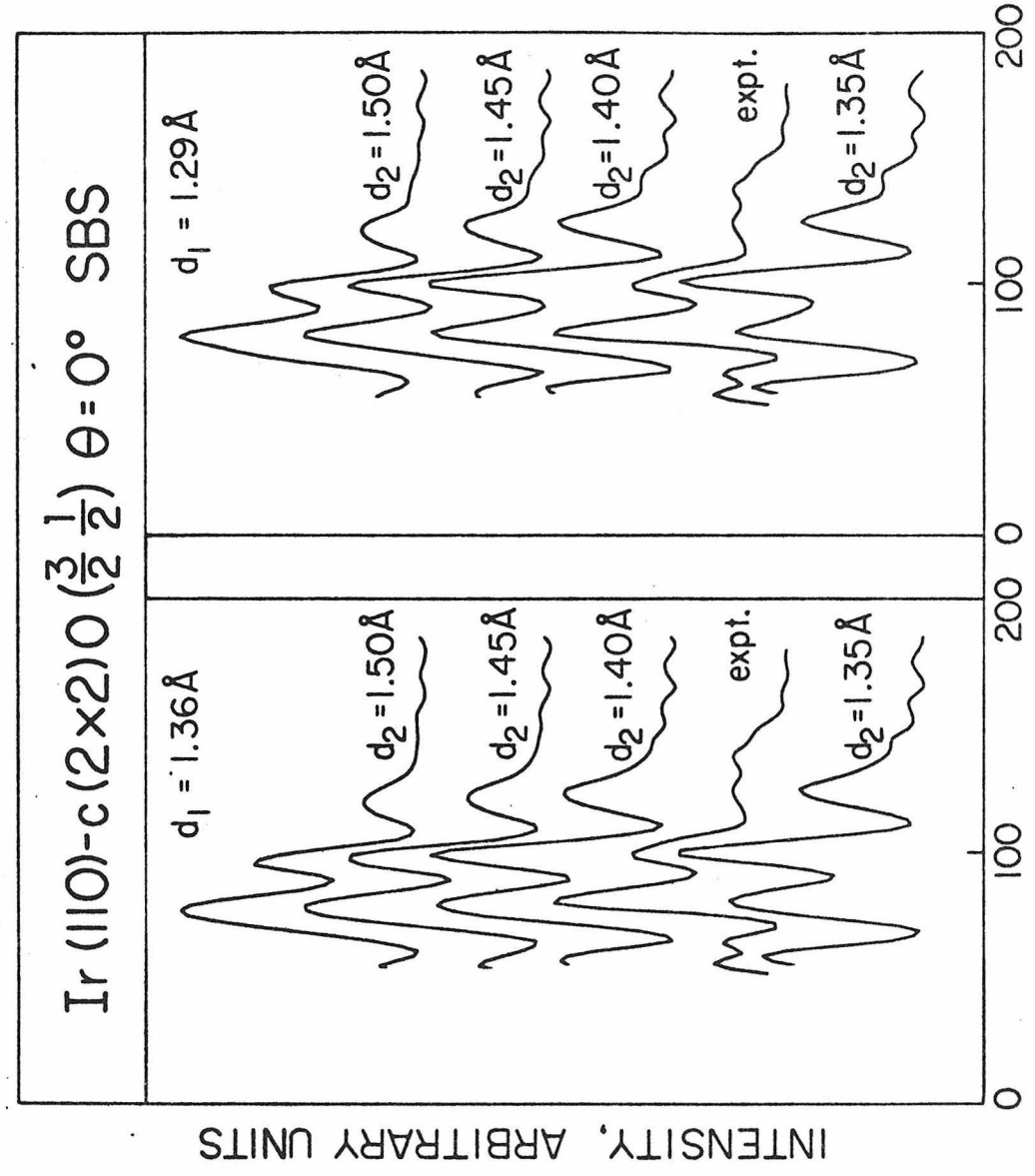
Ir (110)-c(2x2)O $(\frac{3}{2}\ \frac{1}{2})$ θ=0° SBS
d_1 = 1.36Å
d_2=1.50Å
d_2=1.45Å
d_2=1.40Å
expt.
d_2=1.35Å
d_1 = 1.29Å
d_2=1.50Å
d_2=1.45Å
d_2=1.40Å
expt.
d_2=1.35Å
0
100
200
200
100
0
E, eV
INTENSITY, ARBITRARY UNITS

Fig. 12

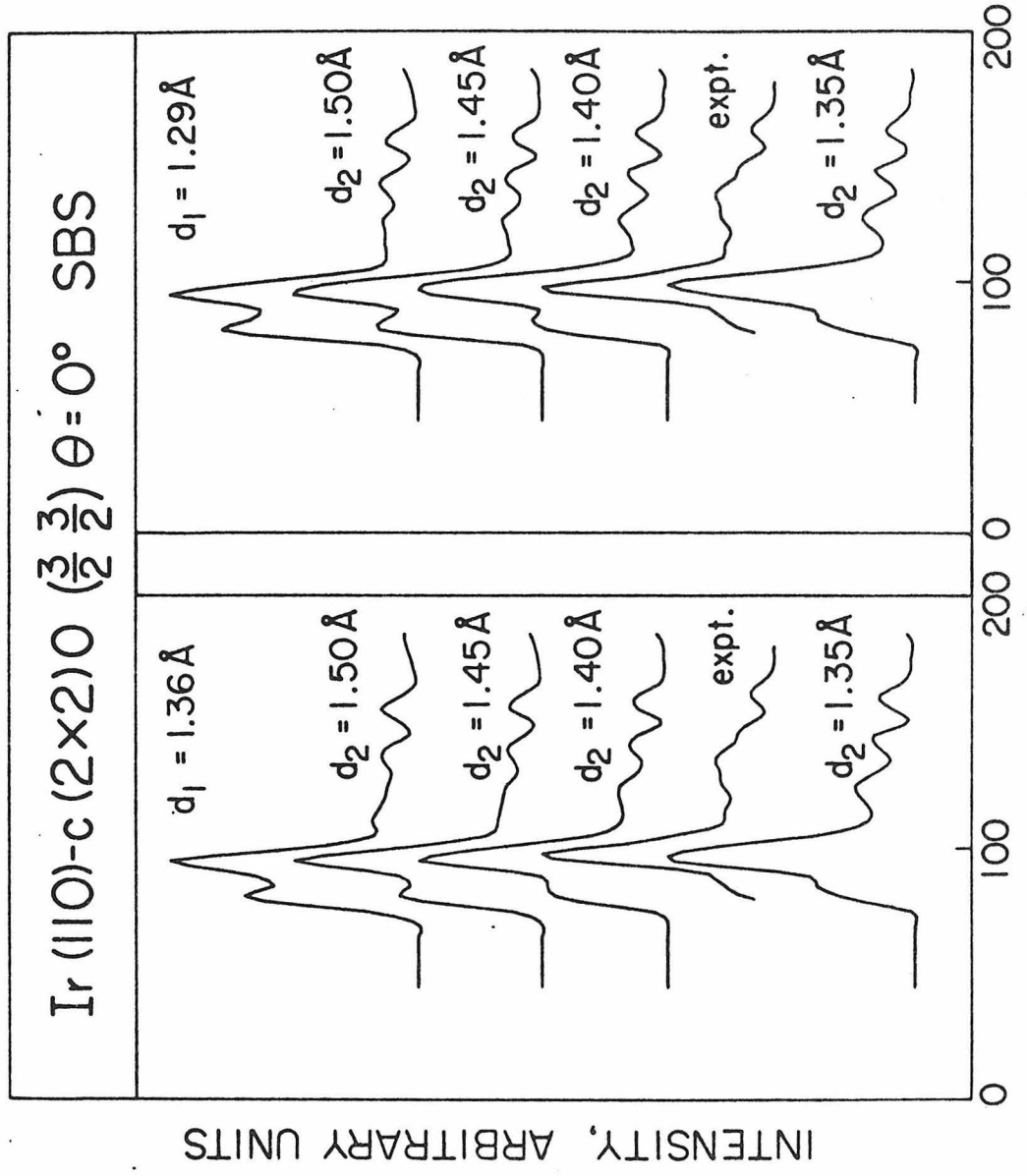
Ir (110)-c (2×2)O $(\frac{3}{2}\frac{3}{2})$ θ=0° SBS
d_1 = 1.36Å
d_2 = 1.50Å
d_2 = 1.45Å
d_2 = 1.40Å
expt.
d_2 = 1.35Å
d_1 = 1.29Å
d_2 = 1.50Å
d_2 = 1.45Å
d_2 = 1.40Å
expt.
d_2 = 1.35Å
0
100
200
200
100
0
E, eV
INTENSITY, ARBITRARY UNITS

Fig. 13

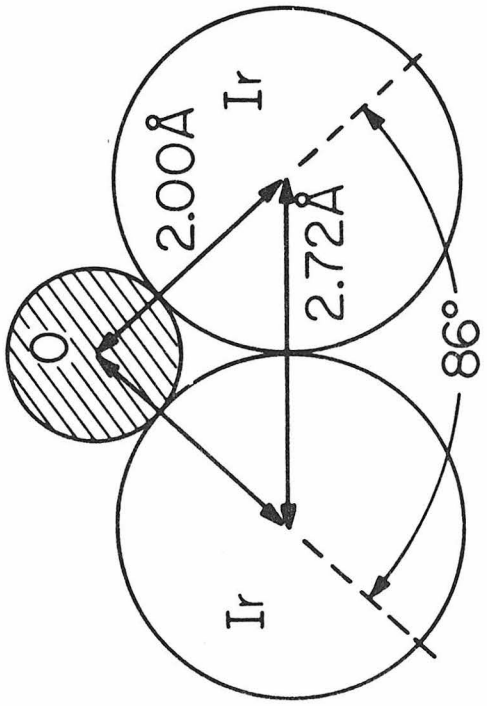

SBS

(a)

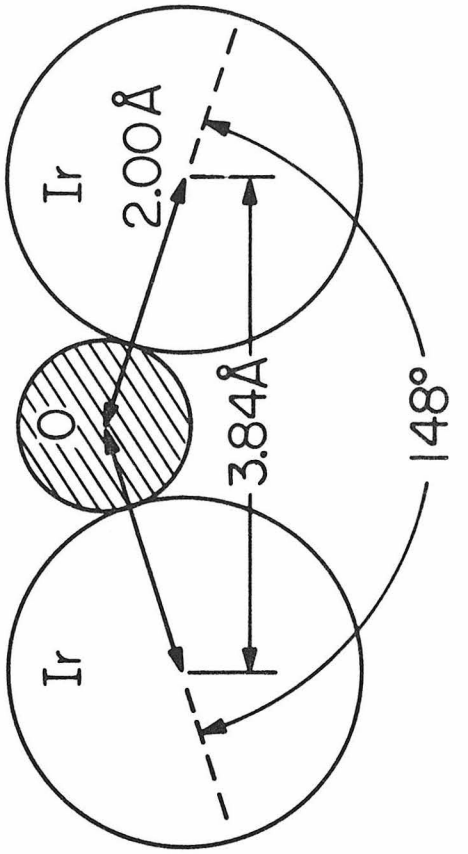

LBS

(b)

Fig. 14

Chapter 6

AN ANALYSIS OF THE STRUCTURE OF THE IRIDIUM (111) SURFACE BY LOW-ENERGY ELECTRON DIFFRACTION

by

C.-M. Chan, S. L. Cunningham, M. A. Van Hove,
W. H. Weinberg and S. P. Withrow

Division of Chemistry and Chemical Engineering
California Institute of Technology
Pasadena, California 91125

Surface Science 66, 394-404 (1977)

ABSTRACT

Elastic low-energy electron diffraction (LEED) intensity vs. voltage (I-V) measurements for the clean Ir(111) surface have been obtained. Seven specular I-V spectra were measured from 15 to 975 eV at incident angles from 7^{o} to 62.5^{o} relative to the surface normal. The outermost atomic layer spacing of the unreconstructed Ir(111) surface was determined both by the convolution-transform method we have presented previously (including certain convenient modifications) and by dynamical calculations. Results from the analysis of the I-V spectra by the convolution-transform method indicate that the outermost Ir(111) layer spacing is either unrelaxed or contracts by 4% of its bulk value depending upon whether the $\theta = 7^{o}$ data or the $\theta = 25^{o}$ data are used. In agreement with this, the dynamical calculations show that the outermost Ir(111) layer spacing contracts by $2.5 \pm 5\%$ and, in addition, that the registry of the first layer of the crystal surface is not shifted, maintaining the fcc structure.

I. INTRODUCTION

The Group VIII transition metals, of which iridium is a member, play a vital role in many important industrial catalytic reactions. Extensive surface studies of the chemisorption of CO, O_2, NO and several hydrocarbons as well as the interaction between CO and O_2 have been made using various experimental techniques including LEED (*1-6*), thermal desorption mass spectrometry (*1,2,7*), work function measurements (*8*), UV photoelectron spectroscopy (*9-12*) and X-ray photoelectron spectroscopy (*12-15*). In spite of these studies on several Ir surfaces, no investigation has been reported concerning the detailed structure of any surface of Ir.

The purpose of this paper is to present surface structural information for clean Ir (111) by an analysis of LEED intensity data. Both a convolution-transform method and a full dynamical calculation are used. It is important at this stage to compare the results from these two methods in order to assess the usefulness of the (kinematic) convolution-transform method. This is the first time that an unknown surface structure has been analyzed by the convolution-transform method.

Previously, we have applied our convolution-transform method to analyze theoretical LEED intensity data for W(110) which were calculated by Van Hove and Tong (*16-18*). That analysis indicated that the convolution-transform method can extract the structural information (top layer relaxation) which is input into the theoretical IV-spectra in spite of the fact that the spectra have very strong multiple-scattering character. In this present work, we test further our convolution-transform method by applying it to experimental data which are highly dynamic. This paper illustrates explicitly the use of a simple analysis method to obtain surface structural information.

In Sec. II, the experimental procedures and apparatus are described. In Sec. III, a brief outline is presented of the convolution-transform method. Here, an improvement to the method is described in detail which allows a more satisfactory presentation of the structural solution for the case of small relaxations. In Sec. IV, the results from the dynamical calculations are presented. The conclusions of our work are brought together in Sec. V.

II. EXPERIMENTAL DETAILS

All experimental results were obtained using a conventional stainless steel ultra-high vacuum (UHV) chamber pumped both by a sputter ion pump as well as a liquid nitrogen cooled cryopanel in conjunction with a titanium sublimation pump. The base pressure of the UHV apparatus is $\lesssim 8 \times 10^{-11}$ torr, and the working pressure is in the low 10^{-10} torr regime. The system is a multitechnique instrument in which LEED, Auger electron spectroscopy, quadrupole mass spectrometry, X-ray and UV photoelectron spectroscopy, and contact potential difference measurements may all be made *in situ*. In particular, the UHV chamber contains four-grid LEED optics with a rotatable Faraday cup collector for measuring directly the diffracted electron beam current. The surface composition was determined by Auger electron spectroscopy using a double-pass cylindrical mirror energy analyzer with a glancing incidence electron gun, while a quadrupole mass spectrometer was used both to monitor gas phase partial pressures as well as to cross check surface composition via thermal desorption measurements.

The Ir single crystal was oriented to within $1/4^{o}$ of the (111) plane using the back-reflection Laue X-ray technique, and it was cut to a thickness of approximately 25 mils with a rotating wire saw and polished on both sides using conventional metallurgical methods. The final polish consisted of 0.25μ diamond paste. The crystal was then mounted on a high precision manipulator which possesses three linear and two angular degrees of freedom. The temperature of the crystal could be varied between approximately 150 and $1500^{o}K$ using liquid N_2 cooling and indirect (radiation) heating. Heating rates of up to $15^{o}K$/sec were possible, and the Ir temperature was measured with a Pt/Pt-10% Rh thermocouple which was spotwelded to the back side of the crystal.

Upon initial installation in the UHV chamber, the Ir crystal was annealed extensively at 1200°K and then subjected to several alternate cycles of Ar^+ bombardment (10^{-4} A/cm^2) and heating to 800°K in 10^{-6} torr O_2. This procedure, coupled with a final anneal at 1500°K to ensure essentially complete desorption of O_2, was sufficient to produce a surface which was free of all impurities as judged by Auger electron spectroscopy. This cleaning procedure also produced a well ordered surface which yielded sharp LEED spots with a low background intensity which is characteristic of an unreconstructed Ir(111) surface in agreement with earlier work (*1,2,3,8*). The maximum exposure to background gases during the measurement of each of the LEED I-V beam profiles was 5×10^{13} molecules/cm^2. This was expected to allow a *maximum* surface contamination of <5% of a monolayer, and this expectation was verified both by thermal desorption measurements and Auger electron spectroscopy.

All I-V beam profiles were recorded by collecting the diffracted beam current with the rotatable Faraday cup. The cup aperture was 40 mils in diameter subtending an angle of 4° at the crystal surface. This allowed the collection of at least 90% of the individual spot intensities. The current measured by the Faraday cup was amplified by a picoammeter and plotted as a function of (corrected) electron beam energy on an XY recorder. A set of six Helmholtz coils, three feet in diameter, was used to reduce residual magnetic fields near the crystal to a value sufficiently low that the specularly diffracted beam remains stationary at incident beam energies from 15 to 1000 electron volts (with an incident beam flux of the order of 1 μA/mm^2).

The angle of incidence of the electron beam incident on the crystal was determined by photographing the LEED pattern as described in detail

elsewhere (*19*). The position of the diffraction beams on the fluorescent screen was calibrated *a priori* in terms of the incident angle by photographing the nonspecular spots with normal incidence of the electron beam for a variety of incident beam voltages. This is useful since the angle of emergence of these nonspecular beams can be calculated from the beam voltage and the known lateral periodicity of the crystal surface. A careful estimate of the error involved in such determinations of the incidence angle is $\pm 0.3^{o}$ (*19*).

Seven I-V specular beam profiles are presented in Fig. 1 for incidence angles between approximately 7^{o} and 63^{o}. The azimuthal angle is constant and corresponds to the $\vec{k}$-vector of the incident electron beam pointing perpendicularly to a close-packed row of Ir surface atoms. All beam profiles extend from 15 to 975 volts, and all were measured at a surface temperature of approximately 350^{o}K. Nonspecular beam profiles are not shown since an analysis of the specular beam only, both by Fourier transform (kinematic) techniques in Sec. III and by full multiple scattering calculations in Sec. IV, is sufficient to describe the surface layer spacing of clean Ir(111).

III. CONVOLUTION-TRANSFORM METHOD

In our earlier work (*16-18*), a variation of the transform-deconvolution method of Landman and Adams (*20,21*), we have described a convolution-transform method to determine the outermost layer spacing of a crystal surface. There, an "observed" Patterson function, $P_o(z)$, (z is the space coordinate perpendicular to the crystal surface) is obtained which is the Fourier transform of the electron beam intensity as a function of electron momentum transfer perpendicular to the crystal surface. Using a kinematic model, a calculated Patterson function, $P_c(z)$, is constructed which is the convolution product of the Fourier transform of a window function and a set of delta functions representing the outer layer spacings of the crystal. It is given as

$$P_c(z) = \sum_i g_i [W(z+z_i) + W(z-z_i)] \quad , \tag{1}$$

where W(z) is the Fourier transform of the windown function, the set (z_i) gives the positions of the trial delta functions, and the coefficients (g_i) are the relative weights of the delta functions. By varying the position of the delta functions to obtain the best fit between the "observed" and calculated Patterson functions, the outermost layer spacing of the crystal surface can be determined. This best fit is determined by finding the minimum of a parameter called the residual, the square of which is given by

$$R^2 = \int_o^\infty [P_o(z) - P_c(z)]^2 \, dz \quad . \tag{2}$$

This method has been discussed in detail in ref. *17*.

Here the method is reviewed briefly by delineating its seven basic steps.

(1) A window function is chosen which delimits the energy range and defines the envelope of the experimental data as shown in Figs. 2(a) and 2(b).

(2) A value of the inner potential V_o (which is one of the two variable parameters) is chosen, as V_o is needed to convert energy space to momentum transfer space.

(3) The "observed" Patterson function $P_o(z)$ is obtained by Fourier transforming the intensity from momentum space into real space.

(4) The position of a set of trial delta functions, $\{z_i\}$, representing interlayer distances is chosen. This set is completely specified by the known bulk interlayer spacing and one parameter t, the percentage of expansion of the surface layer spacing. The relative weights of these delta functions $\{g_i\}$ are unknown.

(5) The set of relative weights $\{g_i\}$ which results in a least square fit between $P_o(z)$ and $P_c(z)$ is determined by minimizing the residual with respect to the unknown weights. In our previous work on the W(110)surface (*17*), nine delta functions were used which resulted in nine linear equations in the nine unknown weights.

(6) The residual in eq. (2) is evaluated using the determined weights and normalized by dividing by the value of R obtained from eq. (2) with $P_c(z) = 0$.

(7) The procedure is repeated with other values of V_o and other sets of interlayer spacings, and the correct surface structure appears as a minimum of the residual as a function of V_o and t. The minimum in the residual surface is characterized by its depth, which we describe by the parameter.

$$\Delta = 100\ (R_{ave} - R_{min})/R_{ave}, \qquad (3)$$

where R_{ave} is the average value of the residual in the residual surface and R_{min} is its value at the minimum. The deepest possible minimum ($R_{min} = 0$) gives $\Delta = 100\%$.

Using these seven steps, solutions from relaxed and unrelaxed surfaces occur as a minimum and a trough, respectively, in the residual surface (*17*).

The reasons for obtaining a trough for the case of the unrelaxed surface, as discussed fully in ref. (*17*), is that for this case the weights of the trial delta functions at the relaxed positions are very small. Therefore, the fit between theory and experiment is hardly dependent on the choice of the relaxation, and this is manifest as a trough in the residual surface.

The appearance of a trough, although a logical consequence of the procedure described above, is not totally satisfactory; one would prefer an unrelaxed surface also to produce a minimum in the residual surface at zero percent relaxation. Therefore, the method has been modified in the following way. A condition is imposed on the relative weights of the delta functions, namely, that they decay into the crystal in accordance with the decay of the electron flux. From kinematic theory, these weights are:

$$\left.\begin{aligned} g_1(z = 0) &= g_o(1 - \alpha^2(1-\alpha^{2t})) \\ g_{2n}(z = nd) &= g_o\alpha^{n+2}\,\alpha^{2t} \\ g_{2n+1}(z = (n+t)d) &= g_o(1-\alpha^2)\alpha^n\alpha^t \end{aligned}\right\} \quad n = 1, 2 \ldots \tag{4}$$

where

$$g_o = \frac{\alpha^{-2t}}{1 - \alpha^2}\,\Omega \tag{5}$$

and

$$\alpha = \exp\left\{-\frac{d}{2\lambda(E)}\left|\frac{1}{\cos\theta} + \frac{1}{\cos\theta'}\right|\right\}. \tag{6}$$

Here d is the known bulk spacing of the crystal, $\lambda(E)$ is the inelastic mean free path of the electron, θ and θ' are the angles relative to the surface normal of the incident and scattered beams, respectively, and Ω is a variable parameter that adjusts the absolute magnitudes of the delta functions. We choose to consider g_o and α to be the only two unknown adjustable parameters, and they are assumed to be independent of energy. Hence, step (5) above has been modified as follows. The residual is minimized now with respect to the

variables α and g_o, for each choice of relaxation t and inner potential V_o. This results in two non-linear equations in two unknowns (instead of nine). The other six steps remain unchanged. Thus, with this change in step (5), the residual automatically contains the information about the "quality" of the relative weights $\{g_i\}$, which in the earlier version of the method had to be examined separately (*17*).

From an examination of the seven measured I-V spectra for the Ir(111) surface, it appears that the I-V spectra at $\theta = 7°$ and $\theta = 25°$ are more kinematic than the spectra obtained at other angles of incidence, and therefore these are particularly suitable for analysis by the convolution-transform method. We have discussed the choice of an energy range and a window function in ref. *17*. In this analysis, we use I-V spectra that contain three Bragg peaks. We neglect the lowest energy peak since uncertainties in the small incident beam current measurement (see Fig. 1) can affect both its location and shape. The window functions used are the drawn envelopes shown in Figs. 2 (a) and 2(b). Figures 2(c) and 2(d) show the residual surfaces from our first version of the convolution-transform method at $\theta = 7°$ and $\theta = 25°$, respectively. Both have a well defined trough; the one in Fig. 2(c) is at $V_o = 11$ eV, and the other in Fig. 2(d) is at $V_o = 8$ eV. The existence of the trough across the residual surfaces indicates the surface is unrelaxed or at most slightly relaxed, but determining a quantitative value is impossible. This unsatisfactory feature has been removed by the new scheme as shown in Figs. 2(e) and 2(f) which show the residual surfaces of the same spectra using the modified convolution-transform method. The minimum in Fig. 2(e) occurs at $V_o = 13$ eV and $t = 0\%$ having a relative depth of $\Delta = 60\%$, while the minimum in Fig. 2(f) occurs

at V_o = 7 eV and t = -4% having a relative depth of Δ = 43%. Comparing the results from the old and new schemes, the latter obviously presents the solution in a more desirable way.

From this, we conclude that the surface layer of the Ir(111) crystal is contracted from 0% to 4% of its bulk value of d = 2.217 Å. We do not yet have enough experience with this method to be able to set accurate error limits on this structure determination.

IV. MULTIPLE-SCATTERING ANALYSIS

Using full dynamical (i.e., multiple scattering) calculations, we have analyzed the LEED intensity spectra of Ir(111) for the (00) beam at three angles of incidence: $\theta = 7^{o}$, 13.5^{o} and 25^{o}. The reason for performing this multiple scattering analysis is to confirm that the structure determined by the convolution-transform method is correct.

The atomic potential for iridium is a band-structure potential obtained from Arbman and Hörnfelt (*22*) and includes a full Slater exchange. Eight phase shifts were used, modified for atomic vibrations. The temperature is 350^{o}K, the bulk Debye temperature is taken as 280^{o}K, and an enhancement factor of 1.43 is chosen for the surface mean-square vibrational amplitudes in all atomic layers (this represents a layer-averaged result of surface dynamics). An assumed value of 15 eV was given to the real part of the inner potential (muffin-tin zero), and this quantity was allowed to be modified *a posteriori* by a rigid shift of the energy scale in the comparison with experiment. An energy-independent imaginary part of the inner potential of 5 eV was used to represent inelastic processes. The thermal and inelastic properties are of secondary importance in structure determination, and these were therefore not optimized in this analysis.

The perturbation scheme called renormalized forward scattering (*23*) was chosen for efficiency (good convergence occurred despite the strong atomic scattering amplitude), while the twofold symmetry present at the selected angles of incidence was exploited.

In the calculations, the outermost layer of the Ir(111) surface was allowed to relax outward and inward. Fig. 3 shows the comparison between theory and experiment. Theoretical curves for no relaxation and 5% contraction (intermediate positions need not be considered) are presented. Expansion

and stronger contraction produced less good agreement with experiment than these. The unrelaxed surface agrees best with an inner potential modified from 15 to 9 eV, while the 5% contracted surface prefers a modification from 15 to 12.5 eV.

The agreement between experiment and theory makes a lateral shift of the top atomic layer to an hcp configuration highly unlikely; calculations with such a shift were therefore not undertaken.

It seems difficult on the basis of these comparisons to decide between an unrelaxed and a 5% contracted surface, which is consistent with the usual accuracy of this calculational method, namely 0.1 Å [the bulk iridium (111) layer spacing is 2.217 Å]. We therefore conclude from dynamical calculations that a contraction of the top iridium (111) spacing by 2.5 ± 5% occurs.

V. CONCLUSIONS

Our major conclusions may be summarized as follows:

(1) Our work shows that both the convolution-transform method and dynamical calculations give the same degree of relaxation in the case of a strongly scattering material which exhibits highly dynamical behavior in many of the measured I-V spectra.

(2) The outermost layer of the Ir(111) surface contracts by less than 5% of its bulk value.

(3) The dynamical calculations show that the first layer of the Ir(111) surface is not shifted to an hcp configuration but maintains an fcc structure.

(4) The results are consistent with LEED analyses reported previously for the (111) surfaces of other fcc metals, e.g., Al (*24*), Ni (*25*), Cu (*26*), Ag (*27*) and Pt (*28*).

(5) Comparing the results from the two versions of the convolution-transform method, the newer version is clearly a more desirable way to present the solution from unrelaxed or slightly relaxed data.

ACKNOWLEDGMENT

We gratefully acknowledge the help of G. O. Arbman and S. Hörnfelt who supplied us with the atomic potential for iridium, and we appreciate the assistance of K. Luke in the data collection. This work was supported by the Army Research Office (Durham) under Grant Number DAH CO4-75-0170. Partial support was also obtained from the Donors of the Petroleum Research Fund administered by the American Chemical Society (Grant Number 6809-AC5,7).

REFERENCES

1. J. Küppers and A. Plagge, J. Vacuum Sci. Technol. 13, 259 (1976).
2. C. M. Comrie and W. H. Weinberg, J. Chem. Phys. 64, 250 (1976); J. Vacuum Sci. Technol. 13, 264 (1976).
3. J. T. Grant, Surface Sci. 25, 45 (1971).
4. J. T. Grant and T. W. Haas, Surface Sci. 21, 76 (1970).
5. G. Brodén, T. Rhodin and W. Capehart, Surface Sci. (to be published).
6. K. Christmann and G. Ertl, Z. Naturforsch. 28a, 1144 (1973).
7. V. P. Ivanov, G. K. Boreskov, V. I. Savchenko, W. F. Egelhoff, Jr. and W. H. Weinberg, J. Catal. (in press).
8. V. P. Ivanov, G. K. Boreskov, V. I. Savchenko, W. F. Egelhoff, Jr. and W. H. Weinberg, Surface Sci. 61, 207 (1976).
9. T. N. Rhodin, C. Brucker, G. Brodén, Z. Hurych and R. Benbow, "Synchrotron Radiation Study of Orbital Symmetries of Chemisorbed CO on Ir(100) using Polarization Dependent Photoemission" (to be published).
0. G. Brodén, T. N. Rhodin, C. Brucker, R. Benbow and Z. Hurych, Surface Sci. 59, 593 (1976).
1. J. Kanski and T. N. Rhodin, Surface Sci. (to be published).
2. P. A. Zhdan, G. K. Boreskov, A. I. Boronin, W. F. Egelhoff, Jr. and W. H. Weinberg, Chem. Phys. Letters 44, 528 (1976).
3. P. A. Zhdan, G. K. Boreskov, W. F. Egelhoff, Jr. and W. H. Weinberg, J. Catal. 45, 281 (1976).
4. P. A. Zhdan, G. K. Boreskov, A.I. Boronin, W. F. Egelhoff, Jr. and W. H. Weinberg, Surface Sci. 61, 25 (1976).
5. P. A. Zhdan, G. K. Boreskov, W. F. Egelhoff, Jr. and W. H. Weinberg, Surface Sci. 61, 377 (1976).

16. G. L. Griffin, S. L. Cunningham and W. H. Weinberg, Bull. Am. Phys. Soc. 21, 320 (1976).

17. S. L. Cunningham, C.-M. Chan and W. H. Weinberg, Phys. Rev. B (in press).

18. S. L. Cunningham. C.-M. Chan and W. H. Weinberg, J. Vacuum Sci. Technol. 14, 312 (1977).

19. S. L. Cunningham, B. M. Hall and W. H. Weinberg (in preparation).

20. U. Landman and D. L. Adams, J. Vacuum Sci. Technol. 11, 195 (1974).

21. D. L. Adams, U. Landman and J. C. Hamilton, J. Vacuum Sci. Technol. 12, 260 (1975).

22. G. O. Arbman and S. Hörnfelt, J. Phys. F: Metal Phys. 2, 1033 (1972); and private communication.

23. J. B. Pendry, Low-Energy Electron Diffraction, Academic Press (London) 1974.

24. D. W. Jepsen and P. M. Marcus, Phys. Rev. B 6, 3684 (1972).

25. J. E. Demuth, P. M. Marcus and D. W. Jepsen, Phys. Rev. B 11, 1460 (1975).

26. P. M. Marcus, D. W. Jepsen and F. Jona, Surface Sci. 31, 180 (1972).

27. D. W. Jepsen, P. M. Marcus and F. Jona, Surface Sci. 39, 27 (1973).

28. L. L. Kesmodel and G. A. Somorjai, Phys. Rev. B 11, 630 (1975).

FIGURE CAPTIONS

Figure 1: The top curve is the correction curve for incident electron beam current as a function of beam voltage. All others are I-V spectra of the (00) beam of the Ir(111) surface at different angles of incidence, θ. The azimuthal angle is constant and corresponds to the $\vec{k}$-vector of the incident electron beam pointing perpendicularly to a row of close-packed surface atoms.

Figures 2: (a) and (b) I-V curves and drawn windows for $\theta = 7°$ and $\theta = 25°$, respectively, from Ir(111) surface.

(c) and (d) Topographic plots for the residual surface, R(in %), from the earlier version of the convolution-transform method as a function of inner potential (V_0) and % relaxation (t) for $\theta = 7°$ and $\theta = 25°$, respectively.

(e) and (f) Same as (c) and (d) from the modified version of the convolution-transform method.

Figure 3: Comparison of experimental and theoretical I-V curves for the (00) beam diffracted from Ir(111) at three angles of incidence $\theta = 7°$, 13.5°, 25° (azimuth described in caption of Fig. 1). The theoretical curves apply to contractions of the top atomic layer spacing by 9% and 5%. The muffin-tin zero is at -9 eV and -12.5 eV, respectively, for these cases.

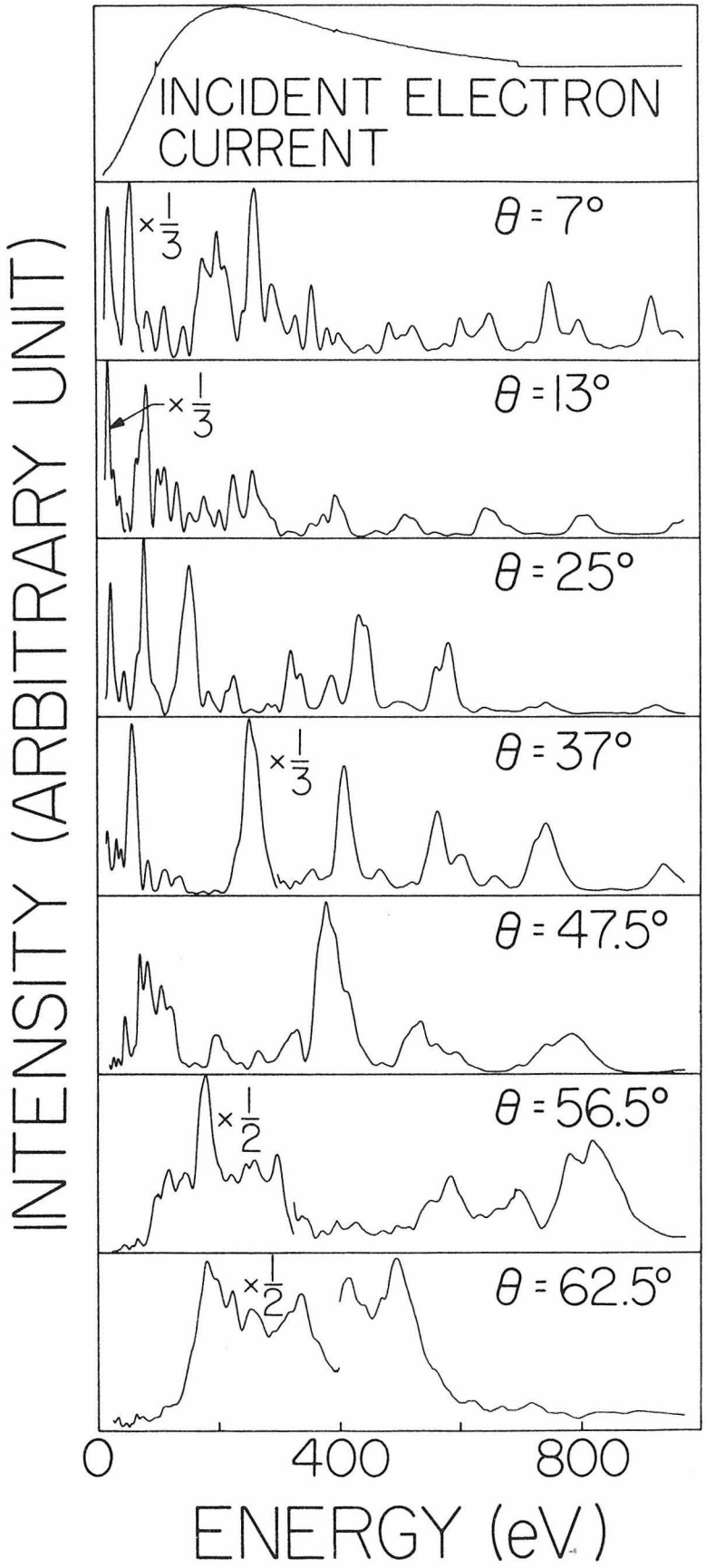
INCIDENT ELECTRON CURRENT
θ = 7°
×1/3
θ = 13°
×1/3
θ = 25°
θ = 37°
×1/3
θ = 47.5°
θ = 56.5°
×1/2
θ = 62.5°
×1/2
INTENSITY (ARBITRARY UNIT)
0
400
800
ENERGY (eV)

Figure 1

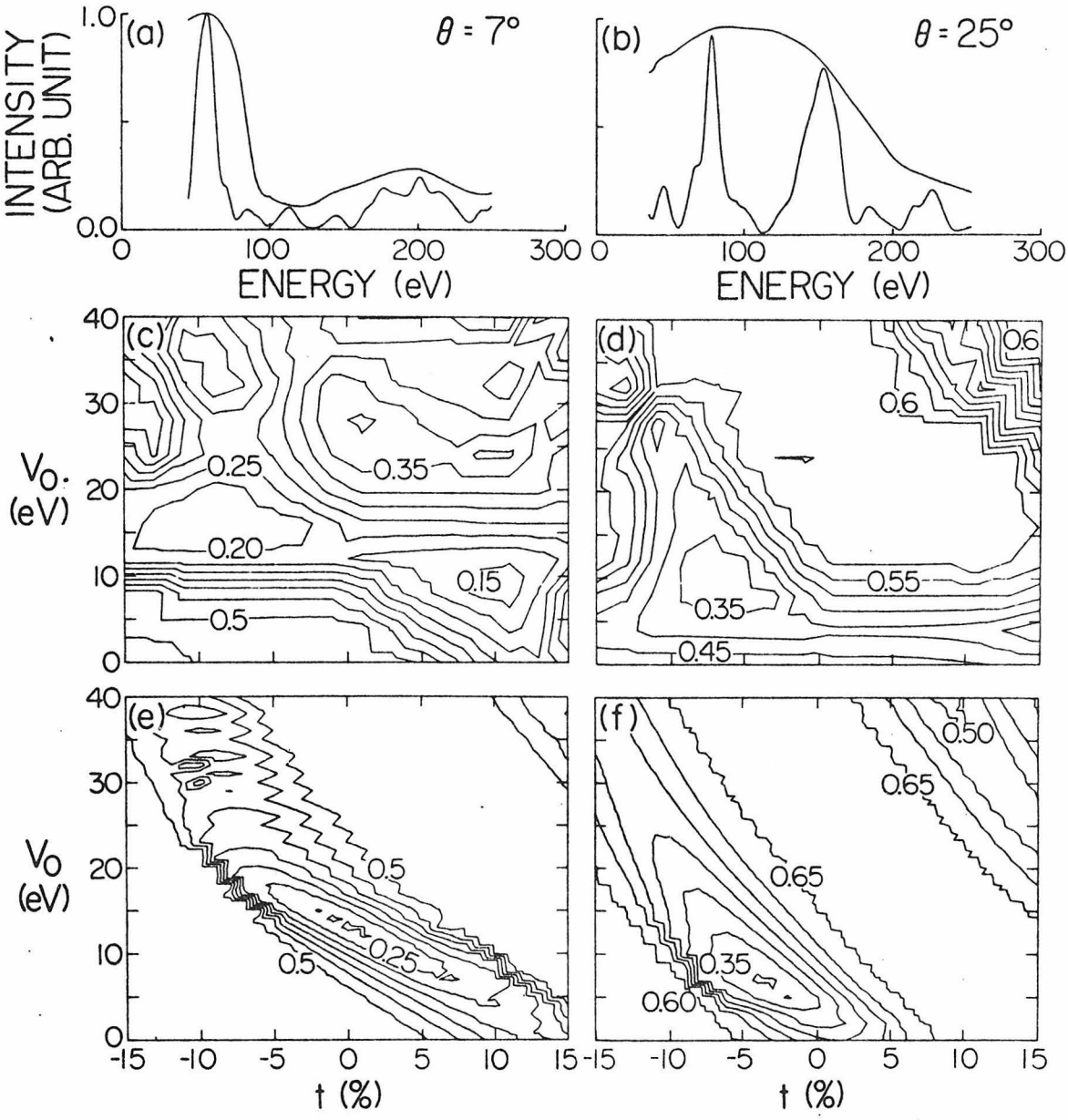
INTENSITY (ARB. UNIT)
1.0
0.0
(a)
θ = 7°
(b)
θ = 25°
0
100
200
300
ENERGY (eV)
(c)
(d)
(e)
(f)
V_0 (eV)
40
30
20
10
0
0.25
0.35
0.20
0.15
0.5
0.6
0.55
0.45
0.50
0.65
0.60
-15
-10
-5
0
5
10
15
t (%)

Figure 2

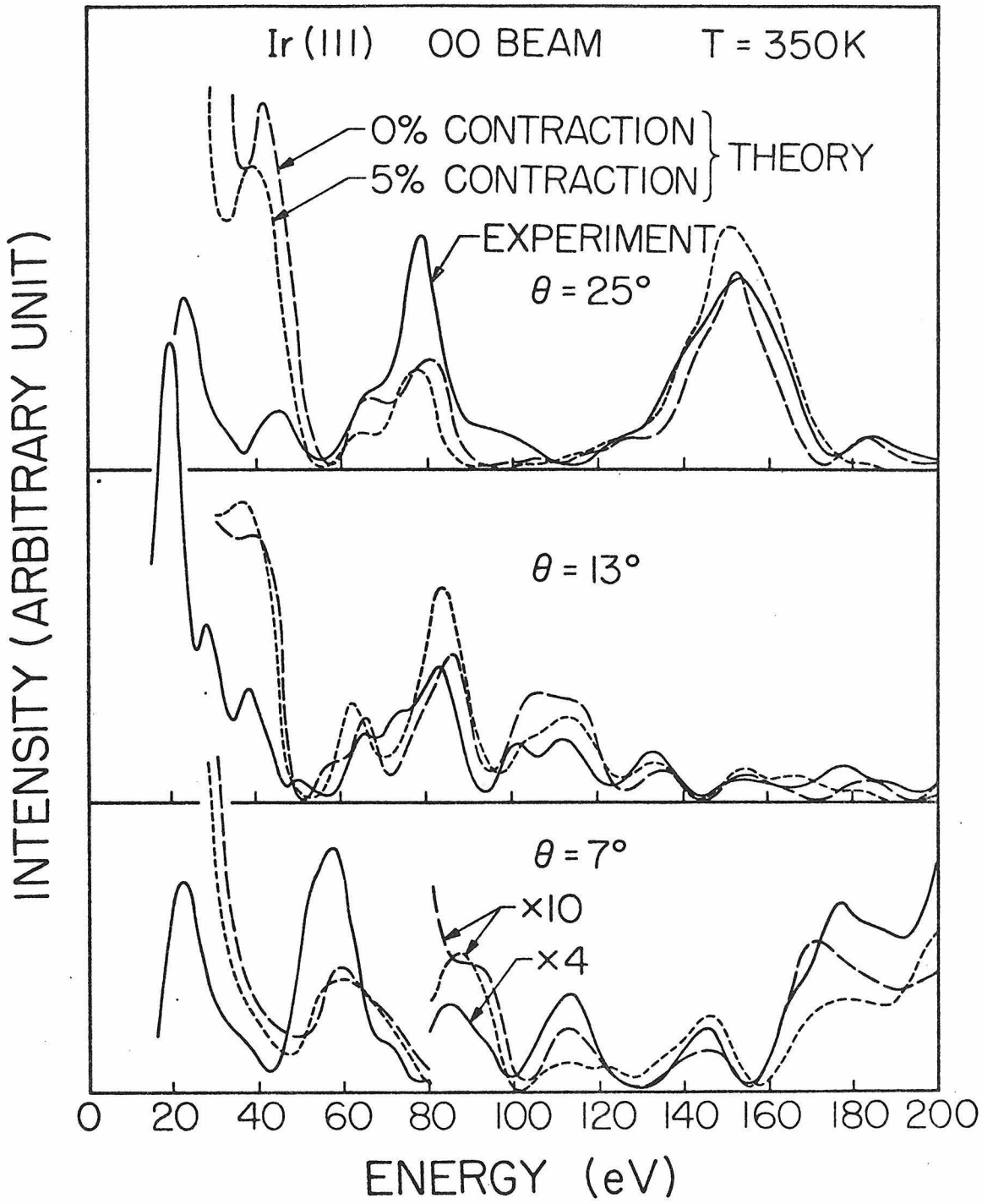
Ir (111) 00 BEAM T = 350K
0% CONTRACTION
5% CONTRACTION
THEORY
EXPERIMENT
θ = 25°
θ = 13°
θ = 7°
×10
×4
INTENSITY (ARBITRARY UNIT)
0 20 40 60 80 100 120 140 160 180 200
ENERGY (eV)

Figure 3

Chapter 7

LOW-ENERGY ELECTRON DIFFRACTION STRUCTURAL ANALYSIS OF THE "(2x2)" OXYGEN OVERLAYER ON THE IRIDIUM (111) SURFACE

by

C.-M. Chan and W. H. Weinberg

Division of Chemistry and Chemical Engineering
California Institute of Technology
Pasadena, California 91125

Submitted to the Journal of Chemical Physics

Abstract

Exposure of a clean Ir(111) surface at room temperature to approximately 20 Langmuirs of oxygen produces a sharp "(2x2)" LEED pattern. This LEED pattern can be caused by two fundamentally different adsorbate superstructures: a p(2x2) array of oxygen atoms (one-quarter monolayer coverage) or three independent, equivalent domains of a (1x2) superstructure rotated 120^{o} with respect to one another (half-monolayer coverage). Dynamical calculations have been performed for the three most symmetric adsites on this surface: the on-top site and the two different types of three-fold sites for both the p(2x2) and the three domains of (1x2) superstructures. The results show that the oxygen adatoms, either forming a p(2x2) superstructure or the three domains of (1x2) superstructure rotated 120^{o} with respect to one another, reside on the three-fold site directly above a vacancy in the second substrate layer with a interlayer spacing of 1.30 $\mathring{A}$ corresponding to an Ir-O bond length of 2.04 $\mathring{A}$.

1. Introduction

It was suggested by Tucker (1) in 1964 that a "(2x2)" overlayer low-energy electron diffraction (LEED) pattern from an fcc (111) substrate surface can be caused either by a p(2x2) surface structure or by three domains of (1x2) surface structure rotated 120^{o} with respect to one another. This problematic situation presents a very challenging and important problem in the field of LEED structural analysis. Overlayer structures of oxygen on the close-packed surfaces of Ni (2), Ru (3), Rh (4), Pd (5), Ir (6) and Pt (7) are typical examples of this uncertainty in the detailed structure. In the course of LEED crystallography, only one preliminary and equivocal result on the study of a (2x2) oxygen overlayer structure on the Ni(111) surface has been published (8). The absence of a successful structural determination reflects the difficulty involved in such an analysis.

To clarify the confusing situation concerning the overlayer structure of oxygen on the (111) surface of an fcc metal, this work set out to determine the adsorption site of oxygen forming a "(2x2)" superstructure on Ir(111). A determination of the binding site was successful in spite of the inability to distinguish between the p(2x2) and the three domains of (1x2) superstructures, a consequence of the fact that the calculated IV beam profiles for the p(2x2) and the (1x2) superstructures are very similar.

2. Experimental Procedure

The experimental apparatus is identical to that described previously (9). A sharp "(2x2)" superstructure was observed when the clean (111) surface of Ir was exposed to approximately 20 Langmuirs (1 Langmuir $\equiv 10^{-6}$ torr-sec) of oxygen at room temperature.

Intensity-voltage (IV) profiles for three integral-order and seven half-order beams were measured at approximately 2 eV intervals. These beams are the (10), (01), (11), $(0\ \frac{1}{2})$, $(\frac{1}{2}\ 0)$, $(\frac{1}{2}\ \frac{1}{2})$, $(0\ \frac{3}{2})$, $(\frac{3}{2}\ 0)$, $(\frac{1}{2}\ 1)$ and $(1\ \frac{1}{2})$. All the IV beam profiles have been normalized to unit incident beam current and measured at normal incidence, the latter in order to exploit simplifications due to symmetry in the calculations. The unit cells of the p(2x2) and the (1x2) superstructures and the schematic LEED pattern for the "(2x2)" structure are shown in Figs. 1(a) and 1(b), respectively.

3. Results

Renormalized Forward Scattering was used for the analysis of the measured LEED IV spectra (10). A band structure potential which includes full Slater exchange was used to describe the Ir substrate (11). A superposition potential obtained by overlapping atomic charge densities was used for the oxygen overlayer (12,13). Seven phase shifts were used for both the Ir substrate and the oxygen overlayer. An assumed inner potential (muffin-tin zero) of 10 eV was used for both the overlayer and the substrate, and this quantity is allowed to vary by a rigid shift of the energy scale in the comparison between experimental and theoretical IV spectra. A constant optical potential (imaginary part of the electron self-energy) of 5 eV was used for both the substrate and overlayer. The interlayer spacing between the overlayer and the substrate

atoms (d) was varied within physically reasonable values ($1.10\ \text{Å} \leq d \leq 2.20\ \text{Å}$). Appropriate symmetry properties of the electron beams at normal incidence for the various structures considered were exploited in the calculations. The Debye temperatures for the substrate and the overlayer were taken to be 280 K and 840 K, respectively. These values which specify the thermal vibrational characteristics of the surface atoms have been applied successfully in our previous analysis (14). Enhancement factors of 1.4 and 2.0 were chosen for the surface mean-square vibrational amplitudes of the substrate and the overlayer, respectively.

In the multiple scattering calculations, three different adsorption sites were considered: the on-top site [site A of Fig. 1(a)] and the two different types of three-fold sites [sites B and C of Fig. 1(a)]. Site B represents the three-fold site directly below which there is another substrate atom in the second layer. Site C represents the three-fold site directly below which there is a vacancy in the second layer. Since a "(2x2)" LEED pattern can be caused either by a p(2x2) superstructure or by three independent domains of (1x2) superstructure rotated 120° with respect to each other, cf. Fig. 2, the calculations were performed for both p(2x2) and (1x2) domain superstructures. In the case where there are three (1x2) domains rotated 120° with respect to one another, the intensities from different domains are averaged in the calculations. It is assumed that each domain is of equal size and is larger than the coherence area of the incident electron beam. In all cases considered for the (1x2) structure, the calculated fractional-order beams from each domain do not mix with each other, while the calculated integral-order beams are mixed as follows: $I_{10} = 2I'_{10} + I'_{11}$, $I_{01} = 2I'_{01} + I'_{11}$, $I_{11} = I'_{11} + I'_{2\bar{1}} + I'_{\bar{1}2}$, etc., where I and I' are calculated intensities of

the beams after and before averaging, respectively.

Comparisons between four of the ten experimentally measured beams and the optimized, calculated IV spectra are shown in Figs. 3 - 6. The calculated IV spectra in these figures correspond to the optimum interlayer spacing and inner potential for each of the three adsorption sites tested for both the (2x2) and (1x2) superstructures. A visual inspection of Figs. 3 - 6 definitely shows that site C for either the (2x2) or the (1x2) structure is the preferred adsite. In Figs. 7 and 8, a comparison is presented between the other six experimentally measured beams and the calculated profiles for the optimum interlayer spacing for site C($d = 1.30$ Å) and the optimum inner potential ($V_o = 10$ eV) for both (2x2) and (1x2) surface structures. One of the important and interesting features observed in Figs. 3 - 8 is that the calculated IV beam profiles for the (2x2) and (1x2) surface structures are very similar. It is practically impossible to differentiate the correct structure by a visual inspection of these figures.

To quantify the comparison between experiment and theory, the reliability (R)-factor was computed according to the procedure of Zanazzi and Jona (15). The criterion used is that an R-factor near 0.2 indicates high reliability of the tested structure, one near 0.35 indicates a possibly correct structure, while one above approximately 0.5 indicates an incorrect structure (15,16). Thus, a relative comparison among the R-factors for the various assumed structures indicates quantitatively the level of agreement between experiment and theory. In Table 1, a comparison is shown among the R-factors using ten experimentally measured beams and the optimum calculated IV spectra for the three different adsites with p(2x2) and (1x2)

superstructures.

Based on the criteria discussed above, the R-factors of 0.22 for site C for both the p(2x2) and the (1x2) surface structures show that the oxygen adatoms occupy the three-fold site with a vacancy in the second substrate layer on Ir(111) forming either a p(2x2) superstructure or three domains of (1x2) superstructure rotated 120^{o} with respect to one another. The inability of the R-factor analysis to distinguish between the p(2x2) and the (1x2) structures indicates that the calculated IV spectra for these two structures are very similar. However, it is clear from both a visual inspection and the R-factor analysis that the correct adsite for oxygen on this surface has been determined. The interlayer spacing between the oxygen adatoms and the Ir surface is 1.30 ± 0.05 Å which corresponds to a bond length between the oxygen and Ir atoms of 2.04 ± 0.08 Å.

4. Discussion

The results of this study indicate that the oxygen atoms forming a "(2x2)" superstructure on the Ir(111) surface reside in the three-fold site directly below which there is a vacancy in the second substrate layer. In a previous study (14), it was shown that oxygen adatoms forming a c(2x2) superstructure on the unreconstructed Ir(110)-(1x1) surface reside in the short-bridged site. A detailed discussion has been presented for the preference of oxygen for the short-bridged sites over either the long-bridged sites or the on-top sites on the Ir(110)-(1x1) surface (14). It has been shown that the activation energies of desorption of oxygen forming a "(2x2)" overlayer structure on the Ir(111) surface and a c(2x2) overlayer structure on the Ir(110)-(1x1) surface are approximately

55 (17) and 45 (18) kcal/mole, respectively. This suggests that oxygen residing in a three-fold site is energetically more stable than oxygen residing in a short-bridged site.

The formation of two different types of surface structures on the (111) and (110)-(1x1) surfaces of Ir is analogous to two of the many types of complexes formed between Ir and oxygen {e.g., $K_{10}[Ir_3O(SO_4)_9]\cdot 3H_2O$ (19) and $K_6H_2[(Ir_2O)_2(H_2PO_4)_{10}\cdot(OH)_8]$ (20)}. Examples of several inorganic complexes and their bond lengths are presented in Table 2. The Ir-O bond lengths in these complexes range from 1.96 to 2.06 Å, supporting the LEED results for the Ir-O bond lengths of 1.93 Å and 2.04 Å for the Ir(110)-c(2x2)O and the Ir(111)-"(2x2)"O structures, respectively. This comparison is only tentative because the nature of chemical bonding between the surface structures and the inorganic complexes may be very different (i.e., the bonding in the surface structure and the inorganic complexes is atomic and molecular, respectively). Also, as expected, the Ir-O bond lengths for these surface structures compare favorably with the sum of the covalent radii of O and Ir, 2.00 Å (25).

Further evidence concerning the covalent character of the bonding between the chemisorbed oxygen and the Ir substrate can be obtained by calculating the charge transfer from the substrate to the overlayer. The work function changes ($\Delta\phi$) for the Ir(111)-"(2x2)"O and Ir(110)-c(2x2)O structures are 0.56 eV (17) and 0.30 eV (18), respectively. The dependence of the change of work function on the coverage is given by (26)

$$\Delta\phi = \frac{-e\mu_o\sigma\theta}{\varepsilon_o} \frac{1}{1 + \kappa\alpha(\sigma\theta)^{3/2}} , \qquad (1)$$

where e is the electron charge, μ_o is the dipole moment of the isolated dipole, σ is the density of adsorption sites, θ is the fractional surface coverage, ε_o is the permitivity of free space, κ is a constant

depending on the geometry of the overlayer structure, and α is the polarizability of the adsorbate. The dipole moment of a partly ionic bond is given by

$$\mu_o = q^* \ell \ , \qquad (2)$$

where q^* is the charge transferred, and ℓ is the dipole length. Neglecting the effect of the depolarizing influence due to surrounding dipoles [the value of $\kappa\alpha(\sigma\theta)^{3/2}$ is estimated to be small] and assuming that the charge is transferred perpendicular to the surface with the reference point the center of the top plane of Ir atoms, the ionic character of the Ir-O bond is either 0.06 (θ = 1/4) or 0.03 (θ = 1/2) for the Ir(111)-"(2x2)" structure, and 0.03 for Ir(110)-c(2x2) structure. These small ionicities of the Ir-O bonds further support the assertion made earlier that the Ir-O bonds of these surface structures are of a covalent character.

5. Conclusions

The oxygen adatoms forming a "(2x2)" overlayer structure on the Ir(111) surface were found to reside in the three-fold site directly below which there is a vacancy in the second layer. The interlayer spacing between the oxygen and Ir atoms is 1.30 $\mathring{A}$ which corresponds to an Ir-O bond length of 2.04 $\mathring{A}$. The LEED analysis, which utilizes the measured spectra at normal incidence, cannot determine whether the "(2x2)" superstructure is caused by a p(2x2) overlayer or three domains of (1x2) structure rotated 120^o with respect to one another. These two structures may be able to be distinguished ultimately by analyzing experimental spectra obtained at off-normal incidence.

Acknowledgment

Very informative conversations with Dr. M. A. Van Hove are gratefully acknowledged.

References

1. C. W. Tucker, J. Appl. Phys. 35, 1897 (1964).
2. J. E. Demuth and T. N. Rhodin, Surface Sci. 45, 249 (1974).
3. T. E. Madey, H. A. Engelhardt and D. Menzel, Surface Sci. 48, 304 (1975).
4. J. T. Grant and T. W. Haas, Surface Sci. 21, 76 (1970).
5. H. Conrad, G. Ertl and J. Küppers, Surface Sci. 76, 323 (1978).
6. J. Küppers and A. Plagge, J. Vacuum Sci. Technol. 13, 259 (1976).
7. J. A. Joebstl, J. Vacuum Sci. Technol. 12, 347 (1975).
8. P. M. Marcus, J. E. Demuth and D. W. Jepsen, Surface Sci. 53, 501 (1975).
9. C.-M. Chan, S. L. Cunningham, M. A. Van Hove, W. H. Weinberg and S. P. Withrow, Surface Sci. 66, 394 (1977).
10. J. B. Pendry, Low-Energy Electron Diffraction, Academic Press, London, 1974.
11. G. O. Arbman and S. Hörnfelt, J. Phys. F2, 1033 (1972).
12. J. E. Demuth, D. W. Jepsen and P. M. Marcus, Phys. Rev. Letters 32, 1182 (1974).
13. J. E. Demuth, D. W. Jepsen and P. M. Marcus, Phys. Rev. Letters 31, 540 (1973).
14. C.-M. Chan, K. L. Luke, M. A. Van Hove, W. H. Weinberg and S. P. Withrow, Surface Sci. 78, 386 (1978).
15. E. Zanazzi and F. Jona, Surface Sci. 62, 61 (1977).
16. F. Jona, J. Phys. C 11, 4271 (1978).
17. V. P. Ivanov, G. K. Boreskov, V. I. Savchenko, W. F. Egelhoff, Jr. and W. H. Weinberg, Surface Sci. 61, 207 (1976).

18. J. L. Taylor, D. E. Ibbotson and W. H. Weinberg, Surface Sci. 79. 349 (1979).

19. M. Delepine, Ann. Chim. (Paris) (13) 4, 1131 (1959).

20. N. K. Pshenitsyn, S. I. Ginzburg and L. G. Sal'skaya, Zh. Neorgan. Khim. 5, 832 (1960); Russ. J. Inorg. Chem. 5, 399 (1960).

21. M. J. Nolte and E. Singleton, Acta Cryst. B 32, 1838 (1976).

22. M. Laing, M. J. Nolte and E. Singleton, Chem. Commun. 660, (1975).

23. P. Herpin, Bull. Soc. Franc. Mineral. Crist. 81, 201 (1958).

24. M. Ciechanowicz, W. P. Griffith, D. Pawson, A. C. Skapski and M. J. Cleare, Chem. Commun. 876 (1971).

25. Lange's Handbook of Chemistry, 12th ed., J. A. Dean, Ed., McGraw-Hill, N.Y., 1979.

26. J. Topping, Proc. Roy. Soc. (London) A114, 67 (1927).

Table 1: Results of an R-Factor Analysis

	V_o,eV	d, Å	R-Factor
p(2x2) Site A	10	1.95	0.35
p(2x2) Site B	16	1.35	0.35
p(2x2) Site C	12	1.30	0.22
(1x2) Site A	10	1.95	0.34
(1x2) Site B	16	1.35	0.34
(1x2) Site C	12	1.30	0.22

Table 2: Complexes between Ir and Oxygen and Their Bond Lengths

Complex	Ir-O Bond Length, Å	Reference
$[Ir(O_2)(P\ Me_2Ph)_4]B\ Ph_4$ [a]	2.04	(21)
$[Ir(O_2)(Ph_2P\ CH_2P\ Ph_2)]ClO_4$	2.06	(22)
$[Ir(O_2)(Ph_2P\ CH_2P\ Ph_2)]PF_6$	2.00	(22)
$K_3[Ir(C_2O_4)_3]$	1.96	(23)
$(NH_4)_4[Ir_3N(SO_4)_6(H_2O)_3]\cdot 3H_2O$	2.005 to 2.059	(24)

[a] Me ≡ methyl

Ph ≡ phenyl

Figure Captions

Fig. 1: (a) Unit cells of the (1x1) substrate, and p(2x2) and (1x2) overlayer structures. Site A is the on-top site; site B is the three-fold site directly beneath which there is another substrate atom; and site C is the three-fold with a vacancy located beneath it in the second layer.

(b) Schematic LEED pattern corresponding to a"(2x2)" superstructure.

Fig. 2: Unit cell of a p(2x2) superstructure and its corresponding LEED pattern; and three domains of a (1x2) superstructure rotated 120^{o} with respect to one another on an fcc (111) surface and the corresponding LEED pattern.

Fig. 3: Comparison between theoretical and experimental IV spectra for the $(\frac{1}{2}\ 0)$ beam for different proposed structures. The theoretical IV spectra for site A for both (2x2) and (1x2) structures are modified with an inner potential of 10 eV, while those for site B are modified with an inner potential of 16 eV, and those for site C are modified with an inner potential of 12 eV. $\theta = 0^{o}$ defines normal incidence, and d is the interlayer spacing between the oxygen overlayer and the topmost layer of Ir substrate atoms.

Fig. 4: As in Fig. 3 except the $(0\ \frac{3}{2})$ beam.

Fig. 5: As in Fig. 3 except the $(\frac{3}{2}\ 0)$ beam.

Fig. 6: As in Fig. 3 except the $(\frac{1}{2}\ 1)$ beam.

Fig. 7: Comparison between experimental IV spectra for three integral-

order beams and the theoretical IV spectra for site C for both (2x2) and (1x2) superstructures with V_o = 12 eV and d = 1.30 Å. $\theta = 0^o$ defines normal incidence.

Fig. 8: As in Fig. 7 except for three fractional-order beams.

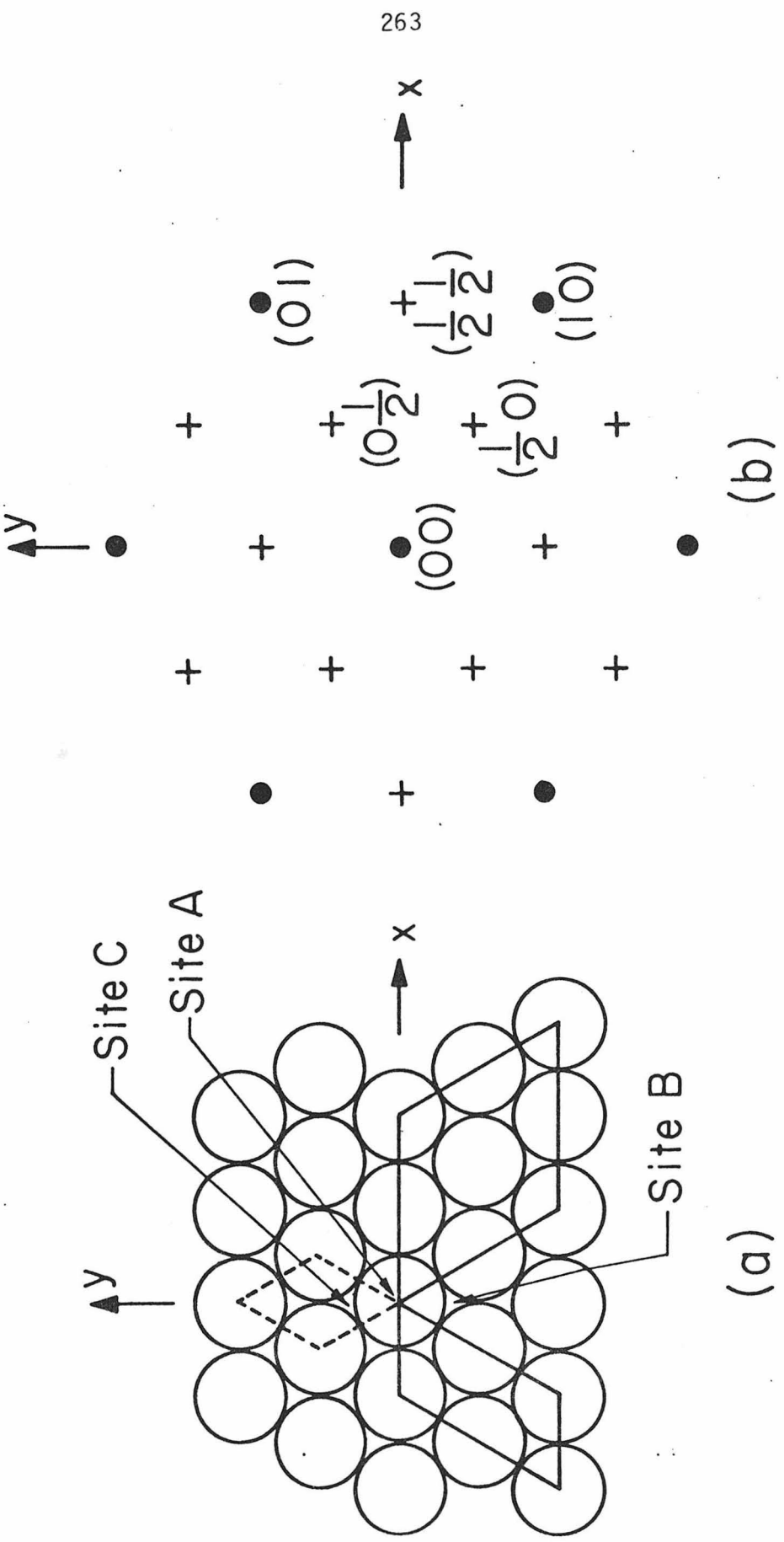

Fig. 1

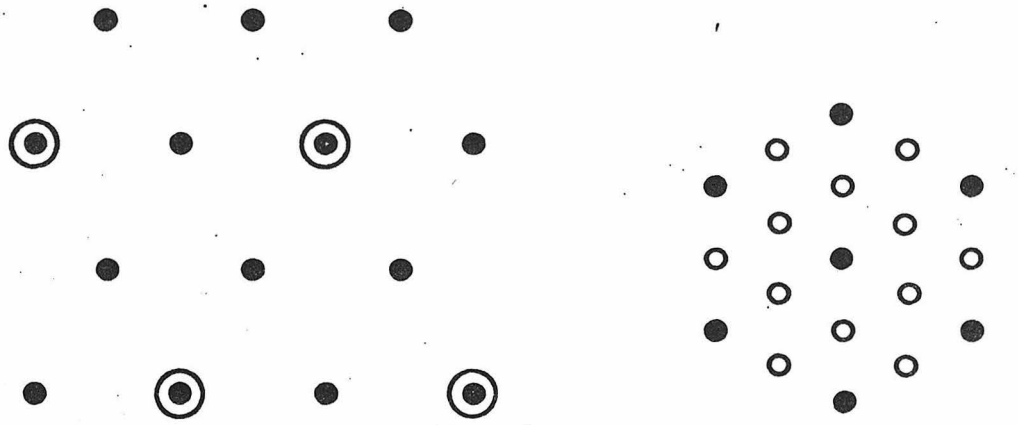

real space reciprocal space

(2×2) structure

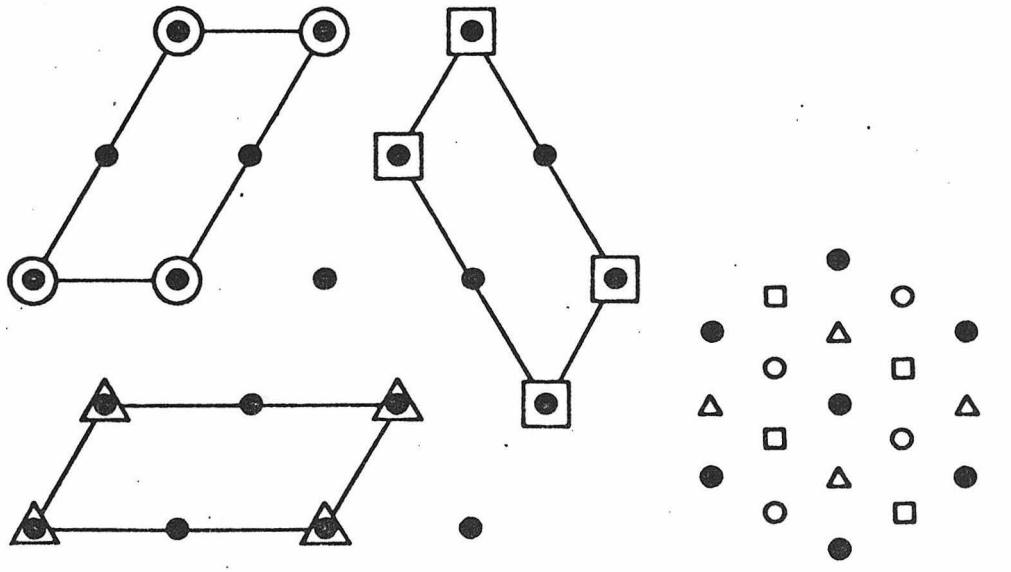

real space reciprocal space

three domains of the (1×2) structure

Fig. 2

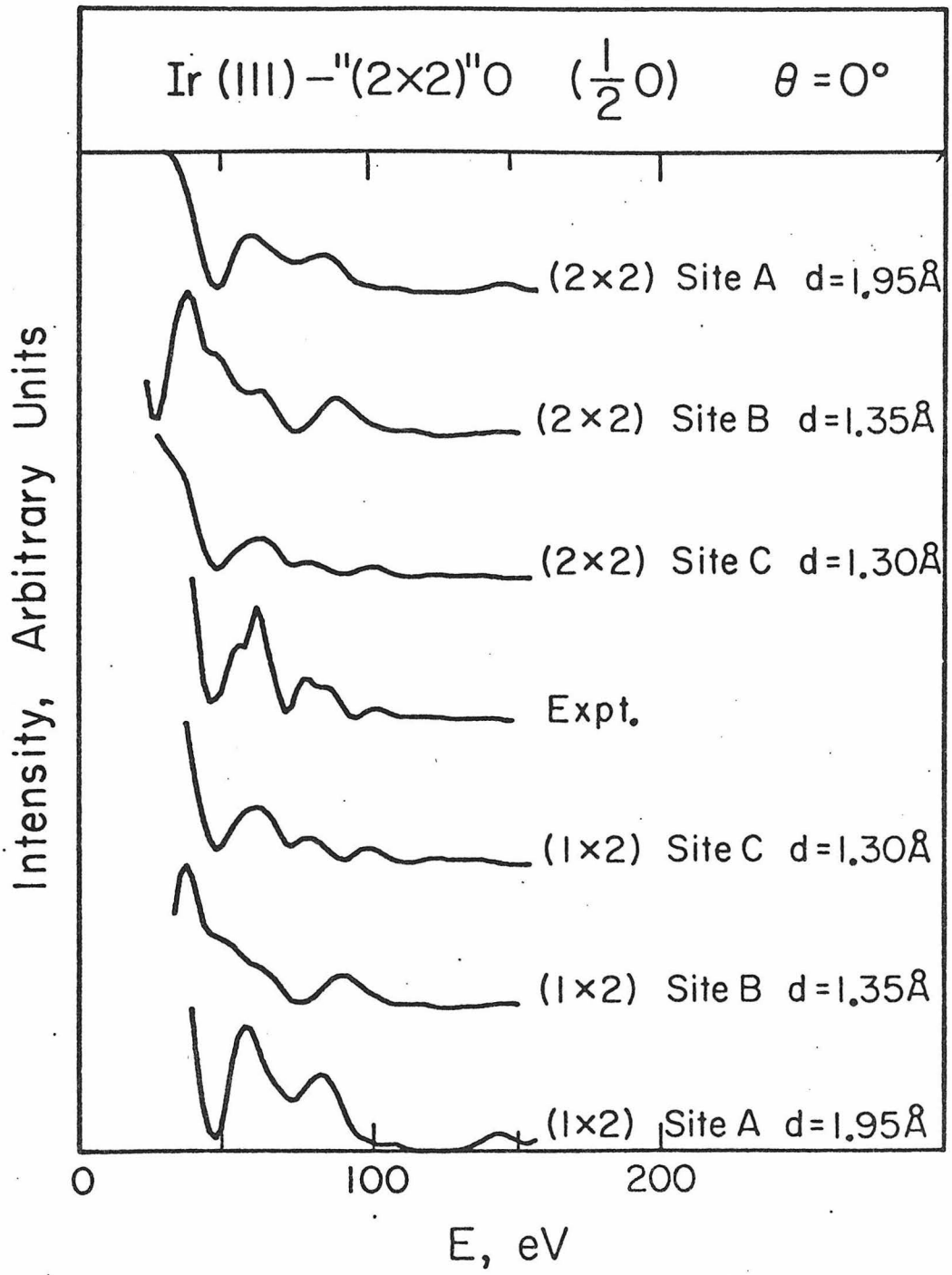
Ir (111) – "(2×2)" O ($\frac{1}{2}$ 0) θ = 0°
(2×2) Site A d=1.95Å
(2×2) Site B d=1.35Å
(2×2) Site C d=1.30Å
Expt.
(1×2) Site C d=1.30Å
(1×2) Site B d=1.35Å
(1×2) Site A d=1.95Å
Intensity, Arbitrary Units
0
100
200
E, eV

Fig. 3

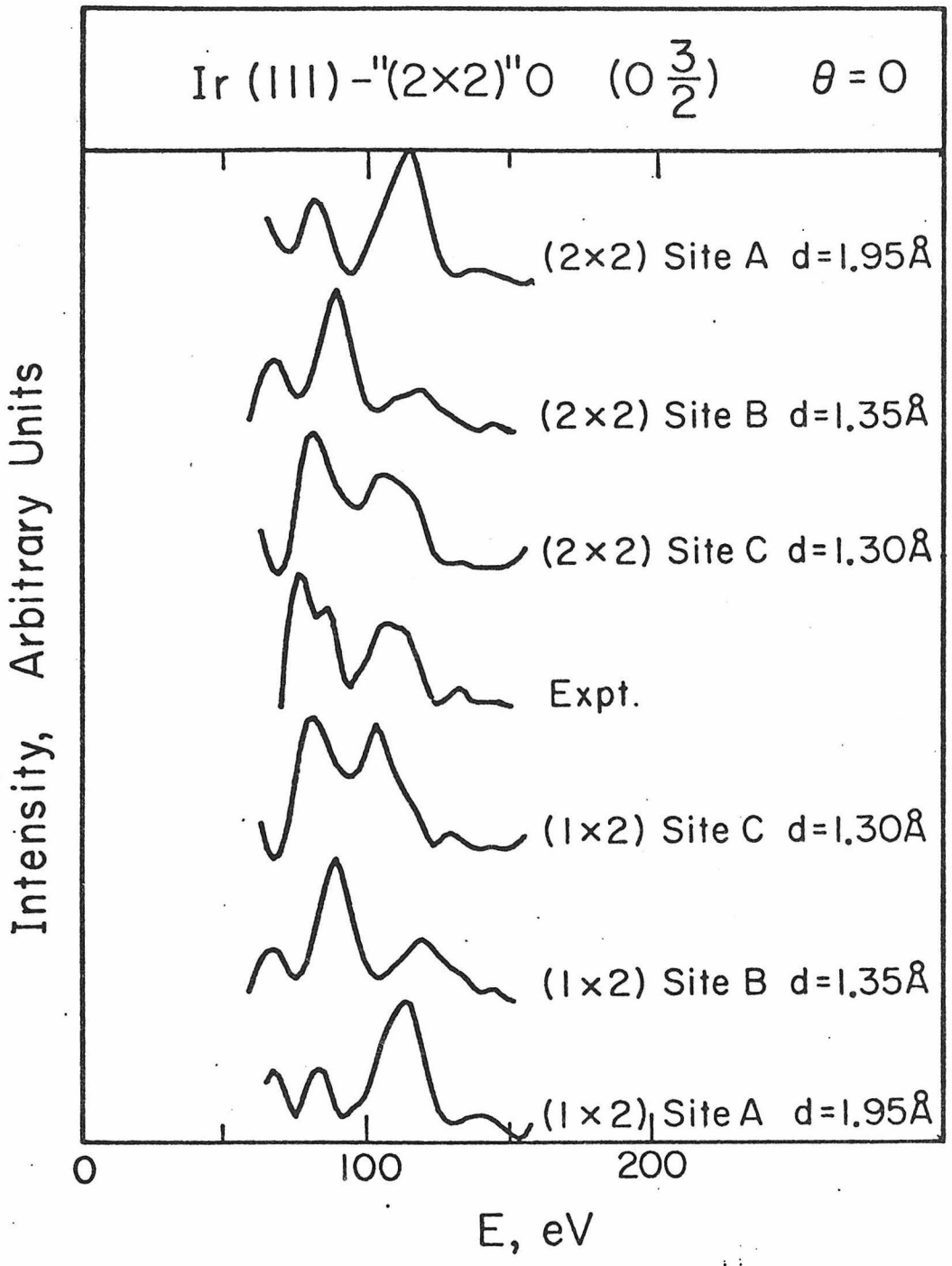
Ir (111) - "(2×2)" O (0 3/2) θ = 0
(2×2) Site A d=1.95Å
(2×2) Site B d=1.35Å
(2×2) Site C d=1.30Å
Expt.
(1×2) Site C d=1.30Å
(1×2) Site B d=1.35Å
(1×2) Site A d=1.95Å
Intensity, Arbitrary Units
0
100
200
E, eV

Fig. 4

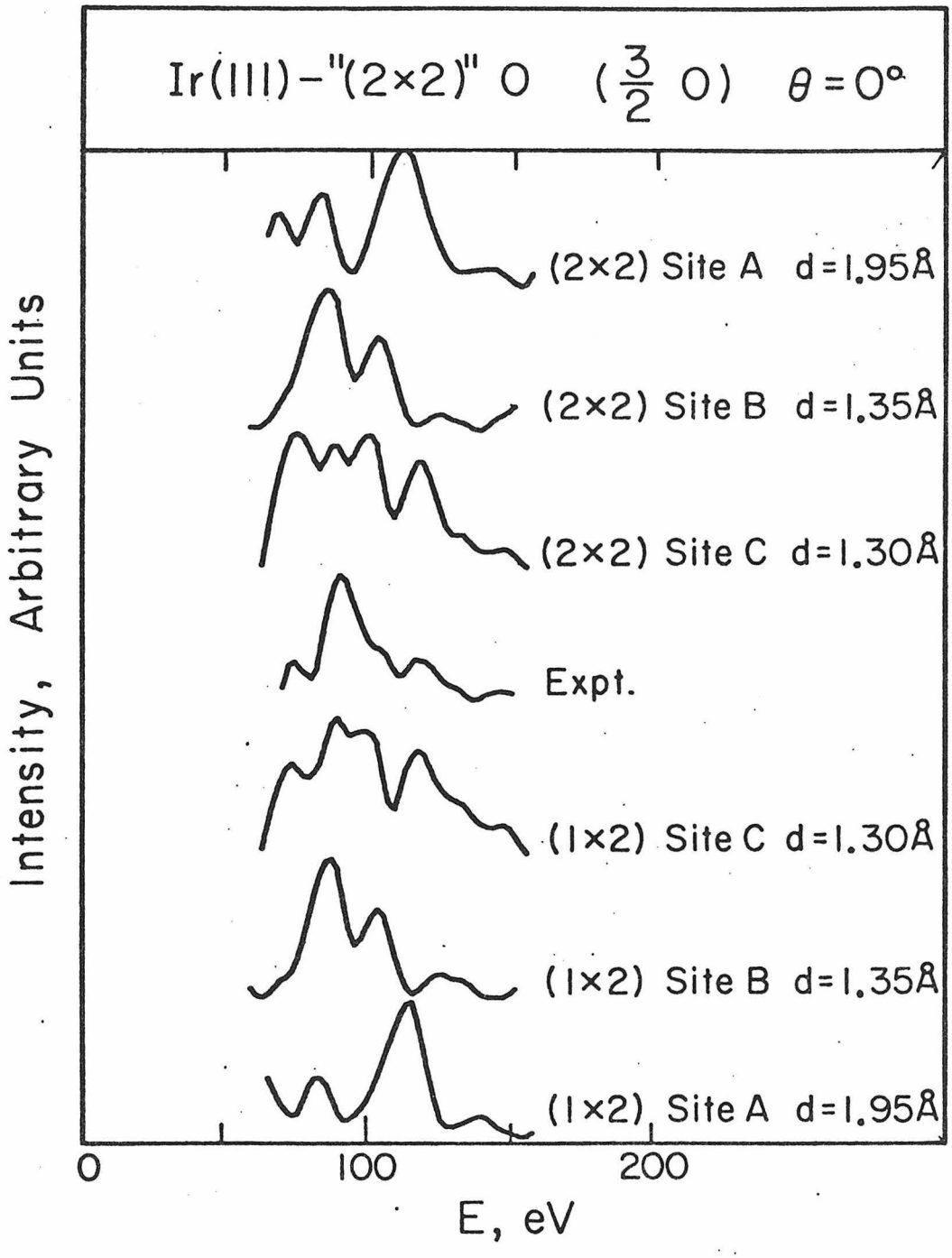
Ir(111)-"(2×2)" O ($\frac{3}{2}$ 0) $\theta = 0°$
(2×2) Site A d=1.95Å
(2×2) Site B d=1.35Å
(2×2) Site C d=1.30Å
Expt.
(1×2) Site C d=1.30Å
(1×2) Site B d=1.35Å
(1×2) Site A d=1.95Å
Intensity, Arbitrary Units
0
100
200
E, eV

Fig. 5

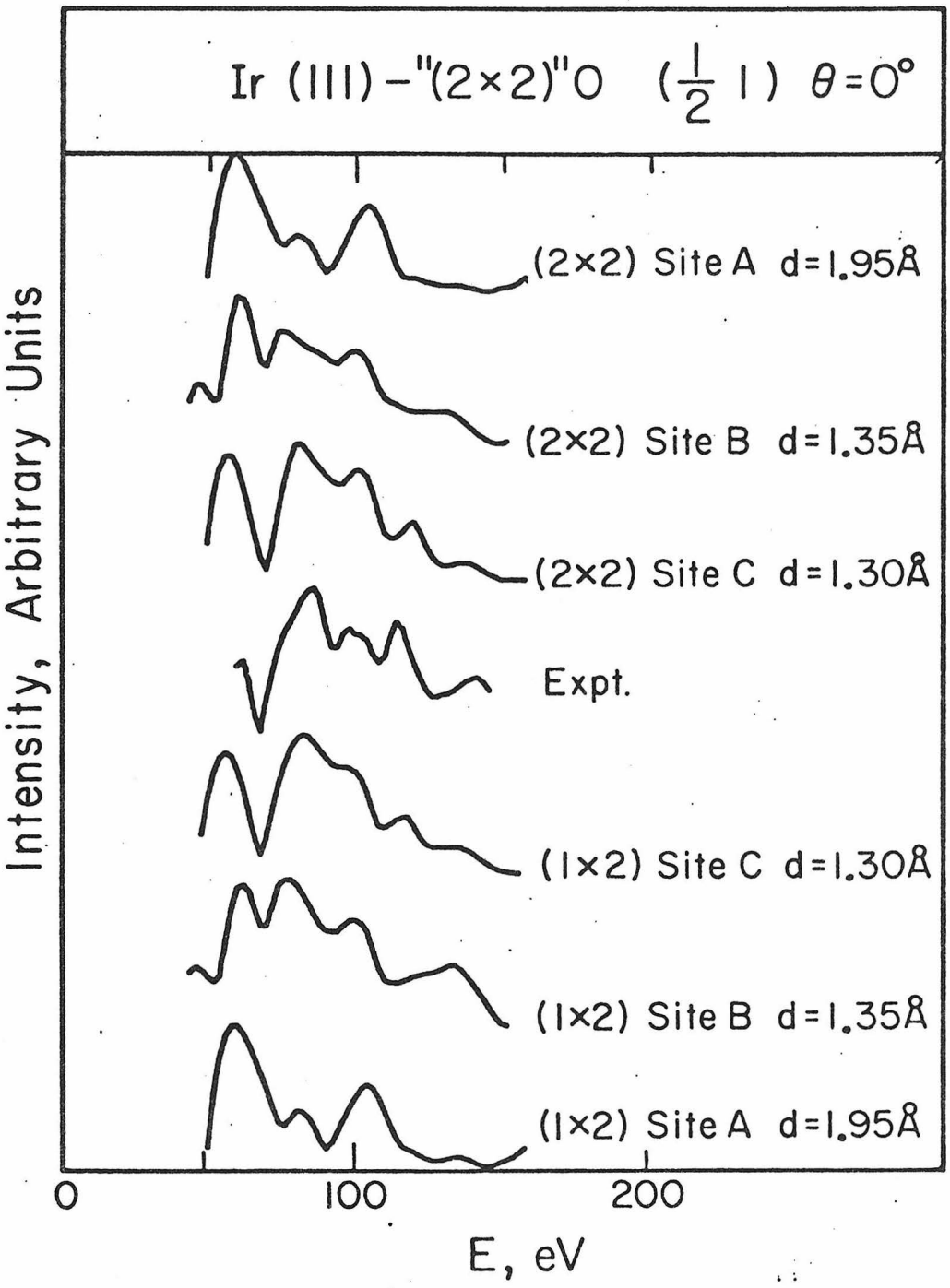
Ir (111) – "(2×2)"O (½ 1) θ=0°
(2×2) Site A d=1.95Å
(2×2) Site B d=1.35Å
(2×2) Site C d=1.30Å
Expt.
(1×2) Site C d=1.30Å
(1×2) Site B d=1.35Å
(1×2) Site A d=1.95Å
Intensity, Arbitrary Units
0
100
200
E, eV

Fig. 6

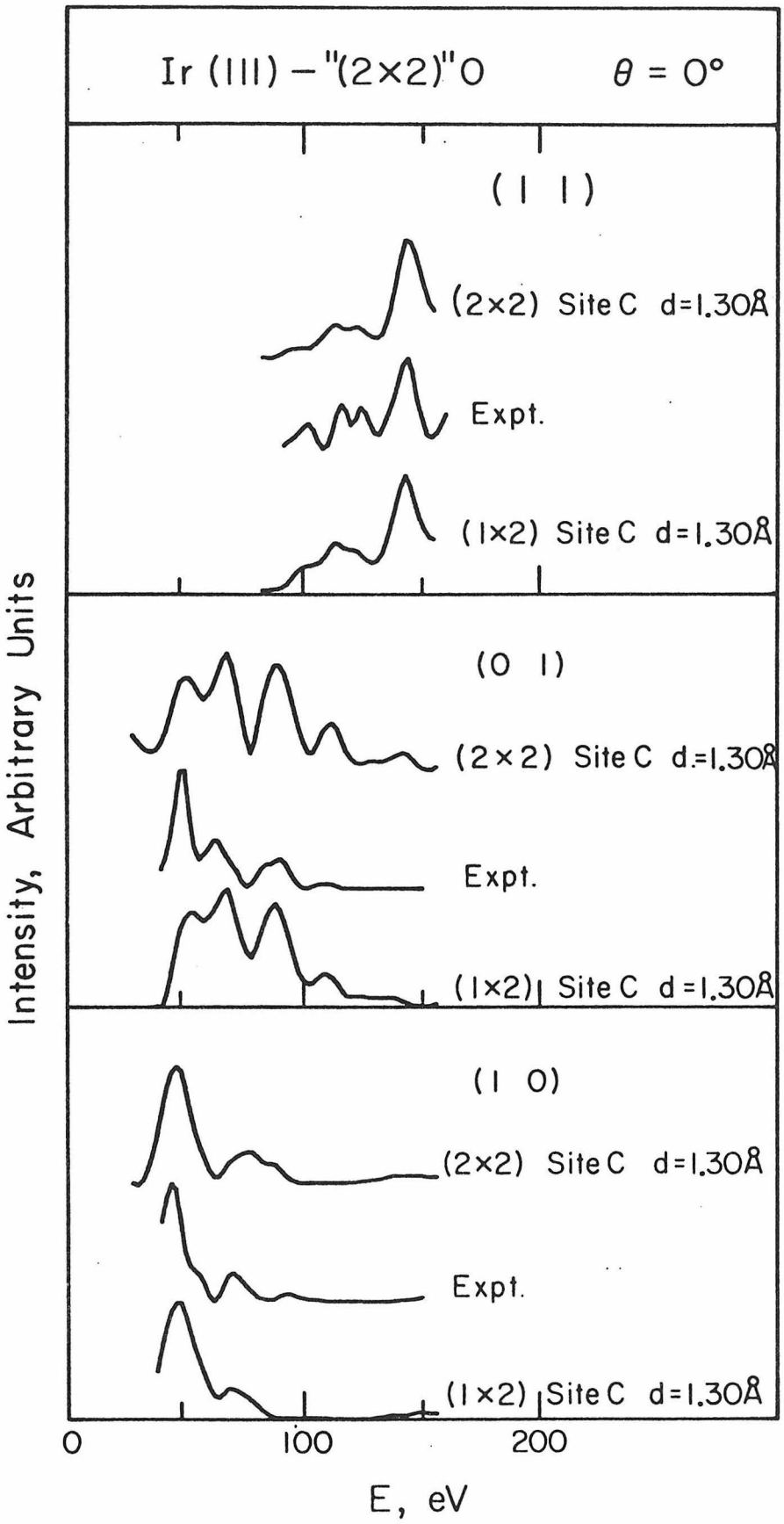
Ir (111) – "(2×2)"O θ = 0°
(1 1)
(2×2) Site C d=1.30Å
Expt.
(1×2) Site C d=1.30Å
(0 1)
(2×2) Site C d.=1.30Å
Expt.
(1×2) Site C d=1.30Å
(1 0)
(2×2) Site C d=1.30Å
Expt.
(1×2) Site C d=1.30Å
Intensity, Arbitrary Units
0
100
200
E, eV

Fig. 7

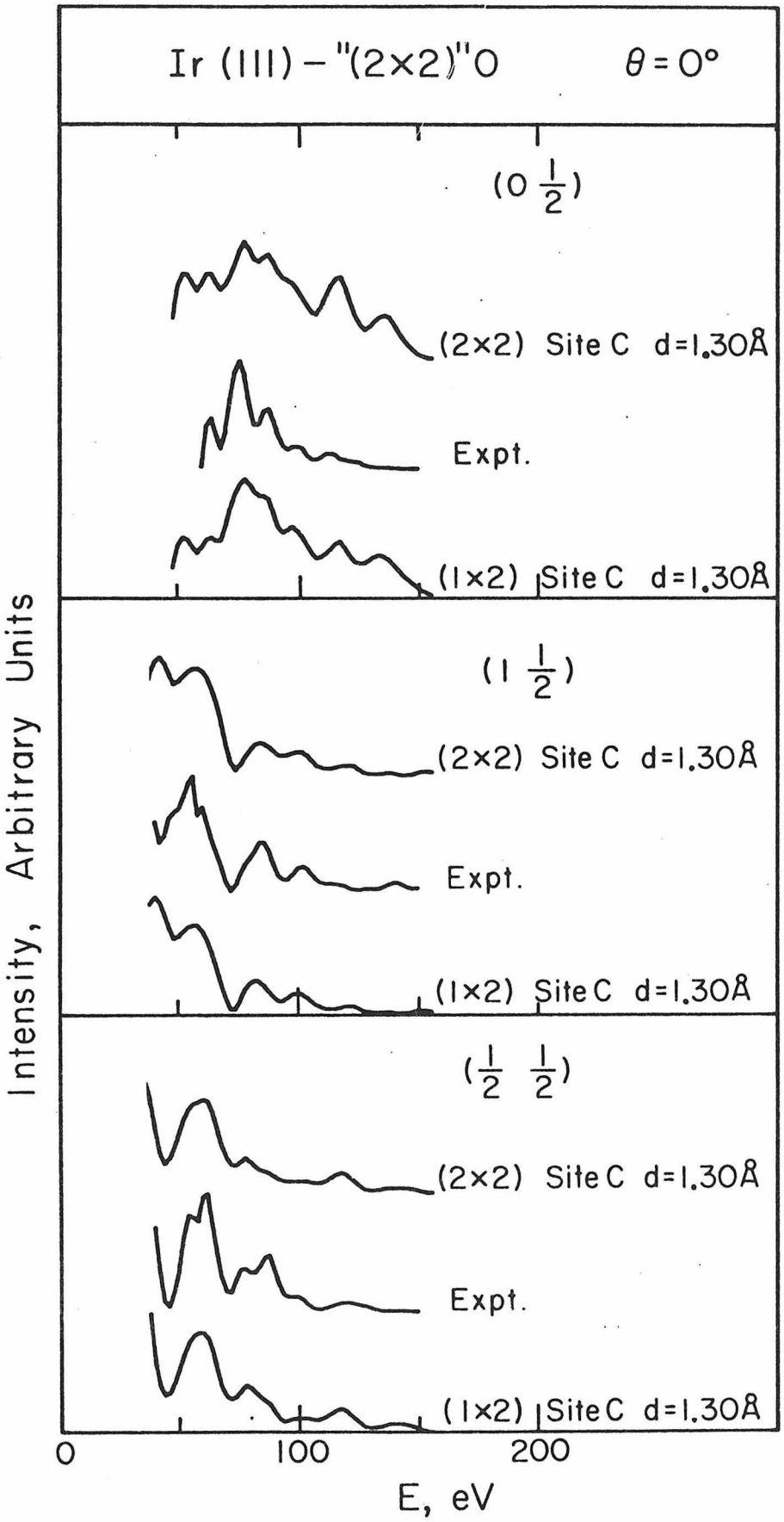
Ir (111) – "(2×2)"O θ = 0°
(0 1/2)
(2×2) Site C d=1.30Å
Expt.
(1×2) Site C d=1.30Å
(1 1/2)
(2×2) Site C d=1.30Å
Expt.
(1×2) Site C d=1.30Å
(1/2 1/2)
(2×2) Site C d=1.30Å
Expt.
(1×2) Site C d=1.30Å
Intensity, Arbitrary Units
0
100
200
E, eV

Fig. 8

Chapter 8

THE STRUCTURE OF THE ($\sqrt{3}$ x $\sqrt{3}$)R30^{o} SULFUR OVERLAYER ON THE IRIDIUM (111) SURFACE

by

C.-M. Chan and W. H. Weinberg

Division of Chemistry and Chemical Engineering
California Institute of Technology
Pasadena, California 91125

Submitted to Physical Review Letters

Abstract

At one-third of a monolayer coverage, sulfur forms an ordered $(\sqrt{3} \times \sqrt{3})R30^{\circ}$ superstructure on the Ir(111) surface. A comparison between dynamic calculations of the intensity-voltage profiles of diffracted beams for different assumed surface geometries and measured low-energy electron diffraction beam profiles demonstrates that the sulfur adatoms occupy one of the two inequivalent types of three-fold hollow sites. In particular, the sulfur resides in the three-fold sites directly above a vacancy in the second substrate layer with an innerlayer spacing of 1.65 Å corresponding to an Ir-S bond length of 2.28 Å.

This Letter reports the first unequivocal surface structural determination of any chalcogen atom (sulfur) on the (111) surface of an fcc metal (iridium). The most symmetric, and hence most probable adsites on this surface are a linear (on-top) site, a bridged site between two surface atoms, and a three-fold site in the hollow among three surface atoms. There are two different types of the latter, either with a vacancy below the hollow in the second substrate layer or with a substrate atom below the hollow in the second layer. A previous study of the p(2x2) sulfur overlayer on the Ni(111) surface suggested that the sulfur adatoms were located in a three-fold hollow site (1). However, this analysis could not distinguish unambiguously between the two different types of three-fold sites since the calculated beam profiles for the two sites were rather similar and only three beams (the specular and two fractional order ones) were analyzed. The only other previous claim of distinguishing between these two very similar surface sites concerns the $(\sqrt{3} \times \sqrt{3})R30^\circ$ superstructure formed by iodine dissociatively chemisorbed on the (111) surface of Ag (2). Although only one fractional order and two integral order LEED beams were analyzed, it was suggested that the iodine atoms occupied the three-fold hollow site with a vacancy in the second Ag layer. However, the analysis of three LEED beams cannot form a credible basis for the claim of having determined an overlayer structure, generally more than ten beams being necessary (3). In this Letter, the first unequivocal distinction is made between the two types of three-fold sites for the particular case of sulfur chemisorbed in a $(\sqrt{3} \times \sqrt{3})R30^\circ$ superstructure on the Ir(111) surface.

The preparation and cleaning procedure for the Ir(111) surface have been described in detail previously (4,5). A ($\sqrt{3}$ x $\sqrt{3}$)R30° superstructure is formed by the decomposition of H_2S on the surface at room temperature. This structure corresponds to one-third monolayer of sulfur adatoms. An exposure of 2.5 x 10^{-6} torr-sec of H_2S at room temperature gives a maximum intensity in the ($\frac{1}{3}\frac{1}{3}$) fractional order LEED beam. Annealing this surface to 800 K insures the complete desorption of hydrogen (sulfur desorbs only near 1600 K), but the diffracted beam profiles are unchanged upon annealing to 800 K. The unit cell of the superstructure and the corresponding (schematic) LEED pattern are shown in Figs. 1(a) and 1(b), respectively. A total of 11 inequivalent LEED intensity-voltage (I-V) beam profiles — five integral order and six fractional order beams — were measured with a rotable Faraday cup collector at approximately 2 eV intervals. All of the I-V profiles were measured at normal incidence to exploit simplifications due to symmetry in the calculations. The achievement of normal incidence was verified by the satisfactory agreement between symmetry-equivalent diffracted beams.

In the multiple scattering calculations, three different adsorption sites were considered: the on-top site [site A of Fig. 1(a)] and the two different types of three-fold sites [sites B and C of Fig. 1(a)]. The I-V beam profiles for these three adsites were calculated using a convergent perturbative scheme known as Renormalized Forward Scattering (6). A band structure potential which includes full Slater exchange was used for the Ir substrate (7), while the potential for the sulfur overlayer was obtained by overlapping atomic potentials (1,8). An equivalent of a maximum of 82 beams was used in the calculation, and symmetry properties of the

diffraction beams at normal incidence were exploited fully. Eight phase shifts were used for both the Ir substrate and the sulfur overlayer. An assumed inner potential (muffin tin zero) of 10 eV and a constant inelastic damping of 5 eV were used for both the overlayer and the substrate. The interlayer spacing between the overlayer and substrate atoms (d) was varied within physically reasonable values (1.4 Å $\leq$ d $\leq$ 2.4 Å).

In Fig. 2, the optimized, calculated I-V beam profiles (based on the optimum interlayer spacing for each of the three surface sites tested in detail) are compared with the experimental measurements for four of the 11 measured beams. Although a visual inspection of Fig. 2 shows clearly that site C is the preferred adsite, a quantitative comparison is made below. The remaining seven beams examined, but not displayed in Fig. 2, show also a clear preference for site C. In Fig. 3, a comparison is presented between the other seven experimentally measured LEED beams and the calculated beam profiles for the optimum interlayer spacing at the C site (d = 1.65 Å) and the optimum inner potential (V_o = 10 eV). Again, the visual (qualitative) agreement between theory and experiment is apparent.

The comparison between theory and experiment has been made quantitative by computing the reliability (R)-factor as suggested by Zanazzi and Jona (9). The current wisdom is that an R-factor below approximately 0.2 indicates high reliability of the tested structure, one near 0.35 indicates a possibly correct structure, while one above approximately 0.5 indicates an incorrect structure (3,9). Thus, a relative comparison among the R-factors of the various assumed structures as well as a low absolute magnitude of the calculated R-factor are the important ingredients in a successful structural determination by LEED. The R-factors calculated using the sets

of 11 measured and calculated beams with the optimum interlayer spacings and inner potentials are shown in Table 1 for the three sites tested. Based on both its relative and its absolute value, the R-factor of 0.19 for site C demonstrates that the sulfur adatoms occupy the three-fold hollow sites with a vacancy in the second substrate layer on the Ir(111) surface. The sensitivity of the R-factor with respect to both the inner potential and the innerlayer spacing is shown in Fig. 4, and the absolute minimum occurs at V_o = 10 eV and d = 1.65 Å. The innerlayer spacing of 1.65 Å between the sulfur adlayer and the surface Ir atoms implies an Ir-S bond length of 2.28 Å. This may be compared with the sum of the covalent radii of S and Ir of 2.26 Å (10), supporting the expected result, namely, neither significant expansion nor contraction of the covalent bond length. Also, as expected, the Ir-S bond length for the sulfur adatoms is slightly shorter than that of sulfur-containing organometallic clusters, e.g., in $[IrS_2(Ph_2PCH_2CH_2PPh_2)_2]\ ClCH_3CH$ the Ir-S bond lengths are 2.422 Å and 2.389 Å (11), whereas in $[Ir_2(SC_6H_5)_2H_2Cl(PPh_3)_4]ClO_4 \cdot 3(CH_3)_2CO$ the Ir-S bond lengths are 2.399 Å, 2.412 Å, 2.416 Å and 2.440 Å (12).

In summary, for the first time the structure of a chalcogen atom adsorbed on an fcc(111) surface has been determined: unambiguously, sulfur occupies the C site on Ir(111). This result serves to illustrate two important points. First, the sulfur adatoms can distinguish between two very similar (both three-fold symmetric) sites on this surface with a preference for the three-fold site above a vacancy in the second layer. Second, and perhaps more important, it has been shown clearly that a multiple scattering LEED analysis can discriminate between these two very similar surface sites.

It is a pleasure to acknowledge support of this research by the National Science Foundation (Grant Number DMR77-14976). We have benefited also from the award of an American Vacuum Society Predoctoral Scholarship (CMC), and a Camille and Henry Dreyfus Foundation Teacher-Scholar Grant (WHW). Finally, we acknowledge very helpful discussions and correspondence with Dr. M. A. Van Hove.

References

1. J. E. Demuth, D. W. Jepsen and P. M. Marcus, Phys. Rev. Letters 32 1182 (1974).
2. F. Forstmann, W. Berndt and P. Büttner, Phys. Rev. Letters 30, 17 (1973).
3. F. Jona, J. Phys. C 11, 4271 (1978).
4. C. M. Comrie and W. H. Weinberg, J. Chem. Phys. 64, 250 (1976).
5. C.-M. Chan, S. L. Cunningham, M. A. Van Hove, W. H. Weinberg and S. P. Withrow, Surface Sci. 66, 394 (1977).
6. J. B. Pendry, Low-Energy Electron Diffraction, Academic Press, London, 1974.
7. G. O. Arbman and S. Hörnfelt, J. Phys. F 2, 1033 (1972).
8. J. E. Demuth, D. W. Jepsen and P. M. Marcus, Phys. Rev. Letters 31, 540 (1973).
9. E. Zanazzi and F. Jona, Surface Sci. 62, 61 (1977).
10. Lange's Handbook of Chemistry, 12th ed., J. A. Dean, Ed., McGraw-Hill, N.Y., 1979.
11. W. D. Bonds and J. A. Ibers, J. Am. Chem. Soc. 94, 3413 (1972).
12. P. J. Roberts, G. Ferguson and C. V. Senoff, J. Organometal. Chem. 94, C26 (1975).

Table 1. Results of an R-Factor Analysis

	V_o, eV	d, Å	R-Factor
Site A	10	2.00	0.40
Site B	12	1.65	0.30
Site C	10	1.65	0.19

Figure Captions

Fig. 1: (a) Unit cell of the $(\sqrt{3} \times \sqrt{3})R30^{\circ}$ superstructure of sulfur on the Ir(111) surface. Site A is an on-top site; site B is the three-fold site with a substrate atom located beneath it in the second layer; and site C is the three-fold site with a vacancy located beneath it in the second layer.

(b) Schematic LEED pattern corresponding to the superstructure of (a).

Fig. 2: Comparison between theoretical and experimental I-V spectra for four beams that are rather sensitive to the different proposed structures. The theoretical I-V spectra for sites A and C are modified with an inner potential of 10 eV, while that for site B is modified with an inner potential of 12 eV. $\theta = 0$ defines normal incidence.

Fig. 3: Comparison between the experimental I-V spectra for seven beams (in addition to the four of Fig. 2) and the theoretical I-V spectra for site C with $V_o = 10$ eV and $d = 1.65$ Å. $\theta = 0$ defines normal incidence.

Fig. 4: The R-factor for site C as a function of the inner potential for various interlayer spacings (d) between the sulfur and iridium.

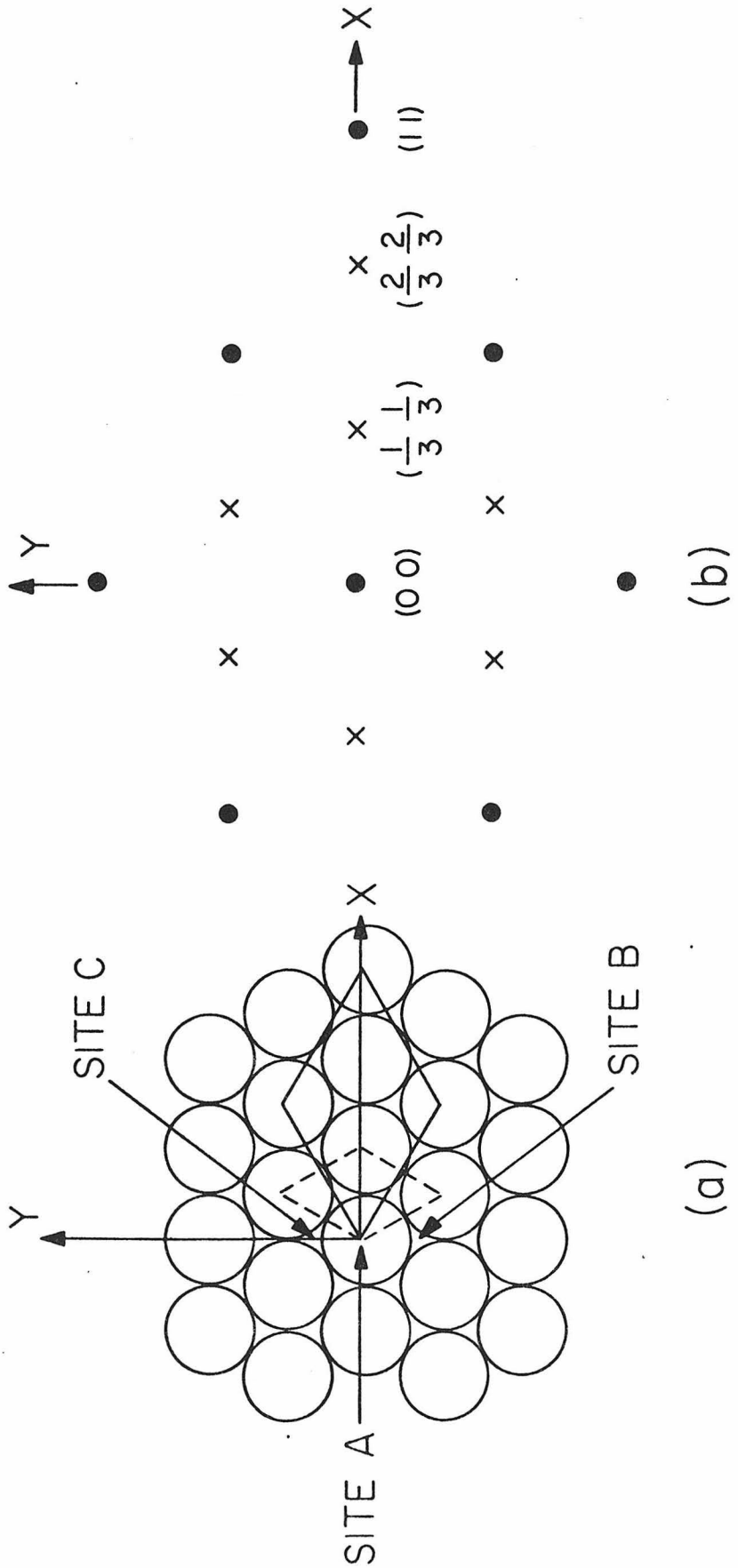

Fig. 1

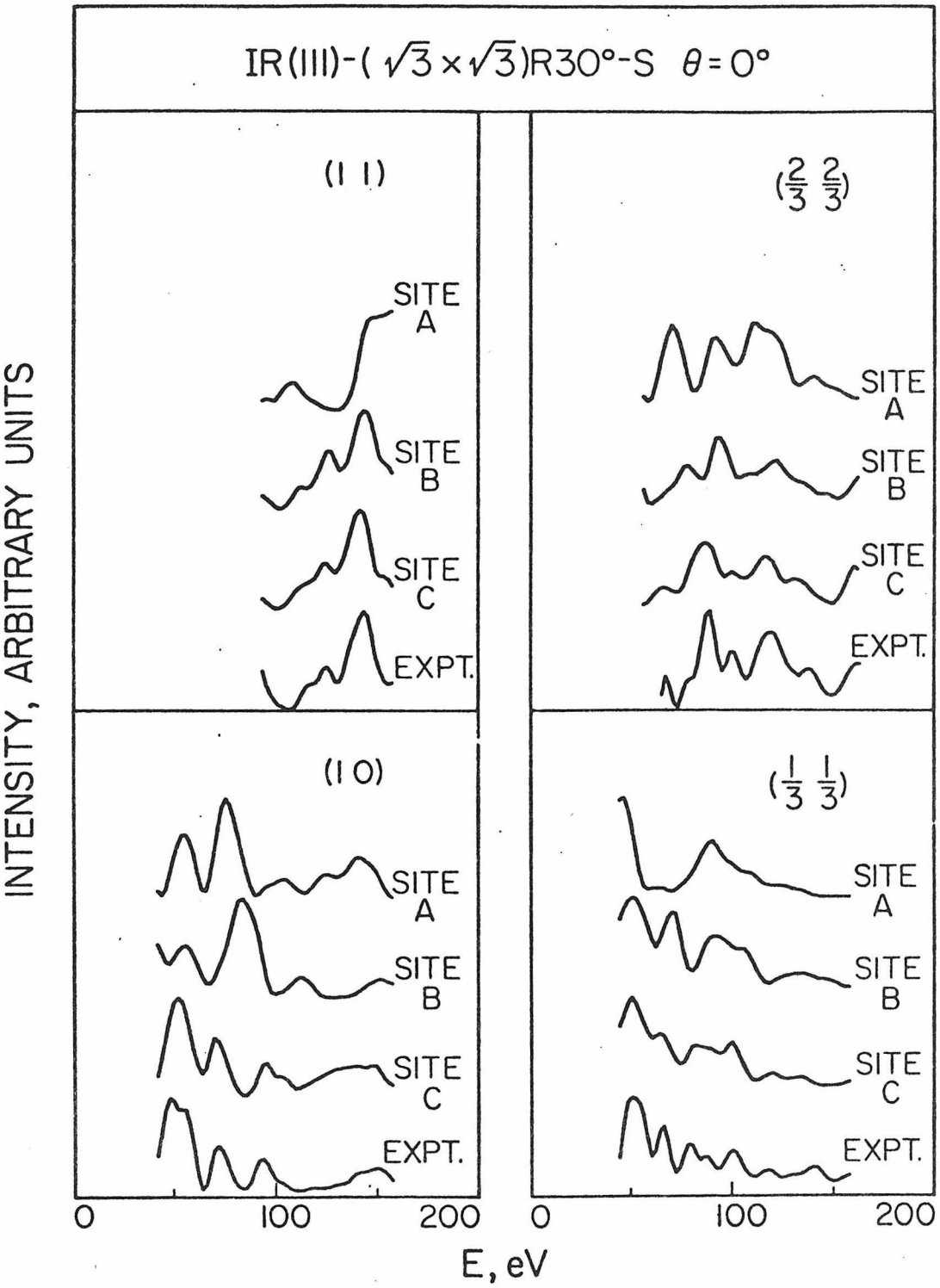
IR(111)-(√3×√3)R30°-S θ=0°
(1 1)
(2/3 2/3)
(1 0)
(1/3 1/3)
SITE A
SITE B
SITE C
EXPT.
INTENSITY, ARBITRARY UNITS
0
100
200
E, eV

Fig. 2

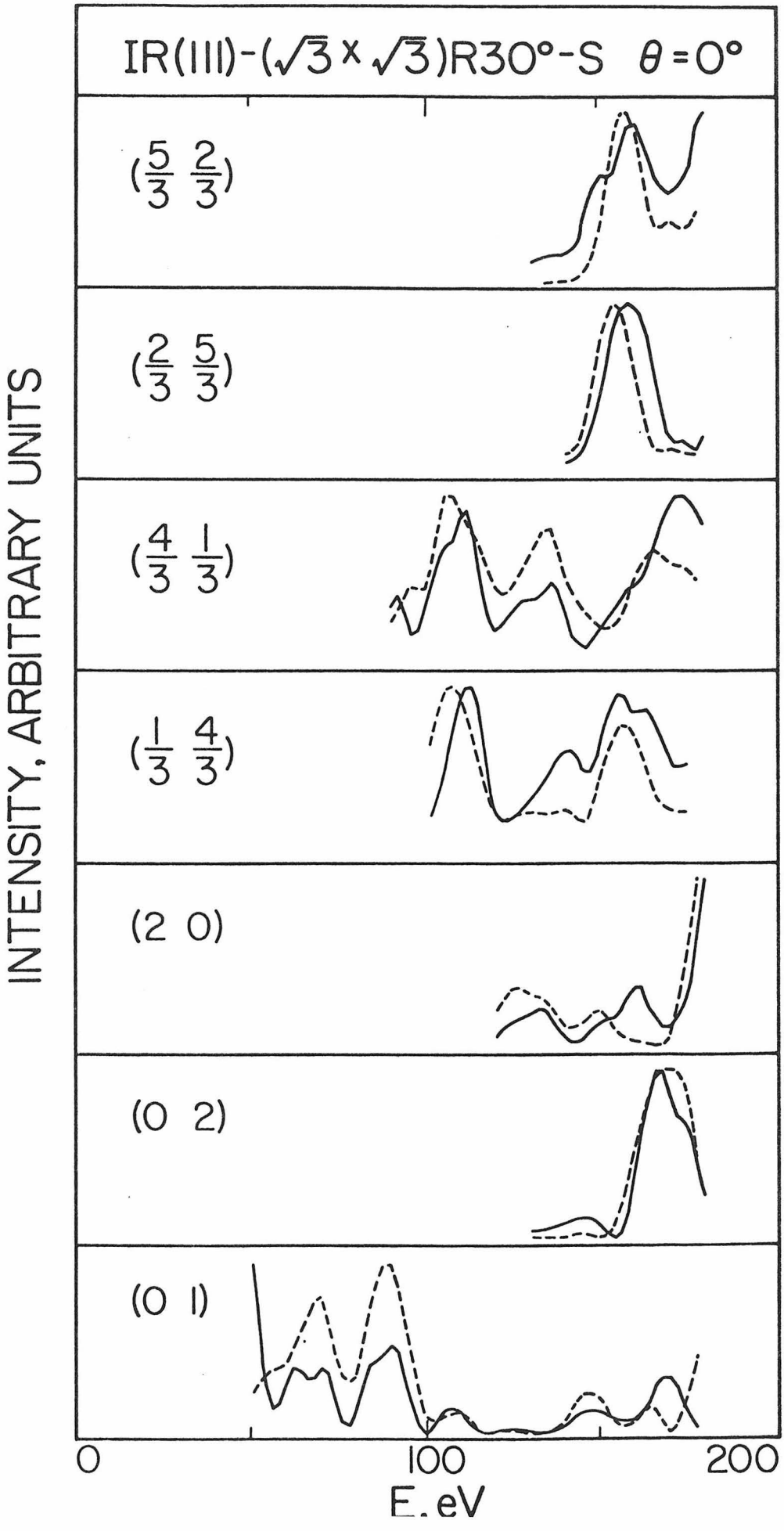
IR(111)-(√3 x √3)R30°-S θ=0°
(5/3 2/3)
(2/3 5/3)
(4/3 1/3)
(1/3 4/3)
(2 0)
(0 2)
(0 1)
INTENSITY, ARBITRARY UNITS
0
100
200
E. eV

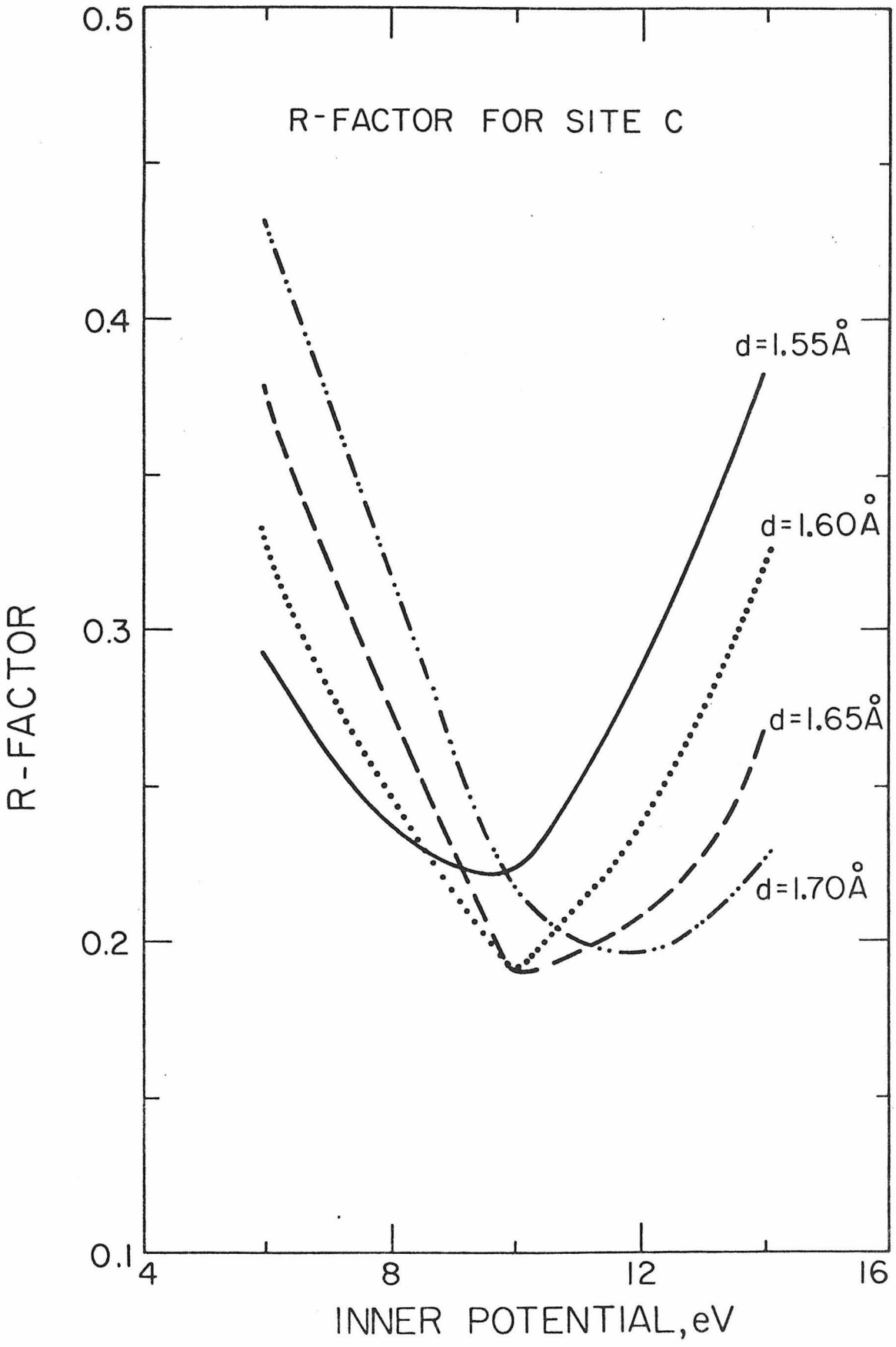
R-FACTOR FOR SITE C
R-FACTOR
INNER POTENTIAL, eV
0.5
0.4
0.3
0.2
0.1
4
8
12
16
d=1.55Å
d=1.60Å
d=1.65Å
d=1.70Å

Fig. 4

Chapter 9

DEBYE TEMPERATURES OF THE (110) and (111) SURFACES OF IRIDIUM DETERMINED BY LEED

by

C.-M. Chan, E. D. Williams and W. H. Weinberg
Division of Chemistry and Chemical Engineering
California Institute of Technology
Pasadena, California 91125

Surface Science 82, L577-L581 (1979)

The Debye temperatures of the clean reconstructed (110) - (1x2) and (111) surfaces of Ir have been determined by Low-Energy Electron Diffraction (LEED) as a function of incident electron energy. Previous studies (1) have shown that the normal component of the root-mean-square displacement of the surface atoms is insensitive to changes in the atomic density of the surface for different crystallographic orientations of Pt. Hence, it is of interest to determine whether the same result obtains for the (110) and (111) orientations of Ir. The atomic arrangement of the Ir(111) surface has been found to have a structure essentially the same as the bulk (2), whereas the Ir(110) - (1x2) surface is reconstructed. The missing row model, in which alternate rows of atoms are absent, has been shown to be the most probable candidate for the clean reconstructed Ir(110) - (1x2) surface (3). Therefore, it would be interesting to determine whether there is any difference in the effective Debye temperature between a rather open (110) - (1x2) surface and a densely packed (111) surface.

The experiments were performed in a UHV system which has been described previously (2,3). The Ir sample, a randomly oriented single crystal rod, was aligned within $\frac{1}{2}^{\circ}$ of the (110) orientation by the back-reflection Laue X-ray method and was cut and polished mechanically using standard techniques (2). The major impurity on this (110) surface initially was carbon. After Ar^{+} bombardment and a series of treatments in 5×10^{-8} torr oxygen at 800 K, followed by brief annealing in vacuum at 1600 K, the surface was found to contain less than 2 atomic % carbon which was shown not to influence the surface structure. No other impurities were detectable by Auger electron spectroscopy. The clean (110)

surface, after further annealing at 1600 K in vacuum, exhibited a (1x2) superstructure.

The (111) crystal was prepared in the same way as the (110) crystal. However, the (111) crystal initially contained carbon, phosphorous and chromium as surface impurities. These impurities were removed by repeated cycles of Ar^+ bombardment. The final surface was estimated to contain less than 2% carbon as the only detectable impurity.

The crystals were tilted so that the (00) diffraction spots were visible on the LEED screen. The beam intensity at a particular electron energy corresponding to a peak maximum in the intensity-voltage (I-V) profile was measured with a Faraday cup collector for both surfaces as the crystals cooled from an initial temperature of 1000 K to approximately 300 K. Ten to twelve such beam intensities were obtained for a particular angle of incidence as a function of temperature at different electron energies corresponding to different peak maxima in the I-V beam profile. Three sets of such data at different angles of incidence were obtained. The angle of incidence of the LEED beam was determined by the procedure of Cunningham and Weinberg (4).

Within the kinematic approximation, the intensity of the back-scattered electrons, I, may be written as

$$I = I_o \exp(-2M), \tag{1}$$

where 2M is the Debye-Waller factor. For the specular beam, the Debye-Waller factor is given by

$$2M = |\Delta k_\perp|^2 \langle u_\perp^2 \rangle , \tag{2}$$

where $\Delta k_\perp$ is the normal component of the momentum transfer of the electron, and $\langle u_\perp^2 \rangle$ is the root-mean-square displacement of the surface atom perpendicular to the crystal surface. In the case of the specular beam,

$$|\Delta k_\perp|^2 = \frac{8m_e}{\hbar^2}(E\cos^2\theta + V_o) \ , \tag{3}$$

where m_e is the mass of the electron, $2\pi\hbar$ is Planck's constant, E is the kinetic energy of the electron, θ is the angle of incidence with respect to the surface normal, and V_o is the inner potential. In the high temperature limit,

$$\langle u_\perp^2 \rangle = \frac{3\hbar^2 T}{m_a k_B (\theta_{D\perp}^{EFF})^2} \ , \tag{4}$$

where m_a is the mass of the (Ir) atom, k_B is the Boltzmann constant, and $\theta_{D\perp}^{EFF}$ is the perpendicular component of the effective Debye temperature. Consequently,

$$2M = 24m_e T(E\cos^2\theta + V_o) / m_a k_B (\theta_\perp^{EFF})^2 \ . \tag{5}$$

The effective Debye temperature can be evaluated from the slope of a plot of $\ell n(I/I_o)$ as a function of surface temperature. However, the experimentally measured intensity of a beam does not necessarily correspond to the true intensity, which results from elastic scattering, due to the presence of the background intensity from phonon-assisted inelastic scattering. To determine the effective Debye temperature correctly, the background intensity must be subtracted from the experimentally measured intensity (5). Hence, Eq. (1) should be rewritten as

$$I - I_{bk} = I_o \exp(-2M), \tag{6}$$

where I_{bk} is the background intensity.

Experimentally, it is difficult to determine an accurate background intensity, especially at high incident electron beam energies (E > 500 eV) where the diffraction spots are closely spaced. Therefore, in the least-squares fitting procedure (5) for the plot of $\ell n(I - I_{bk})$ as a function of T, the value of I_{bk} is varied within physically reasonable limits (between the asymptotic value of the intensity at high temperature and zero) until the best straight line for the representation of $\ell n(I - I_{bk})$ as a function of T is obtained. In the least-squares fitting procedure, we have the option to assign a weighting factor to each datum point. The data taken at low temperature can be measured more accurately and are less sensitive to the variation of the background intensity. Hence, the value of $\theta_{D\perp}^{EFF}$ is determined from the slope of the best straight line in the plot of $\ell n(I - I_{bk})$ as a function of T with a weighting factor for each datum point proportional to its experimentally measured intensity. In the calculation of $|\Delta k_\perp|^2$, a value of 10 eV was used for the inner potential. This value was obtained from the results of dynamical LEED calculations (2,3).

Fig. 1 is a representation of $\theta_{D\perp}^{EFF}$ as a function of $\Delta k_\perp$ for the (00) beam of the (1x2)-(110) surface at three different angles of incidence with respect to the surface normal: $\theta = 8.5°$, $\theta = 16.5°$ and $\theta = 25.3°$. The solid line is a second degree least-squares polynomial fit to all data points (5). The value of $\theta_{D\perp}^{EFF}$ at the lowest value of $\Delta k_\perp (6.5\ \mathring{A}^{-1})$ obtained experimentally is taken as the "surface" value of $\theta_{D\perp}$ which is 150 ± 12 K. The high energy asymptote of the polynomial fit to the data gives a value for the bulk θ_D of 310 ± 22 K. The errors were estimated from the standard deviation of the measured data. In Fig. 2, a plot of

the results for the (111) surface at angles of incidence: $\theta = 8.9°$, $\theta = 22.5°$ and $\theta = 29.6°$ is shown. The "surface" $\theta_{D\perp}$ and the bulk θ_D were determined to be 170 ± 12 K and 315 ± 22 K, respectively.

The results presented in Figs. 1 and 2 are indistinguishable within experimental uncertainties. This indicates that the difference in the packing of the surface atoms in this case does not affect the perpendicular component of the effective "surface" Debye temperature at a level detectable experimentally, and the bulk Debye temperatures obtained from these two surfaces are identical also. Our bulk θ_D is in good agreement with the value of 285 K reported earlier (6). Further work is in progress to investigate the effect of different packings on the parallel component of the effective Debye temperature.

References

1. H. B. Lyon and G. A. Somorjai, J. Chem. Phys. 44, 3703 (1966).

2. C.-M. Chan, S. L. Cunningham, M. A. Van Hove, W. H. Weinberg and S. P. Withrow, Surface Sci. 66, 394 (1977).

3. C.-M. Chan, M. A. Van Hove, W. H. Weinberg and E. D. Williams, Solid State Commun. (submitted); C.-M. Chan, K. L. Luke, M. A. Van Hove, W. H. Weinberg and E. D. Williams, J. Vacuum Sci. Technol. (March/April, 1979).

4. S. L. Cunningham and W. H. Weinberg, Rev. Sci. Instrum. 49, 752 (1978).

5. C.-M. Chan, P. A. Thiel, J. T. Yates, Jr. and W. H. Weinberg, Surface Sci. 76, 296 (1978).

6. International Tables for X-Ray Crystallography, Vol. III, Kynoch Press, Birmingham, England, 1952.

7. G. T. Furukawa, M. L. Reilly and J. S. Gallagher, J. Phys. Chem. Ref. Data 3, 175 (1974).

Figure Captions

Fig. 1 $\theta_{D\perp}^{EFF}$ as a function of $\Delta k_{\perp}$ for the (00) beam of the (110) - (1x2) reconstructed surface of Ir at three different angles of incidence: θ = 8.5°, θ = 16.5° and θ = 25.3°. The solid line is a second degree least-squares polynomial fit to the data.

Fig. 2 Same as Fig. 1 except the (111) surface of Ir at angles of incidence: θ = 8.9°, θ = 22.5° and θ = 29.6°.

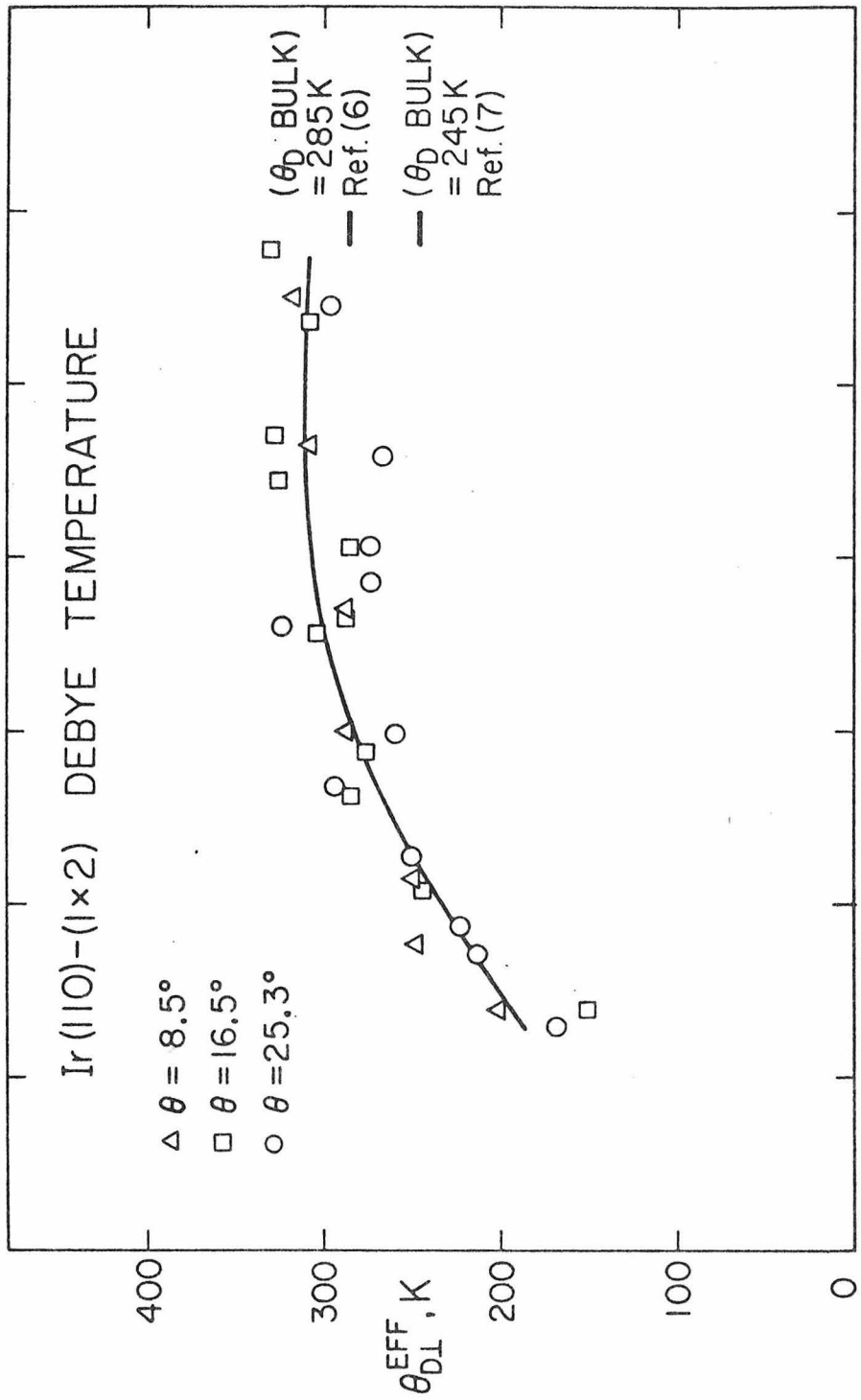
Ir(110)-(1×2) DEBYE TEMPERATURE
△ θ = 8.5°
□ θ = 16.5°
○ θ = 25.3°
(θD BULK) = 285 K Ref. (6)
(θD BULK) = 245 K Ref. (7)
θDL EFF, K
ΔK⊥, Å-1
0
100
200
300
400
5
10
15
20
25
30

Fig. 1

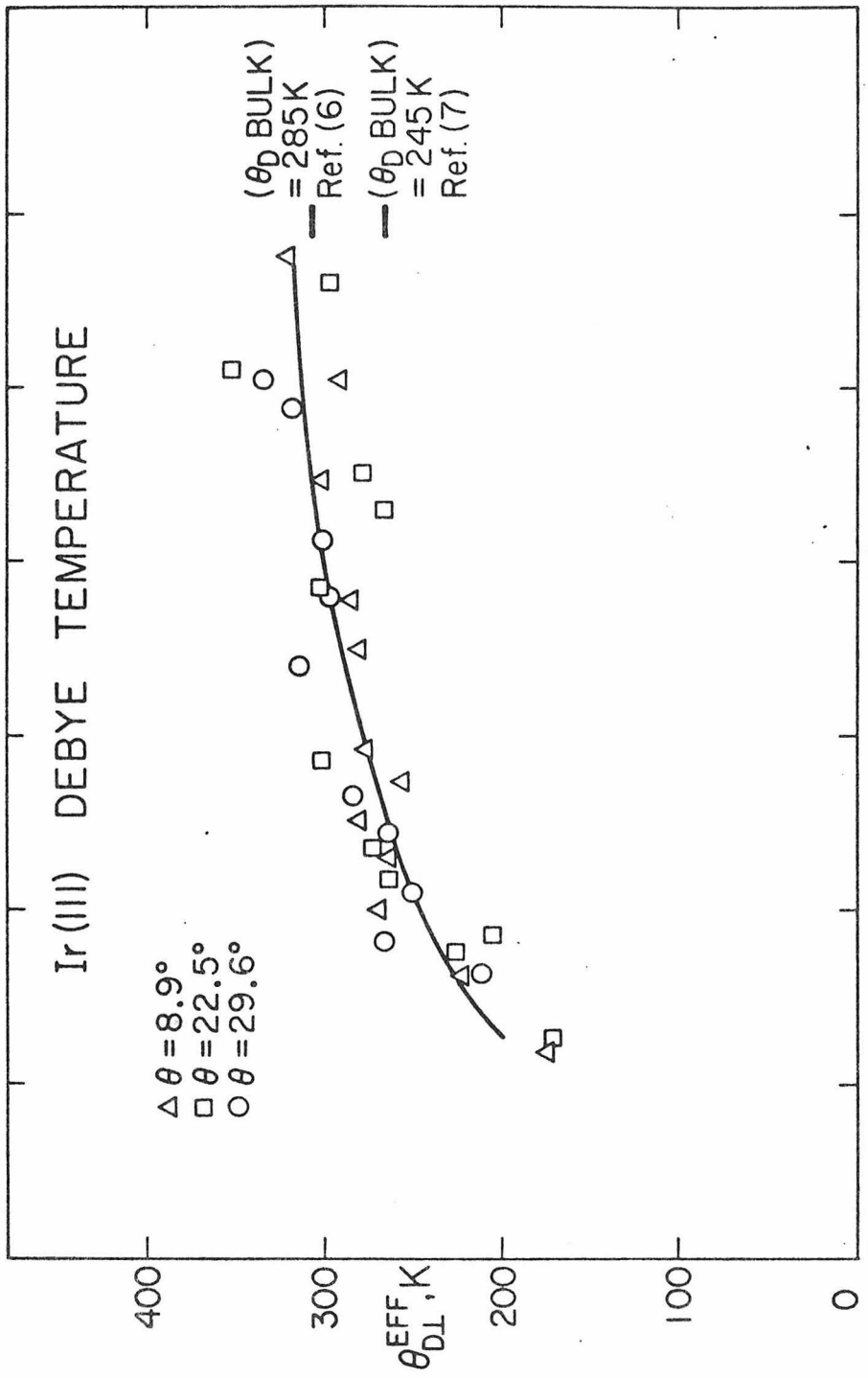
Ir(111) DEBYE TEMPERATURE
△θ=8.9°
□θ=22.5°
○θ=29.6°
(θD BULK) =285K Ref.(6)
(θD BULK) =245K Ref.(7)
θ⊥EFF, K
Δk⊥, Å-1
0
100
200
300
400
5
10
15
20
25
30

Fig. 2

Part IV

Theoretical Studies of Thermal Desorption Mass Spectra

Chapter 1

AN ANALYSIS OF THERMAL DESORPTION MASS SPECTRA. I.

by

C.-M. Chan, R. Aris and W. H. Weinberg

Division of Chemistry and Chemical Engineering
California Institute of Technology
Pasadena, California 91125

Application of Surface Science 1, 360-376 (1978)

Abstract

Analytic expressions have been derived which allow a determination of the activation energy of desorption and the pre-exponential factor of the desorption rate coefficient using parameters obtained easily from thermal desorption mass spectra. In particular, the spectral peak widths and the temperature at which the maximum rate of desorption occurs may be used to describe both first and second order desorption kinetics. An explicit application of this method in the analysis of several important classes of desorption reactions is presented.

1. Introduction

In order to understand heterogeneously catalyzed surface reactions, it is of prime importance to measure the reaction rate parameters. During a heterogeneously catalyzed reaction (ignoring mass transfer), reactants first are adsorbed on a surface, then the reaction takes place with one (Eley-Rideal) or both (Langmuir-Hinshelwood) of the reactants chemisorbed on the surface (for example, in a bimolecular reaction), and finally the products of the reaction desorb from the surface. Desorption is the final step in any catalytic reaction, so it is necessary to be able to calculate desorption rate parameters for different operating conditions. Thermal desorption mass spectrometry has been used extensively to determine these kinetic parameters. In this technique, the temperature of the substrate is increased, and the change in the partial pressure in the reactor is detected mass spectrometrically.

There are four important kinetic parameters which may be determined by a thermal desorption experiment: (1) the kinetic order of the desorption reaction, (2) the activation energy of desorption, (3) the pre-exponential

factor of the desorption rate coefficient and (4) the number of binding states of the admolecule. Methods of analyzing thermal desorption spectra to obtain these kinetic parameters have been reviewed elsewhere (1-4).

Redhead (1) has shown that

$$\frac{E_d}{kT_M^2} = \frac{\nu_o^{(1)}}{\beta} \exp\left(-\frac{E_d}{kT_M}\right), \text{ for } m=1 \qquad (1)$$

and

$$\frac{E_d}{kT_M^2} = \frac{\nu_o^{(2)}\sigma_o}{\beta} \exp\left(-\frac{E_d}{kT_M}\right), \text{ for } m = 2 \qquad (2)$$

where E_d is the activation energy of desorption, k is the Boltzmann constant, T_M is the temperature at which the maximum desorption rate occurs, σ_o is the initial surface coverage, m is the order of the desorption reaction, β is the heating rate, and $\nu_o^{(m)}$ is the pre-exponential factor of the desorption rate coefficient for order m. The assumption in the analysis of Redhead (1) are the following: (1) A pumping speed is rapid compared to the rate of thermal desorption; (2) a uniform substrate temperature; and (3) a constant E_d with respect to time and temperature. Eqs. (1) and (2) may be used to calculate E_d for an assumed pre-exponential factor. However, using an assumed value for the pre-exponential factor may result in a considerable error in the determination of E_d. This will be discussed in greater detail in Sec 3. An alternate way to determine the value of E_d without having to assume a value for the pre-exponential factor *à priori* has been suggested (1). Using this method, one has to obtain first the value of $d(\ell n\beta)/d(\ell nT_M)$ and then calculate the value of E_d for first order desorption kinetics from the expression

$$2 + \frac{E_d}{kT_M} = d(\ell n\beta)/d(\ell nT_M) \; . \qquad (3)$$

For second order desorption kinetics, a plot of $\ln(\sigma_o T_M^2)$ versus $1/T_M$ must be constructed, and the value of E_d/k is determined from the slope of the curve.

To obtain an accurate determination of E_d, β has to be varied by several orders of magnitude. This is not always possible for the interesting case of desorption from the surfaces of bulk single crystals. If β is very small, wall or readsorption effects may be important; alternately β may not be too large due to limitations in heating massive single crystals. Even if β could be made very large, then multiple peaks might not be resolved (5). Furthermore, a plot of $\ell n\beta$ versus $\ell n T_M$ is not linear; hence, the application of Eq. (3) to determine an accurate value of E_d is difficult. These two methods of analyzing thermal desorption mass spectra have been used extensively by workers in this field, but they both have their own drawbacks, as mentioned above.

In this paper, we describe a simple and rapid method to determine both the pre-exponential factor and the activation energy of the desorption rate coefficient. In principle, if the kinetic order of the desorption reaction is known, our method may be used to determine the activation energy as well as the pre-exponential factor easily with one thermal desorption spectrum, i.e., only one value of β is needed. In our method of analysis, the following information has to be extracted from a thermal desorption spectrum: T_M and the widths of various peaks in the thermal desorption spectrum. Schmidt (2) has shown that $\Delta W_{1/2}$ (full width of the thermal desorption peak at half maximum) is related to E_d, β and T_M by the following expressions:

$$\frac{\Delta W_{1/2}}{T_M} = 0.200\text{-}0.00845\ \ell n\left(\frac{\nu_o^{(1)} T_M}{\beta}\right) \qquad (4)$$

and

$$\frac{\Delta W_{1/2}}{T_M} = 0.233\text{-}0.0083\ \ell n\left(\frac{\nu_o^{(2)} n_o T_M}{\beta}\right) \qquad (5)$$

for first and second order desorption kinetics, respectively. He also showed that plots of $\Delta W_{1/2}$ versus T_M are very nearly straight lines. However, Eqs. (4) and (5) are only valid for a limited range of E_d, β and T_M. For example, if $\nu_o^{(1)} = 3.16 \times 10^9$, T_M = 300 K and β = 50K/s^{-1}, then $\Delta W_{1/2}$ = 0 from Eq. (4). This break down of Eqs. (4) and (5) is due to the erroneous assumption of linearity in Eqs. (4) and (5). The results of this calculation as well as earlier results of Edwards (6) show that plots of $\Delta W_{1/2}/T_M$ versus E_d/T_M are hyperbolic curves rather than straight lines. Edwards (6) has expressed $\Delta W_{1/2}/T_M$ as a series in E_d/kT_M, i.e.,

$$\frac{\Delta W_{1/2}}{T_M} = \frac{2.4464}{E_d/kT_M}\left[1 - \frac{1.4005}{E_d/kT_M} + \frac{3.5325}{(E_d/kT_M)^2} + \ldots.\right] \qquad (6)$$

and

$$\frac{\Delta W_{1/2}}{T_M} = \frac{3.5255}{E_d/kT_M}\left[1 - \frac{2.000}{E_d/kT_M} + \frac{6.941}{(E_d/kT_M)^2} + \ldots.\right] \qquad (7)$$

for first and second order desorption kinetics, respectively. However, equations in the form of a series expansion are not so convenient as those in an analytical form. It is the purpose of this paper to derive analytical expressions relating the kinetic parameters and to present the first detailed application of this method in the analysis of several important classes of desorption reactions.

In Sec. 2, we present a detailed discussion of the theory. In Sec. 3, we apply our method in the determination of pre-exponential factors and activation energies from several different thermal desorption mass spectra. Finally, our conclusions are summarized in Sec. 4.

2. Theory

In a thermal desorption measurement, a gas is adsorbed on the surface of a solid substrate, and a thermal desorption spectrum is obtained by increasing the temperature of the substrate. The change in the partial pressure in the reactor is detected mass spectrometrically. As is generally the case, we shall assume that the variation in temperature with time is linear and the product of the pumping speed and the heating rate has a value commensurate with a "normal" thermal desorption mass spectrum, i.e., the desorption rate is proportional to the change in pressure with time (7).

To obtain a thermal desorption spectrum theoretically, the (Polanyi-Wigner) differential equation must be solved, i.e.,

$$R(t) = \frac{-dn}{dt} = \nu_o^{(m)} n^m \exp(-E_d/kT_s) \qquad (8)$$

where R(t) is the rate of desorption which is a function of time, T_s is the temperature of the substrate, and n is the two-dimensional molecular concentration on the surface. If the thermal desorption spectra are measured by increasing the temperature of the substrate linearly with time, then the relationship between the substrate temperature and time is given by

$$T_s = T_{so} + \beta t \qquad (9)$$

where T_{so} is the initial temperature of the substrate, and β is the heating rate, i.e., $\frac{dT_s}{dt}$.

This differential equation contains all the desorption kinetic parameters ($\nu_o^{(m)}$, E_d and m) which have to be determined. As will be discussed in more detail below, the order of the desorption kinetics may be determined by the position of the peak maxima (the temperatures at which the desorption rate is greatest) as a function of initial surface coverage as well as by the skewness of the peaks.

With a view of obtaining expressions for $\nu_o^{(m)}$ and E_d, Eqs. (8) and (9) may be combined to yield

$$R(T_s) = -\beta\frac{dn}{dT_s} = \nu_o^{(m)} n^m \exp(-E_d/kT_s) \quad . \tag{10}$$

Figs. 1 and 2 show theoretically calculated thermal desorption spectra obtained by solving Eq. (10) for the case of first and second order desorption kinetics, respectively. It is evident from Fig. 1 that for first order desorption kinetics, the temperature at which the maximum rate of desorption occurs is invariant with surface coverage. On the other hand, Fig. 2 shows that for second order desorption kinetics, the temperature at which the maximum rate of desorption occurs shifts to lower values as surface coverage increases.

In order to put Eq. (10) in a more useful form, two characteristic quantities T^* and n^* are defined as

$$\begin{aligned} T^* &\equiv 1 \text{ K} \\ \text{and} \quad n^* &\equiv n_s \end{aligned} \tag{11}$$

where n_s is the saturation surface coverage at T_{so}. Using these two characteristic quantities, two other dimensionless quantities, Z and θ, may be defined as

$$\begin{aligned} Z &\equiv T_s/T^* \\ \text{and} \quad \theta &\equiv n/n^* \end{aligned} \tag{12}$$

Substituting Eq. (12) into Eq. (10) gives

$$-\beta \frac{d\theta}{dZ} = \nu_o^{(m)} (n^*)^{m-1} T^* \theta^m \exp(-E_d/kT^*Z) \tag{13}$$

Since Z and θ are dimensionless, Eq. (13) suggests two additional dimensionless groups E and $\nu^{(m)}$ defined as

$$E \equiv E_d/kT^* \tag{14}$$

and $$\nu^{(m)} \equiv \nu_o^{(m)} (n^*)^{m-1} T^*/\beta \quad . \tag{14}$$

Eq. (13) may now be rendered dimensionless with the result

$$R(Z) = \frac{-d\theta}{dZ} = \nu^{(m)} \theta^m \exp(-E/Z) \tag{15}$$

where $$R(Z) = \frac{R(T_s)T^*}{\beta n^*} \quad .$$

Consequently, since at Z_M, $\frac{dR(Z)}{dZ} = 0$,

$$mN^{(m)} = \theta_M^{1-m} E_M \exp(E_M) \quad , \tag{16}$$

where $$N^{(m)} \equiv \nu^{(m)} Z_M \quad , \quad ,$$

and $$E_M \equiv E/Z_M \quad . \tag{17}$$

In Eqs. (16) and (17), Z_M and θ_M are the values of Z and θ at the peak maxima, respectively. Eq. (16) may be rewritten as

$$N^{(1)} = E_M \exp(E_M) \tag{18}$$

and $$N^{(2)} = \frac{1}{2\theta_M} E_M \exp(E_M) \tag{19}$$

for first and second order desorption kinetics, respectively.

Once E_M and θ_M have been determined, both $\nu^{(m)}$ and $\nu_o^{(m)}$ may be calculated from Eqs. (18), (19) and (14). Consequently, it is necessary to formulate a method by which it is possible to obtain both θ_M and E_M from experimental thermal desorption mass spectra. This may be accomplished by changing variables in Eq. (15) according to the identity $y \equiv E/Z$ and performing an integration. The result is

$$\int_{\theta_o}^{\theta_M} \frac{d\theta}{\theta^m} = \int_{y_o}^{y_M} \nu^{(m)} E y^{-2} \exp(-y) dy, \tag{20}$$

where y_o and y_M are values of y at the initial temperature and at the temperature at which the maximum rate of desorption occurs, respectively. Since all experimentally observed values of y_o and y_M are greater than ten, the right-hand-side of Eq. (20) may be evaluated using the incomplete factorial function (8) giving

$$\left[\frac{(E_o-2)\exp(-E_o)}{E_o^3} - \frac{(E_M-2)\exp(-E_M)}{E_M^3}\right]\nu^{(m)}E \qquad (21)$$

Since $\exp(-E_M)>>\exp(-E_o)$ (9), Eq. (20) may be written quite accurately for m=1 as

$$\ell n\left(\frac{\theta_M}{\theta_o}\right) = \frac{-\nu^{(1)}E(E_M-2)\exp(-E_M)}{E_M^3} \quad , \qquad (22)$$

and for $m \neq 1$, as

$$\frac{\theta_M^{1-m} - \theta_o^{1-m}}{1-m} = \frac{-\nu^{(m)}E(E_M-2)\exp(-E_M)}{E_M^3} \quad . \qquad (23)$$

The maximum desorption rate from Eq. (15) is given by

$$R_M = \nu^{(m)}\theta_M^m \exp(-E_M) \quad . \qquad (24)$$

Using Eq. (16), Eq. (24) may be rewritten as

$$R_M = \frac{\theta_M E_M}{mZ_M} \quad . \qquad (25)$$

For first order desorption kinetics,

$$\theta_M = \theta_o \exp\left(-\frac{E_M-2}{E_M}\right) \quad , \qquad (26)$$

and

$$R_M = \frac{E_M\theta_o}{Z_M}\exp\left(-\frac{E_M-2}{E_M}\right) \quad ; \qquad (27)$$

whereas for second order desorption kinetics,

$$\theta_M = \frac{(E_M + 2)\theta_o}{2E_M} \quad , \tag{28}$$

and

$$R_M = \frac{(E_M + 2)\theta_o}{4Z_M} \quad . \tag{29}$$

Making use of Eqs. (19) and (28), $N^{(2)}$ (and consequently $\nu^{(2)}$) may be expressed in terms of E_M and θ_o

$$N^{(2)} = \frac{E_M^2}{(E_M + 2)\theta_o} \exp(E_M) \quad . \tag{30}$$

Eq. (18) expresses already $N^{(1)}$ in terms of E_M only. Hence, in order to determine the pre-exponential factor of the desorption rate coefficient for second order desorption kinetics, both E_M and θ_o must be known. For first order desorption kinetics, only E_M need be known.

For the determination of E_M from the experimental thermal desorption mass spectra, relationships between E_M and other experimentally measurable quantities (e.g., peak widths) are needed. The peak widths at one-half and three-fourths the peak maximum (the half-width and 3/4-width, respectively) are chosen since they can be determined easily and accurately.

The dimensionless desorption rate may be expanded in a Taylor series about Z_M, and the resulting expression with $\frac{d}{dZ} R(Z)\Big|_{Z=Z_M} = 0$ is

$$R(Z) = R(Z_M) + \frac{1}{2} \frac{d^2}{dZ^2} R(Z)\Big|_{Z=Z_M} (Z_M - Z)^2 + \ldots\ldots\ldots \tag{31}$$

Defining

$$Z \equiv Z_M(1 + \zeta) \quad , \tag{32}$$

making use of Eq. (25), and retaining only the first two terms in Eq. (31), the final expression for R(Z) is found to be

$$R(Z) = \left[1 - \frac{E_M (E_M + 2m) \zeta^2}{2m}\right] R_M \quad . \tag{33}$$

When $$R(Z) = \frac{1}{2} R_M \quad , \tag{34}$$

$$\zeta = \left[\frac{m}{E_M(E_M + 2m)}\right]^{\frac{1}{2}} \quad . \tag{35}$$

The width of a peak (in terms of the dimensionless temperature Z) is defined as

$$\Delta W \equiv Z' - Z'' \quad , \tag{36}$$

where

$$Z' = Z_M(1 + \zeta) \tag{37}$$

and $$Z'' = Z_M(1 - \zeta) \, . \tag{38}$$

Combining Eqs. (35), (36), (37) and (38), the half-width of the desorption peak is

$$\Delta W_{\frac{1}{2}} = 2Z_M \, [m/E_M(E_M + 2m)]^{\frac{1}{2}} \quad . \tag{39}$$

When $$R(Z) = \frac{3}{4} R_M \quad , \tag{40}$$

$$\Delta W_{\frac{3}{4}} = Z_M \, [2m/E_M(E_M + 2m)]^{\frac{1}{2}} \quad . \tag{41}$$

However, the expansion of R(Z) in a Taylor series about Z_M is valid only for rather small values of $|Z - Z_m|$. In deriving Eqs. (39) and (41), the expansion of R(Z) has been made for rather large values of $|Z - Z_M|$. Therefore, the validity of both Eqs. (39) and (41) has to be determined.

For the case of both first and second order desorption kinetics, Eq. (15) was solved numerically, and values for $\Delta W_{\frac{1}{2}}$ and $\Delta W_{\frac{3}{4}}$ for $10 < E_d < 50$ kcal/mole (corresponding to $5{,}033 \leq E \leq 25{,}164$) and $10^8 \leq \nu^{(m)} \leq 10^{15}$ were obtained. In order to compensate for the error introduced in the expansion of R(Z) about $|Z - Z_M|$, Eqs. (39) and (41) were used in a least squares fit to obtain the numerical prefactors that replace 2 and $\sqrt{2}$ in these equations. Hence, for

first order desorption kinetics,

$$Y_{1/2} = 2.415\ [1/E_M\ (E_M + 2)]^{1/2} \quad , \tag{42}$$

and

$$Y_{3/4} = 1.534\ [1/E_M(E_M + 2)]^{1/2} \quad ; \tag{43}$$

whereas for second order desorption kinetics,

$$Y_{1/2} = 3.531\ [1/E_M(E_M + 4)]^{1/2} \quad , \tag{44}$$

and

$$Y_{3/4} = 2.199\ [1/E_M(E_M + 4)]^{1/2} \quad , \tag{45}$$

where

$$Y \equiv \Delta W/Z_M \quad . \tag{46}$$

Eqs. (42)-(45) can reproduce values of $\Delta W_{1/2}$ and $\Delta W_{3/4}$ in agreement with the numerically calculated values to within 0.5% over the range of E_d and $\nu^{(m)}$ considered. Figs. 3 and 4 show explicitly the hyperbolic relationship between Y and E_M for the first and second order desorption kinetics, respectively.

The peak widths and positions of the peak maxima may be determined from the thermal desorption mass spectra. Consequently, for first order desorption kinetics E_M may be calculated by using the following expressions

$$E_M = -1 + \frac{1}{Y_{1/2}} \sqrt{Y_{1/2}^2 + 5.832} \tag{47}$$

and

$$E_M = -1 + \frac{1}{Y_{3/4}} \sqrt{Y_{3/4}^2 + 2.353} \quad , \tag{48}$$

and for second order desorption kinetics, by using

$$E_M = 2\left[-1 + \frac{1}{Y_{1/2}} \sqrt{Y_{1/2}^2 + 3.117}\right] \tag{49}$$

and

$$E_M = 2\left[-1 + \frac{1}{Y_{3/4}}\sqrt{Y_{3/4}^2 + 1.209}\right] . \qquad (50)$$

After E_M is calculated from the above expressions, $\nu^{(m)}$ can be determined by using Eqs. (18) and (30). Then $\nu_o^{(m)}$ can be obtained from Eq. (14) if β is measured experimentally. For second order desorption kinetics, n_s must be measured also.

Redhead (1) has shown that second order desorption spectra are approximately symmetrical about the peak maxima, whereas first order desorption spectra are asymmetric. To quantify the above statement, we define a skewness parameter as

$$\chi \equiv [(Z' + Z'' - 2Z_M)/\Delta W] \times 100 . \qquad (51)$$

The peak is symmetrical about the peak maximum when $\chi = 0$. The peak is skewed toward high temperatures or low temperatures for $\chi > 0$ or $\chi < 0$, respectively. The results of our calculation indicate that values of χ vary from -15.5 to -17.6 at half the peak maxima for first order desorption kinetics, and the values of χ vary from 3.2 to 5.1 at half the peak maxima for second order desorption kinetics, over the range of E_d and $\nu^{(m)}$ considered. The values of χ at three-fourths the peak maxima vary from approximately-10 to-11 and 2 to 3 for first and second desorption kinetics, respectively. Eq. (51) may be used as a supplementary test to determine the order of the desorption kinetics. Table 1 summarizes the characteristics for both first and second order desorption kinetics discussed in this paper.

3. Applications

Many calculations of E_d using thermal desorption data have been carried out by assuming *a priori* a value for the pre-exponential factor of the desorption rate coefficient. In particular, often for first order desorption kinetics, the pre-exponential factor has been assumed to be $10^{13} s^{-1}$. However, the pre-exponential factor for first order desorption kinetics has been found experimentally to be as low as $10^{4} s^{-1}$ for the ν state of CO on a W(110) surface (10) and as high as $3 \times 10^{16} s^{-1}$ for O_2 on polycrystalline tungsten (11). Evidently, an *a priori* assumed value for the pre-exponential factor may result in a considerable error in the determination of E_d.

Figs. 5 and 6 show the calculated shift in the position of peak maxima and the variation in the magnitude of the peak widths as $\nu^{(m)}$ is varied from 10^{8} to 10^{15} for first and second order desorption kinetics, respectively. To show the applicability of our method, we have analyzed several thermal desorption spectra from previously published experimental data (12 - 14, 17).

A. CO on Ni(110)

Thermal desorption spectra of α_2 CO on a (110) surface measured by Falconer and Madix (12) will be used to represent a prototype example of first order desorption kinetics. Fig. 7 shows two thermal desorption spectra (12) at a fractional surface coverage of 0.041 (spectrum a) and 0.013 (spectrum b). At these low coverages, the peak maxima are invariant within experimental error. The half- and three-fourths- widths of both spectra are approximately equal. The values of $\chi_{1/2}$ and $\chi_{3/4}$ are -15 and -11, respectively. These values of χ are typical for first order desorption kinetics as discussed in Sec. 2. These experimental data represent a good illustration of the characteristics for first order desorption kinetics listed in Table 1. The activation energy of

desorption and the pre-exponential factor were determined to be 30.0 kcal/mole and 4 x $10^{14}s^{-1}$, respectively, by using both the half- and three-fourths-widths of both spectra. The values of E_d and $\nu_o^{(1)}$ were reported by Falconer and Madix (12) to be 33 ±1 kcal/mole and 8.5 x $10^{15}s^{-1}$, respectively. Other values of E_d for CO desorption from Ni(110) were measured by Madden et al. (15) as well as Taylor and Estrup (16) to be 31 ± 2 kcal/mole and 30 kcal/mole, respectively. The agreement between these measurements and the results of our analysis is excellent.

B. CO on Pt(110)

A detailed study of the thermal desorption of CO from various crystallographic orientations of Pt has been carried out by McCabe and Schmidt (13). They found that the desorption of CO from a Pt(110) surface is a first order reaction with a coverage dependent activation energy of desorption given, in kcal/mole, by $E_d = 26.0 - 2.5\theta$, assuming the value of $\nu_o^{(1)}$ to be $10^{13}s^{-1}$. However, their experimental spectra are much broader than their theoretically calculated spectra (13). This broadening was believed to be caused by desorption from crystal support leads at low temperature , and desorption from edge, defect and oxide sites at high temperature (13). While there is certainly some validity to these arguments, the thermal desorption spectra of McCabe and Schmidt, reproduced in Fig. 8, are somewhat broader than would be expected even taking these effects into account. We have re-examined these thermal desorption spectra by the method described in Sec. 2 assuming that not all the broadening is due to the experimental artifacts. The values of $\Delta W_{\frac{1}{2}}$ and T_M at a low surface coverage were measured to be 50 K and 460 K, respectively. At low coverages, the activation energy of desorption is nearly constant; hence, our method of analysis can be applied directly. The activation energy of desorption is found to be 19.5 kcal/mole

considering only the thermal desorption spectrum corresponding to McCabe and Schmidt's lowest surface coverage. The value of E_d then was varied by ±5% to fit the temperature shifts and the shapes of all the experimental spectra. The result of this calculation indicates that the energy of activation for desorption is given, in kcal/mole, by $E_d = 19.2 - 1.9\theta$, and the value of the pre-exponential factor is $3.8 \times 10^9 s^{-1}$. Fig. 8 shows the experimental and calculated spectra both from ref. (13) and from this work. It is evident that the new kinetic parameters produce better agreement between the calculated and the experimental spectra, but the experimental spectra are still broader than the calculated ones. It is clear from Fig. 8 the calculated desorption rates approach zero at approximately 460K, while the desorption rate, measured experimentally, is still significant at this temperature.

If the high temperature tails of the experimental thermal desorption spectra are accounted for as a background, then the agreement between theory and experiment is improved markedly. Fig. 9 shows that nearly perfect agreement is obtained between the experimental spectra and our calculated ones by adding this background into the calculation of the theoretical spectra.

C. Xe on W(111)

Thermal desorption spectra of Xe from a W(111) surface, measured by Dresser, Madey and Yates (14), represent an interesting case to which our method of analysis cannot be applied directly since the characteristic pumping time τ for their experiment is large ($\tau \sim 1.3$ s), and their heating rate is $\beta = 5.15$K/s. Hence, the product of the heating rate and the pumping speed is not commensurate with a "normal" thermal desorption spectrum (7). The desorption of Xe from the W(111) surface was found to follow first order desorption kinetics as discussed in Ref. (14). Fig. 10 shows a thermal desorption spectrum at a fractional surface coverage of 0.134. The values of $\chi_{1/2}$ and $\chi_{3/4}$ were found to be positive

rather than negative, undoubtedly due to the large value of the product of τ and β for the experimental system for Xe. Hence, it would be logical to assume that the distortion on the low temperature side of the peak is less significant than that on the high temperature side (7). Consequently, only the values of $\Delta W_{\frac{1}{2}}'$ and $\Delta W_{\frac{3}{4}}'$ (defined in Fig. 10) were used. The half-width, $\Delta W_{\frac{1}{2}}$, and the three-fourths-width, $\Delta W_{\frac{3}{4}}$, were calculated, assuming (see Sec. 2) the values of $\chi_{\frac{1}{2}}$ and $\chi_{\frac{3}{4}}$ to be -15 and -10, respectively, using

$$\Delta W = \frac{200\ \Delta\ W_{\frac{1}{2}}'}{(100 - \chi)} \qquad (52)$$

The activation energy of desorption and the pre-exponential factor were determined to be 9.3 kcal/mole and $3 \times 10^{14} s^{-1}$, respectively, whereas the values of E_d and $\nu_o^{(1)}$ reported in ref. (14) were 9.3 kcal/mole and $10^{15} s^{-1}$, respectively. Fig. 11 shows that the agreement between our calculated spectrum and the experimental spectrum on the low temperature side of the peak is excellent. Hence our assumption of the small distortion of the values of $\Delta W_{\frac{1}{2}}'$ and $\Delta W_{\frac{3}{4}}'$ caused by a finite pumping speed is justified. However, the experimental spectrum is nevertheless broader than the calculated one on the high temperature side due to the large value of the product of β and τ.

D. N_2 on Platinum

Thermal desorption spectra of β-N_2 from a Pt filament measured by Wilf and Dawson (17) will be used to represent an example of second order desorption kinetics. Fig. 12 shows thermal desorption spectra (17) at a fractional surface coverage of θ = 0.22 (spectrum a) and θ= 0.17 (spectrum b). The values of $\chi_{\frac{1}{2}}$ for both spectra and the value of $\chi_{\frac{3}{4}}$ for spectrum a are higher than the typical values of χ for second order desorption kinetics. The broadening of $\Delta W_{\frac{1}{2}}''$ and $\Delta W_{\frac{3}{4}}''$ (defined in Fig. 10) is believed to be caused by a low pumping

speed of the system coupled with a high heating rate as discussed in Sec. 3c. The half-width, $\Delta W_{1/2}$, and three-fourths-width, $\Delta W_{1/4}$, were calculated using the measured values of $\Delta W'_{1/2}$ and $\Delta W'_{1/4}$, assuming the values of $\chi_{1/2}$ and $\chi_{1/4}$ to be 5 and 3, respectively (see Sec. 3c and Sec. 2). The activation energy of desorption and the pre-exponential factor were determined to be 20.3 kcal/mole and 9.6 x 10^{-8} cm^2/s, respectively; whereas the values of E_d and $\nu_o^{(2)}$ reported in Ref. (17) are 19 kcal/mole and 4 x 10^{-8} cm^2/s, respectively. The agreement between the results of this work and that reported in Ref. (17) is excellent.

4. Conclusions

Our major conclusions may be summarized as follows:

(1) Our work demonstrates a rapid and easy method to analyze thermal desorption spectra based both on peak positions and peak shapes.

(2) The method has been shown to work for first order desorption kinetics with coverage-independent E_d and $\nu_o^{(1)}$. In the case of CO adsorbed on Ni(110), E_d = 30.0 kcal/mole and $\nu_o^{(1)}$ = 4 x $10^{14}s^{-1}$. These results are in good agreement with various previous measurements (12, 15, 16).

(3) In the case of CO on a Pt(110) surface, our work demonstrates a successful application for first order kinetics with a coverage-dependent desorption activation energy. A new set of kinetic parameters, determined by our method, was able to produce better agreement with the experimental measurements (13). The surface coverage-dependent value of E_d is given by E_d = (19.2 - 1.9θ) kcal/mole, and the value of $\nu_o^{(1)}$ was determined to be 3.8 x $10^{9}s^{-1}$. The agreement between the experimental data and the calculation was improved greatly by including a finite CO background in the calculation of the theoretical spectra.

(5) In the case of Xe physically adsorbed on W(111), our method of analysis successfully measures desorption kinetic parameters for first order

desorption under conditions where the pumping speed is low. This was achieved by measurements on the leading edge of the desorption peak. The values of E_d and $\nu_o^{(1)}$ were determined to be 9.3 kcal/mole and 3 x 10^{14} sec^{-1}, respectively, in excellent agreement with the kinetic parameters deduced by fitting the desorption curve completely using known values of the pumping speed.

(5) In the case of N_2 on polycrystalline Pt, our work demonstrates a successful application of analysis of second order desorption kinetics. The values of E_d and $\nu_o^{(2)}$ were determined to be 20.3 kcal/mole and 9.6 x 10^{-8} cm^2/s, respectively.

Acknowledgment

This work was supported by the Army Research Office (Durham) under Grant Number DAHC04-75-0170.

References

1. P. A. Redhead, Vacuum 12, 203 (1962).
2. L. D. Schmidt, Catal. Rev.-Sci. Eng. 9, 115 (1974).
3. D. A. King, Surface Sci. 47, 384 (1975).
4. G. Ehrlich, Advan. Catal. 14, 255 (1963).
5. D. Menzel, in Interactions on Metal Surfaces, p. 101, Ed., R. Gomer, Springer-Verlag, New York, 1975.
6. D. Edwards, Jr., Surface Sci. 54, 1 (1976).
7. C.-M. Chan and W. H. Weinberg, Appli. Surface Sci. (following paper).
8. R. L. Walker and J. Mathews, Mathematical Methods of Physics, W. A. Benjamin, New York, 1965.
9. For example, if E_d = 25 kcal/mole, $\nu_o^{(1)} = 10^{13} s^{-1}$, T_o = 300K and T_M = 386K, then E_o = 41.7 and E_M = 32.4. Therefore, $\exp(-E_M) = 8.6 \times 10^{-15} >> \exp(-E_o) = 7.8 \times 10^{-19}$.
10. C. Kohrt and R. Gomer, Surface Sci. 24, 77 (1971).
11. C. G. Goymour and D. A. King, J. Chem. Soc: Faraday I 68, 280 (1972).
12. J. L. Falconer and R. J. Madix, Surface Sci. 48, 393 (1975).
13. R. W. McCabe and L. D. Schmidt, Surface Sci. 60, 85 (1976); Surface Sci. 66, 101 (1977).
14. M. J. Dresser, T. E. Madey and J. T. Yates, Jr., Surface Sci. 42, 533 (1974).
15. H. H. Madden, J. Küppers and G. Ertl, J. Chem. Phys. 58, 3401 (1973).
16. T. N. Taylor and P. J. Estrup, J. Vac. Sci. Technol. 10, 26 (1973).
17. M. Wilf and P. T. Dawson, Surface Sci. 60, 561 (1976).

Table Caption

Table 1: Summary of the characteristics of first and second order desorption kinetics as discussed in the text.

Table 1. Characteristics of Thermal Desorption Mass Spectra

	m = 1	m = 2
1.	The position of peak maxima are invariant with surface coverage.	The position of the peak maxima shift to lower temperature as the surface coverage increases.
2.	$\chi < 0$	$\chi > 0$
3.	$-10 \lesssim \chi_{3/4} \lesssim -11$	$2 \lesssim \chi_{3/4} \lesssim 3$
4.	$-15 \lesssim \chi_{1/2} \lesssim -18$	$3 \lesssim \chi_{1/2} \lesssim 5$
5.	The magnitudes of $\Delta W_{1/2}$ and $\Delta W_{3/4}$ are invariant with surface coverage.	The magnitudes of $\Delta W_{1/2}$ and $\Delta W_{3/4}$ increase as surface coverage increases.
6.	$R_M = \frac{E_M \theta_o}{Z_M} \exp\left(-\frac{E_M - 2}{E_M}\right)$	$R_M = \frac{(E_M + 2)\theta_o}{4Z_M}$
7.	$\theta_M = \theta_o \exp\left(-\frac{E_M - 2}{E_M}\right)$	$\theta_M = \frac{(E_M + 2)\theta_o}{2E_M}$
8.	$Y_{1/2} = \Delta W_{1/2}/Z_M$	$Y_{1/2} = \Delta W_{1/2}/Z_M$
9.	$Y_{1/4} = \Delta W_{1/4}/Z_M$	$Y_{1/4} = \Delta W_{1/4}/Z_M$
10.	$Y_{1/2} = 2.415[1/E_M(E_M+2)]^{1/2}$	$Y_{1/2} = 3.531\ [1/E_M(E_M+4)]^{1/2}$
11.	$Y_{3/4} = 1.534\ [Y_M/E_M(E_M+2)]^{1/2}$	$Y_{3/4} = 2.199[1/E_M(E_M+4)]^{1/2}$
12.	$E_M = -1 + \frac{1}{Y_{1/2}}\sqrt{Y_{1/2}^2+5.832}$	$E_M = 2\left[-1 + \frac{1}{Y_{1/2}}\sqrt{Y_{1/2}^2+3.117}\right]$
13.	$E_M = -1 + \frac{1}{Y_{3/4}}\sqrt{Y_{3/4}^2+2.353}$	$E_M = 2\left[-1 + \frac{1}{Y_{3/4}}\sqrt{Y_{3/4}^2+1.209}\right]$
14.	$E_d = E_M k Z_M T^*$	$E_d = E_M k Z_M T^*$
15.	$\nu_o^{(1)} = \frac{\beta E_M \exp(E_M)}{Z_M T^*}$	$\nu_o^{(2)} = \frac{\beta E_M^2 \exp(E_M)}{(E_M + 2)\theta_o n^* Z_M T^*}$

Figure Captions:

Figure 1: Calculated dimensionless desorption rate for first order desorption kinetics with E_d = 25 kcal/mole and $\nu^{(1)} = 10^{13}$ at different fractional surface coverages. Spectrum a: θ = 1.0; spectrum b: θ = 0.75; spectrum c: θ = 0.5; spectrum d: θ = 0.25.

Figure 2: Same as Fig. 1 for second order desorption kinetics with $\nu^{(2)} = 10^{13}$.

Figure 3: Plot of E_M versus $Y_{3/4}$ and $Y_{1/2}$ for first order desorption kinetics.

Figure 4: Same as Fig. 3 for second order desorption kinetics.

Figure 5: Calculated dimensionless desorption rate for first order desorption kinetics with E_d = 25 kcal/mole and different values of $\nu^{(1)}$. The value of $\nu^{(1)}$ for spectrum a is 10^{15}. The values of $\nu^{(1)}$ for spectra b, c, d, e, f, g and h are successively decreased by a factor of ten compared to spectrum a.

Figure 6: Same as Fig. 5 for second order desorption kinetics.

Figure 7: Thermal desorption spectra for CO on Ni(110) surface at fractional coverages of 0.075 and 0.023 for spectra a and b, respectively (12).

Figure 8: Comparison of experimental thermal desorption spectra of CO from a Pt(110) surface (solid line) (13), calculated spectra from ref. (13) (——+——+——+——), and calculated spectra from this work (----o----o----o----o).

Figure 9: Same as Fig. 8 with addition of a finite high temperature CO background to the calculated spectra.

Figure 10: Experimental thermal desorption spectrum of Xe from a W(111) surface (14).

Figure 11: Comparison of experimental thermal desorption spectrum in Fig. 10 and calculated spectrum.

Figure 12: Thermal desorption spectra of β - N_2 from a Pt filament at coverages of 0.22 and 0.15 for spectra a and b, respectively (17).

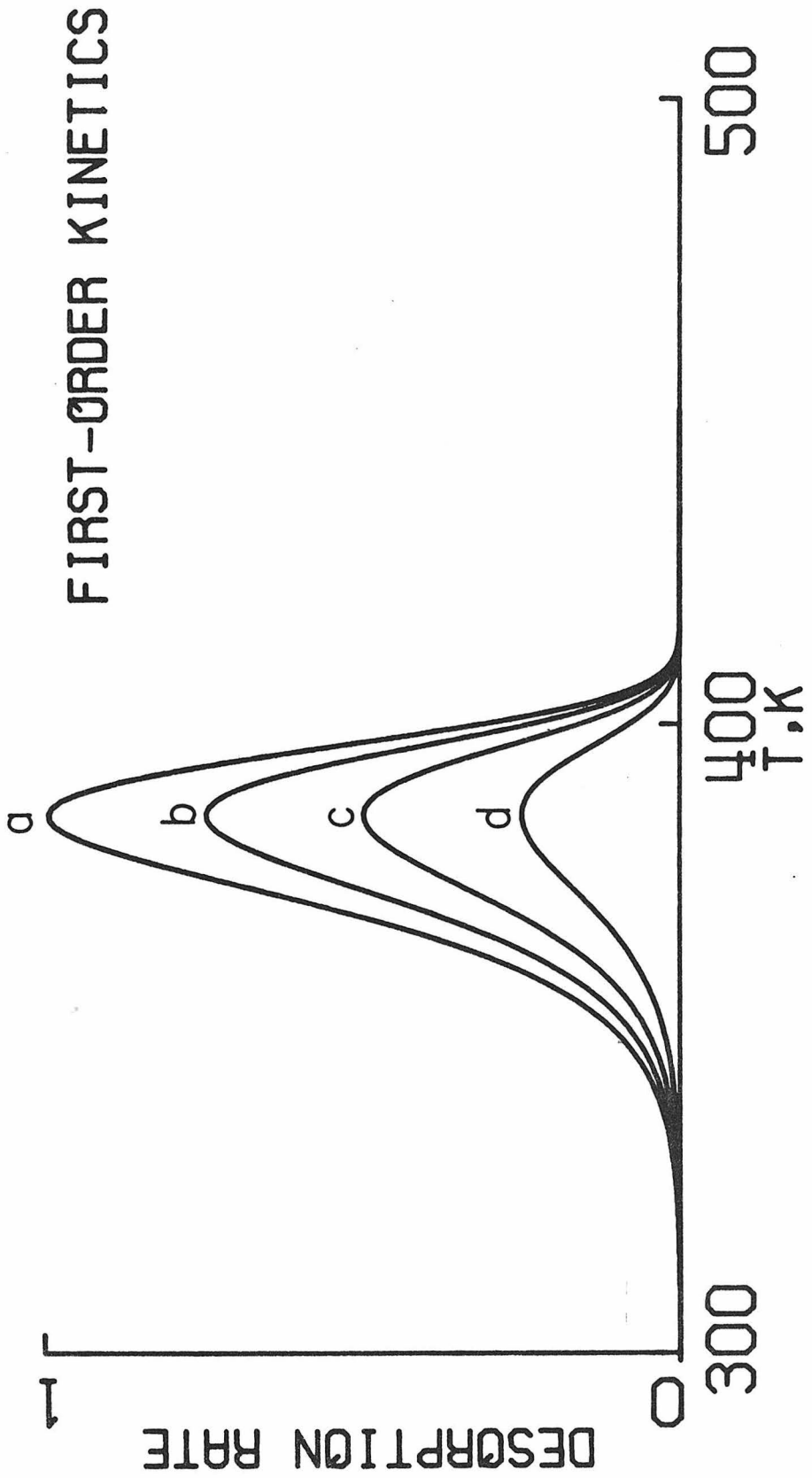

Fig.1

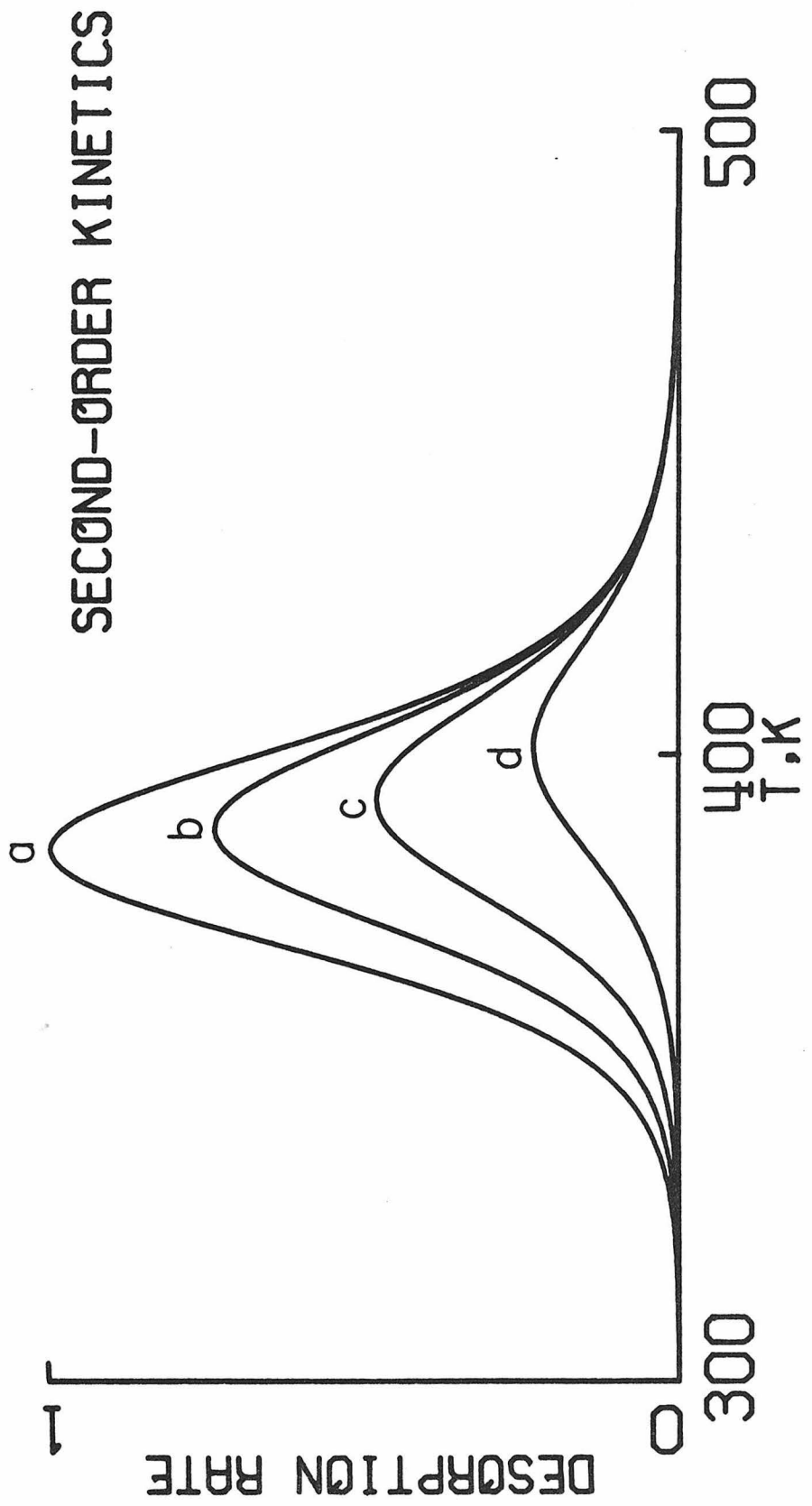
SECOND-ORDER KINETICS
DESORPTION RATE
1
0
300
400
500
T,K
a
b
c
d

Fig.2

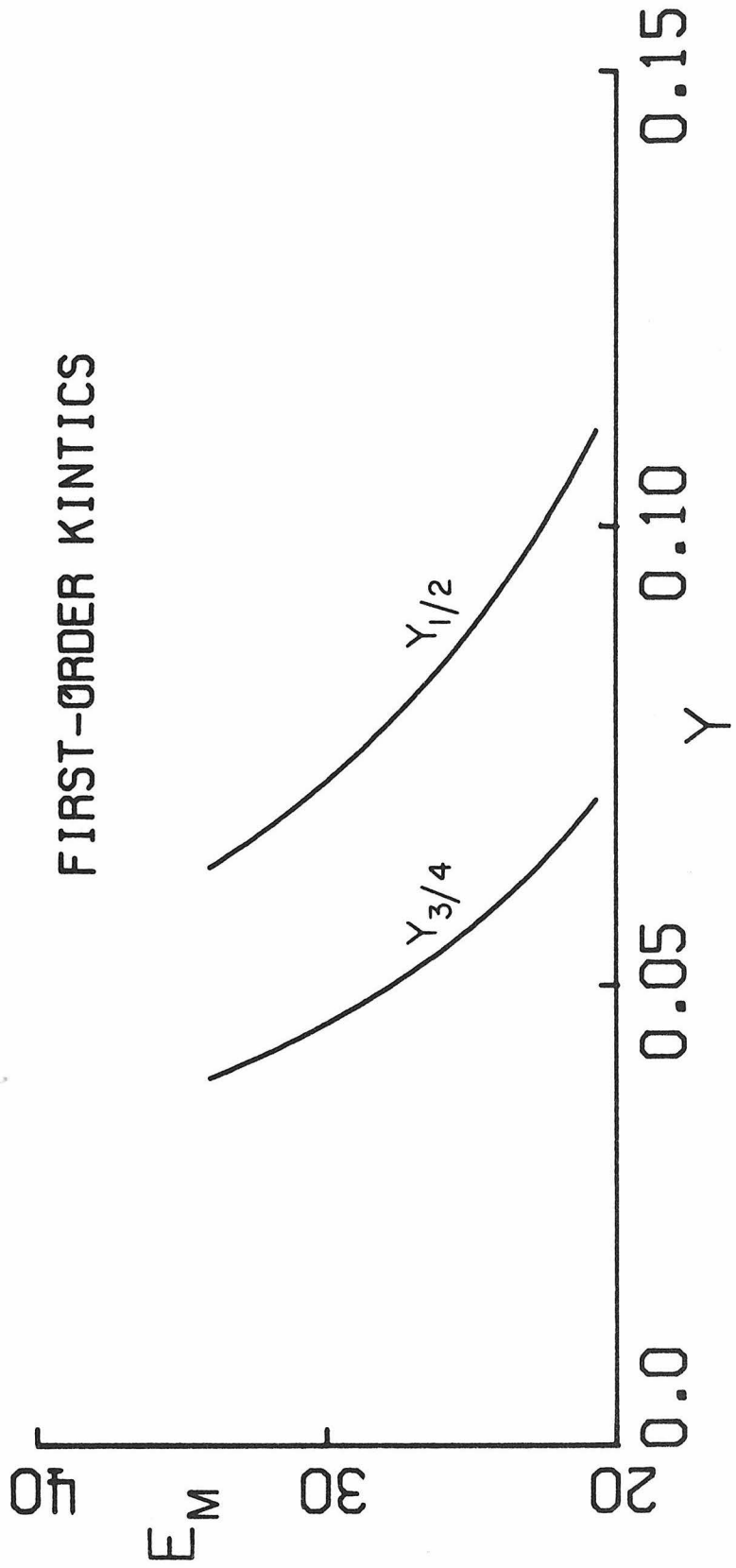

Fig.3

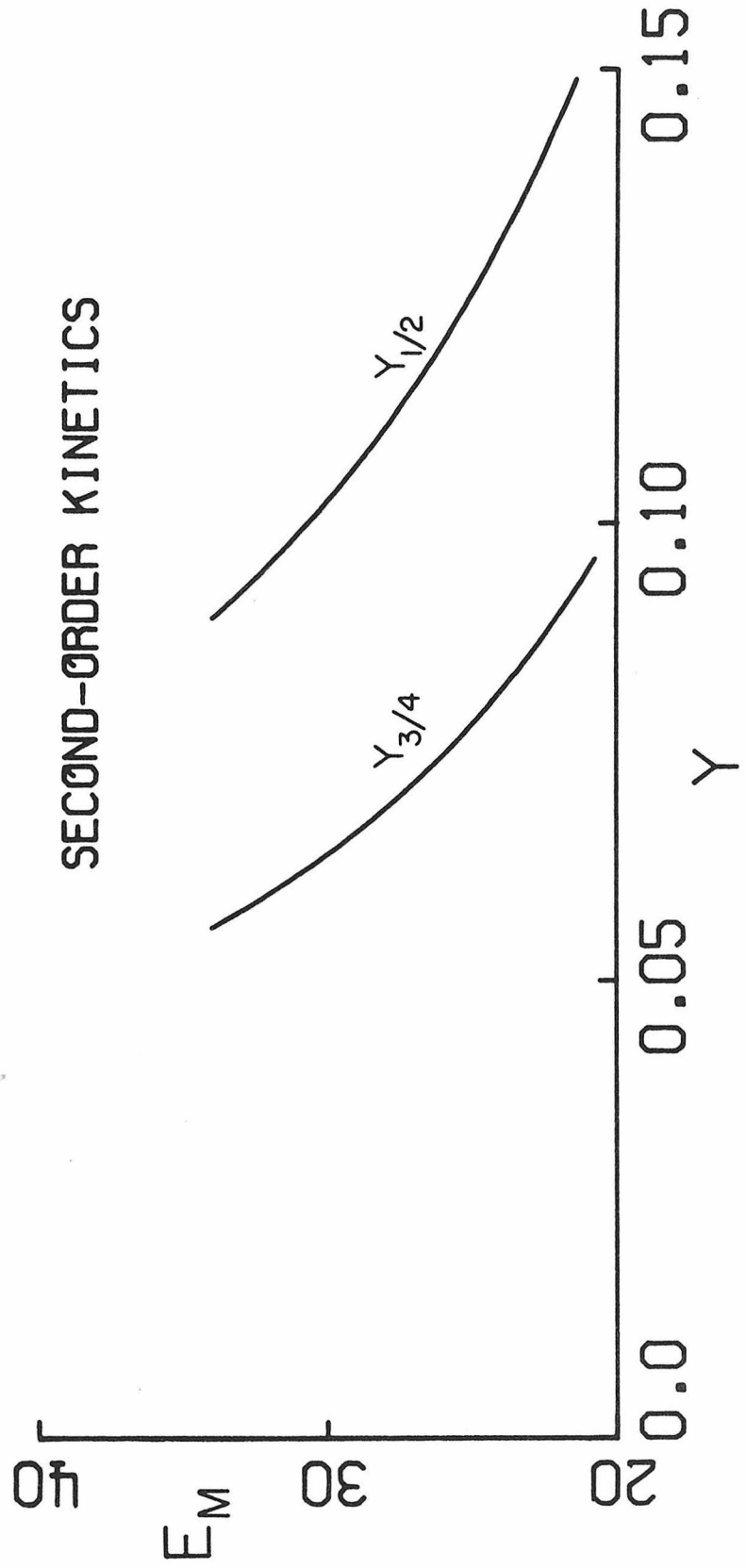

Fig.4

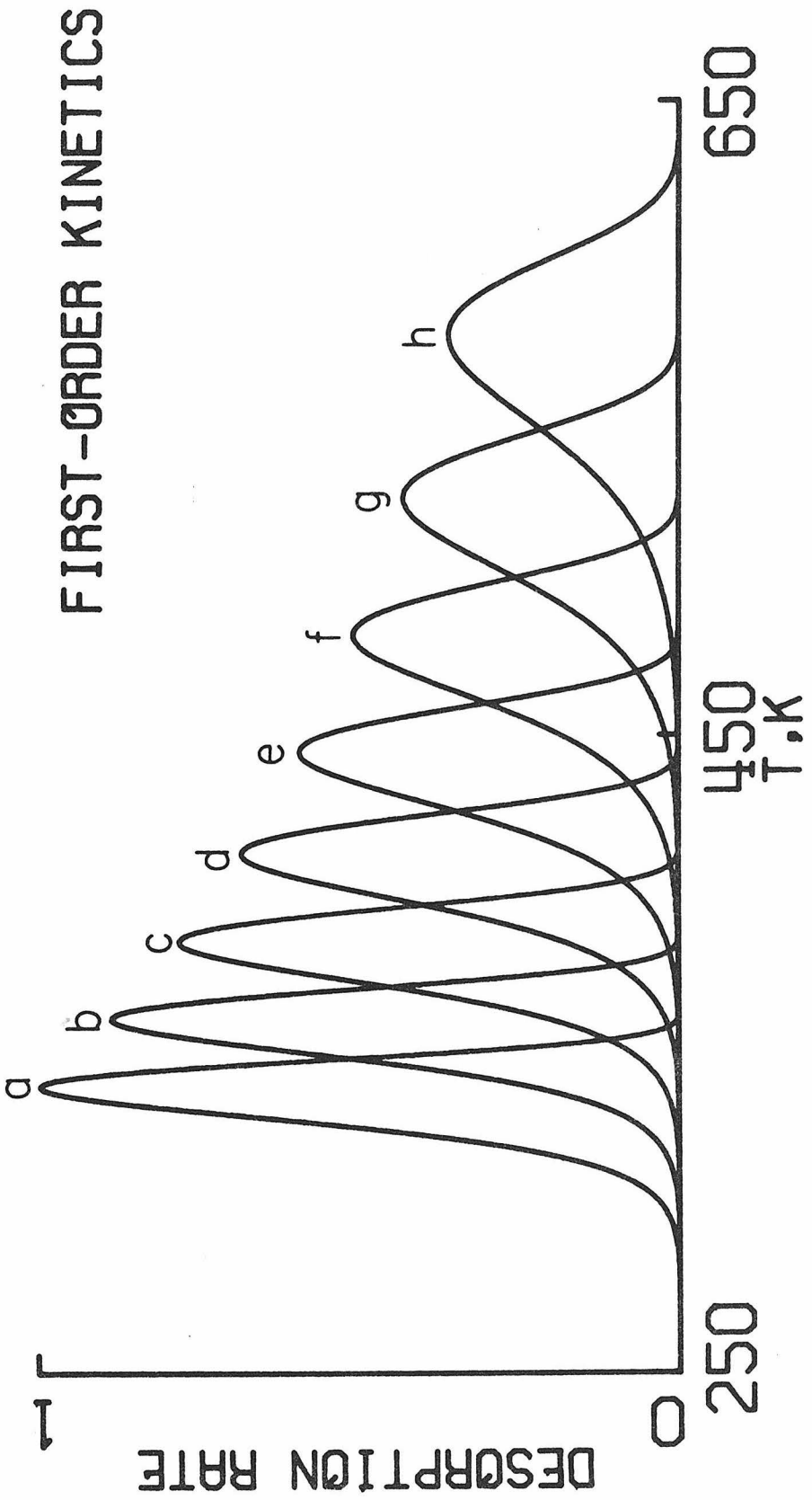
FIRST-ORDER KINETICS
DESORPTION RATE
1
0
250
450
T,K
650
a
b
c
d
e
f
g
h

Fig.5

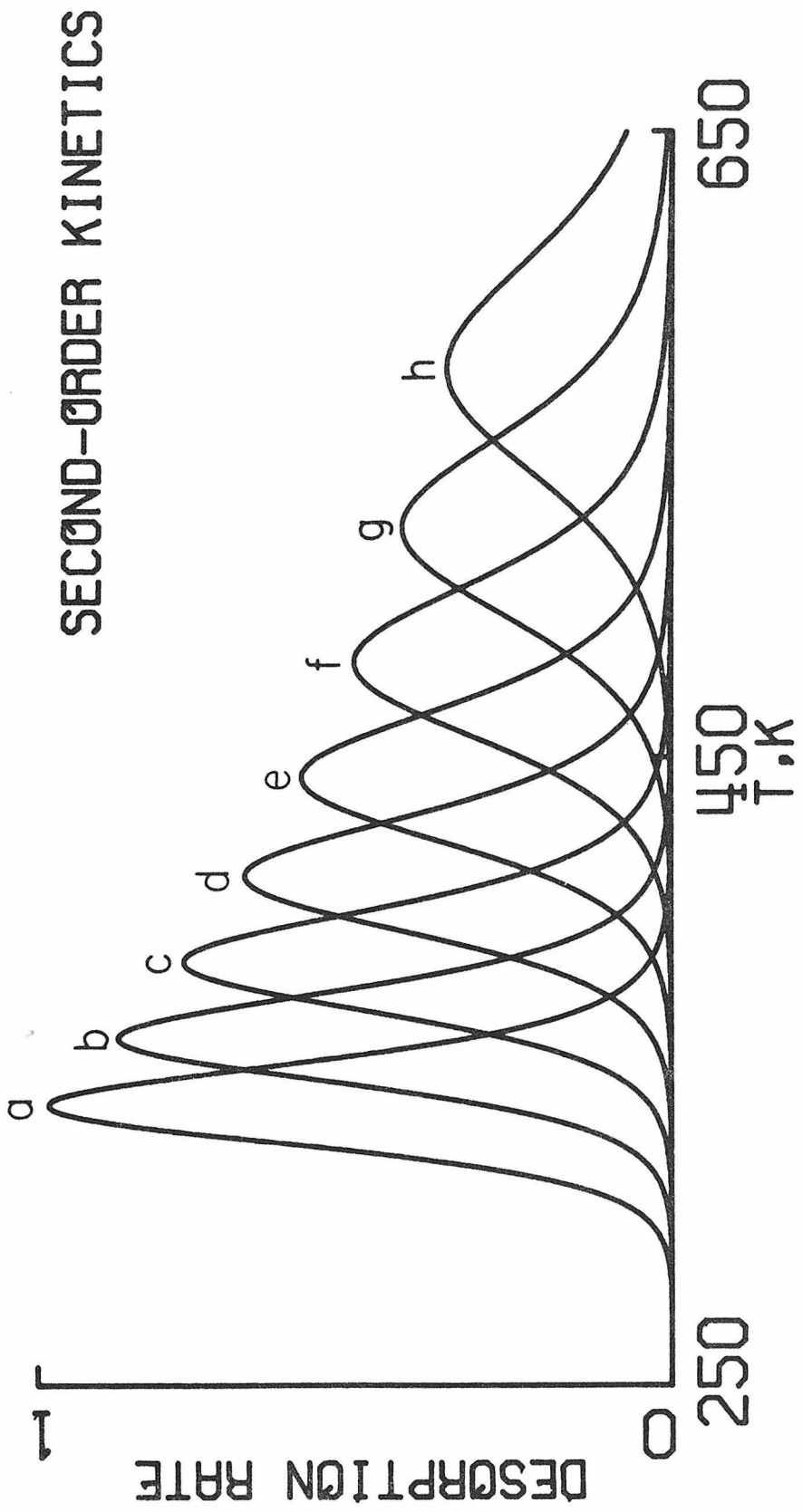
SECOND-ORDER KINETICS
DESORPTION RATE
1
0
250
450
T,K
650
a
b
c
d
e
f
g
h

Fig.6

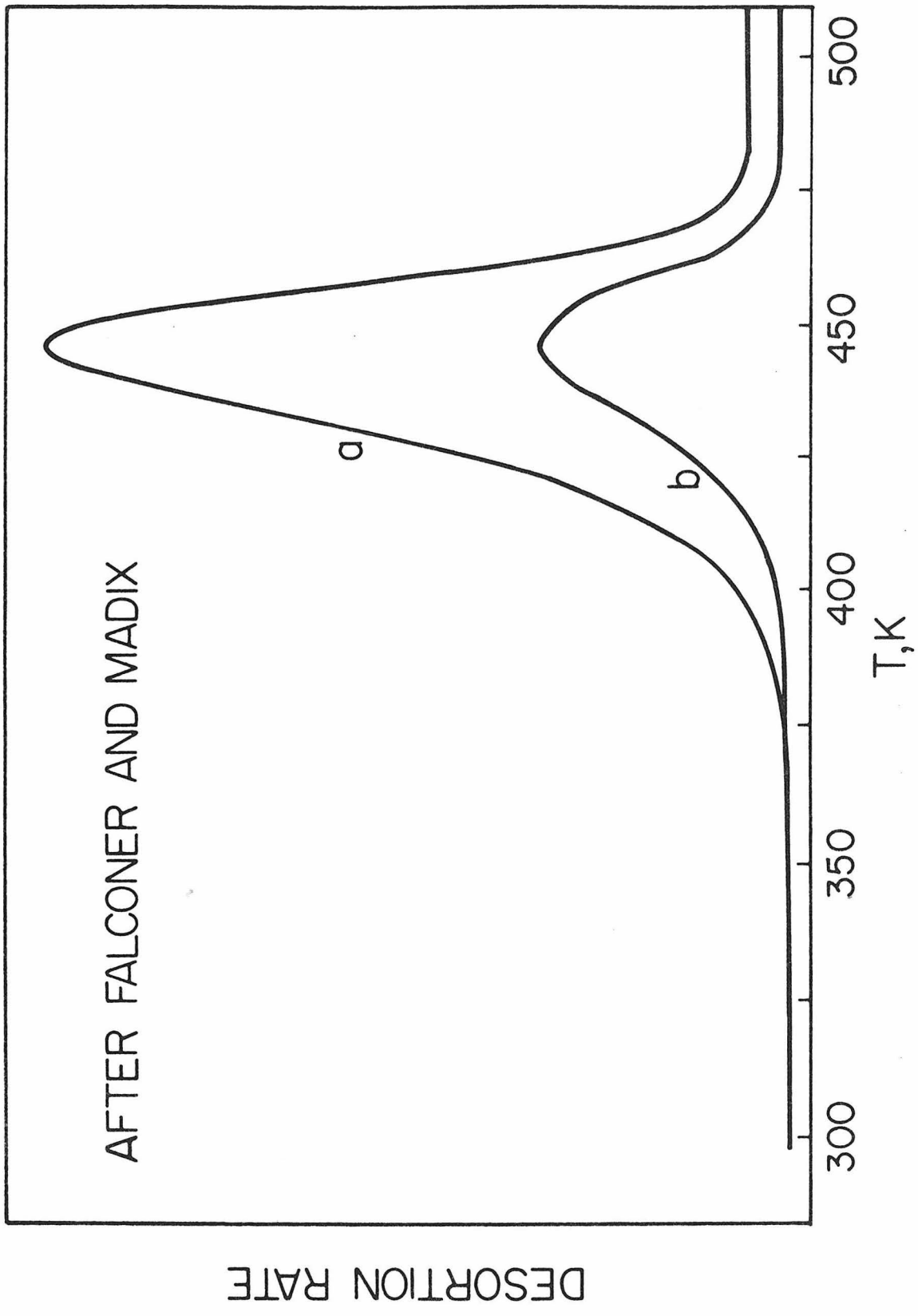
AFTER FALCONER AND MADIX
a
b
300
350
400
450
500
T,K
DESORTION RATE

Fig.7

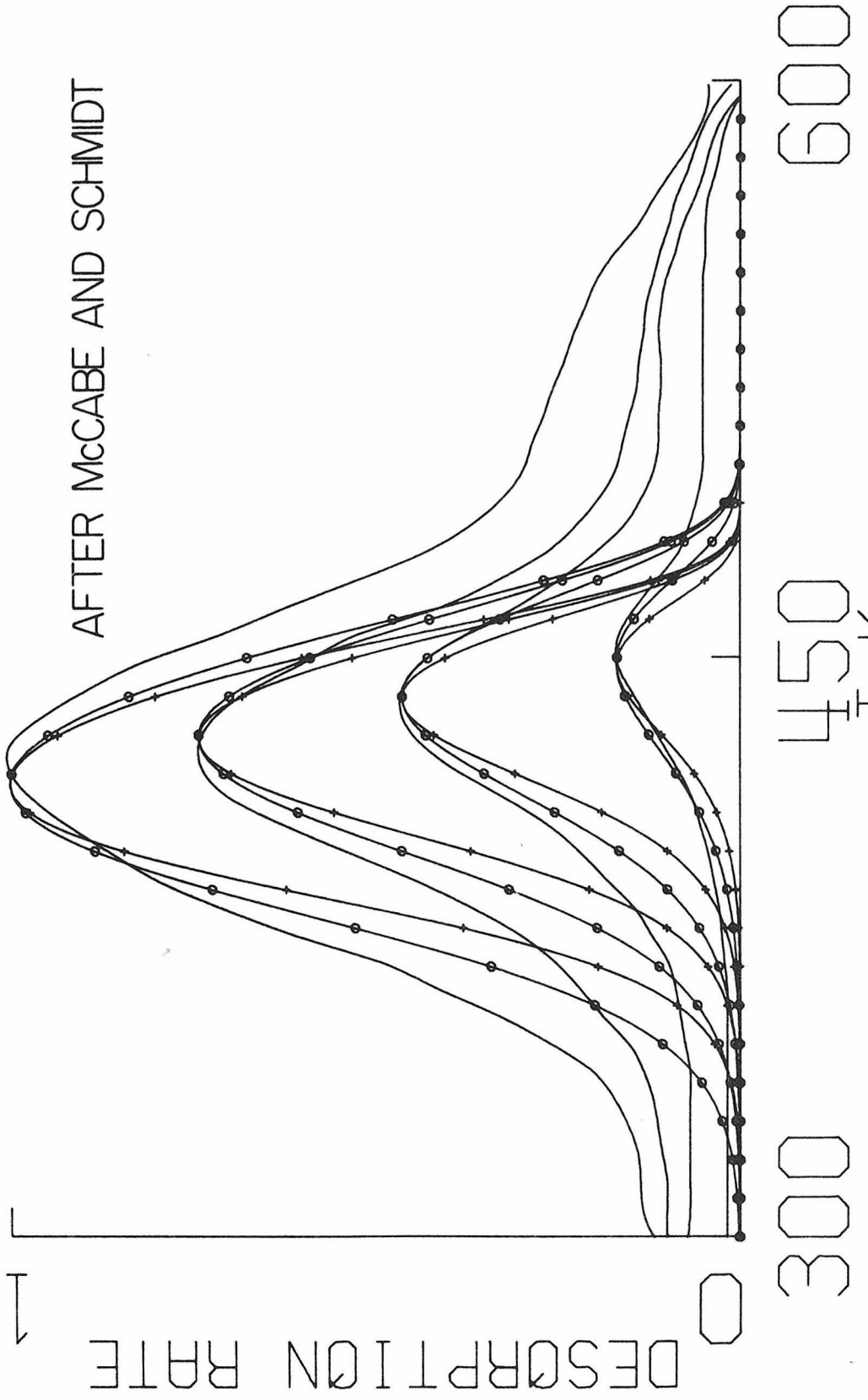

Fig.8

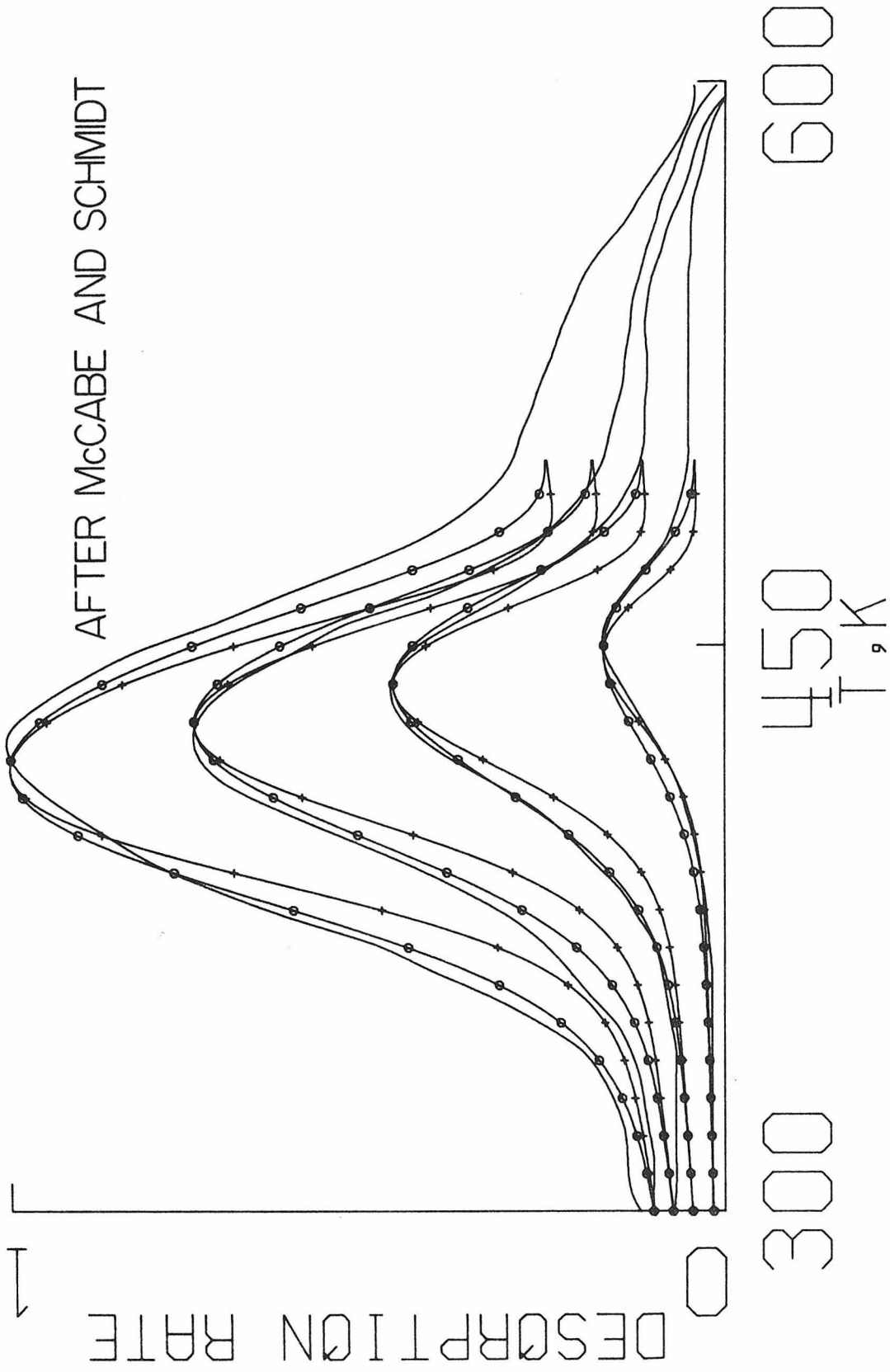

Fig.9

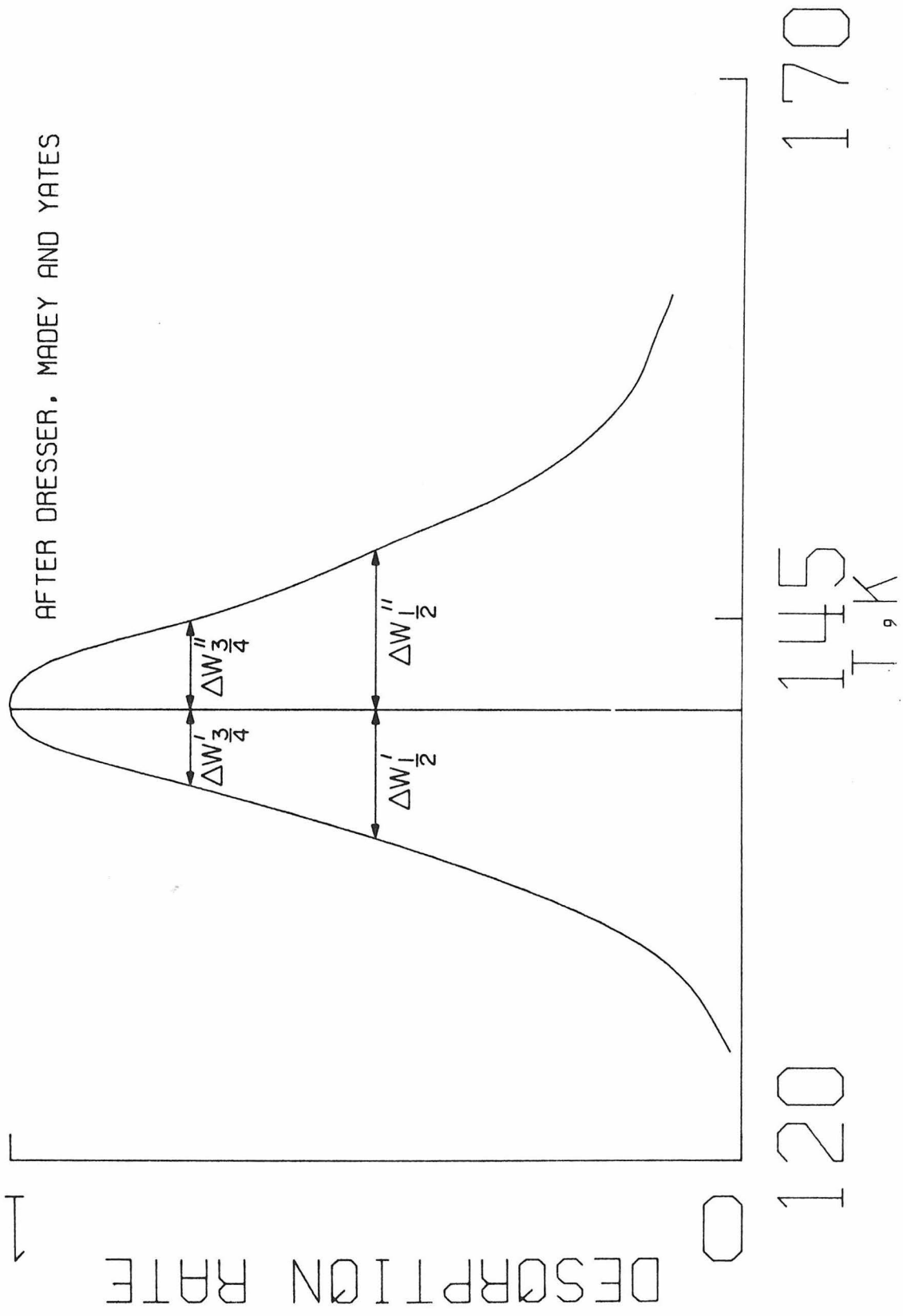
AFTER DRESSER, MADEY AND YATES
DESORPTION RATE
0
120
145
170
T_g K
$\Delta W''_{\frac{3}{4}}$
$\Delta W''_{\frac{1}{2}}$
$\Delta W'_{\frac{3}{4}}$
$\Delta W'_{\frac{1}{2}}$

Fig.10

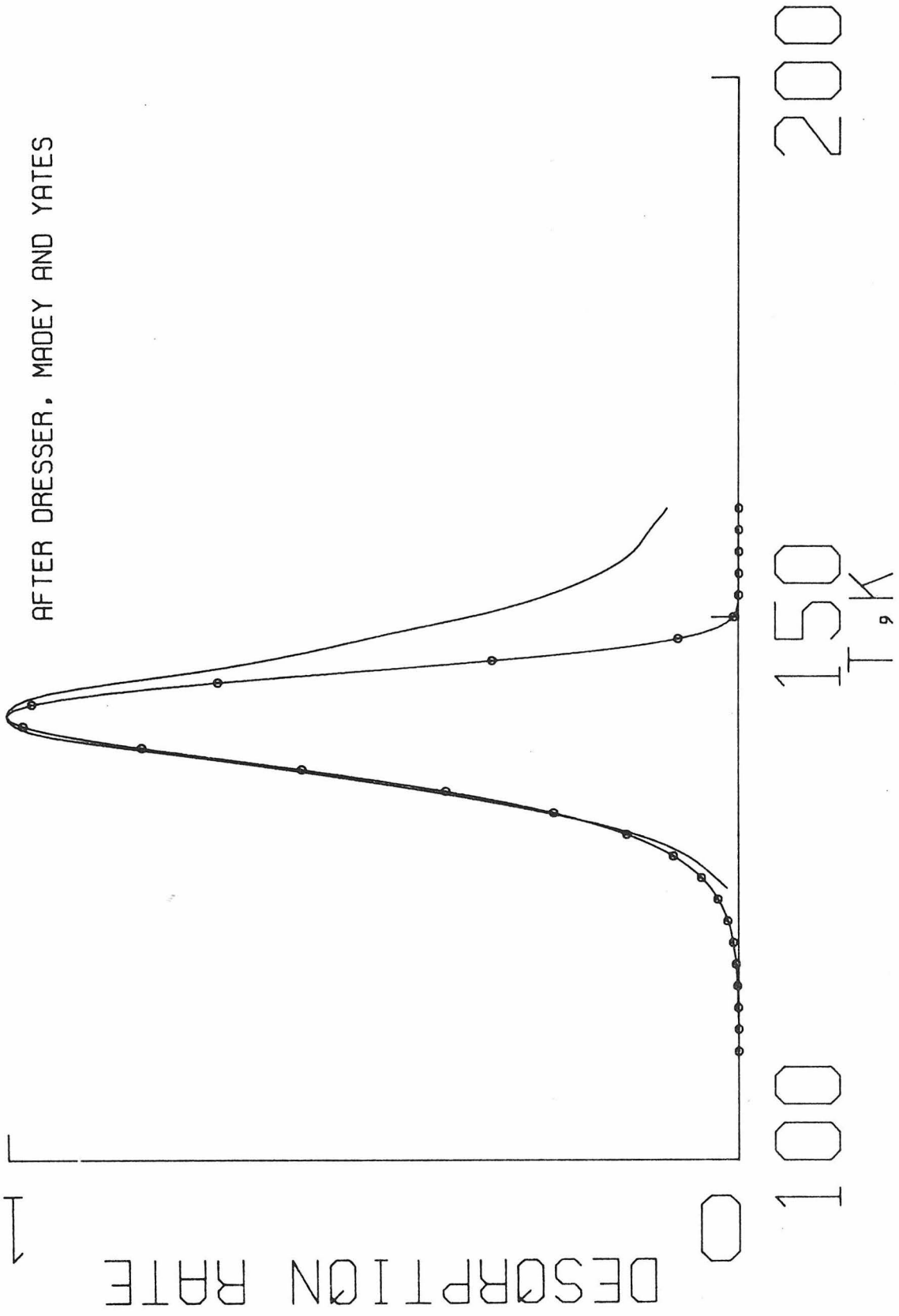
AFTER DRESSER, MADEY AND YATES
DESORPTION RATE
1
0
100
150
200
T, K
g

Fig.11

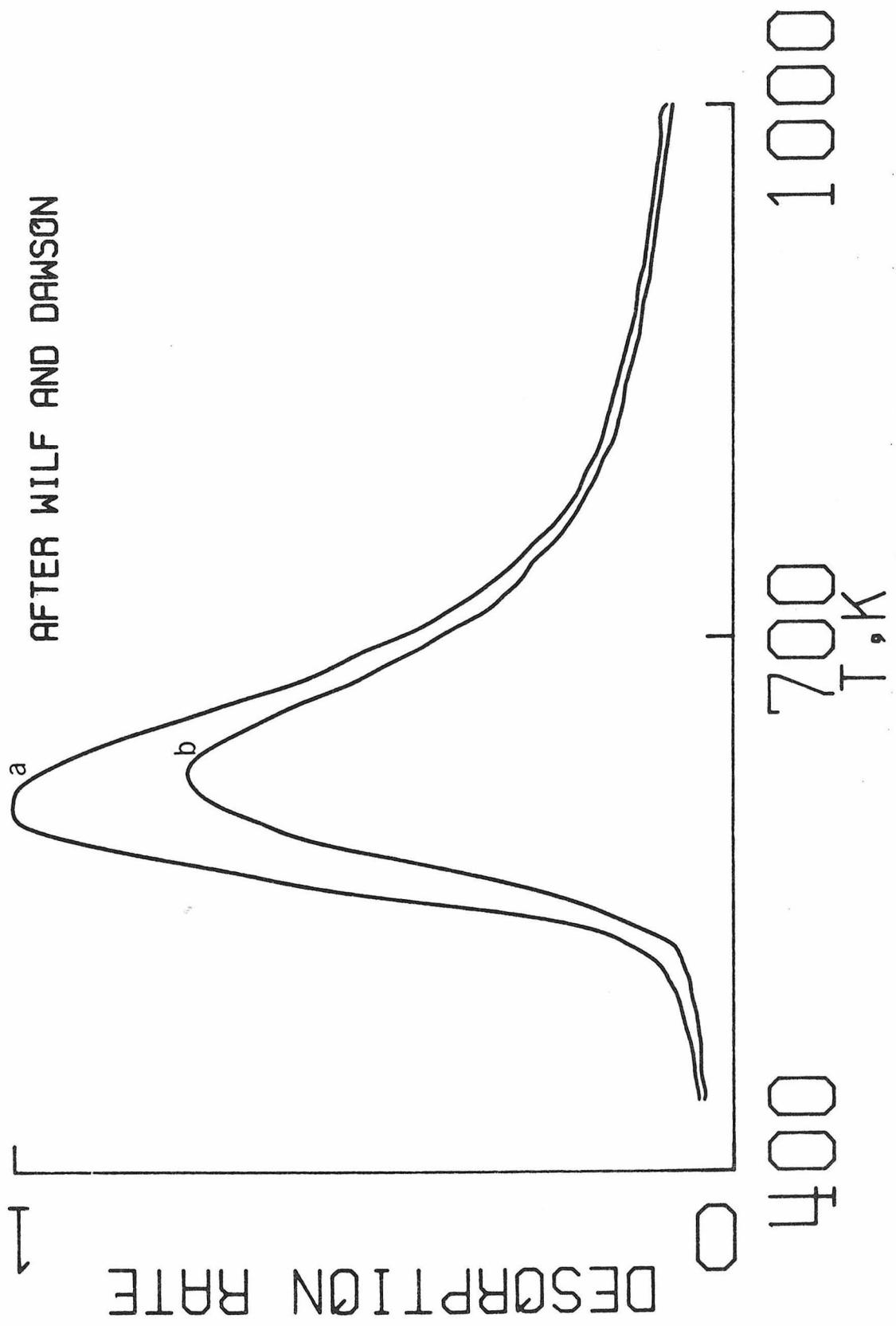

Fig. 12

Chapter 2

AN ANALYSIS OF THERMAL DESORPTION MASS SPECTRA. II.

by

C.-M. Chan and W. H. Weinberg
Division of Chemistry and Chemical Engineering
California Institute of Technology
Pasadena, California 91125

Application of Surface Science 1, 377-387 (1978)

Abstract

A quantitative analysis is given concerning the combined effect of heating rate and pumping speed on thermal desorption mass spectra. It is shown that considerable error in the determination of the activation energy and the pre-exponential factor of desorption can be introduced by the combined effects of high heating rate and low pumping speed. It is found that for an accurate determination of the activation energy and the pre-exponential factor of first-order desorption, the reciprocal of the product of heating rate and pumping time constant
Λ should be large, i.e., greater than approximately 0.5.

1. Introduction

Thermal desorption mass spectrometry is one of the most important experimental techniques to study the kinetic parameters for admolecules desorbing from solid surfaces. Numerous methods of analyzing thermal desorption spectra to determine both the activation energy of desorption, E_d, and the pre-exponential factor of the desorption rate coefficient $\nu_o^{(m)}$, have been presented (1-5). Redhead (1) and Ehrlich (2) have shown qualitatively the individual effect of pumping speed and heating rate on the shape and the peak position of a thermal desorption spectrum. However, no quantitative error analysis of the combined effects of heating rate and pumping speed has been made to date.

The purpose of this paper is to show the importance of the combined effect of heating rate and pumping speed. It is shown that the "goodness" of a thermal desorption spectrum can be judged by the product of heating rate and pumping speed and not by the magnitude of each one individually. Furthermore, it is shown that in order to obtain a pressure profile during a thermal desorption measurement which is proportional to the desorption rate, the reciprocal of the product of heating rate and pumping $\left(\frac{\text{time constant}}{\Lambda}\right)$ must be large, e.g., greater than approximately 0.5. In Section 2, a detailed discussion of the formalism is presented. In Section 3, the results are presented and discussed. Finally, the major conclusions are summarized in Section 4.

2. Formalism

Schmidt (6) has shown that the relationship between the pressure profile and the desorption rate for a system with a constant leakage rate is

$$\frac{dn}{dT_s} = \frac{V}{AkT_g}\left[\frac{P_{sy} - P_{eq}}{\beta\tau} + \frac{dP_{sy}}{dT_s}\right] , \qquad (1)$$

and

$$\frac{dn}{dT_s} = \frac{\nu_o^{(m)} \exp\left(-E_d/kT_s\right)}{\beta} , \qquad (2)$$

where n is the two-dimensional molecular concentration on the surface, T_s and T_g are the temperature of the gas and the surface, respectively, V is the system volume, A is the area of the adsorbing surface, k is the Boltzmann constant, P_{eq} and P_{sy} are the equilibrium partial pressure and the instantaneous partial pressure of the system, respectively, τ is the pumping time constant, β is the heating rate, $\nu_o^{(m)}$ is the pre-exponential factor for a desorption order of m, and E_d is the activation energy of desorption.

Defining

$$P^* \equiv P_{sy} - P_{eq} , \qquad (3)$$

Eq. (1) becomes

$$\frac{dP^*}{dT_s} = -\frac{kT_gA}{V}\frac{dn}{dT_s} + \frac{P^*}{\tau\beta} . \qquad (4)$$

To solve Eq. (4) following the procedure of Redhead (1), τ is set equal to infinity, giving

$$\frac{dP^*}{dT_s} = - \frac{kT_g A}{V} \frac{dn}{dT_s} \quad . \tag{5}$$

Integrating Eq. (5) yields

$$P^*_{max} = - \frac{kT_g A}{V} \int_{n_o}^{0} dn = \frac{kT_g A n_o}{V} \tag{6}$$

where P^*_{max} is the maximum pressure observed during a desorption measurement in a closed system for an initial surface coverage of n_o. Defining a dimensionless pressure

$$P \equiv P^*/P^*_{max} \quad , \tag{7}$$

and combining Eqs. (4) and (2) gives

$$\frac{dP}{dT_s} + \frac{P}{\beta\tau} = \frac{\nu_o^{(m)} n^m \exp(-E_d/kT_s)}{\beta n_o} \quad . \tag{8}$$

To render Eq. (8) dimensionless, two quantities, Z, the dimensionless temperature, and θ, the fractional surface coverage, are introduced and defined as

$$Z \equiv T_s/T^* \tag{9}$$

and

$$\theta \equiv n/n_s \quad , \tag{10}$$

where $T^* \equiv 1$ K, and n_s is the saturation surface coverage. Substituting Eq. (9) and (10) into Eq. (8) gives

$$\frac{dP}{dZ} + \frac{T^* P}{\beta\tau} = \frac{T^* \nu_o^{(m)} n_o^{m-1} \theta^m \exp(-E_d/kT^* Z)}{\beta} \tag{11}$$

Eq. (11) suggests three other dimensionless groups, namely, E, $\nu^{(m)}$ as well as Ω and defined as

$$E \equiv \frac{E_d}{kT^*} \tag{12}$$

$$\nu^{(m)} \equiv \frac{\nu_o^{(m)} n_o^{m-1} T^*}{\beta} \tag{13}$$

and

$$\Omega \equiv \frac{T^*}{\beta\tau} \tag{14}$$

Hence, Eq. (11) may be rewritten as

$$\frac{dP}{dZ} + \Omega P = \nu^{(m)} \theta^m \exp(-E/Z) = R(Z) \ . \tag{15}$$

In order to eliminate θ^m from Eq. (15), it is useful to recall the following previously derived results (4):

$$\frac{\theta_M}{\theta_o} = \frac{-\nu^{(1)} E(E_M - 2) \exp(-E_M)}{E_M^3} \tag{16}$$

$$\frac{1}{\theta_o} - \frac{1}{\theta_M} = \frac{-\nu^{(2)} E(E_M - 2) \exp(-E_M)}{E_M^3} \tag{17}$$

for m = 1 and m = 2, respectively, where θ_M is the fractional surface coverage at the maximum rate of desorption; and $E_M \equiv E/Z_M$, where Z_M is the dimensionless temperature at the maximum rate of desorption. To a very good approximation, Eqs. (16) and (17) are valid for all coverages, i.e., it is possible to replace

θ_M with θ. Therefore, Eqs. (16) and (17) become

$$\theta = \theta_o \exp\left\{\frac{-\nu^{(1)}E(E_T - 2)\exp(-E_T)}{E_T^3}\right\} ,$$

and

$$\theta = \frac{E_T^3\theta_o}{E_T^3 + \nu^{(2)}\theta_o E(E_T - 2)\exp(-E_T)} ,$$

for m = 1 and m = 2, respectively, where $E_T = E/Z$. Inserting Eqs. (17) and (18) into Eq. (15) yields the following expressions for P(Z):

$$P(Z) = \nu^{(1)}\theta_o \exp(-\Omega Z)\int_{Z_o}^{Z} dZ \exp\left\{\Omega Z - \frac{E}{Z} - \frac{\nu^{(1)}E(E_T - 2)\exp(-E_T)}{E_T^3}\right\} \quad (20)$$

and

$$P(Z) = \nu^{(2)}\theta_o^2 \exp(-\Omega Z)\int_{Z_o}^{Z} dZ \left\{\frac{E_T^3}{E_T^3 + \nu^{(2)}\theta_o E(E_T-2)\exp(-E_T)}\right\}^2 \exp\{\Omega Z - E_T\} , \quad (21)$$

for m = 1 and m = 2, respectively. Hence, P(Z), the normalized pressure profile of a desorption spectrum, can be evaluated by solving Eqs. (20) and (21) numerically for the cases m = 1 and m = 2, respectively.

To determine the conditions under which P(Z) represents a "normal" thermal desorption spectrum, i.e., one in which the desorption rate is proportional to the change of pressure with time, Eq. (15) must be examined carefully. Dividing Eq. (15) by $\frac{dP}{dZ}$ yields

$$1 + \frac{\Omega P}{\frac{dP}{dZ}} = \frac{R(Z)}{\frac{dP}{dZ}} . \quad (22)$$

For P(Z) to represent a "normal" thermal desorption spectrum, the magnitude of the second term on the left-hand side of Eq. (22) must be much greater than

unity, so that

$$P(Z) \simeq \frac{R(Z)}{\Omega} \tag{23}$$

It is the product of β and τ that determines the validity of Eq. (23) and not β and τ individually, and it is found that Eq. (23) is valid only when Ω is large. Fig. 1 shows different normalized pressure profiles for $\Omega = 0.001$ to $\Omega = 0.1$ for $E_d = 25$ kcal/mole and $\nu^{(1)} = 10^{13}$. It is clear from Fig. 1 that Eq. (23) is valid only for "large" values of Ω and invalid for "small" values of Ω. Therefore, it is extremely important to maintain Ω as large as possible when performing a thermal desorption experiment in order to minimize distortions of the peak shape and the peak position in thermal desorption spectra. The concept of "large" and "small" values of Ω is quantified, by example, in the next section.

3. Results and Discussion

In an earlier paper (4), a method of determining E_d and $\nu_o^{(m)}$ by using spectral peak widths and peak temperatures has been introduced. This analysis works best when Ω is "large", and the pressure profiles obtained from an experiment are proportional to the desorption rates. However, this method has been applied successfully (4) to thermal desorption spectra of Xe from a W(111) surface which were measured under conditions corresponding to $\Omega = 0.149$ (7). This value of Ω is not sufficiently large that the experimental pressure profiles represent the desorption rates. (It is found that for most cases, the approximation in Eq. (23) is satisfactory for values of Ω greater than 0.5). Hence, the measured half-width at half maximum on the low temperature side of the thermal desorption peak, $\Delta W_{\frac{1}{2}}$, was used to calculate the full-width at half maximum, $\Delta W_{\frac{1}{2}}$, via

$$\Delta W_{\frac{1}{2}} = \frac{200\Delta W_{\frac{1}{2}}'}{(100-\chi)} \quad , \tag{24}$$

where χ is the dimensionless skewness of the thermal desorption peak as defined in Ref. (4). In the case of a small value of Ω, the calculated value of $\Delta W_{\frac{1}{2}}$ using Eq. (24) is more accurate than the directly measured value of $\Delta W_{\frac{1}{2}}$ from a thermal desorption spectrum. This is a consequence of the fact that the approximation in Eq. (23) is better over a larger range of temperature on the low temperature side than on the high temperature side of the thermal desorption peak.

Eq. (20) was solved numerically to obtain pressure profiles for E_d = 10, 25, and 50 kcal/mole, $\nu^{(1)} = 10^8$, 10^{13} and 10^{15} and different values of Ω. Hence, the values of $\Delta W_{\frac{1}{2}}'$ may be measured from the calculated pressure profiles. In this way, the effect of the magnitude of Ω on the value of the activation energy of desorption, E_d', calculated by using $W_{\frac{1}{2}}$ which is obtained from Eq. (24), is clarified. Fig. 2 shows that the error in the determination of E_d is negligible

for values of $\Omega \gtrsim 0.5$. Thus, it is important to maintain a large value of Ω when performing a thermal desorption experiment.

Falconer and Madix (3) have presented two methods which may be used to analyze thermal desorption spectra. One method uses the measured shift in peak temperature (T_M) with changes in heating rate, and the other one uses the measured shift in peak temperature with changes in peak amplitude (I_M). In the first method, the activation energy of desorption is determined from the slope of a plot of $\ln (\beta/T_M^2)$ as a function of $1/T_M$ for a series of thermal desorption spectra measured at various heating rates. In the second method, the activation energy of desorption is determined from the slope of a plot of $\ln (I_M)$ as a function of $1/T_M$ for a series of thermal desorption spectra measured with different heating rates.

To illustrate the effect of different values of Ω on the results of an analysis using the above two methods, Eq. (15) was solved numerically. The input parameters and the calculated results are summarized in Table 1. Figs. 3 and 4 show a comparison between the calculated desorption rates and pressure profiles for a series of heating rates for τ=0.1 sec and τ=0.5 sec, respectively. Both Figs. 3 and 4 show clearly that as Ω decreases, the resmblance between the desorption rate and the pressure profile decreases.

To determine the value of E_d from the pressure profiles $\ln (\beta/T_M^2)$ is plotted as a function of $(1/T_M)$ using the parameters listed in Table 1. There are three curves shown in Fig. 5; curve (a) is obtained using the results from the numerically calculated desorption rates [Eq. (2)]; curve (b) is obtained using results from the calculated pressure profiles [Eq. (20)] for τ=0.1 sec and values of β ranging from 1 to 60 K/sec; and curve (c) is the analogue of curve (b) except that the values of β range from 20 to 100 K/sec in this case. The slope of curve (a) in Fig. 5, (determined by a least squares fit) gives a value of E_d = 25 kcal/mole which is the value of E_d inserted initially into the calculation of the desorption

rates. However, the values of E_d determined from the slope of curves (b) and (c) in Fig. 5 (by a least squares fit) are 23.1 and 21.0 kcal/mole, respectively. The slope of curve (b) gives a more nearly correct value for E_d than that of curve (c) since curve (b) is obtained using a set of pressure profiles having larger values of Ω. Fig. 6 is similar to Fig. 5 except curves (b) and (c) are obtained by using results from the calculated pressure profiles for τ=0.5 sec. Since this corresponds to smaller values of Ω, the values of E_d determined from curves (b) and (c) in Fig. 6 have a greater error than those determined from curves (b) and (c) in Fig. 5.

The value of E_d may also be determined by the slope of a plot of ln (I_M) as a function of $1/T_M$ using the parameters listed in Table 1. Figs. 7 and 8 should be compared with Figs. 5 and 6, respectively. The slopes of curves (b) and (c) in Fig. 7 (determined by a least squares fit) give more accurate values of E_d than those provided by curves (b) and (c) in Fig. 8 for the reasons discussed above, i.e., larger values of Ω.

The results of Figs. 5-8 demonstrate that the value of E_d determined by both these methods of analysis is always lower than the correct one due to a finite value of Ω in actual experimental measurements. For a series of pressure profiles with a fixed set of values of Ω, the method of analysis employing the relationship between the shift in peak temperature with a variation in heating rate is superior to the method using the variation in peak amplitude with peak temperature.

4. Conclusions

Our major conclusions may be summarized as follows:

(1) This work demonstrates quantitatively the importance of the combined effect of heating rate and pumping speed in thermal desorption mass spectrometry experiments. In order to assess the "goodness" of the kinetic parameters obtained by using thermal desorption spectra, the magnitudes of both the pumping time constant and the heating rate should be measured. Many previously published papers concerned with a determination of kinetic parameters by thermal desorption mass spectra have not reported the magnitude of the pumping time constant. Consequently, it is not possible to evaluate the accuracy of these published results. It is important for all future work concerning thermal desorption spectral analysis to report explicitly both the magnitude of the pumping time constant and the heating rate.

(2) It is shown that the error associated with a determination of first order kinetic parameters using half-widths and three-fourths-widths of desorption peaks (4) is negligible in the case of thermal desorption spectra having values of $\Omega \geq 0.5$. In the case of a system having a smaller value of Ω, the calculated half-widths obtained using Eq. (24) can be used to obtain a better estimate of the kinetic parameters. The pressure profiles can be calculated using the estimated kinetic parameters. The values of the estimated kinetic parameters are adjusted in the calculation until a good agreement between the calculated pressure profiles and experimental data is achieved, hence the correct values of the kinetic parameters can be obtained.

(3) Both of the more established methods of analyzing thermal desorption spectra (1-3), discussed in Sec. 3, require a set of thermal desorption spectra which have large values of Ω in order to yield an accurate determination of the desorption kinetic parameters.

Acknowledgment

Principal support of this research was derived from the Army Research Office-Durham under Grant Number DAHC04-75-0170. Additional support was derived from the American Vacuum Society, the Camille and Henry Dreyfus Foundation and the Alfred P. Sloan Foundation.

References

1. P. A. Redhead, Vacuum 12, 203 (1962).

2. G. Ehrlich, Advan. Catal. 14, 255 (1963).

3. J. L. Falconer and R. J. Madix, Surface Sci. 48, 393 (1975).

4. C.-M. Chan, R. Aris and W. H. Weinberg, Appl. Surface Sci. (previous paper).

5. D. A. King, Surface Sci. 47, 384 (1975).

6. L. D. Schmidt, Catal. Rev. - Sci. Eng. 9, 115 (1974).

7. M. J. Dresser, T. E. Madey and J. T. Yates, Jr., Surface Sci. 42, 533 (1974).

Table Caption

Table 1: Results of the calculated desorption rates and pressure profiles for different values of the heating rate (β, K/sec) and the time constant of the pumping system (τ, sec) for E_d = 25 kcal/mole and $\nu_o^{(1)} = 10^{13}$ sec $^{-1}$. T_M is the peak temperature, and I_M is the peak amplitude normalized with respect to the maximum peak amplitude in the calculated data set.

Table 1.

	Desorption Rate		Pressure Profile					
			τ = 0.1 sec			τ = 0.5 sec		
β, K/sec	T_M, K	I_M	Ω	T_M, K	I_M	Ω	T_M,	I_M
1	385.4	0.013	10	385.8	0.015	2	386.2	0.027
5	404.4	0.060	2	405.0	0.067	0.4	406.8	0.122
10	413.0	0.116	1	414.2	0.130	0.2	417.4	0.226
20	422.2	0.222	0.5	424.2	0.247	0.1	429.2	0.397
40	431.6	0.425	0.25	435.2	0.463	0.05	442.2	0.637
60	437.4	0.621	0.167	442.4	0.662	0.033	450.6	0.799
80	441.6	0.814	0.125	447.8	0.837	0.025	456.2	0.908
100	444.8	1.000	0.1	452.0	1.000	0.02	461.0	1.000

Figure Captions

Fig. 1: Calculated pressure profiles for different values of Ω with E_d = 25 kcal/mole and $\nu_o^{(1)} = 10^{13}$ sec^{-1}.

Fig. 2: The error introduced in desorption activation energies deduced from pressure profiles for first-order desorption and finite values of Ω.

Fig. 3: Comparison between calculated desorption rates and pressure profiles for first-order desorption with E_d = 25 kcal/mole and $\nu_o^{(1)} = 10^{13}$ sec^{-1}. The values of β in K/sec are the following: a, 100; b, 80; c, 60; d, 40; e, 20; f, 10; g, 5; and h, 1. The value of τ is 0.1 sec for the calculated pressure profiles.

Fig. 4: Same as Fig. 3. The value of τ for the pressure profiles is 0.5 sec.

Fig. 5: Plots of $\ln\left(\frac{\beta}{T_M^2}\right)$ as a function of $1/T_M$. Curve (a) is obtained using parameters for the calculated desorption rate shown in Table 1. Curves (b) and (c) are obtained using results from the calculated pressure profiles having values of β ranging from one to 60 K/sec and 10 to 100 K/sec, respectively, for τ = 0.1 sec. The points in the figure correspond to the eight values of β listed in Table 1. The values of E_d determined from the slope of the curves by least squares fits are shown in the figure.

Fig. 6: Same as Fig. 5. The values of τ used for the calculation of the pressure profiles is 0.5 sec.

Fig. 7: Plots of $\ln(I_M)$ as a function of $1/T_M$. Curves (a), (b), and (c) are the analogue of those in Fig. 5.

Fig. 8: Plots of $\ln(I_M)$ as a function of $1/T_M$. Curves (a), (b), and (c) are the analogue of those in Fig. 6.

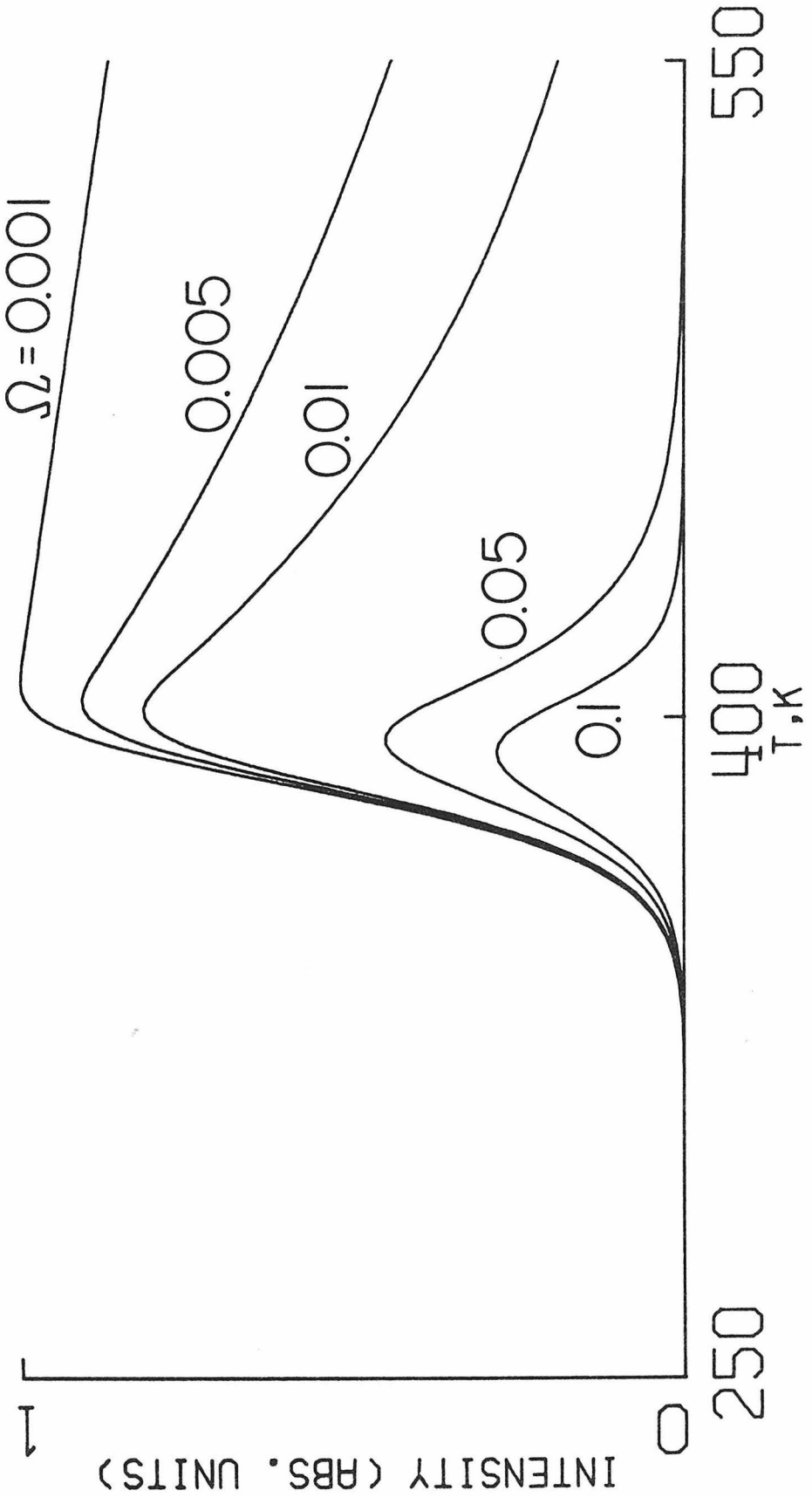

Fig. 1

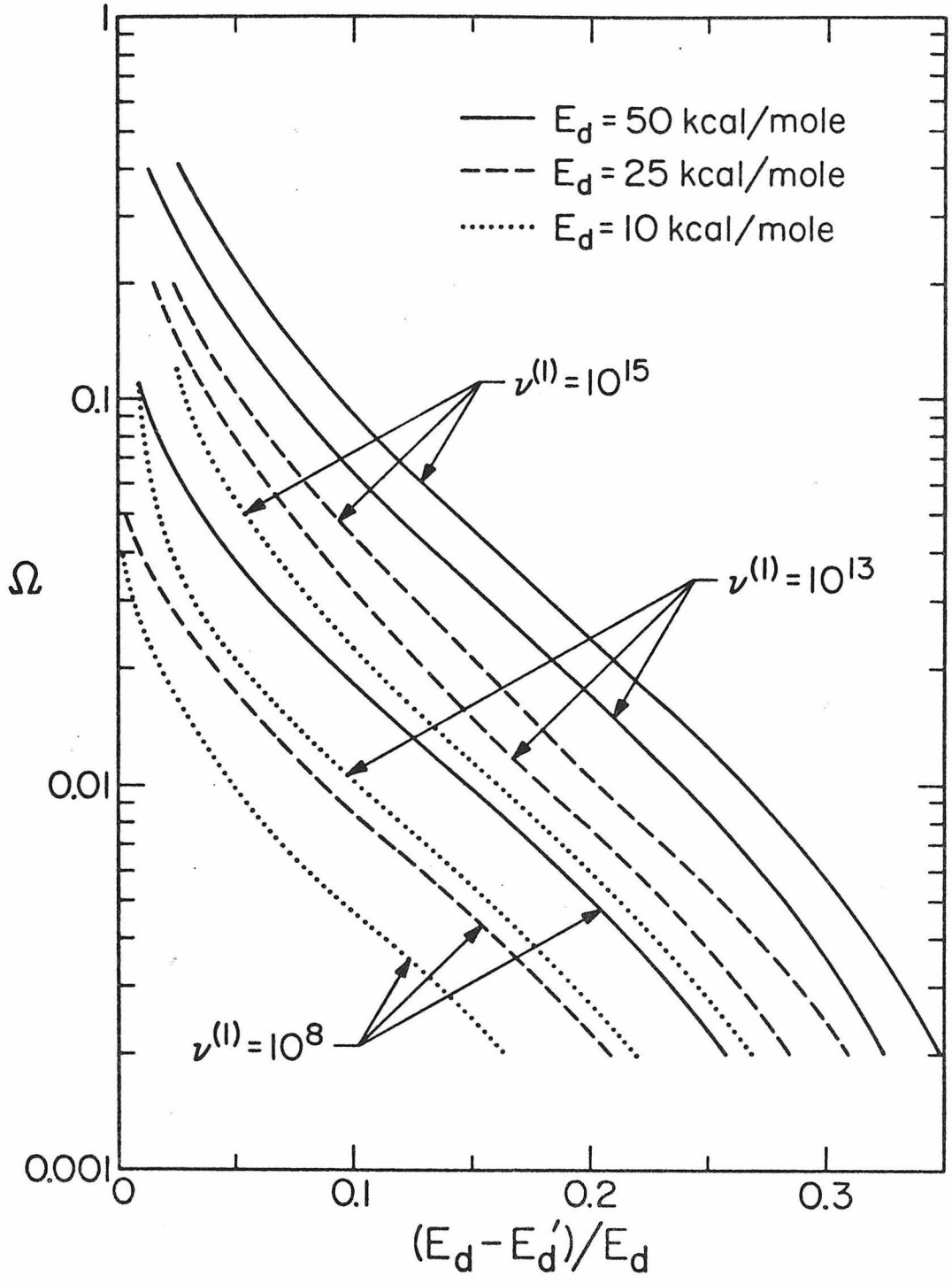
1
0.1
0.01
0.001
Ω
0
0.1
0.2
0.3
$(E_d - E_d')/E_d$
E_d = 50 kcal/mole
E_d = 25 kcal/mole
E_d = 10 kcal/mole
$\nu^{(1)} = 10^{15}$
$\nu^{(1)} = 10^{13}$
$\nu^{(1)} = 10^{8}$

Fig. 2

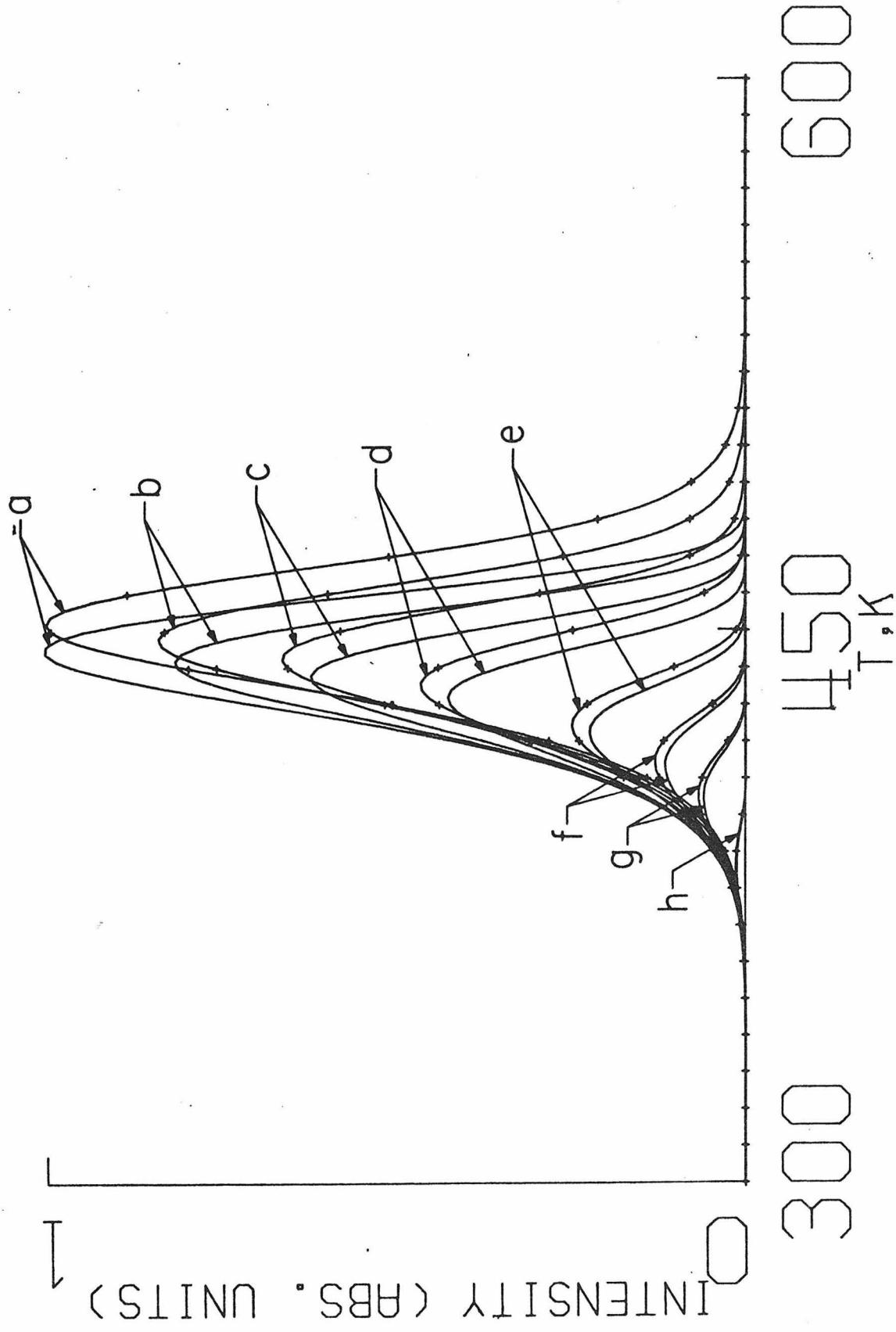

Fig. 3

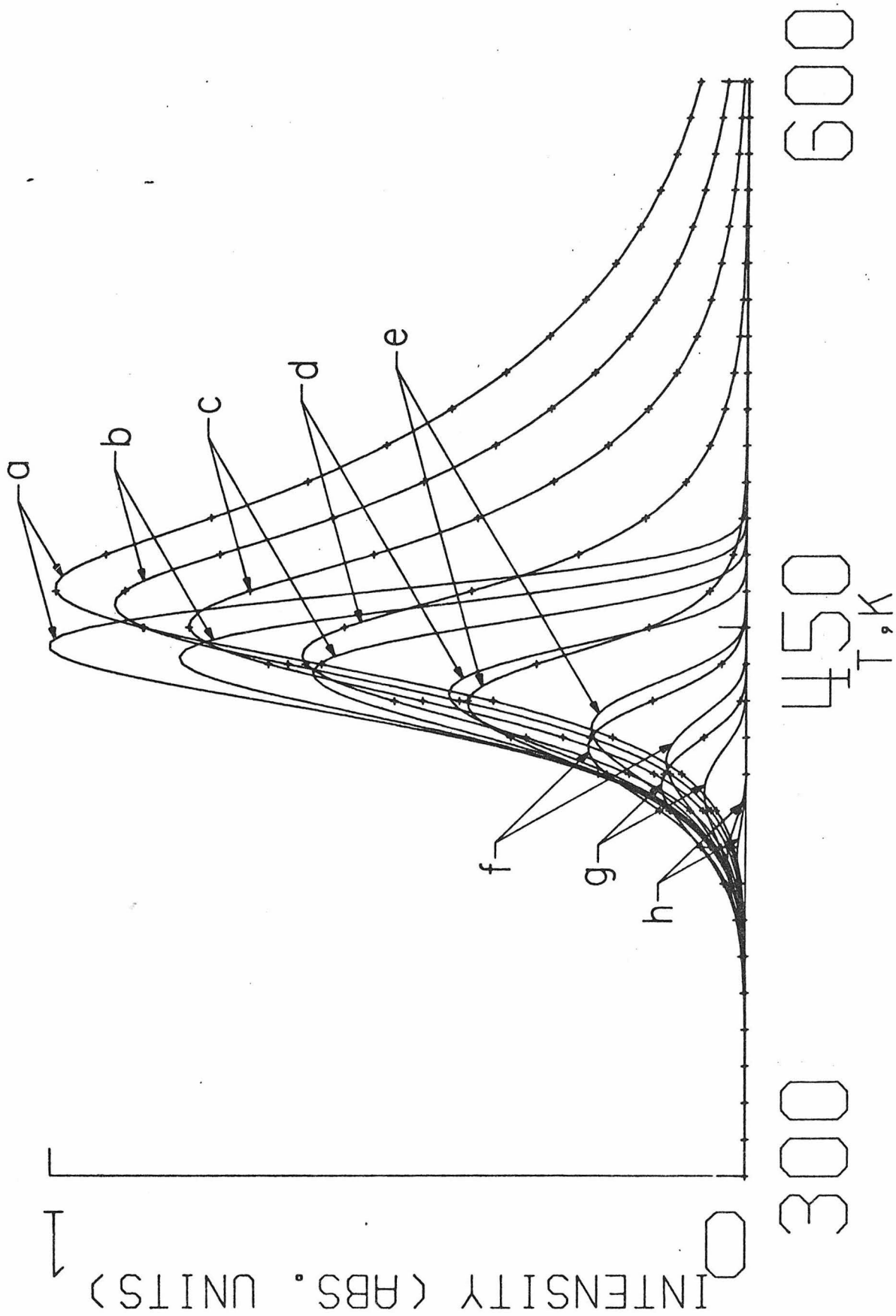
INTENSITY (ABS. UNITS)
1
0
300
450
600
T, K
a
b
c
d
e
f
g
h

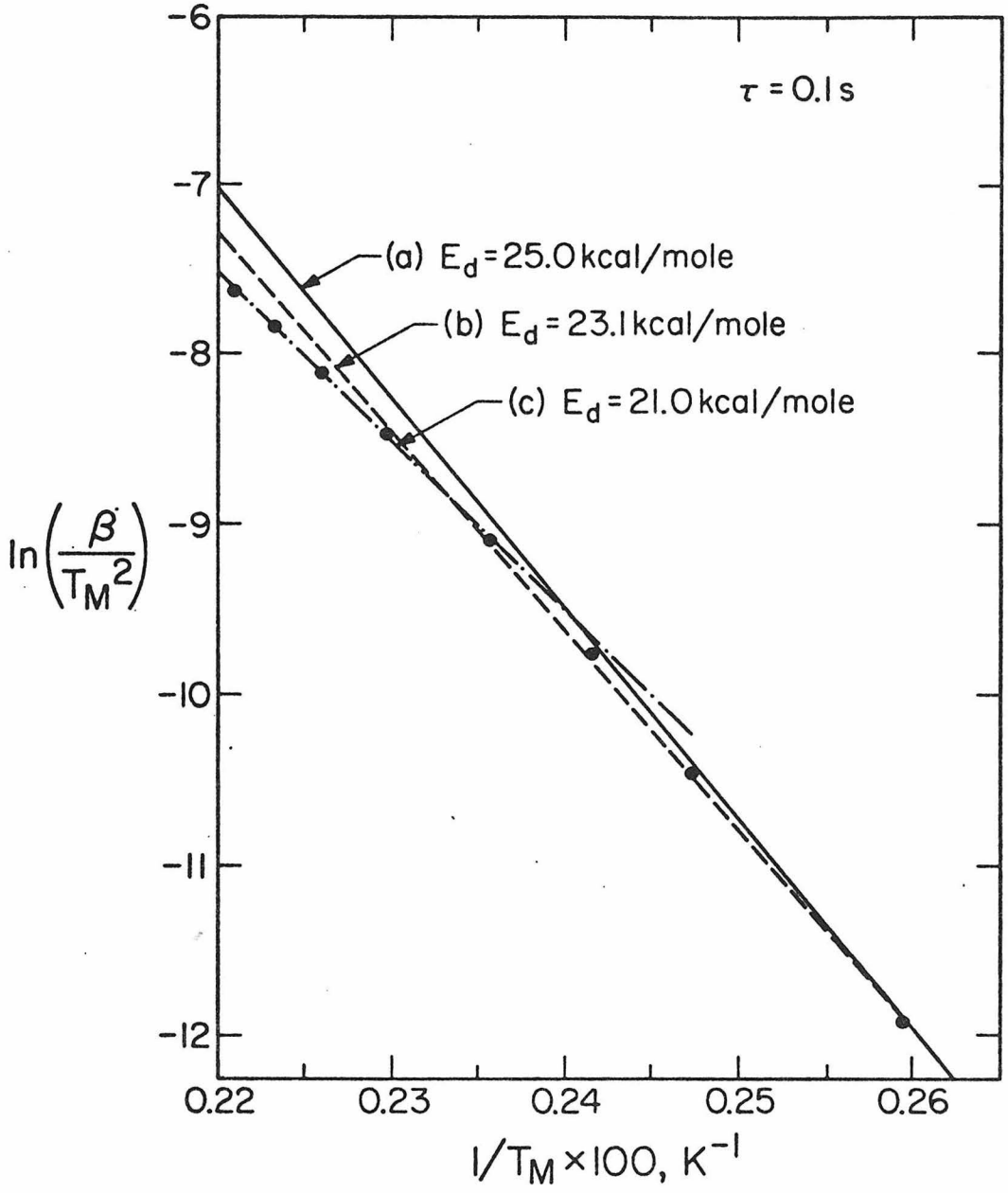
τ = 0.1 s
(a) E_d = 25.0 kcal/mole
(b) E_d = 23.1 kcal/mole
(c) E_d = 21.0 kcal/mole
$\ln\left(\frac{\beta}{T_M^2}\right)$
-6
-7
-8
-9
-10
-11
-12
0.22
0.23
0.24
0.25
0.26
$1/T_M \times 100$, K^{-1}

Fig. 5

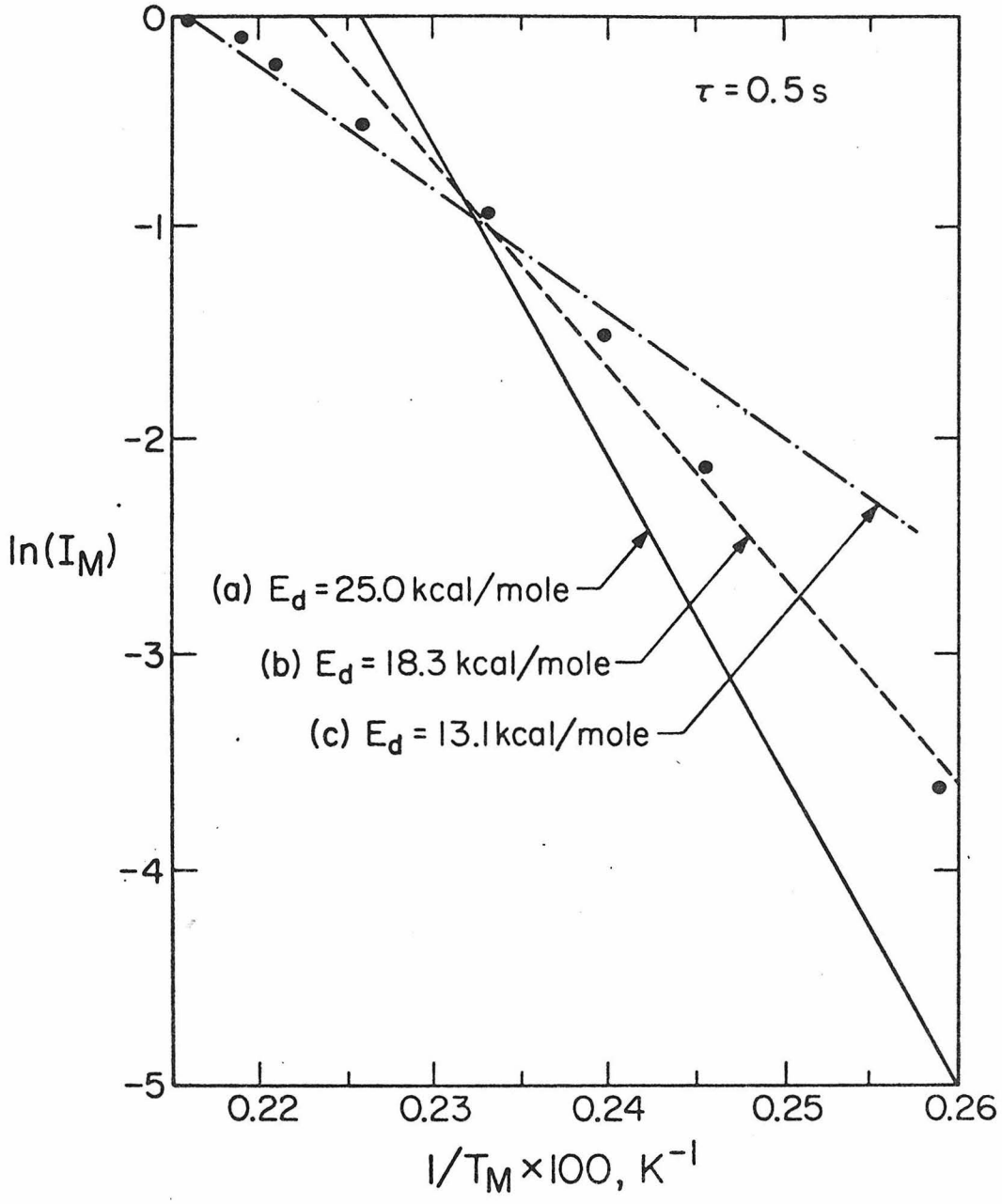
0
-1
-2
-3
-4
-5
$\tau = 0.5$ s
$\ln(I_M)$
(a) $E_d = 25.0$ kcal/mole
(b) $E_d = 18.3$ kcal/mole
(c) $E_d = 13.1$ kcal/mole
0.22
0.23
0.24
0.25
0.26
$1/T_M \times 100$, K^{-1}

Fig. 6

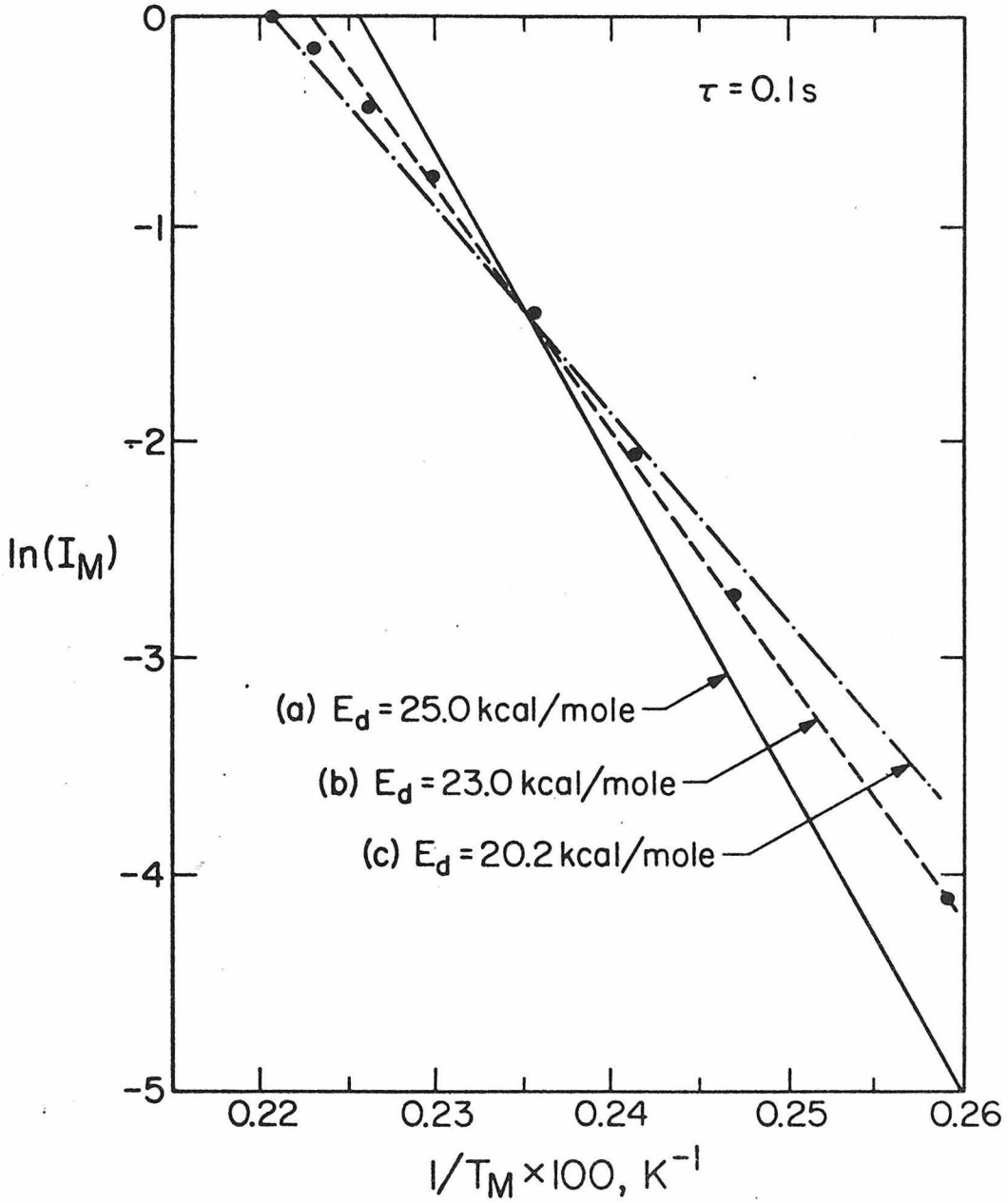
0
-1
-2
-3
-4
-5
ln(I_M)
τ = 0.1 s
(a) E_d = 25.0 kcal/mole
(b) E_d = 23.0 kcal/mole
(c) E_d = 20.2 kcal/mole
0.22
0.23
0.24
0.25
0.26
1/T_M × 100, K^-1

Fig. 7

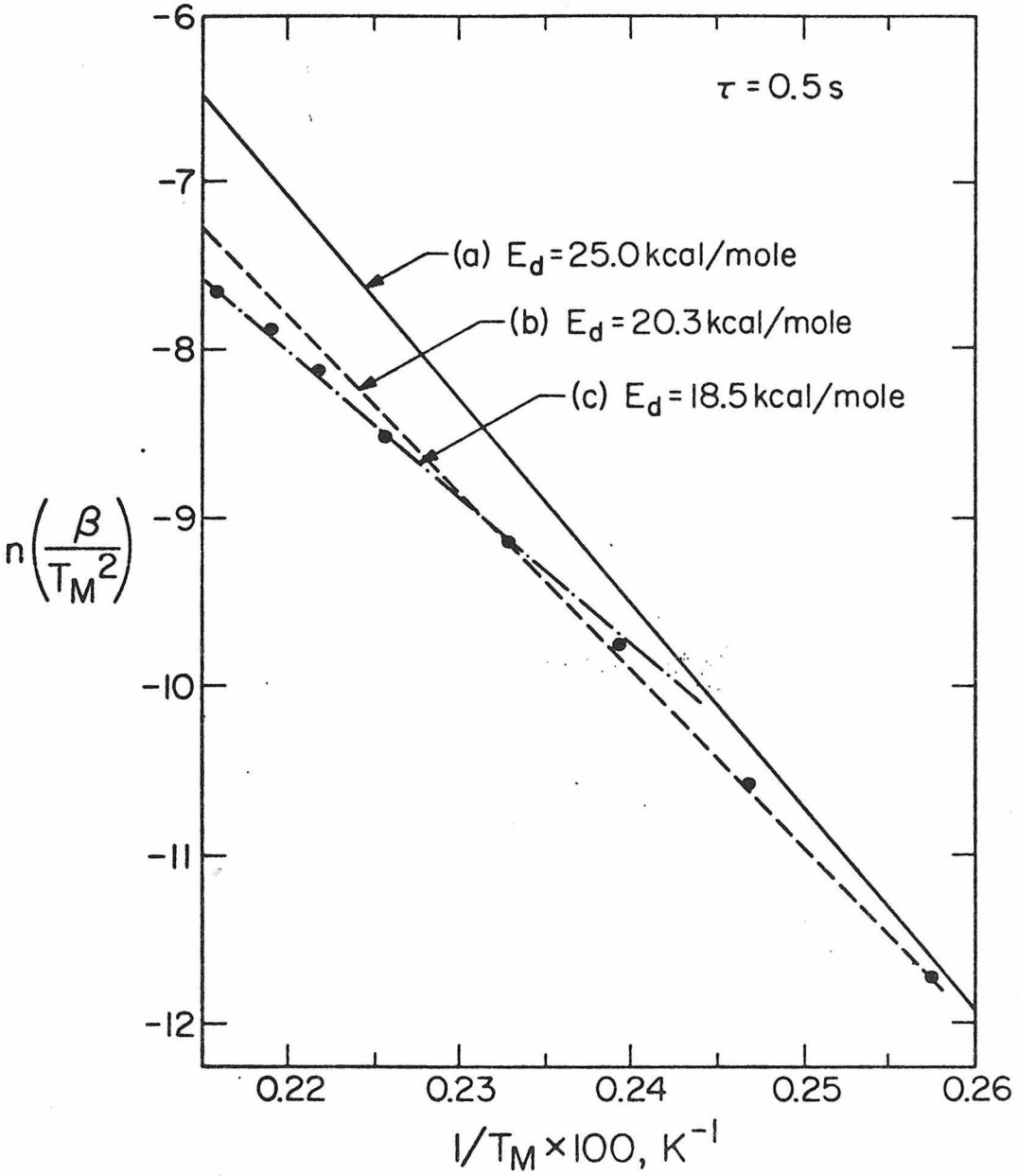
τ = 0.5 s
(a) E_d = 25.0 kcal/mole
(b) E_d = 20.3 kcal/mole
(c) E_d = 18.5 kcal/mole
$n\left(\frac{\beta}{T_M^2}\right)$
-6
-7
-8
-9
-10
-11
-12
0.22
0.23
0.24
0.25
0.26
$1/T_M \times 100$, K^{-1}

Fig. 8

Part V

Conclusions

The Conclusions of Parts II and III of this thesis are summarized in Tables 1 and 2. In Part IV, our work demonstrates a simple and rapid method to analyze thermal desorption spectra based on both peak positions and peak shapes. Our work also demonstrates quantitatively the importance of the combined effect of heating rate and pumping speed in thermal desorption mass spectrometry experiments. In order to assess the "goodness" of the value of the kinetic parameters obtained by using thermal desorption spectra, the magnitudes of both the pumping time constant and the heating rate should be measured.

Table 1. Summary of results obtained by the convolution-transform method and comparison of these results with those obtained by dynamical calculations.

	Surface Relaxation in % of the Bulk Interlayer Spacing[a)]	
Surface	Convolution-Transform Method	Dynamical Calculations
Ni(110)	-5	-5 (1)
Al(110)	-4	-10 (2)
Ag(110)	-6	-7 (3)
		-10 (4)
Pt(111)	-3	0
Ir(111)	+3	0
Rh(111)	-4	-2.5

a)- indicates a contraction while + indicates an expansion.

Table 2. Summary of results of studies of the (110) and (111) surfaces of Ir and overlayer structures on these surfaces.

System	Super-structure	Surface Structure or Overlayer Position	d_1, Å	ℓ, Å
Ir(110)[a]	(1x2)	Missing Row Model	1.16 ± 0.07	
Ir(110)[b]	(1x1)	Bulk Structure	1.26 ± 0.05	
O/Ir(110)	c(2x2)	Short-Bridged Site	1.37 ± 0.05[c]	1.93 ± 0.07
Ir(111)	(1x1)	Bulk Structure	2.20 ± 0.10	
O/Ir(111)	"(2x2)"[d]	Three-Fold Site[e]	1.30 ± 0.05	2.04 ± 0.08
S/Ir(111)	($\sqrt{3}$ x $\sqrt{3}$)	Three-Fold Site[e]	1.65 ± 0.05	2.28 ± 0.08

[a] Clean Ir(110) surface.

[b] Oxygen stabilized Ir(110) surface.

[c] The topmost substrate interlayer spacing is 1.33 ± 0.07 Å.

[d] The choice as to whether the "(2x2)" structure is caused by a p(2x2) surface structure or by three domains of (1x2) surface structure rotated 120° with respect to one another cannot be made at this time.

[e] Three-fold site refers to the three-fold site directly below which there is a vacancy in the second layer.

d_1 refers to either the topmost interlayer spacing of the clean surface or the interlayer spacing between the overlayer and the topmost layer of the substrate in the case of an overlayer structure.

ℓ refers to the bond length between the adatom and the substrate atoms.

References

1. J. E. Demuth, P. M. Marcus and D. W. Jepsen, Phys. Rev. B 11, 1460 (1978).

2. C. B. Duke, G. E. Laramore, B. W. Holland and A. M. Gibbons, Surface Sci. 27, 523 (1971); G. E. Laramore and C. B. Duke, Phys. Rev. B 5, 267 (1972).

3. W. Moritz, PhD Thesis, University of Munich (1976); and M. Alff, PhD Thesis, University of Munich (1976).

4. M. Maglietta, E. Zanazzi, F. Jona, D. W. Jepsen and P. M. Marcus, J. Phys. C 10, 3287 (1977).

Part IV

Appendixes

APPENDIX 1

THE ADSORPTION OF SULFUR ON THE RECONSTRUCTED Ir(110)-(1x2) SURFACE

by

Ellen D. Williams, C.-M. Chan and W. H. Weinberg
Division of Chemistry and Chemical Engineering
California Institute of Technology
Pasadena, California 91125

Surface Science 81, L309-L314 (1979)

An important and intriguing problem in surface science is the reconstruction of the surface layers of atoms with respect to the bulk structure. This phenomenon has been observed for the (110) surfaces of Ir, Pt and Au (1,2,3), which all reconstruct into a (1x2) structure. Recently, experimental and theoretical work has been carried out to determine the structures of the clean (1x2)-and oxygen stabilized (1x1)-(110) surfaces of Ir(4 - 7). As a complement to and an extension of this work, a study of the interaction of sulfur with the reconstructed Ir(110) surface has been undertaken. The structural analysis of the clean reconstructed Ir(110) - (1x2) surface showed that the missing row model with a topmost interlayer spacing of 1.22 ± 0.07Å is the preferred structure (4,5,7). It is this surface on which the overlayers of sulfur were adsorbed.

The experiments were carried out in a UHV system which has been described previously (6). Sulfur was introduced onto the surface by exposure to H_2S gas (cp. grade, 99.5% purity). The presence of sulfur on the surface was monitored by Auger Electron Spectroscopy (AES). Even at saturation coverages of sulfur (exposure $\sim$ 35 L H_2S, where 1 L $\equiv 10^{-6}$ torr-sec), the intensities of the Ir transitions in the Auger spectrum were nearly unattenuated. It was found that the sulfur could be removed from the surface by heating the crystal briefly in vacuum at 1600 K. As this treatment caused some carbon to migrate to the surface, the crystal was then cleaned by heating in 5×10^{-8} torr of oxygen at 950 K, followed by flashing to 1630 K in vacuum.

A series of Low-Energy Electron Diffraction (LEED) patterns was observed upon exposure of the crystal to H_2S at 350 K. A (2x2) pattern with the $\left(\frac{2n+1}{2}\ 0\right)$ beams absent was observed at low exposures and reached its

maximum intensity after an exposure of 4 L H_2S. This pattern is illustrated in Fig. 1. The intensity of this LEED pattern was not changed after heating to temperatures as high as 1200 K and then cooling back to 350 K. This indicates that either no hydrogen is left on the surface at 350 K, or that it is in a disordered state that doesn't affect the LEED pattern. As the exposure to H_2S was increased above 4 L, the "extra" (2x2) beams disappeared leaving the original beams of the (1x2) structure. Meanwhile, a streaky, diffuse pattern developed between the rows of the (1x2) pattern. Heating the crystal to 950 K after an exposure to 8 L H_2S caused the diffuse pattern to transform into a weak c(2x4) one. At higher exposures to H_2S (up to 35 L), a more intense c(2x4) structure with streaks parallel to the y-axis and located at $x = \frac{2n + 1}{4}$ was observed after heating to 950 K. Comparison of the amplitude of the S transitions in the Auger spectra shows that the coverage at saturation is approximately twice that at the maximum intensity of the (2x2) pattern. Work is in progress to determine quantitatively the relative coverages corresponding to these LEED patterns, as well as the adsorption and desorption kinetics using thermal desorption mass spectrometry.

The observation that the (1x2) substrate beams remain bright and sharp throughout the growth and disappearance of the (2x2) pattern suggests that the adsorption of sulfur does not cause the Ir(110) surface to relax from the reconstructed (1x2) form. This, together with the occurrence of the missing beams in the (2x2) pattern, allows the structure corresponding to the (2x2) pattern to be delimited.

The absence of certain beams at all incident electron energies indicates destructive interference due to equivalent scatterers within

the (2x2) unit cell. Specifically, the extinction of the $\left(\frac{2n+1}{2}\ 0\right)$ beams indicates a surface structure of either p1g1 or p2mg symmetry (8). Both of these symmetries include glide planes* parallel to the x-axis and located at y = 0, 1 and 2 within the unit cell. Due to the low symmetry of the (1x2) surface, as illustrated in Fig. 2 for the missing row model for Ir(110) - (1x2) (4), there is only one possible set of locations for these glide planes. This restriction is equally valid for any other model of the reconstructed (1x2) surface.

For the p1g1 symmetry, there are two atoms within the unit cell, located at (x,y) and $(1 + x,\bar{y})$, with x and y such that the glide planes are the only symmetry elements of the structure. A possible p1g1-(2x2) structure is shown in Fig. 3. In this illustration, the S atoms are prevented from occupying the sites on the "missing row" by S-S interactions.

Either two or four atoms per unit cell are allowed for the p2mg structure. The four-atom structure (which would correspond to a fractional coverage of unity) is considered unlikely on the basis of the evidence that much higher coverages of S are possible than that required for the (2x2) structure without attenuation of the Ir Auger signals. In the case of two atoms per unit cell, the S atoms would be located so that a mirror plane parallel to the y-axis runs through each S atom. Two possible p2mg structures are shown in Fig. 4. The structures depicted would arise if S atoms with a covalent radius of 1.0 Å (9) were adsorbed in the three-fold sites of the terraces of (111) planes exposed by the missing row.

*A glide plane indicates invariance under the operation: translation parallel to the plane by one-half the length of the [(2x2)] unit cell, followed by reflection across the plane.

Other p2mg structures, generated by changing the y-coordinates shown in Fig. 4a and b, are also plausible. For instance, a structure similar to that shown in Fig. 3 but with a p2mg symmetry would be a reasonable hypothesis.

In an attempt to distinguish between the possibility of a p1g1 and a p2mg symmetry, the intensity versus voltage (I-V) profiles for two sets of corresponding beams in three quadrants were measured. As shown in Fig. 5, the I-V spectra for the three beams of each set are identical. If the (n/2, ± m/2) beams had had different I-V spectra than the (- n/2, ± m/2) beams, it would have shown that one domain of a p1g1 structure (see caption, Fig. 3) predominated on the surface (10). Since the I-V spectra are the same, it is not possible to determine which of the two symmetries is present, as the observed equivalence could be due either to equal representation of the two domains of a p1g1 structure or to a p2mg structure.

Therefore, symmetry considerations allow the structure of the (2x2) sulfur overlayer on the reconstructed Ir(110) surface to be limited to one of three possible types. The three types are the following: (1) a p1g1 structure with sulfur atoms at (x,y), $(1 + x,\bar{y})$, $x \neq 0$, 1/2 or 1, $y \neq 0$, 1/2 or 1; (2) a p2mg structure with sulfur atoms at $(1/2,y)$, $(3/2,\bar{y})$, $y \neq 0$, 1/2 or 1; and (3) a p2mg structure with sulfur atoms at $(0,y)$ $(1,\bar{y})$, $y \neq 0$, 1/2 or 1. Structures with reasonable values for the x- (in the case of the p1g1) and y-coordinates of the sulfur atoms are shown for the three types in Figs. 3 and 4. Of the three, the p1g1 seems the least likely, as it would require unsymmetrical interactions of the

S atoms with neighboring Ir atoms. The structures shown in Fig. 4a and b seem quite plausible, as S is known to adsorb in a three-fold site on Ni(111) (11).

A determination of the correct model of the three described above and of the coordinates of the S atoms within that model, will be made by a dynamical analysis of the LEED I-V beam profiles (12).

References

1. K. Christmann and G. Ertl, Z. Naturforschung 28a, 1144 (1973).
2. H. P. Bonzel and R. Ku, J. Vac. Sci. Technol. 9, 663 (1972).
3. D. G. Fedak and N. A. Gjostein, Acta. Met. 15, 827 (1967).
4. C.-M. Chan, M. A. Van Hove, W. H. Weinberg and E. D. Williams, submitted to Phys. Rev. Letters.
5. C.-M. Chan, M. A. Van Hove, W. H. Weinberg and E. D. Williams, in preparation.
6. C.-M. Chan, S. L. Cunningham, K. L. Luke, W. H. Weinberg and S. P. Withrow, Surface Sci. 77, 000 (1978).
7. C.-M. Chan, K. L. Luke, M. A. Van Hove, W. H. Weinberg and E. D. Williams, J. Vacuum Sci. Technol. (March/April, 1979).
8. International Tables for X-Ray Crystallography, Vol. I, Kynoch Press, Birmingham, England, 1952.
9. F. Tuinstra, Structural Aspects of the Allotropy of Sulfur and the other Divalent Elements, Uitgeverij Waltman-Delft (The Netherlands), 1967.
10. M. K. Debe and D. A. King, Phys. Rev. Letters 39, 708 (1977).
11. J. E. Demuth, D. W. Jepsen and P. M. Marcus, Phys. Rev. Letters 32, 1182 (1974).
12. M. A. Van Hove, C.-M. Chan, E. D. Williams and W. H. Weinberg, in preparation.

Figure Captions

Fig. 1. p1g1 - (2x2) LEED pattern observed after exposure of Ir(110) - (1x2) to 4 L H_2S at 350 K. Solid circles, ● , indicate substrate (1x2) beams; open circles, O , the "extra" beams due to the (2x2) structure.

Fig. 2. Location of glide planes, ———, for a p1g1 or p2mg-(2x2) unit cell on the Ir(110) - (1x2) surface (missing row model). Open circles indicate first and third layer Ir atoms; shaded circles, second layer Ir atoms.

Fig. 3. A possible p1g1 - (2x2) structure for sulfur on Ir (110) - (1x2). Sulfur atoms (cross-hatched) are shown with a hard sphere radius of 1.7 Å (9). The radius of an Ir atom is 1.36 Å. Sulfur atoms are located at (x,y) and (1 + x,$\bar{y}$). Translating the S atoms to ($\bar{x}$,y), (1 + $\bar{x}$,$\bar{y}$) results in an equivalent (mirror image) domain of the structure shown.

Fig. 4. Two possible p2mg - (2x2) structures for sulfur on Ir(110) - (1x2). The inner circle on the S atoms shows the covalent radius of 1.0 Å (9).

(a) S located in three-fold site formed by two top layer and one second layer Ir atoms.

(b) S located in three-fold site formed by one top layer and two second layer Ir atoms.

Fig. 5. LEED I-V spectra showing the equivalence of corresponding beams in three quadrants.

(a) The (1/2, 1/2) beams.

(b) The (1/2, 3/2) beams.

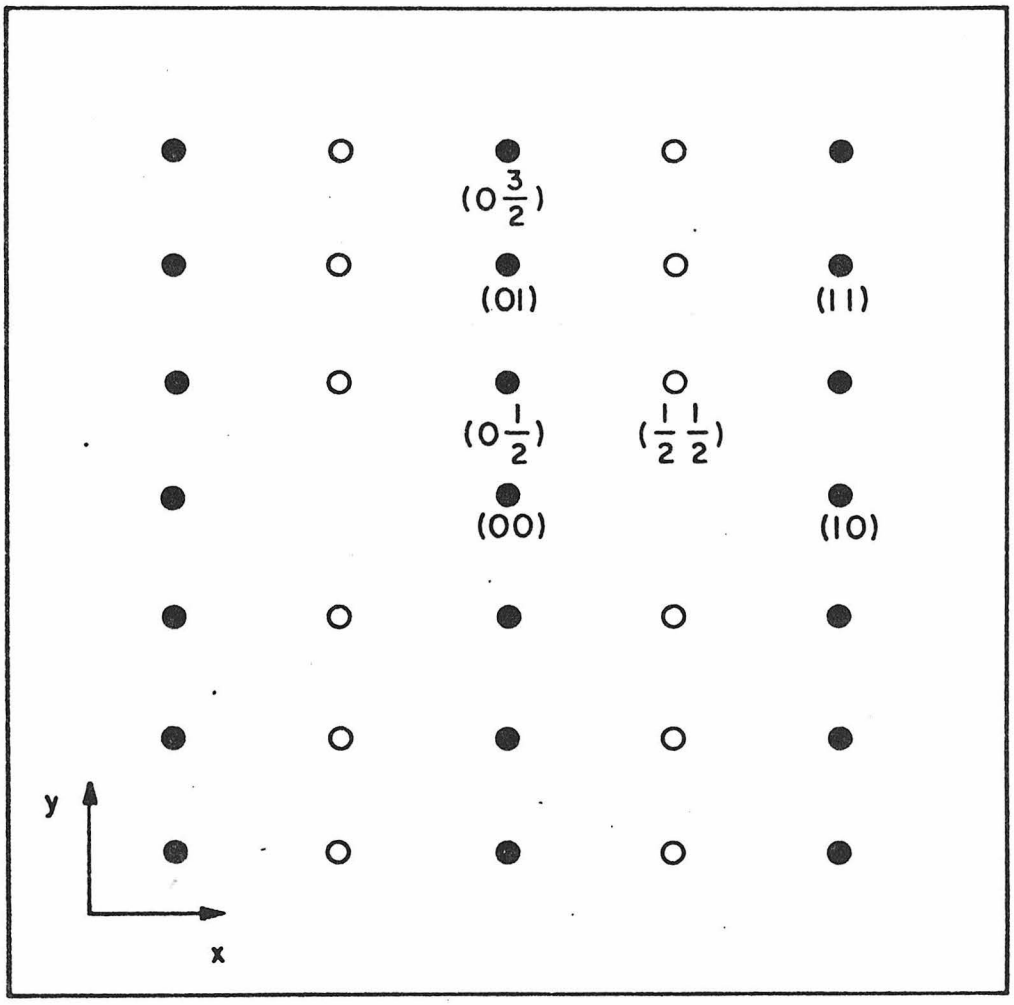

Figure 1

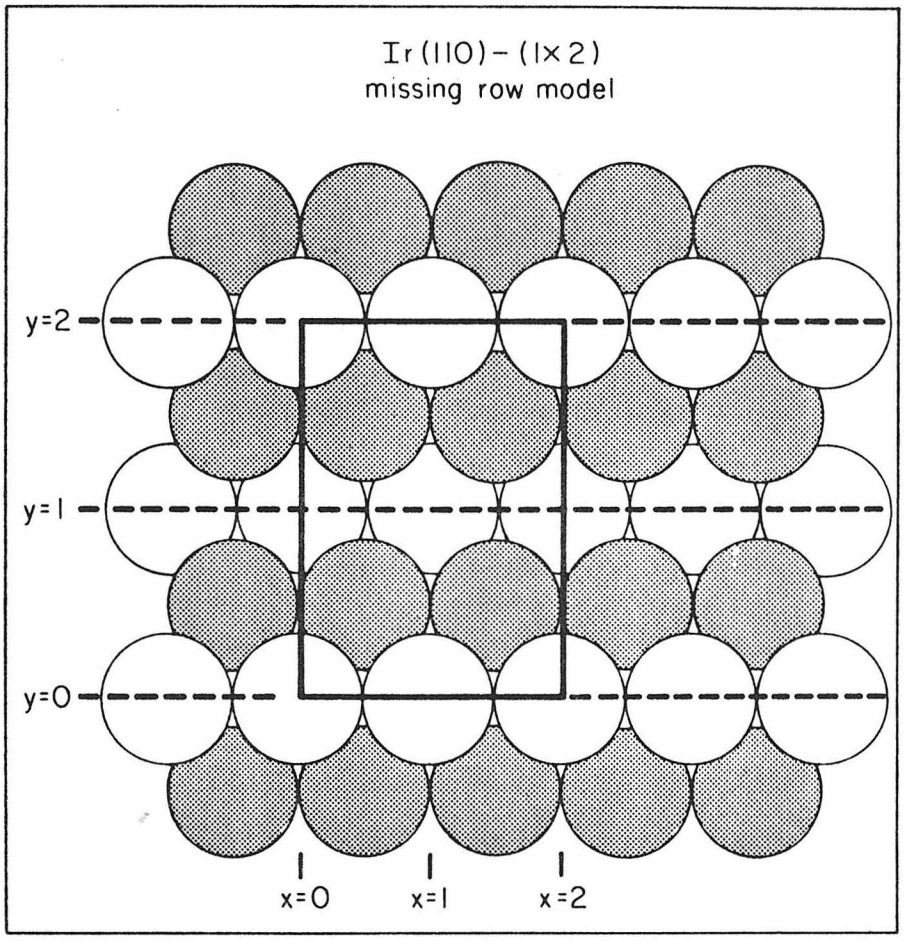

Figure 2

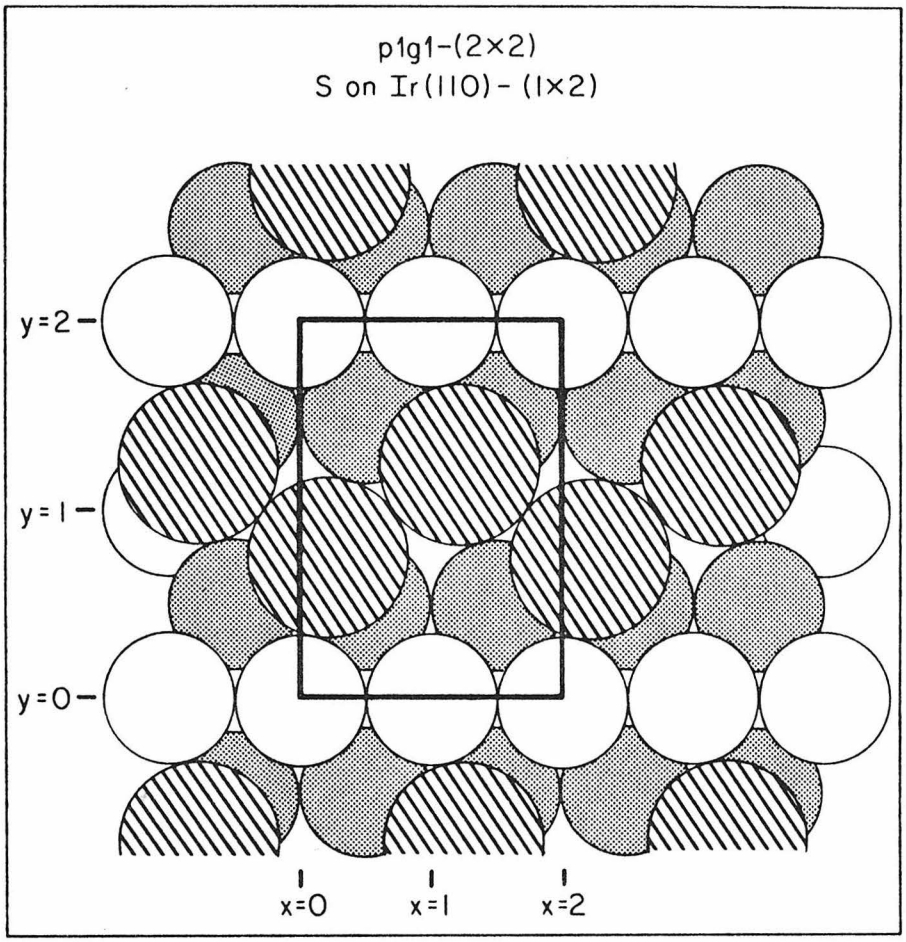

Figure 3

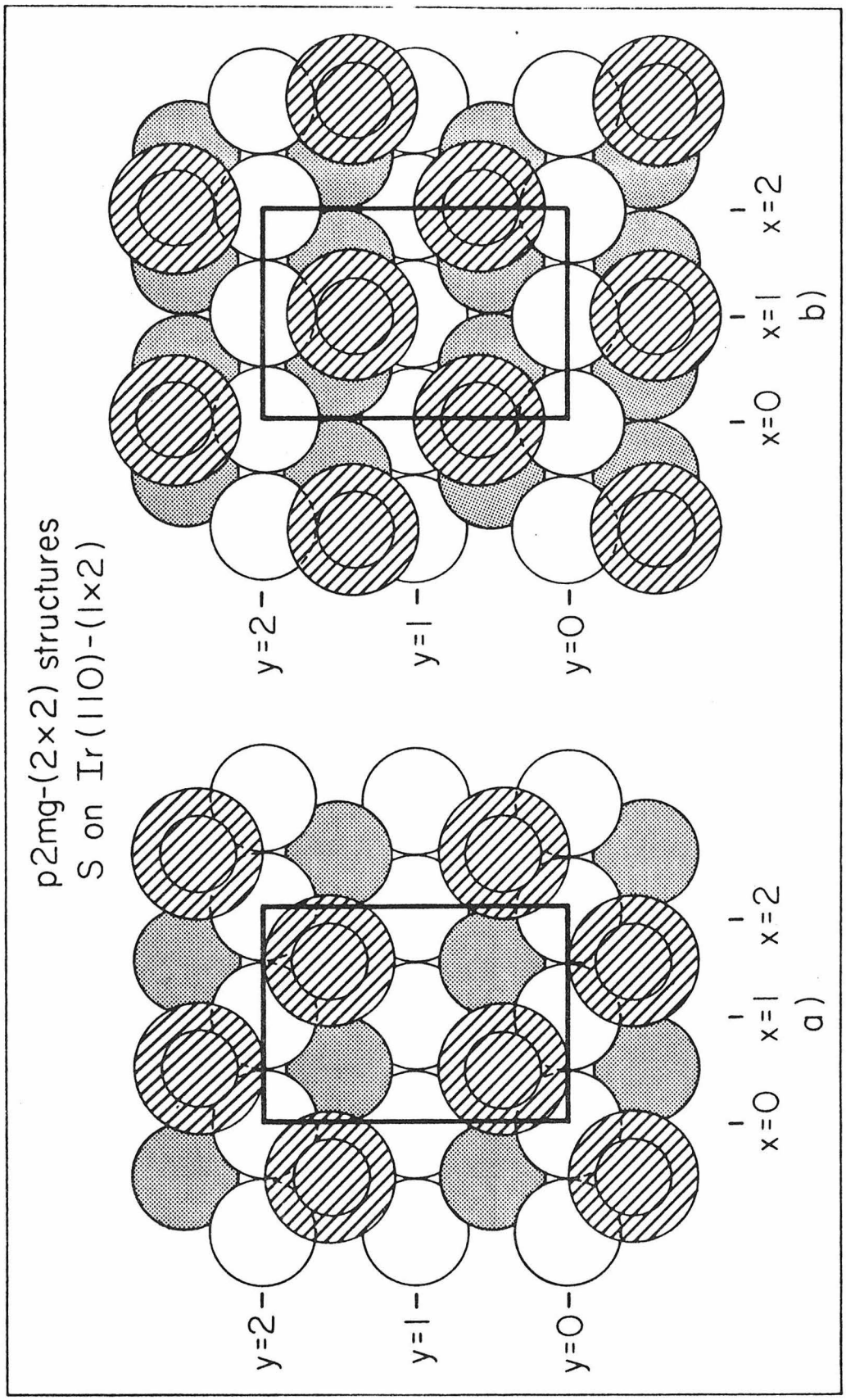

Figure 4

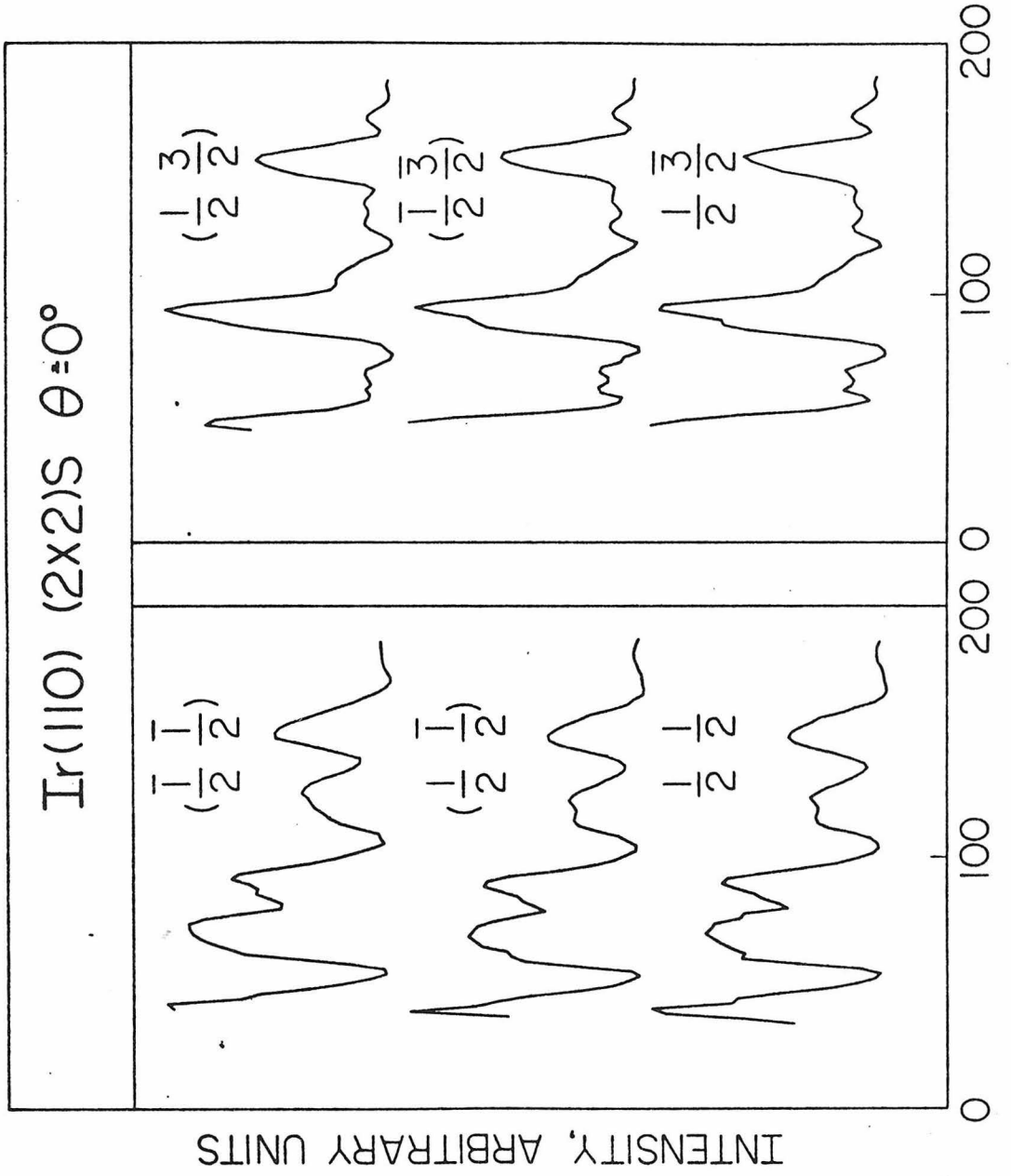
Ir(110) (2x2)S θ=0°
INTENSITY, ARBITRARY UNITS
E, eV
0
100
200
200
100
0
$\bar{1}\,\bar{1}/\bar{1}\,\bar{1}/2$
$\bar{1}\,\bar{1}/\bar{1}\,1/2$
$\bar{1}\,\bar{1}/1\,\bar{1}/2$
$\bar{1}\,\bar{1}/1\,1/2$
$\bar{1}\,1/\bar{1}\,\bar{1}/2$
$\bar{1}\,1/\bar{1}\,1/2$
$\bar{1}\,1/1\,\bar{1}/2$
$\bar{1}\,1/1\,1/2$
$1\,\bar{1}/\bar{1}\,\bar{1}/2$
$1\,\bar{1}/\bar{1}\,1/2$
$1\,\bar{1}/1\,\bar{1}/2$
$1\,\bar{1}/1\,1/2$
$1\,1/\bar{1}\,\bar{1}/2$
$1\,1/\bar{1}\,1/2$
$1\,1/1\,\bar{1}/2$
$1\,1/1\,1/2$

Figure 5

APPENDIX 2

ISOTHERMAL CONCENTRATION OSCILLATIONS ON CATALYTIC SURFACES: NONLINEAR ANALYSIS

by

H. C. Lau, C.-M. Chan and W. H. Weinberg
Division of Chemistry and Chemical Engineering
California Institute of Technology
Pasadena, California 91125

Submitted to the Chemical Engineering Science

ABSTRACT

A theoretical study of an isothermal, irreversible heterogeneously catalyzed reaction in which the activation energy of the rate limiting step is dependent on the surface concentration has been carried out using a multi-timing perturbation method. It is shown that, depending on the kinetic parameters and the initial conditions of the system, various periodic oscillatory phenomena are possible.

1. Introduction

Recently, a number of experimental studies by Belayaev et al. (1), Dauchoet and Van Cakenberghe (2), McCarthy, et al. (3), Zuniga and Luss (4), Shientuch and Schmitz (5,6), and Cutlip and Kenney (7) have indicated that the occurrence of oscillations in the concentration of surface species in heterogeneously catalyzed reactions is possible. Experimental data have shown that such oscillations are caused by surface rate processes rather than gas phase transport processes. Various mechanisms, proposed to explain these oscillations, have led to nonlinear governing equations which demand more than a linear theory to facilitate a detailed mathematical analysis. Although various mathematical techniques are available for this analysis, often they have certain limitations associated with them. In this paper, we present a theoretical study of an isothermal, irreversible reaction occurring on a catalytic surface, where the activation energy of the rate limiting step is allowed to depend on the surface coverage of an intermediate species. A nonlinear analysis using a multi-timing perturbative scheme is used.

Studies of chemically oscillating systems are important for the design and control of commercial reactors. In the case of competing reactions, chemical oscillations may be used to enhance the yield of the most valuable of the several reaction products. Finally, an analysis of chemical oscillations may provide insight into the microscopic nature of the catalytic surface and provide new methods of testing rival kinetic models.

Results of our calculations predict that periodic oscillations can occur when a unique steady state loses stability due to a perturbation in the solution from the region of neutral stability. However, the first order solution of our perturbative analysis may be either stable periodic oscillations,

damped oscillations, or unstable periodic oscillations,depending on the values of the kinetic parameters and the initial conditions. Different behavior may be observed experimentally although the underlying mechanism is the same.

A two-time scale perturbative method is applied to the chemical system described previously by Pikios and Luss (8). The first order solution derived from this method indicates that sustained oscillations can exist. Our numerical results are in agreement with those reported previously. We simulate also four cases for which the system has two stable steady states and one unstable steady state, and our results indicate that no periodic oscillation bifurcates from the unstable steady states.

The multi-timing perturbative procedure that we employ offers several advantages. When applicable, this method is straightforward to apply and, unlike other methods, gives not only information concerning the stability of the system but also the solution as exactly, in an asymptotic sense, as desired. The necessary numerical computation for implementation of the method can be carried out easily on a digital computer, and it is much more economical than a direct numerical integration of the governing equations.

This multi-timing perturbative method can be applied also to study the stability of a wide variety of chemically reacting systems.

2. Kinetic Model and Governing Equations

We shall consider here a kinetic model proposed recently by Pikios and Luss (8). These authors have shown that a variation in activation energy due to surface heterogeneity can induce sustained kinetic oscillations when the following isothermal reaction sequence occurs on a catalytic surface

$$A(g) + [S] \underset{k_{-1}}{\overset{k_1}{\rightleftharpoons}} [AS] \tag{1}$$

$$B(g) + [S] \underset{k_{-2}}{\overset{k_2}{\rightleftharpoons}} [BS] \tag{2}$$

$$[AS] + [BS] \xrightarrow{k_3} AB + 2[S] \tag{3}$$

where A(g) and B(g) are gas phase reactants which occupy sites [AS] and [BS] on the surface, respectively, and [S] denotes the unoccupied surface sites. It is assumed that the activation energy of the elementary reaction of Eq. (3) is a linear function of the surface coverage of species B, i.e.,

$$E_3 = E_3^0 + \alpha y \ , \tag{4}$$

where $y = [BS]/L$, $L = [AS] + [BS] + [S]$, and α is a constant.

Consequently,

$$k_3 = k' \exp(-\mu y) \tag{5}$$

where

$$k' = k_3(0)\exp(-E^0_3/kT) \tag{6}$$

and $\mu(\equiv \alpha/kT)$ is the coefficient of surface heterogeneity. All other rate coefficients are assumed to be independent of surface coverage. The total number of sites, which is the sum of unoccupied and occupied sites, is constant.

The surface coverages of the two surface species (A and B) are described by two dimensionless differential equations

$$\frac{dx}{dt} = a_1(1 - x - y) - b_1 x - xye^{-\mu y} \equiv f_1 \tag{7}$$

$$\frac{dy}{dt} = a_2(1 - x - y) - b_2 y - xye^{-\mu y} \equiv f_2 \tag{8}$$

where

$$x = [AS]/L$$

$$a_1 = k_1[A(g)]/k_3^0$$

$$b_1 = k_{-1}/k_3^0$$

$$t = k'L\tau \equiv k_3^0 \tau$$

$$a_2 = k_2[B(g)]/k_3^0$$

and

$$b_2 = k_{-2}/k_3^0 \quad ,$$

with the initial conditions

$$\left.\begin{aligned} x &= x_0 \\ \text{and} \\ y &= y_0 \end{aligned}\right\} \tag{9}$$

at $t = 0$.

Pikios and Luss (8) have studied the steady state solutions, the uniqueness and the stability (in a linearized analysis) of Eqs. (7) and (8). They have set the right-hand-sides of Eqs. (7) and (8) equal to zero and have solved the resulting simultaneous algebraic equations, thereby defining a range of parameters which guarantees the occurrence of a unique solution.

Perhaps their most interesting result was a linearized stability analysis wherein they have shown that when the coefficient of surface heterogeneity exceeds a certain minimum value, which depends only on the kinetic parameters, the steady state solution becomes unstable. Direct numerical integration of the governing equations for one set of these kinetic parameters has confirmed the occurrence of limit cycles.

In this paper, we carry the problem further by conducting a nonlinear stability analysis on the same system. We determine the fate of the system if a steady state loses stability and explain the numerical results of Pikios and Luss in a more physical sense. The nonlinear technique used is a multi-timing perturbative method described by Nayfeh (9), and Keener and Cohen (10). The main advantage of this technique is that it enables us to solve the nonlinear governing equations as exactly, in an asymptotic sense, as we desire. The resulting solution takes a simple form from which the stability of oscillatory solutions, if they exist, can be determined immediately. No further mathematical technique,such as a phase plane analysis, is necessary. Moreover, the numerical computations necessary for our nonlinear analysis are relatively easy to perform and are much less expensive than a direct numerical integration of the governing equations.

3. Linearized Stability Analysis and Stability Boundary

At steady state, $f_1 = f_2 = 0$ in Eqs. (7) and (8). Solving for x_s and y_s gives

$$x_s = \frac{a_1(1 - y_s)}{a_1 + b_1 + y_s e^{-\mu y_s}} \tag{10}$$

and

$$a_2(1 - y_s) - b_2 y_s - \frac{a_1(1 - y_s)}{a_1 + b_1 + y_s e^{-\mu y_s}} (a_2 + y_s e^{-\mu y_s}) = 0 \quad . \tag{11}$$

Eqs. (10) and (11) determine the steady state values, x_s and y_s, as functions of the parameters a_1, a_2, b_1, b_2 and μ. Depending on the values of these parameters, it can be shown that up to a maximum of three steady states is possible. The stability of a steady state can be determined by examining the eigenvalues of the Jacobian matrix

$$\underset{\approx}{P} \equiv \left[\begin{array}{cc} \frac{\partial f_1}{\partial x} & \frac{\partial f_1}{\partial y} \\ \frac{\partial f_2}{\partial x} & \frac{\partial f_2}{\partial y} \end{array}\right]_{\substack{x=x_s \\ y=y_s}} \quad . \tag{12}$$

If all eignevalues have negative real parts, the system is asymptotically stable at the steady state. If at least one eigenvalue has a positive real part, a linearized stability analysis predicts an exponentially increasing solution which becomes unbounded as time increases. To find the region of neutral stability where the solution changes from stable to unstable, we set the real part of the eigenvalues of the Jacobian matrix, $\underset{\approx}{P}$, equal to zero. This gives

$$(a_1 + a_2 + b_1 + b_2) + y_s e^{-\mu y_s} + \left[\frac{a_1(1 - y_s)}{a_1 + b_1 + y_s e^{-\mu y_s}}\right] (1 - \mu y_s) e^{-\mu y_s} = 0 \; . \tag{13}$$

Eliminating y_s between Eqs. (11) and (13) gives the region of neutral stability.

This yields a surface in the 5-dimensional hyperspace in variables a_1, a_2, b_1, b_2 and μ.

Figures 1 - 4 show the steady state values of y as a function of one parameter, maintaining all other parameters constant. The numerical values of the constant parameters are taken to be identical to those used by Pikios and Luss (8) where only one unique steady state was observed.

4. Nonlinear Stability Analysis

Based on linear theory, a system becomes unstable if one of the eigenvalues of the Jacobian matrix has a positive real part. The exponentially increasing solutions derived from linear theory fail to represent the solutions as nonlinear effects become important. However, the exponentially increasing solutions may tend to oscillatory solutions on another time scale. Mathematically, this is equivalent to a two-variable expansion procedure where the solution to Eqs. (7)-(9) can be expressed in the form

$$x(t) = x(\xi,\eta) = A_1(\xi)B_1(\eta)$$

and

$$y(t) = y(\xi,\eta) = A_2(\xi)B_2(\eta)$$

where $A_k(\xi)$ portrays "slow time" (ξ) modulations, and $B_k(\eta)$ portrays periodic oscillations on a "fast time" scale, η. This method of multiple time scales is a very powerful mathematical technique which is applicable to highly nonlinear systems.

5. Perturbation Scheme

Here, we develop a two-timing perturbative analysis of a general autonomous system governed by two simultaneous, coupled first order ordinary differential equations. The task of transforming the system described by Eqs. (1) and (2) into a form amenable to this analysis is discussed later. We quote here the following lemma which is needed in the perturbation scheme.

Lemma: The general solution of

$$\frac{du}{dt} + v = m \sin t + n \cos t$$

$$\frac{dv}{dt} - u = p \sin t + q \cos t$$

is

$$u(t) = A \sin t + B \cos t + \left(\frac{m - q}{2}\right) t \sin t$$

$$+ \left(\frac{n + p}{2}\right) t \cos t + \left(\frac{n - p}{2}\right) \sin t$$

$$v(t) = - A \cos t + B \sin t + \left(\frac{n + p}{2}\right) t \sin t$$

$$- \left(\frac{m - q}{2}\right) t \cos t + \left(\frac{m + q}{2}\right) \sin t \, .$$

Hence, in order to suppress secular terms, i.e., terms which would yield unbounded solutions, we require $m - q = 0$ and $n + p = 0$.

To apply the two-timing perturbative analysis, Eqs. (7) and (8) are transformed into the matrix equation (the transformation procedure will be given in a later section)

$$\frac{d\underset{\sim}{x}}{dt} = \underset{\approx}{Q}\,\underset{\sim}{x} + \varepsilon^2 \underset{\approx}{S}\,\underset{\sim}{x} + \underset{\sim}{H}(\underset{\sim}{x}) \qquad (14)$$

for small ε, where

$$\underset{\sim}{x} = \begin{pmatrix} x \\ y \end{pmatrix}, \qquad \underset{\approx}{Q} = \begin{pmatrix} 0 & C \\ -C & 0 \end{pmatrix}, \qquad \underset{\sim}{H}(\underset{\sim}{x}) = \begin{pmatrix} h_1(x,y) \\ h_2(x,y) \end{pmatrix}, \tag{15}$$

$\underset{\approx}{Q}$ is the matrix obtained by transformation of matrix $\underset{\approx}{P}$, C is a constant which will be shown to be the oscillatory frequency in a later section, $\underset{\approx}{S}$ is a constant matrix, and $h_k(x,y)$ are nonlinear functions satisfying the following conditions:

$$h_k(0,0) = h_{kx}(0,0) = h_{ky}(0,0) = 0, \quad k = 1 \text{ and } 2.$$

Both $\underset{\approx}{S}$ and $\underset{\sim}{H}(\underset{\sim}{x})$ will be determined in the transformation procedure. We assume that

$$\begin{aligned} x &= x(\xi,\eta) = \varepsilon x_1(\xi,\eta) + \varepsilon^2 x_2(\xi,\eta) + \ldots \\ y &= y(\xi,\eta) = \varepsilon y_1(\xi,\eta) + \varepsilon^2 y_2(\xi,\eta) + \ldots \end{aligned} \tag{16}$$

i.e.,

$$\underset{\sim}{x} = \underset{\sim}{x}(\xi,\eta) = \sum_{k=1}^{\infty} \varepsilon^k \underset{\sim}{x}_k(\xi,\eta) \quad \text{and} \quad \underset{\sim}{x}_k = \begin{pmatrix} x_k \\ y_k \end{pmatrix}, \tag{17}$$

where

$$\xi = \varepsilon^2 t \quad \text{and} \quad \eta = (1 + \varepsilon\omega_1 + \varepsilon^2\omega_2 + \ldots)t, \tag{18}$$

with constant ω_k. In this case, the time derivative may be transformed according to

$$\frac{d}{dt} = \varepsilon^2 \frac{\partial}{\partial \xi} + (1 + \varepsilon\omega_1 + \varepsilon^2\omega_2 + \ldots) \frac{\partial}{\partial \eta}.$$

Substituting Eqs. (17) and (18) into Eq. (14) and equating like powers of ε, we find

$$\frac{\partial \underset{\sim}{x}_1}{\partial \eta} - \underset{\approx}{Q}\, \underset{\sim}{x}_1 = 0 \tag{19}$$

$$\frac{\partial \underset{\sim}{x}_2}{\partial \eta} - \underset{\approx}{Q}\, \underset{\sim}{x}_2 = -\omega_1 \frac{\partial \underset{\sim}{x}_1}{\partial \eta} + \underset{\sim}{\theta}(\underset{\sim}{x}_1) \tag{20}$$

$$\frac{\partial \underset{\sim}{x}_3}{\partial \eta} - \underset{\approx}{Q}\, \underset{\sim}{x}_3 = \underset{\approx}{S}\, \underset{\sim}{x}_1 - \omega_2 \frac{\partial \underset{\sim}{x}_1}{\partial \eta} - \omega_1 \frac{\partial \underset{\sim}{x}_2}{\partial \eta} - \frac{\partial \underset{\sim}{x}_1}{\partial \xi} + \underset{\sim}{\Phi}(\underset{\sim}{x}_1, \underset{\sim}{x}_2) \tag{21}$$

where

$$\theta_k(x_1,y_1) = \frac{1}{2} h_{kxx}(0)x_1^2 + \frac{1}{2} h_{kyy}(0)y_1^2 + h_{kxy}(0)x_1y_1 \tag{22}$$

and

$$\begin{aligned}\Phi_k(x_1,y_1;x_2,y_2) = {} & h_{kxx}(0)x_1x_2 + h_{kxy}(x_1y_2 + x_2y_1) + h_{kyy}(0)y_1y_2 \\ & + \frac{1}{6}\left[h_{kxxx}(0)x_1^3 + 3h_{kxxy}(0)x_1^2y_1 + 3h_{kxyy}(0)x_1y_1^2\right. \\ & \left. + h_{kyyy}(0)y_1^3\right] .\end{aligned} \tag{23}$$

The general solution of Eq. (19) is

$$\begin{aligned} x_1(\xi,\eta) &= R(\xi)\sin[C\eta + \phi(\xi)] \\ y_1(\xi,\eta) &= R(\xi)\cos[C\eta + \phi(\xi)] , \end{aligned} \tag{24}$$

where $R(\xi)$ and $\phi(\xi)$ must be determined later. Substituting Eq. (24) into Eq. (22) we obtain

$$\begin{aligned}\theta_k(x_1,y_1) = {} & \frac{1}{4} R^2 \left[h_{kxx}(0) + h_{kyy}(0)\right] + \frac{1}{4} R^2 \left[h_{kyy}(0) - h_{kxx}(0)\right] \cos(2\beta) \\ & + \frac{1}{2} R^2 h_{kxy}(0)\sin(2\beta) ,\end{aligned} \tag{25}$$

where $\beta = C\eta + \phi(\xi)$. Consequently, Eq. (20) becomes

$$\frac{\partial x_2}{\partial \eta} - C y_2 = \frac{1}{4} R^2 [h_{1xx}(0) + h_{1yy}(0)] - \omega_1 C R \cos\beta$$

$$+ \frac{1}{4} R^2 [h_{1yy}(0) - h_{1xx}(0)] \cos(2\beta) + \frac{1}{2} R^2 h_{1xy}(0) \sin(2\beta) \tag{26}$$

$$\frac{\partial y_2}{\partial \eta} + C x_2 = \frac{1}{4} R^2 [h_{2xx}(0) + h_{2yy}(0)] + \omega_1 C R \sin\beta$$

$$+ \frac{1}{4} R^2 [h_{2yy}(0) - h_{2xx}(0)] \cos(2\beta) + \frac{1}{2} R^2 h_{2xy}(0) \sin(2\beta) .$$

Using our lemma, secular terms will be eliminated if we set $\omega_1 = 0$. Thus, the general solution of Eq. (26) becomes

$$x_2(\xi,\eta) = k_1 + k_2 \sin(2\beta) + k_3 \cos(2\beta) + F(\xi)\sin[C\eta + \lambda(\xi)] \tag{27}$$

$$y_2(\xi,\eta) = k_4 + k_5 \sin(2\beta) + k_6 \cos(2\beta) + F(\xi)\sin[C\eta + \lambda(\xi)] .$$

Substituting Eq. (27) into Eq. (26) and equating like terms, we find

$$k_1 = \frac{1}{4C} R^2 [h_{2xx}(0) + h_{2yy}(0)] ,$$

$$k_2 = \frac{1}{6C} R^2 [- h_{1xx}(0) + h_{1yy}(0) - h_{2xy}(0)] ,$$

$$k_3 = \frac{1}{3C} R^2 [\frac{1}{4} h_{2xx}(0) - \frac{1}{4} h_{2yy}(0) - h_{1xy}(0)] , \tag{28}$$

$$k_4 = - \frac{1}{4C} R^2 [h_{1xx}(0) + h_{1yy}(0)] ,$$

$$k_5 = \frac{1}{6C} R^2 \left[- h_{2xx}(0) + h_{2yy}(0) + h_{1xy}(0) \right] ,$$

$$k_6 = \frac{1}{3C} R^2 \left[- \frac{1}{4} h_{1xx}(0) + \frac{1}{4} h_{1yy}(0) - h_{2xy}(0) \right] ,$$

and both $F(\xi)$ as well as $\lambda(\xi)$ must be determined later. Substituting Eqs. (24) - (28) into Eq. (21), we obtain

$$\begin{aligned} \frac{\partial x_3}{\partial \eta} - C y_3 &= \left[S_{11} R - \frac{dR}{d\xi} + R^3 (A_1 + B_1) \right] \sin\beta \\ &\quad + \left[(S_{12} - \omega_2 C - \frac{d\phi}{d\xi}) R + R^3 (C_1 + D_1) \right] \cos\beta + \text{higher harmonics} \end{aligned} \tag{29}$$

$$\begin{aligned} \frac{\partial y_3}{\partial \eta} + C x_3 &= \left[(S_{21} + \omega_2 C + \frac{d\phi}{d\xi}) R + R^3 (A_2 + B_2) \right] \sin\beta \\ &\quad + \left[S_{22} R - \frac{dR}{d\xi} + R^3 (C_2 + D_2) \right] \cos\beta + \text{higher harmonics} \end{aligned}$$

where

$$\begin{aligned} A_k &= \frac{1}{24C} h_{kxx}(0) \left[5 h_{2xx}(0) + 7 h_{2yy}(0) + 4 h_{1xy}(0) \right] \\ &\quad + \frac{1}{24C} h_{kxy}(0) \left[-7 h_{1xx}(0) - 5 h_{1yy}(0) + 2 h_{2xy}(0) \right] \\ &\quad + \frac{1}{12C} h_{kyy}(0) \left[-h_{2xx}(0) + h_{2yy}(0) + h_{1xy}(0) \right] \end{aligned} \tag{30}$$

$$\begin{aligned} C_k &= \frac{1}{12C} h_{kxx}(0) \left[-h_{1xx}(0) + h_{1yy}(0) - h_{2xy}(0) \right] \\ &\quad + \frac{1}{24C} h_{kxy}(0) \left[5 h_{2xx}(0) + 7 h_{2yy}(0) - 2 h_{1xy}(0) \right] \\ &\quad + \frac{1}{24C} h_{kyy}(0) \left[-7 h_{1xx}(0) - 5 h_{1yy}(0) - 4 h_{2xy}(0) \right] \end{aligned}$$

$$B_k = \frac{1}{8}\left[h_{kxxx}(0) + h_{kxyy}(0)\right]$$

$$D_k = \frac{1}{8}\left[h_{kxxy}(0) + h_{kyyy}(0)\right].$$

The secular terms in Eq. (29) are eliminated if

$$2\frac{dR}{d\xi} = (S_{11} + S_{22})R + (A_1 + B_1 + C_2 + D_2)R^3 \tag{31}$$

and

$$2R\frac{d\phi}{d\xi} = (S_{12} - S_{21} - 2\omega_2 C)R + (C_1 + D_1 - A_2 - B_2)R^3. \tag{32}$$

The periodic nature of the $O(\varepsilon)$ solution, x_1 and y_1, can be determined entirely from Eq. (31), the solution of which is easily found to be

$$R^2(\xi) = \left(\frac{\gamma_1}{\gamma_2}\right)\frac{1}{1 + \kappa e^{-\gamma_1 \xi}}, \tag{33}$$

where
$$\gamma_1 = S_{11} + S_{22}$$

$$\gamma_2 = -(A_1 + B_1 + C_2 + D_2) \tag{34}$$

$$\kappa = \left(\frac{\gamma_1}{\gamma_2}\right)\frac{1}{R^2(0)} - 1.$$

Note that κ is a constant to be determined from initial conditions and may be either positive or negative. The stability of the oscillatory solution is dependent upon the signs of γ_1 and γ_2 as well as the initial condition.

We summarize all the possible cases for different values of γ_1, γ_2 and κ in Table 1. The empty boxes in Table 1 correspond to nonphysical situations where

$R^2(0) < 0$. It must be emphasized that the results shown in Table 1 describe the solution to the posed problem only to $\mathcal{O}(\varepsilon)$. All effects due to higher order terms are not included. As will be shown in the next section, Eq. (14) describes the bifurcation of the solution to the original system [Eqs.(7) and (8)] near the point of neutral stability (bifurcation point), where the steady state solution changes from being stable to unstable, or vice versa. For the case where $\gamma_1 > 0$ and $\gamma_2 > 0$, we conclude from Eqs.(31) and (33) that stable sustained oscillations always occur. A limit cycle exists in the (x_1,y_1) plane with amplitude given by

$$\left(\frac{\gamma_1}{\gamma_2}\right)^{1/2} \varepsilon = \left[\frac{S_{11} + S_{22}}{-(A_1 + B_1 + C_2 + D_2)}\right]^{1/2} \varepsilon.$$

For the case in which $\gamma_1 < 0$ and $\gamma_2 > 0$, the $\mathcal{O}(\varepsilon)$ solution decays exponentially with time. This implies the existence of an unstable limit cycle around the stable steady state in the (x_1,y_1) plane. For the case in which $\gamma_1 > 0$ and $\gamma_2 < 0$, our perturbative analysis predicts a periodic solution, the amplitude of which increases with time. It is expected that terms of higher order become dominant as time increases, and the solution bifurcates to a stable limit cycle around the unstable steady state. However, in this case, our two-timing method is no longer applicable to the determination of the amplitude of the limit cycle. The situation where $\gamma_1 < 0$ and $\gamma_2 < 0$ deserves special comment. In all the cases discussed above, the initial conditions do not enter explicitly. However, for this case where $\gamma_1 < 0$ and $\gamma_2 < 0$, periodic oscillations or growing periodic oscillations occur depending on the initial conditions. For $\kappa > 0$, i.e., small R(0), decaying oscillations occur, whereas growing

oscillations occur when $-1 < \kappa < 0$, i.e., large R(0). This implies the existence of an unstable limit cycle around a stable steady state. When the initial conditions are such that R(0) is within the unstable limit cycle, the solution always tends to the stable steady state. On the other hand, when the initial conditions are such that R(0) is outside the unstable limit cycle, the oscillatory solution has an amplitude which increases with time, possibly tending to a stable limit cycle. Therefore, what is observed experimentally depends on the number of catalytic sites occupied by the reactants initially, as well as the values of the kinetic parameters. From the above discussion, the nature of the bifurcation can be determined easily once the signs of γ_1 and γ_2 are known.

6. Transformation Procedure

In order that we may use the results of the last section, we have to transform the system of Eqs. (7) and (8) into the matrix form of Eq. (14). For illustrative purposes, we consider the case where the effects of varying the parameter b_1 is studied while maintaining all other parameters constant. (If more than one parameter is varied simultaneously, the transformation procedure is similar, but algebraically more complicated.) First, we have to find the value b_{10} of the parameter b_1, where the eigenvalues of the Jacobian matrix $\underset{\approx}{P}$, defined in Eq. (12), are purely imaginary. Since the characteristic equation of $\underset{\approx}{P}$ is quadratic, the imaginary eigenvalues are complex conjugates. This step amounts to solving Eqs. (11) and (13) simultaneously, for fixed a_1, a_2, b_2 and μ. Note that y_s enters as a parameter in both equations. We have to find the value of b_1 (and y_s) for which both equations are satisfied simultaneously. This can be done easily by means of

a numerical search. At $b_1 = b_{10}$, the eigenvalues of the Jacobian matrix $\underset{\approx}{P}$ are then given by

$$\pm iC = \pm i \left(\frac{\partial f_1}{\partial x} \frac{\partial f_2}{\partial y} - \frac{\partial f_1}{\partial y} \frac{\partial f_2}{\partial x} \right)^{\frac{1}{2}} . \tag{35}$$

Next, we have to find the transformation which transforms $\underset{\approx}{P}$ into the $\underset{\approx}{Q}$ of Eq. (14), i.e., the matrix $\underset{\approx}{T}$ which satisfies

$$\underset{\approx}{T}^{-1} \underset{\approx}{P} \underset{\approx}{T} = \underset{\approx}{Q} = \begin{pmatrix} 0 & C \\ -C & 0 \end{pmatrix} . \tag{36}$$

Let $\underset{\sim}{t}_1$ and $\underset{\sim}{t}_2$ denote the column vectors of $\underset{\approx}{T}$, so that $\underset{\approx}{T} = (\underset{\sim}{t}_1, \underset{\sim}{t}_2)$. Then, Eq. (36) can be written in the form

$$\underset{\approx}{P} \underset{\sim}{t}_1 = - C \underset{\sim}{t}_2 , \tag{37}$$

and $$\underset{\approx}{P} \underset{\sim}{t}_2 = C \underset{\sim}{t}_1 .$$

Hence, we obtain

$$(\underset{\approx}{P}^2 + C^2 \underset{\approx}{I}) \underset{\sim}{t}_1 = \underset{\sim}{0} . \tag{38}$$

Eq. (38) shows that $\underset{\sim}{t}_1$ is an eigenvector of the matrix $\underset{\approx}{P}^2$ with corresponding eigenvalue equal to $-C^2$. Having determined $\underset{\sim}{t}_1$ from Eq. (38), $\underset{\sim}{t}_2$ can be found from the first relation in Eq. (37).

The next step in the transformation procedure involves a Taylor series expansion of Eqs. (7) and (8) about the point $b_1 = b_{10}$ for fixed values of a_1, a_2, b_2 and μ. Converting these equations into matrix form yields

$$\frac{d\underset{\sim}{x}}{dt} = \underset{\sim}{f}(\underset{\sim}{x}, b_1) \ , \tag{39}$$

where

$$\underset{\sim}{x} = \begin{pmatrix} x \\ y \end{pmatrix} \quad \text{and} \quad \underset{\sim}{f} = \begin{pmatrix} f_1(x,y,b_1) \\ f_2(x,y,b_1) \end{pmatrix} .$$

At steady state,

$$f_1\left(x_s(b_1),\, y_s(b_1),\, b_1\right) = 0 \ ,$$

and

$$f_2\left(x_s(b_1),\, y_s(b_1),\, b_1\right) = 0 \ .$$

Let δ be the deviation of b_1 from the critical value b_{10}, so that

$$b_1 = b_{10} + \delta. \tag{40}$$

Hence, expanding $\underset{\sim}{x}_s(b_1)$ about b_{10}, we obtain

$$\underset{\sim}{x}_s(b_1) = \underset{\sim}{x}_s(b_{10}) + \delta\underset{\sim}{x}_1 + \ldots \ , \tag{41}$$

where

$$\underset{\sim}{x}_1 = - \underset{\approx}{P}^{-1} \left.\frac{\partial \underset{\sim}{f}}{\partial b_1}\right|_{\substack{b_1=b_{10} \\ \underset{\sim}{x} = \underset{\sim}{x}_s(b_{10})}} \equiv \begin{pmatrix} \bar{x} \\ \bar{y} \end{pmatrix} . \tag{42}$$

Therefore,

$$x_s(b_1) = x_s + \delta\bar{x} + O(\delta^2)$$

and

$$y_s(b_1) = y_s + \delta\bar{y} + O(\delta^2) \ ,$$

where

$$x_s = x_s(b_{10}) \quad \text{and} \quad y_s = y_s(b_{10}) \ .$$

Let
$$\underset{\sim}{x} = \underset{\sim}{x}_s(b_1) + \underset{\sim}{G}, \quad \text{where} \quad \underset{\sim}{G} = \begin{pmatrix} g_1 \\ g_2 \end{pmatrix} . \tag{43}$$

Then, Eq. (39) can be written, for k = 1 and 2, as

$$\begin{aligned}
\frac{dg_k}{dt} &= f_k\Big(x_s(b_1) + g_1,\ y_s(b_1) + g_2,\ b_1\Big) \\
&= g_1 \frac{\partial f_k}{\partial x}\bigg|_{\substack{x=x_s(b_1) \\ y=y_s(b_1)}} + g_2 \frac{\partial f_k}{\partial y}\bigg|_{\substack{x=x_s(b_1) \\ y=y_s(b_1)}} \\
&+ \frac{1}{2!}\left[g_1^2 \frac{\partial^2 f_k}{\partial x^2} + 2g_1 g_2 \frac{\partial^2 f_k}{\partial x \partial y} + g_2^2 \frac{\partial^2 f_k}{\partial y^2}\right]_{\substack{x=x_s(b_1) \\ y=y_s(b_1)}} \\
&+ \frac{1}{3!}\left[g_1^3 \frac{\partial^3 f_k}{\partial x^3} + 3g_1^2 g_2 \frac{\partial^3 f_k}{\partial x^2 \partial y} + 3g_1 g_2^2 \frac{\partial^3 f_k}{\partial x \partial y^2} + g_2^3 \frac{\partial^3 f_k}{\partial y^3}\right]_{\substack{x=x_s(b_1) \\ y=y_s(b_1)}} \\
&+ \ldots
\end{aligned} \tag{44}$$

Now, setting $b_1 = b_{10} + \delta$, we obtain

$$\begin{aligned}
\frac{\partial f_k}{\partial x}\bigg|_{\substack{x=x_s(b_1) \\ y=y_s(b_1)}} &= \frac{\partial}{\partial x} f_k\Big(x_s(b_{10} + \delta),\ y_s(b_{10} + \delta),\ b_{10} + \delta\Big) \\
&= \frac{\partial}{\partial x} f_k\Big(x_s(b_{10}) + \delta\bar{x},\ y_s(b_{10}) + \delta\bar{y},\ b_{10} + \delta\Big) \\
&= \frac{\partial f_{ko}}{\partial x} + \frac{\partial^2 f_{ko}}{\partial x^2}\delta\bar{x} + \frac{\partial^2 f_{ko}}{\partial x \partial y}\delta\bar{y} + \frac{\partial^2 f_{ko}}{\partial x \partial b_1}\delta + O(\delta^2) ,
\end{aligned} \tag{45}$$

where $f_{ko} = f_k\left(x_s(b_{10}),\, y_s(b_{10}),\, b_{10}\right)$. Other terms on the right-hand-side of Eq. (44) can be expanded likewise. Therefore, Eq. (44) can be rewritten as

$$\begin{aligned}
\frac{dg_k}{dt} &= g_1 \frac{\partial f_{ko}}{\partial x} + \delta\left(\frac{\partial^2 f_{ko}}{\partial x^2}\,\bar{x} + \frac{\partial^2 f_{ko}}{\partial x \partial y}\,\bar{y} + \frac{\partial^2 f_{ko}}{\partial x \partial b_1}\right) g_1 \\
&+ g_2 \frac{\partial f_{ko}}{\partial y} + \delta\left(\frac{\partial^2 f_{ko}}{\partial x \partial y}\,\bar{x} + \frac{\partial^2 f_{ko}}{\partial y^2}\,\bar{y} + \frac{\partial^2 f_{ko}}{\partial y \partial b_1}\right) g_2 \\
&+ \frac{1}{2}\left[g_1^2 \frac{\partial^2 f_{ko}}{\partial x^2} + 2 g_1 g_2 \frac{\partial^2 f_{ko}}{\partial x \partial y} + g_2^2 \frac{\partial^2 f_{ko}}{\partial y^2}\right] \\
&+ \frac{1}{6}\left[g_1^3 \frac{\partial^3 f_{ko}}{\partial x^3} + 3 g_1^2 g_2 \frac{\partial^3 f_{ko}}{\partial x^2 \partial y} + 3 g_1 g_2^2 \frac{\partial^3 f_{ko}}{\partial x \partial y^2} + g_2^3 \frac{\partial^3 f_{ko}}{\partial y^3}\right] + \ldots
\end{aligned} \tag{46}$$

In matrix notation, neglecting terms of $O(\delta^2)$ and $O(g_k^4)$, we obtain

$$\frac{d\underset{\sim}{G}}{dt} = \underset{\approx}{P}\underset{\sim}{G} + \varepsilon^2 \hat{\underset{\approx}{S}}\underset{\sim}{G} + \hat{\underset{\sim}{H}}(\underset{\sim}{G}) \,, \tag{47}$$

where we have set $\delta = \varepsilon^2$, and

$$\hat{\underset{\approx}{S}} = \begin{bmatrix}
\dfrac{\partial^2 f_{10}}{\partial x^2}\,\bar{x} + \dfrac{\partial^2 f_{10}}{\partial x\, \partial y}\,\bar{y} + \dfrac{\partial^2 f_{10}}{\partial x\, \partial b_1} & \dfrac{\partial^2 f_{10}}{\partial x\, \partial y}\,\bar{x} + \dfrac{\partial^2 f_{10}}{\partial y^2}\,\bar{y} + \dfrac{\partial^2 f_{10}}{\partial y\, \partial b_1} \\
\dfrac{\partial^2 f_{20}}{\partial x^2}\,\bar{x} + \dfrac{\partial^2 f_{20}}{\partial x\, \partial y}\,\bar{y} + \dfrac{\partial^2 f_{20}}{\partial x\, \partial b_1} & \dfrac{\partial^2 f_{20}}{\partial x\, \partial y}\,\bar{x} + \dfrac{\partial^2 f_{20}}{\partial y^2}\,\bar{y} + \dfrac{\partial^2 f_{20}}{\partial y\, \partial b_1}
\end{bmatrix} \tag{48}$$

and

$$\hat{\underset{\sim}{H}}(\underset{\sim}{G}) = \begin{bmatrix} \frac{1}{2}\left(g_1^2 \frac{\partial^2 f_{10}}{\partial x^2} + 2g_1g_2 \frac{\partial^2 f_{10}}{\partial x \partial y} + g_2^2 \frac{\partial^2 f_{10}}{\partial y^2}\right) \\ + \frac{1}{6}\left(g_1^3 \frac{\partial^3 f_{10}}{\partial x^3} + 3g_1^2g_2 \frac{\partial^3 f_{10}}{\partial x \partial y} + 3g_1g_2^2 \frac{\partial^3 f_{10}}{\partial x \partial y^2} + g_2^3 \frac{\partial^3 f_{10}}{\partial y^3}\right) \\ \\ \frac{1}{2}\left(g_1^2 \frac{\partial^2 f_{20}}{\partial x^2} + 2g_1g_2 \frac{\partial^2 f_{20}}{\partial x \partial y} + g_2^2 \frac{\partial^2 f_{20}}{\partial y^2}\right) \\ + \frac{1}{6}\left(g_1^3 \frac{\partial^3 f_{20}}{\partial x^3} + 3g_1^2g_2 \frac{\partial^3 f_{20}}{\partial x^2 \partial y} + 3g_1g_2^2 \frac{\partial^3 f_{20}}{\partial x \partial y^2} + g_2^3 \frac{\partial^3 f_{20}}{\partial y^3}\right) \end{bmatrix} . \tag{49}$$

Finally, we set $\underset{\sim}{G} = \underset{\approx}{T}\underset{\sim}{Z}$, and Eq. (47) can be put into the form of Eq. (14)

$$\frac{d\underset{\sim}{Z}}{dt} = \underset{\approx}{Q}\underset{\sim}{Z} + \varepsilon^2 \underset{\approx}{S}\underset{\sim}{Z} + \underset{\sim}{H}(\underset{\sim}{Z}) , \tag{50}$$

where

$$\underset{\approx}{S} = \underset{\approx}{T}^{-1}\hat{\underset{\approx}{S}}\underset{\approx}{T} \tag{51}$$

and

$$\underset{\sim}{H}(\underset{\sim}{Z}) = \underset{\approx}{T}^{-1}\hat{\underset{\sim}{H}}(\underset{\approx}{T}\underset{\sim}{Z}) . \tag{52}$$

The matrix elements of $\underset{\approx}{S}$ can be evaluated by means of Eqs. (48) and (51). Hence, the value of γ_1 can be determined from Eq. (34). Since

$$\underset{\sim}{G} = \underset{\approx}{T}\underset{\sim}{Z} = \begin{pmatrix} t_{11}z_1 + t_{12}z_2 \\ t_{21}z_1 + t_{22}z_2 \end{pmatrix} ,$$

we obtain $\hat{\underset{\sim}{H}}(\underset{\approx}{T}\underset{\sim}{Z})$ from $\hat{\underset{\sim}{H}}(\underset{\sim}{G})$ by associating

$$g_1 \to t_{11}z_1 + t_{12}z_2$$

$$g_2 \to t_{21}z_1 + t_{22}z_2$$

in $\hat{\underset{\sim}{H}}(\underset{\sim}{G})$.

It is worthwhile to report the explicit formulae for the vector $\underset{\sim}{H}(\underset{\sim}{Z})$ so as to facilitate implementation of the numerical computations in the final step. For k = 1 and 2, we have

$$\begin{aligned}
\hat{h}_k(\underset{\sim}{\underset{\sim}{T}}\underset{\sim}{Z}) = {} & \frac{1}{2}\Big[(t_{11}z_1 + t_{12}z_2)^2 \frac{\partial^2 f_{ko}}{\partial x^2} \\
& + 2(t_{11}z_1 + t_{12}z_2)(t_{21}z_1 + t_{22}z_2) \frac{\partial^2 f_{ko}}{\partial x \partial y} + (t_{21}z_1 + t_{22}z_2)^2 \frac{\partial^2 f_{ko}}{\partial y^2}\Big] \\
& + \frac{1}{6}\Big[(t_{11}z_1 + t_{12}z_2)^3 \frac{\partial^3 f_{ko}}{\partial x^3} + 3(t_{11}z_1 + t_{12}z_2)^2(t_{21}z_1 + t_{22}z_2) \frac{\partial^3 f_{ko}}{\partial x^2 \partial y} \\
& + 3(t_{11}z_1 + t_{12}z_2)(t_{21}z_1 + t_{22}z_2)^2 \frac{\partial^3 f_{ko}}{\partial x \partial y^2} + (t_{21}z_1 + t_{22}z_2)^3 \frac{\partial^3 f_{ko}}{\partial y^3}\Big].
\end{aligned} \tag{53}$$

Therefore, successive differentiation yields the following expressions necessary for the calculation of A_K, B_K, C_K and D_K in Eq. (30)

$$\begin{aligned}
\hat{h}_{k z_1 z_1} = {} & t_{11}^2 \frac{\partial^2 f_{ko}}{\partial x^2} + 2t_{11}t_{21} \frac{\partial^2 f_{ko}}{\partial x \partial y} + t_{21}^2 \frac{\partial^2 f_{ko}}{\partial y^2} + t_{11}^2(t_{11}z_1 + t_{12}z_2) \frac{\partial^3 f_{ko}}{\partial y^3} \\
& + \Big[3t_{11}^2 t_{21}z_1 + t_{11}(2t_{12}t_{21} + t_{11}t_{22})z_2\Big] \frac{\partial^3 f_{ko}}{\partial x^2 \partial y} \\
& + \Big[3t_{11}t_{21}^2 z_1 + t_{21}(2t_{11}t_{22} + t_{12}t_{21})z_2\Big] \frac{\partial^3 f_{ko}}{\partial x \partial y^2} \\
& + t_{21}^2(t_{21}z_1 + t_{22}z_2) \frac{\partial^3 f_{ko}}{\partial y^3}
\end{aligned}$$

$$\hat{h}_{kz_1z_2} = t_{11}t_{12}\frac{\partial^2 f_{ko}}{\partial x^2} + (t_{11}t_{22} + t_{12}t_{21})\frac{\partial^2 f_{ko}}{\partial x\,\partial y} + t_{21}t_{22}\frac{\partial^2 f_{ko}}{\partial y^2}$$
$$+ t_{11}t_{12}(t_{11}z_1 + t_{12}z_2)\frac{\partial^3 f_{ko}}{\partial x^3}$$
$$+ \left[t_{11}(t_{11}t_{22} + 2t_{12}t_{21})z_1 + t_{12}(2t_{11}t_{22} + t_{12}t_{21})z_2\right]\frac{\partial^3 f_{ko}}{\partial x^2\partial y}$$
$$+ \left[t_{21}(2t_{11}t_{22} + t_{12}t_{21})z_1 + t_{22}(t_{11}t_{22} + 2t_{12}t_{21})z_2\right]\frac{\partial^3 f_{ko}}{\partial x\partial y^2}$$
$$+ t_{21}t_{22}(t_{21}z_1 + t_{22}z_2)\frac{\partial^3 f_{ko}}{\partial y^3}$$

$$\hat{h}_{kz_2z_2} = t_{12}^2\frac{\partial^2 f_{ko}}{\partial x^2} + 2t_{12}t_{22}\frac{\partial^2 f_{ko}}{\partial x\partial y} + t_{22}^2\frac{\partial^2 f_{ko}}{\partial y^2}$$
$$+ t_{12}^2(t_{11}z_1 + t_{12}z_2)\frac{\partial^3 f_{ko}}{\partial x^3}$$
$$+ \left[t_{12}(2t_{11}t_{22} + t_{12}t_{21})z_1 + 3t_{12}^2t_{22}z_2\right]\frac{\partial^3 f_{ko}}{\partial x^2\partial y} \qquad (54)$$
$$+ \left[t_{22}(t_{11}t_{22} + 2t_{12}t_{21})z_1 + 3t_{12}t_{22}^2z_2\right]\frac{\partial^3 f_{ko}}{\partial x\partial y^2}$$
$$+ t_{22}^2(t_{21}z_1 + t_{22}z_2)\frac{\partial^3 f_{ko}}{\partial y^3}$$

$$\hat{h}_{kz_1z_1z_1} = t_{11}^3\frac{\partial^3 f_{ko}}{\partial x^3} + 3t_{11}^2t_{21}\frac{\partial^3 f_{ko}}{\partial x^2\partial y} + 3t_{11}t_{21}^2\frac{\partial^3 f_{ko}}{\partial x\partial y^2} + t_{21}^3\frac{\partial^3 f_{ko}}{\partial y^3}$$

$$\hat{h}_{kz_1z_1z_2} = t_{11}^2t_{12}\frac{\partial^3 f_{ko}}{\partial x^3} + t_{11}(2t_{12}t_{21} + t_{11}t_{22})\frac{\partial^3 f_{ko}}{\partial x^2\partial y}$$
$$+ t_{21}(2t_{11}t_{22} + t_{12}t_{21})\frac{\partial^3 f_{ko}}{\partial x\partial y^2} + t_{21}^2t_{22}\frac{\partial^3 f_{ko}}{\partial y^3}$$

$$\hat{h}_{kz_1z_2z_2} = t_{11}t_{12}^2 \frac{\partial^3 f_{ko}}{\partial x^3} + t_{12}(2t_{11}t_{22} + t_{12}t_{21}) \frac{\partial^3 f_{ko}}{\partial x^2 \partial y}$$

$$+ t_{22}(t_{11}t_{22} + 2t_{12}t_{21}) \frac{\partial^3 f_{ko}}{\partial x \partial y^2} + t_{21}t_{22}^2 \frac{\partial^3 f_{ko}}{\partial y^3}$$

$$\hat{h}_{kz_2z_2z_2} = t_{12}^3 \frac{\partial^3 f_{ko}}{\partial x^3} + 3t_{12}^2 t_{22} \frac{\partial^3 f_{ko}}{\partial x^2 \partial y} + 3t_{12}t_{22}^2 \frac{\partial^3 f_{ko}}{\partial x \partial y^2} + t_{22}^3 \frac{\partial^3 f_{ko}}{\partial y^3} \quad .$$

Making use of Eq. (52), we arrive at the final result for k=1 and 2,

$$\begin{aligned}
h_{kz_1z_1}(0) &= \bar{t}_{k1}\hat{h}_{1z_1z_1}(0) + \bar{t}_{k2}\hat{h}_{2z_1z_1}(0) \\
h_{kz_1z_2}(0) &= \bar{t}_{k1}\hat{h}_{1z_1z_2}(0) + \bar{t}_{k2}\hat{h}_{2z_1z_2}(0) \\
h_{kz_2z_2}(0) &= \bar{t}_{k1}\hat{h}_{1z_2z_2}(0) + \bar{t}_{k2}\hat{h}_{2z_2z_2}(0) \\
h_{kz_1z_1z_1}(0) &= \bar{t}_{k1}\hat{h}_{1z_1z_1z_1}(0) + \bar{t}_{k2}\hat{h}_{2z_1z_1z_1}(0) \\
h_{kz_1z_1z_2}(0) &= \bar{t}_{k1}\hat{h}_{1z_1z_1z_2}(0) + \bar{t}_{k2}\hat{h}_{2z_1z_1z_2}(0) \\
h_{kz_1z_2z_2}(0) &= \bar{t}_{k1}\hat{h}_{1z_1z_2z_2}(0) + \bar{t}_{k2}\hat{h}_{2z_1z_2z_2}(0) \\
h_{kz_2z_2z_2}(0) &= \bar{t}_{k1}\hat{h}_{1z_2z_2z_2}(0) + \bar{t}_{k2}\hat{h}_{2z_2z_2z_2}(0) \quad ,
\end{aligned} \tag{55}$$

where $\bar{t}_{ij}$ are components of the matrix $\underset{\approx}{T}^{-1}$. Using Eqs. (54) and (55), the values of A_k, B_k, C_k and D_k can be calculated. Hence, the value of γ_2 can be determined.

7. Results

The results of our computations for the cases where there is a unique steady state are summarized in Table 2, and the stability curves are shown in Figs. 1 - 4. The non-varying parameters are chosen to be identical to those reported previously by Pikios and Luss (8). From the signs of γ_1 and γ_2, we can determine the nature of the periodic oscillations that emerge from each bifurcation point.

For the cases where we vary b_1 and a_2, keeping all other parameters constant (c.f. Figs. 1 and 4), our results indicate that sustained periodic oscillations of $\mathcal{O}(\varepsilon)$ bifurcate from the unstable steady solutions. Since a stable limit cycle can only exist around an unstable steady state, the oscillatory solution bifurcates to the right of the bifurcation point as shown in Figs. 1 and 4. For these cases, the frequencies and amplitudes of the periodic oscillations predicted by our nonlinear analysis are compared in Table 3 to those obtained from direct numerical integration of the governing equations.

It is seen in Table 3 that for b_1 close to the bifurcation point, the amplitudes of the oscillatory solutions predicted by our analysis agree almost exactly with those obtained by direct numerical integration of the governing equations. The discrepancies between the theoretically predicted amplitude and that obtained by numerical integration increase gradually as b_1 deviates from the bifurcation point. Since the perturbative analysis is local in nature, it is not expected to give accurate predictions for b_1 far from the critical value. The predicted frequency is larger than that found numerically. The discrepancy may be caused by neglecting higher harmonics in the analysis. Similar results were found

near the lower bifurcation point when a_2 was varied keeping all other parameters constant, except that the discrepancy between the theoretically predicted frequency and that found numerically is much smaller. At the upper bifurcation points, our calculations indicate the occurrence of an unstable limit cycle. Since an unstable limit cycle can only exist around a stable steady state, the oscillatory solutions bifurcate to the right of the bifurcation point.

For the cases where a_1 and b_2 are varied, maintaining all other parameters constant, decaying periodic oscillations of $\mathcal{O}(\varepsilon)$ emerge from the lower bifurcation points, indicating the occurrence of an unstable limit cycle around a stable steady state. Hence, the solution bifurcates to the right. At the upper bifurcation points, growing oscillations of $\mathcal{O}(\varepsilon)$ are predicted. Based on the discussion of the previous section, it is expected that a stable limit cycle exists around an unstable steady state. The oscillatory solutions thus bifurcate to the right.

8. Synopsis

Results of our computations indicate that in the case where stable periodic oscillations emerge from the bifurcation point, a perturbative analysis gives accurate predictions of the amplitudes of limit cycles for values of the kinetic parameters close to those of the bifurcation point. Furthermore, the predicted direction of bifurcation is confirmed by the results of direct numerical integration of the governing equations. However, global extension of the perturbative theory is not recommended.

References

1 Belyaev, V. D., Slinko, M. M., Timeoshenko, V. I. and Slinko, M. G., Kinet. Katal. 1973 14 810.

2 Dauchoet, J. P. and Van Cakenberghe, J., Nature (London) Phys. Sci. 1973 246 61.

3 McCarthy, E., Zahradnik, J., Kuczynski, G. C. and Carberry J. J., J. Catal. 1975 39 29.

4 Zuniga, E. J. and Luss, D., J. Catal. 1978 53 312.

5 Sheintuch, M. and Schmitz, R. A., Catal. Rev. 1975 15 107.

6 Sheintuch, M. and Schmitz, R. A., Chemical Reaction Engineering - Houston, ACS Symposium Series 1978 165 487.

7 Cutlip, M. B. and Kenney, C. N., Chemical Reaction Engineering - Houston, ACS Symposium Series 1978 165 475.

8 Pikios, C. A. and Luss, D., Chem. Eng. Sci. 1977 32 191.

9 Nayfeh, A. Perturbation Methods, Wiley, New York 1973.

10 Keener, J.P. and Cohen, D. S., Nucl. Sci. Eng. 1975 56 354.

Notation

a_1	kinetic parameter
a_2	kinetic parameter
[A(g)]	concentration of reactant A(g)
AB	reaction product
[AS]	number of surface sites occupied by A(g)
b_1	kinetic parameter
b_2	kinetic parameter
[B(g)]	concentration of reactant B(g)
[BS]	number of surface sites occupied by B(g)
E_3	activation energy for the third reaction step
E_3^o	activation energy for the third reaction step for a bare catalytic surface
f_1	function defined by Eq. (7)
f_2	function defined by Eq. (8)
h_k	kth component of the vector $\underset{\sim}{H}(\underset{\sim}{x})$
h_{kz_i}	the derivative of the kth component of the vector $\underset{\sim}{H}(\underset{\sim}{x})$ with respect to z_i; $h_{kz_i}(0,0) \equiv h_{kz_i}(0)$.
k_1, k_{-1}	reaction rate coefficients defined by Eq. (1)
k_2, k_{-2}	reaction rate coefficients defined by Eq. (2)
k_3	reaction rate coefficient defined by Eq. (3)
L	total number of surface sites
$\underset{\approx}{P}$	Jacobian matrix defined by Eq. (12)
k	Boltzmann constant
[S]	number of unoccupied surface sites
t	dimensionless time
T	temperature
x	fractional surface coverage of adsorbed A(g)
x_-	initial value of x

x_s steady state value of x

y fractional surface coverage of adsorbed B(g)

y_o initial value of y

y_s steady state value of y

Greek Letters

$\alpha = \mu kT$

τ time

μ coefficient of surface heterogeneity

Table Captions

Table 1: Summary of the stability of the oscillatory solutions for different values of γ_1, γ_2 and the initial conditions.

Table 2: Summary of the results obtained from a perturbation from a unique steady state at the lower and upper bifurcation points.

Table 3: Comparison of frequencies and amplitudes of oscillatory solutions predicted theoretically with those obtained by numerical integration of the governing equations. The lower bifurcation point corresponds to $b_1 = 6.30 \times 10^{-4}$.

Table 1

Case	$\kappa > 0$	$-1 < \kappa < 0$	$\kappa < -1$
$\gamma_1 > 0, \gamma_2 > 0$	Stable periodic oscillations.	Stable periodic oscillations.	
$\gamma_1 < 0, \gamma_2 > 0$			Decaying periodic oscillations.
$\gamma_1 > 0, \gamma_2 < 0$			Growing periodic oscillations.
$\gamma_1 < 0, \gamma_2 < 0$	Decaying periodic oscillations.	Growing periodic oscillations.	

Table 2

Variation with respect to b_1	Variation with respect to b_2	Variation with respect to a_1	Variation with respect to a_2
	Lower Bifurcation		
$y_s = 0.159$	0.160	0.160	0.160
$x_s = 0.270$	0.270	0.270	0.270
$C = 3.41 \times 10^{-3}$	3.42×10^{-3}	2.90×10^{-3}	2.89×10^{-3}
$a_i = 8.40 \times 10^{-3}$	8.40×10^{-3}	8.43×10^{-3}	8.40×10^{-3}
$b_1 = 6.30 \times 10^{-4}$	7.00×10^{-4}	7.00×10^{-4}	7.00×10^{-4}
$a_2 = 8.40 \times 10^{-3}$	8.40×10^{-3}	8.40×10^{-3}	8.38×10^{-3}
$b_2 = 1.10 \times 10^{-3}$	1.18×10^{-3}	1.10×10^{-3}	1.10×10^{-3}
$\mu = 14.0$	14.0	14.0	14.0
$\gamma_1 = 103$	-62.3	-300	309
$\gamma_2 = 0.333$	0.316	0.216	0.217
	Upper Bifurcation		
$y_s = 0.276$	0.278	0.277	0.277
$x_s = 0.407$	0.411	0.409	0.410
$C = 2.06 \times 10^{-3}$	2.04×10^{-3}	2.63×10^{-3}	2.61×10^{-3}
$a_1 = 8.40 \times 10^{-3}$	8.40×10^{-3}	8.34×10^{-3}	8.40×10^{-3}
$b_1 = 7.61 \times 10^{-4}$	7.00×10^{-4}	7.00×10^{-4}	7.00×10^{-4}
$a_2 = 8.40 \times 10^{-3}$	8.40×10^{-3}	8.40×10^{-3}	8.46×10^{-3}
$b_2 = 1.10 \times 10^{-3}$	1.03×10^{-3}	1.10×10^{-3}	1.10×10^{-3}
$\mu = 14.0$	14.0	14.0	14.0
$\gamma_1 = -136$	97.8	63.2	-68.5
$\gamma_2 = -0.117$	-0.119	-3.03×10^{-2}	-3.36×10^{-2}

Table 3

b_1	Frequency			|x|			|y|		
	Theoretical Prediction	Numerical Solution	% Error*	Theoretical Prediction	Numerical Solution	% Error*	Theoretical Prediction	Numerical Solution	% Error*
6.60×10^{-4}	3.41×10^{-3}	2.24×10^{-3}	52%	9.68×10^{-2}	9.45×10^{-1}	2%	9.37×10^{-2}	9.49×10^{-2}	1%
6.70×10^{-4}	3.41×10^{-3}	2.24×10^{-3}	52%	1.12×10^{-1}	1.06×10^{-1}	6%	1.08×10^{-1}	1.07×10^{-1}	1%
6.80×10^{-4}	3.41×10^{-3}	2.24×10^{-3}	52%	1.25×10^{-1}	1.11×10^{-1}	13%	1.21×10^{-1}	1.14×10^{-1}	6%
6.90×10^{-4}	3.41×10^{-3}	2.24×10^{-3}	52%	1.37×10^{-1}	1.14×10^{-1}	20%	1.33×10^{-1}	1.14×10^{-1}	17%
7.00×10^{-4}	3.41×10^{-3}	2.24×10^{-3}	52%	1.48×10^{-1}	1.11×10^{-1}	33%	1.43×10^{-1}	1.17×10^{-1}	22%

*% error found by $\left|\frac{\text{Numerical Solution - Theoretical Prediction}}{\text{Numerical Solution}}\right| \times 100$

Figure Captions

Figure 1: $a_1 = a_2 = 8.40 \times 10^{-3}$

$b_2 = 1.10 \times 10^{-3}$

$\mu = 14.0$

—— stable steady state

++++++ unstable steady state

~~~ stable limit cycle

●● unstable limit cycle

Figure 2: $a_1 = a_2 = 8.40 \times 10^{-3}$

$b_1 = 7.00 \times 10^{-4}$

$\mu = 14.0$

—— stable steady state

++++++ unstable steady state

~~~ stable limit cycle

●●● unstable limit cycle

Figure 3: $a_2 = 8.40 \times 10^{-3}$

$b_1 = 7.00 \times 10^{-4}$

$b_2 = 1.10 \times 10^{-3}$

$\mu = 14.0$

—— stable steady state

++++++ unstable steady state

~~~ stable limit cycle

●●● unstable limit cycle
~~~

Figure 4: $a_1 = 8.40 \times 10^{-3}$

$b_1 = 7.00 \times 10^{-4}$

$b_2 = 1.10 \times 10^{-3}$

$\mu = 14.0$

—— stable steady state

++++ unstable steady state

ϖϖ stable limit cycle

●● unstable limit cycle

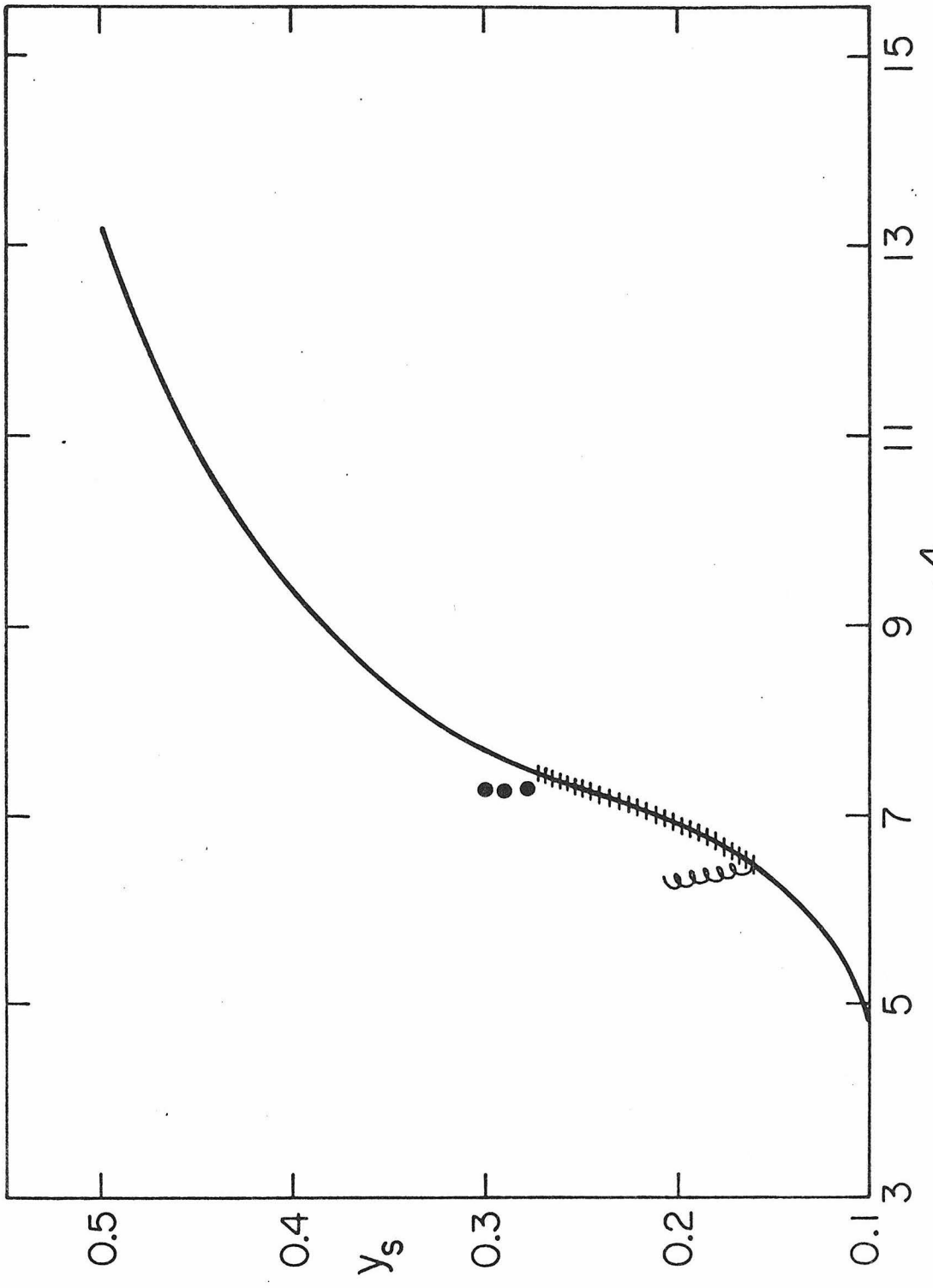

Fig. 1

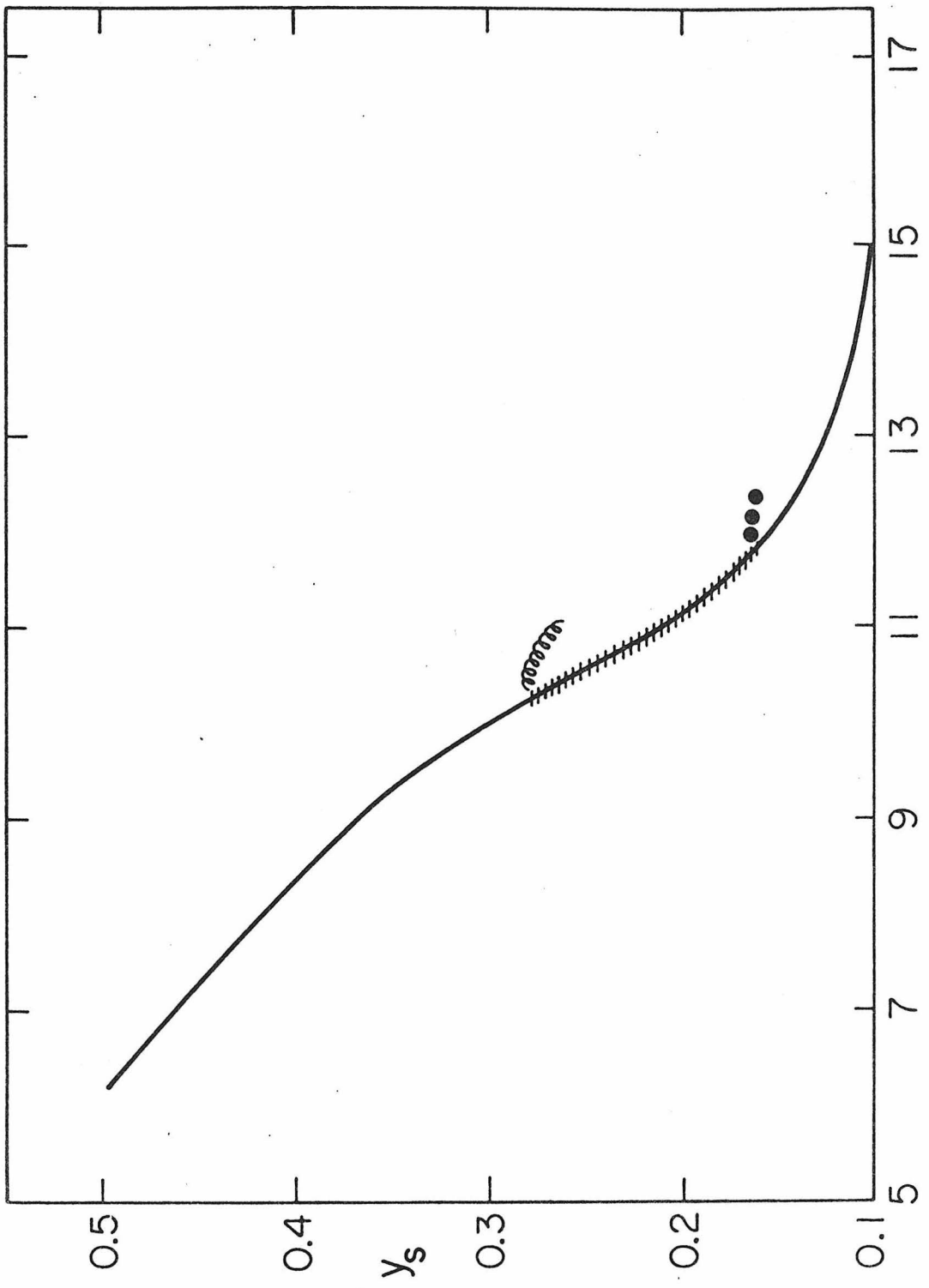

Fig. 2

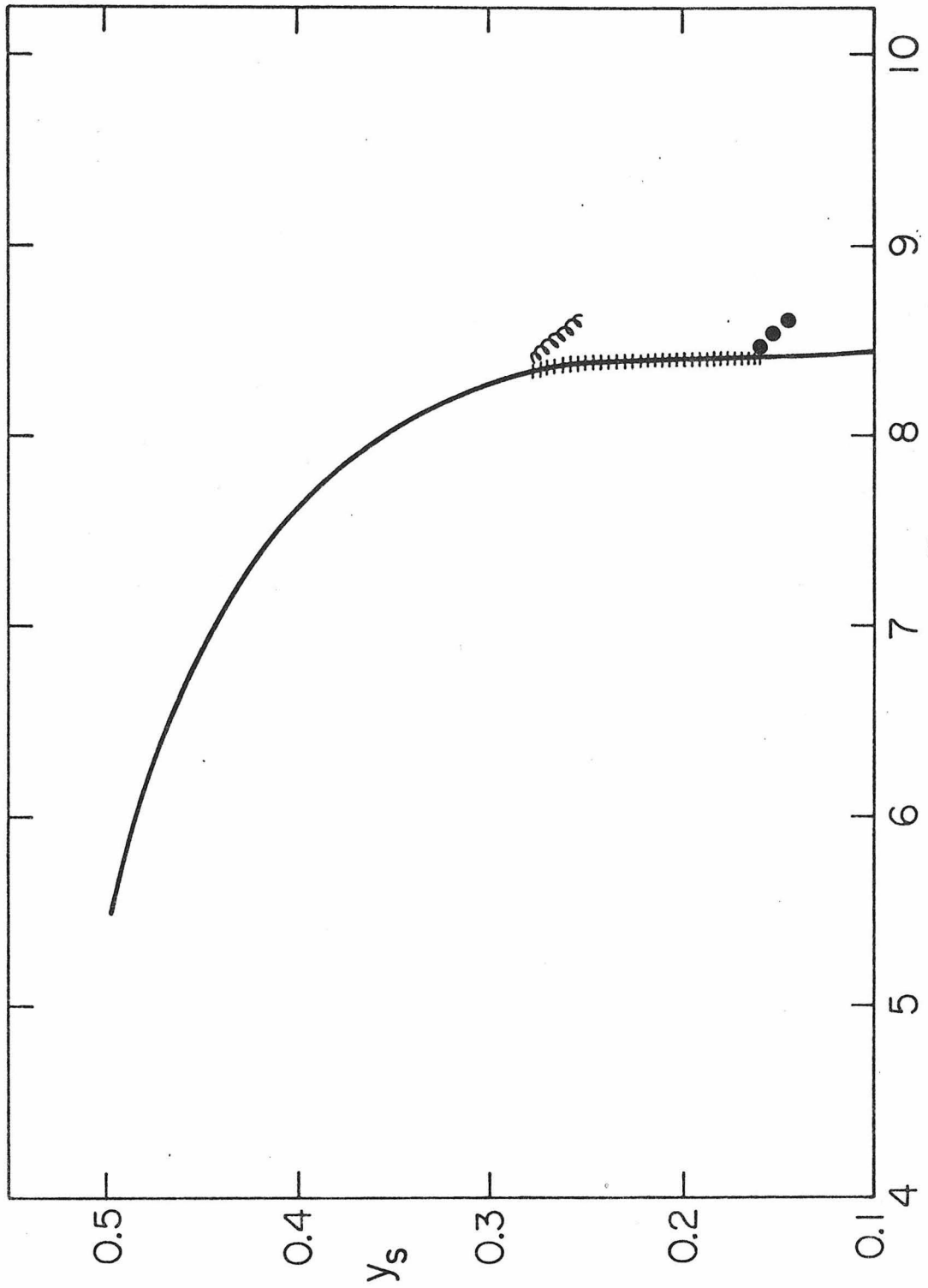

Fig. 3

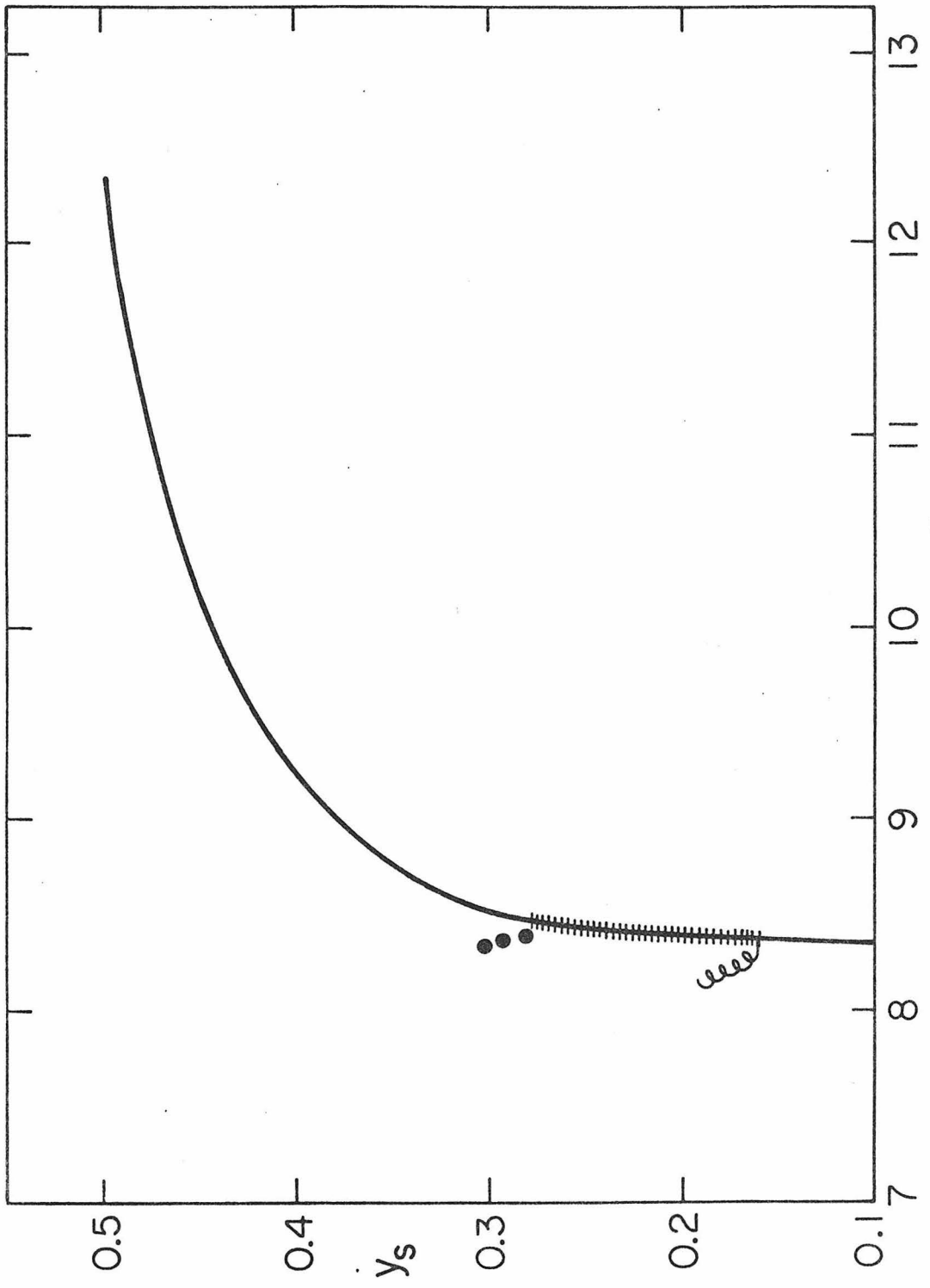

Fig. 4